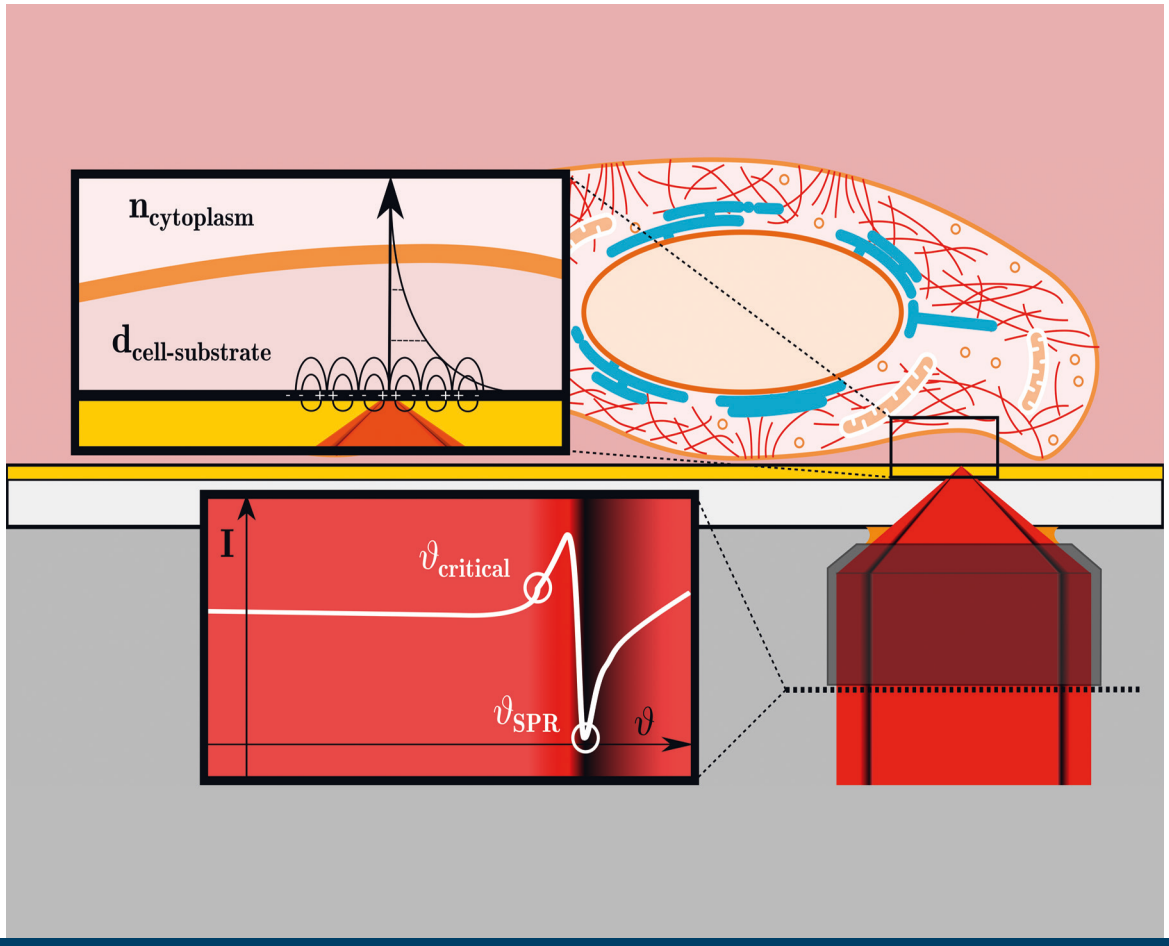


Surface Plasmon Resonance Microscopy for the Characterization of Cell-Substrate Distances

Justus Nándor Bednár

Schlüsseltechnologien / Key Technologies
Band / Volume 294
ISBN 978-3-95806-830-8

Mitglied der Helmholtz-Gemeinschaft

JÜLICH
Forschungszentrum

Schriften des Forschungszentrums Jülich
Reihe Schlüsseltechnologien / Key Technologies Band / Volume 294

Forschungszentrum Jülich GmbH
Institut für Biologische Informationsprozesse (IBI)
Bioelektronik (IBI-3)

Surface Plasmon Resonance Microscopy for the Characterization of Cell-Substrate Distances

Justus Nándor Bednár

Schriften des Forschungszentrums Jülich
Reihe Schlüsseltechnologien / Key Technologies Band / Volume 294

ISSN 1866-1807 ISBN 978-3-95806-830-8

Bibliografische Information der Deutschen Nationalbibliothek.
Die Deutsche Nationalbibliothek verzeichnet diese Publikation in der
Deutschen Nationalbibliografie; detaillierte Bibliografische Daten
sind im Internet über http://dnb.d-nb.de abrufbar.

Herausgeber und Vertrieb:	Forschungszentrum Jülich GmbH Zentralbibliothek, Verlag 52425 Jülich Tel.: +49 2461 61-5368 Fax: +49 2461 61-6103 zb-publikation@fz-juelich.de www.fz-juelich.de/zb
Umschlaggestaltung:	Grafische Medien, Forschungszentrum Jülich GmbH
Druck:	Grafische Medien, Forschungszentrum Jülich GmbH
Copyright:	Forschungszentrum Jülich 2025

Schriften des Forschungszentrums Jülich
Reihe Schlüsseltechnologien / Key Technologies, Band / Volume 294

D 82 (Diss. RWTH Aachen University, 2025)

ISSN 1866-1807
ISBN 978-3-95806-830-8

Vollständig frei verfügbar über das Publikationsportal des Forschungszentrums Jülich (JuSER)
unter www.fz-juelich.de/zb/openaccess.

This is an Open Access publication distributed under the terms of the Creative Commons Attribution License 4.0, which permits unrestricted use, distribution, and reproduction in any medium, provided the original work is properly cited.

Declaration in lieu of an oath

I, Justus Nándor Bednár, born on 26 December 1995 in Worms, Germany, hereby declare that this dissertation and the contents set out herein are mine and were generated independently as a result of my own original research.

I hereby declare in lieu of an oath that

- this thesis was written entirely during my time as a doctoral student at this faculty and university;
- to the extent that any part of this thesis has previously been used for an academic degree or other qualification at this or any other institution, this has been clearly indicated;
- whenever other third party or my own publications have been used, these have been clearly named;
- whenever quotations were made from third party publications or my own, the source has been indicated. This dissertation is entirely my own work, with the exception of these excerpts;
- all significant sources of support have been acknowledged;
- whenever any part of this thesis is based on collaboration with others, I have clearly labeled what others have done and what I have done;
- no part of this thesis has been published prior to its submission.

I am aware that a false declaration can cause legal action.

Aachen, Germany, 29 Nov 2024 **Justus Nándor Bednár**



"Our comforting conviction that the world makes sense rests on a secure foundation: our almost unlimited ability to ignore our ignorance."

– Daniel Kahneman

Abstract

Cell-substrate distances play an important role in many biomedical applications, including cancer therapies, drug development, implants, and fundamental neuroscience research. Several microscopic approaches have been established to measure cell-substrate distances, including surface plasmon resonance microscopy (SPRM). (Amplitude-scanning) SPRM, like other leading methods, provides nanometer-precise imaging of the cell-substrate distance with diffraction-limited lateral resolution. Also, it has the advantage of being both non-invasive and label-free. In addition to cell-substrate distances, the employed variant of SPRM provides simultaneously the cytoplasmic RI, which can be seen as a complement and a necessity.

One goal of this work is to make SPRM more accessible and reproducible through the development of an automated and robust data analysis, thereby reducing existing barriers for users and requirements for sample and measurement data. Related objectives are to determine the resulting measurement uncertainties, demonstrate the achievable, analyzable fraction of measurements, and to discuss measurement results in a method comparison.

In addition to primary measurements on an SPRM prototype, X-ray reflectometry (XRR), optical microscopy and atomic force microscopy (AFM) are used as secondary methods for verification and substrate-quality assessment. In particular, XRR offers untapped potential for the characterization of SPRM sensors.

The results of this work include the development and publication of a new data analysis software and the successful implementation and evaluation of a sphere-substrate distance measurement to validate the setup and data analysis. The latter allows the experimental determination of statistical and systematic measurement errors, rounded up to $\pm 5.8\,\mathrm{nm}$ (stat) $-5.2\,\mathrm{nm}$ (syst) on Au substrates and $\pm 8.9\,\mathrm{nm}$ (stat) $+6.3\,\mathrm{nm}$ (syst) on SiO_2 substrates. A data set of 68 SPRM measurements of HEK293 cell-substrate distances on SiO_2-coated substrates is then presented, comparing six common biochemical cell adhesion coatings with untreated SiO_2 surfaces. SPRM and XRR sensor characterizations are in agreement within measurement uncertainties. Analyzed cell-substrate distances are compared with previously published values measured by electron microscopy (TEM). It is noticeable that SPRM cell-substrate distances below $50\,\mathrm{nm}$ are rather rare ($8.9\,\%$) in contrast to TEM measurements ($44.5\,\%$). Another series of 25 neuron-substrate distance measurements on bare Au substrates, with or without one of two common cell adhesion coatings, is also presented. For those who are familiar with the challenges of amplitude-scanning SPRM, it should be emphasized that the presented series of cell-substrate distance measurements could be fully evaluated.

Zusammenfassung

Zell-Substrat-Abstände spielen eine wichtige Rolle in vielen biomedizinischen Anwendungen, einschließlich Krebstherapien, Arzneimittelentwicklung, Implantaten, und neurowissenschaftlicher Grundlagenforschung. Für die Messung des Zell-Substrat-Abstandes haben sich bereits einige Mikroskopieverfahren etabliert, darunter die Oberflächen-Plasmon-Resonanz-Mikroskopie (SPRM). (Amplituden-Raster) SPRM, wie andere führende Methoden, erlaubt eine nanometerpräzise, lateral beugungsbegrenzte Abbildung des Zell-Substrat Abstands. Darüber hinaus bietet sie dies nicht-invasiv und markerfrei. Zusätzlich zu Zell-Substrat-Abständen liefert die verwendete SPRM-Variante gleichzeitig den zytoplasmatischen Brechungsindex. Dies ist nicht nur eine interessante Ergänzung, sondern auch eine Notwendigkeit für die Genauigkeit dieser Art von Messung.

Ein Ziel dieser Arbeit ist es, durch die Entwicklung einer automatisierten und robusten Datenanalyse SPRM zugänglicher und reproduzierbarer zu machen. Bisher bestehende Hürden für Anwendende sowie Anforderungen an Proben und Messdaten sollen gesenkt werden. Ein damit verbundenes Ziel ist die Bestimmung der resultierenden Messunsicherheiten, die Demonstration des erreichbaren Anteils auswertbarer Messungen sowie die Diskussion der Messergebnisse im Methodenvergleich.

Neben der primären Durchführung von Messungen an einem SPRM-Prototypen werden Röntgenreflektometrie (XRR), Lichtmikroskopie und Rasterkraftmikroskopie als sekundäre Methoden ergänzend hinzugezogen. Insbesondere XRR bietet hier ein bisher ungenutztes Potential zur Charakterisierung von SPRM-Sensoren.

Die Ergebnisse dieser Arbeit umfassen die Entwicklung und Veröffentlichung einer neuen Datenanalyse-Software sowie die erfolgreiche Durchführung und Auswertung einer Kugel-Substrat-Abstandsmessung zur Validierung des Aufbaus und der Datenanalyse. Letztere ermöglicht erstmals die experimentelle Bestimmung von statistischen und systematischen Messfehlern, jeweils aufgerundet zu $\pm 5.8\,\mathrm{nm}$ (stat) $-5.2\,\mathrm{nm}$ (syst) auf Au-Substraten und $\pm 8.9\,\mathrm{nm}$ (stat) $+6.3\,\mathrm{nm}$ (syst) auf SiO_2-Substraten. Folgend wird ein Datensatz von 68 SPRM-Messungen von HEK293-Zell-Substrat-Abständen auf SiO_2-beschichteten Substraten präsentiert, wobei sechs gängige biochemische Zelladhäsionsbeschichtungen mit unbehandelten SiO_2-Oberflächen verglichen werden. Die Sensorcharakterisierungen mittels SPRM und XRR stimmen im Rahmen der Messunsicherheiten überein. Die ausgewerteten Zell-Substrat-Abstände werden mit elektronenmikroskopisch (TEM) gemessenen, bereits publizierten Werten verglichen. Am auffälligsten ist hier, dass SPRM-gemessene Zell-Substrat-Abstände unter $50\,\mathrm{nm}$ selten (8.9 %) sind im Gegensatz zu TEM-Messergebnissen (44.5 %). Eine weitere Messreihe von 25 Neuronen-Substrat Abstandsmessungen auf reinen Au-Substraten, mit oder ohne einer von zwei gängigen Zelladhäsionsbeschichtungen wird ebenfalls vorgestellt. Insbesondere für jene, die mit den Herausforderungen der Amplituden-Raster-SPRM vertraut sind, sei betont, dass die vorgestellten Messreihen vollständig ausgewertet werden konnten.

Contents

Abstract vii

Zusammenfassung viii

List of Figures xii

List of Tables xvii

List of Acronyms xviii

List of Symbols xxii

1. Introduction 1
1.1. General Introduction . . . 1
1.2. Project History . . . 2
1.3. Thesis Layout . . . 3

2. Review of Fundamentals 5
2.1. Cells and Cell Adhesion . . . 5
2.1.1. Neurons . . . 6
2.1.2. HEK293 Cells . . . 7
2.1.3. Cell Membranes . . . 8
2.1.4. Cell Adhesion . . . 9
2.2. Characterizing Cell-Substrate-Interfaces . . . 12
2.2.1. Non-Optical Methods . . . 12
2.2.2. Optical Methods . . . 13
2.3. Optics of Interfaces and Stratified Media . . . 17
2.3.1. Electromagnetic Waves in Dielectrics . . . 18
2.3.2. Reflection and Refraction at Interfaces . . . 19
2.3.3. Reflection at a Stratified Medium : Transfer-Matrix-Method . 22
2.3.4. Absorption . . . 27
2.3.5. Scattering . . . 28
2.4. Surface Plasmon Resonance . . . 29
2.4.1. Electromagnetic Waves in Metals . . . 29
2.4.2. Plasma Frequency of the Free Electron Gas . . . 30
2.4.3. Surface Plasmon Polariton (SPP) and Surface Plasmon (SP) . 31

2.4.4. SPP Excitation and Surface Plasmon Resonance (SPR) 33
2.5. Surface Plasmon Resonance Microscopy (SPRM) 34
2.5.1. Prism Based SPRM 35
2.5.2. Objective Based SPRM 36
2.5.3. Objective Focused Scanning SPRM 37
2.5.4. Objective Widefield Imaging SPRM 38
2.5.5. Amplitude Response SPRM 39
2.5.6. Phase Response SPRM 39
2.5.7. Holographic SPRM 39

3. Materials, Methods and Instrumentations 41
3.1. Substrate Fabrication 42
3.1.1. N-LAF21 Cover Glass 42
3.1.2. Metal Coatings and Passivation 42
3.2. Sample Preparation 44
3.2.1. Sensor Assembly 44
3.2.2. Sensor Sterilization 45
3.2.3. Cell-Adhesive Coatings on SiO_2 46
3.2.4. Cell-Adhesive Coatings on Au 48
3.3. Cell Culture 50
3.3.1. HEK293 Medium 50
3.3.2. Thawing and Freezing of HEK293 Cells 50
3.3.3. Maintenance of HEK293 Cells 51
3.3.4. Neuron Medium 52
3.3.5. Isolation of primary rat neurons 52
3.3.6. Maintenance of primary rat neurons 52
3.3.7. Buffers 52
3.4. Auxiliary Methods 53
3.4.1. Atomic Force Microscopy 53
3.4.2. X-Ray Reflectometry 54
3.4.3. Refractometry of Liquids 54
3.4.4. Compound Microscopes 54
3.4.5. Osmometry 55

4. Amplitude Response, Combined Scanning and Widefield SPRM 57
4.1. The Prototype Setup 57
4.2. Analysis Step I : Back-Focal Plane (BFP) Parametrization 62
4.2.1. Edge Detection 63
4.2.2. Aperture Fitting 64
4.2.3. Center Detection 67
4.3. Analysis Step II : Intensity-Angle-Profile Extraction 69
4.3.1. Radial Binning 69

4.3.2. Radius-to-Angle Mapping 70
4.3.3. Center Refinement 70
4.3.4. Handling of Defocusing 73
4.4. Necessary assumptions and simplifications 79
4.5. Analysis Step III : Layer Model Parameter Optimization 80
4.5.1. Objective Function 80
4.5.2. Optimization Algorithms 82
4.6. Reference Intensity Measurements 86

5. Sensor Characterization Results **91**
5.1. Brightfield Characterization 91
5.2. AFM Characterization 91
5.3. XRR Characterization 93
5.4. SPRM Characterization 94
5.5. Refractometry of Liquids 97
5.6. SPRM Refractive Index Validation Measurements 98
5.7. SPRM Specimen-Substrate-Distance Validation Measurements 99
5.8. SPRM Statistical and Systematic Uncertainty Estimation 106

6. SPRM Cell-Substrate-Distance Measurements **111**
6.1. HEK293-Substrate-Distance Measurements 111
6.2. Neuron-Substrate-Distance Measurements 116

7. Summary and Outlook **119**
7.1. Summary 119
7.2. Outlook 120

Acknowledgments **123**

A. Appendix **127**

B. Bibliography **175**

C. Chemicals List **187**

List of Figures

2.1. Sketch of a eukaryotic cell with selected organelles to indicate the complexity of cellular organization. 5
2.2. Sketch of the cell membrane and some of its main components. 8
2.3. Sketch of the cell-cell and cell-matrix interface, visualizing different types of adhesion junctions. 10
2.4. Summarizing overview of methods for cell-substrate interface investigation. 12
2.5. Reflection and transmission of electromagnetic plane waves at interfaces. 20
2.6. SPP (excitation) at an interface. SPP field components and SPP dispersion relation. 33
2.7. Timeline of selected Surface Plasmon Resonance Microscopy (SPRM) milestones. 35
2.8. Sketch of an SPRM configuration with prism-coupling and objective-coupling. 36
2.9. Euler diagram of SPRM types and their relationship to each other. . 38

3.1. Visualization of sensor and sample (cross section) to clarify related terminology. 41
3.2. Technical drawing of the substrate cover glass, including dimensions and tolerances. 43
3.3. Non-proportional representation of the different substrate types used in this work. Not shown are reference substrates and substrates for lateral resolution characterization. Refractive Index Microscopy (RIM) substrates are only used for the RI validation measurements in section 5.6. 44
3.4. Photograph of two SPRM sensors (substrates glued to the bottom hole of Petri dishes) 45
3.5. Illustration of the molecular structure of Poly-L-Lysine, Poly-D-Lysine, Concanavalin-A, Fibronectin and Laminin. 49
3.6. Picture of the Abbe refractometer used and photographs taken through the left and right eyepieces. 56

4.1. Simplified sketch of relevant beam paths in the SPRM prototype setup used throughout this work. 58

4.2. Sketch of the light-sample interaction in the measurement setup. A magnified view of the dotted area in fig. 4.1 60
4.3. Photo of the tiltable sample holder mounted in the piezo xy stage. . . 61
4.4. Visualized steps during Back-Focal Plane (BFP) image edge-detection. 65
4.5. Compressed representation of detected (aperture) edges in Cartesian and polar coordinates together with a fit. 66
4.6. Compressed representation of detected (resonance) edges in Cartesian and polar coordinates together with a fit. 68
4.7. Sketch of the beam path from the OP through the objective to the BFP. 71
4.8. Plot of segment-wise extracted BFP intensity profiles. 72
4.9. Violin plot with distributions of evaluated SPR positions in each BFP segment for example measurement MID007. 73
4.10. Spatial mapping of SPR angles for example measurement MID007. . . 74
4.11. Illustration of the relationship between reflected beam cross-section and BFP beam cross-section, depending on defocus. 76
4.12. Illustration of a concept to compensate for defocus effects after BFP intensity profile extraction. 78
4.13. Illustrations BFP intensity distribution, BFP polar coordinate system and BFP light polarization. 81
4.14. Contour plot of SPR angle and critical angle as a function of cell-substrate distance and cytoplasm RI. 84
4.15. Contour plot of SPR angle and SPR width as a function of cell-substrate distance and cytoplasm RI. 85
4.16. Structure of reference intensity measurement substrate and example images of BFP reference intensity distribution. 87
4.17. Evaluation of reference intensity measurements for illumination reconstruction. 88

5.1. EVOS^{TM} M5000 brightfield images of SiO_2 sensor substrates SID100 and SID138. 92
5.2. Angular XRR spectrum of a Au substrate and its fit. 93
5.3. Refractive indices of EtOH, H_2O (MilliQ) and air determined by RIM at room temperature ($\sim$20 C). 99
5.4. SiO_2 ball lens sample photo and 3D plot of the sphere-substrate distance. 100
5.5. Evaluation of sphere-substrate distance validation measurement with SiO_2 sphere on Au substrate. 101
5.6. Refractive Indexs (RIs) of the SiO_2 sphere determined with a Au sensor around the sphere-substrate contact. 102
5.7. Estimation of specimen-substrate separation measurement statistical and systematic error. (SiO_2 sphere on Au substrate) 103
5.8. Evaluation of sphere-substrate distance validation measurement with SiO_2 sphere on SiO_2 substrate. 104

5.9. RIs of the SiO_2 sphere determined with a SiO_2 sensor around the sphere-substrate contact. 104
5.10. Estimation of specimen-substrate separation measurement statistical and systematic error. (SiO_2 sphere on SiO_2 substrate) 105
5.11. Evaluation of both sphere-substrate distance validation measurements with and without defocus compensation. 106
5.12. Relationship between SPR angle and specimen-substrate distance for Au and SiO_2 sensors with given sample RI values. 107
5.13. Distance dependent factors for uncertainty propagation. 109

6.1. Histograms of HEK293 cell-substrate distances by substrate coating. . 113
6.2. Histograms of neuron-substrate distances by substrate coating. 117

A.1. Illustration of the working distance adjusting role of cover glass and immersion oil. 128
A.2. Plot of remaining reflectance between objective and cover glass, depending on RI matching. 128
A.3. Top camera view of the objective before and after cleaning. 129
A.4. Image of two Au substrate SPRM sensors, with and without thermally induced substrate curvature. 129
A.5. Photographs showing the visible thickness difference between two Cr coatings produced at different vacuum qualities. 130
A.6. AFM measurement of substrate layer thickness. 131
A.7. AFM measurements (5 µm x 5 µm) of Cr- and Au-layer topography. . . 132
A.8. AFM measurements (50 µm x 50 µm and 100 µm x 100 µm) of Cr- and Au-layer topography. 133
A.9. Sketch of halogen illumination light paths for top camera reflection mode imaging and OP camera transmission mode imaging. 134
A.10. Radial coordinate distribution of detected edge pixels around the radial position of SPR minimum in multiple angular segments. 135
A.11. Radial coordinate distribution of detected edge pixels around the radial position of aperture in multiple angular segments. of aperture in multiple angular segments. 136
A.12. Comparison of AIC values for the four BFP image aperture fitting models. 137
A.13. Distribution of the aperture size parameter r_{max}, extracted from the double ellipse model. 137
A.14. A geometrical construction of relevant light rays at the sample interface 138
A.15. Overview of all determined PRP coordinates in example measurement MID007 together with possible aggregate values. 139
A.16. Spatial mapping of PRP coordinate deviation from mean values for example measurement MID007. 140

A.17. Spatial mapping of SPR radii, visualizing the selection of control measurement spots to find substrate parameters. 141
A.18. Overview of cell-substrate distance errors in the evaluation of a simulated data set (cell on SiO_2 sensor), showing the error propagation of the BFP parameters x_0 and r_{max}. 142
A.19. Up to linear contribution to the median systematic cell-substrate distance error, depending on the error in cell medium RI. 143
A.20. Visualization of deviations from ground truth cell-substrate interface parameters for different weighting and fitting methods, using a simulated noise-free dataset. 145
A.21. Example fit of SPRM reflectance data with Gaussian weighting. . . . 146
A.22. Example fit of SPRM reflectance data with uniform weighting carried out in three steps. 147
A.23. Evaluation of both sphere-to-substrate distance validation measurements with comparison of both fit algorithms on each. 148
A.24. Estimated errors of single-fit (Gaussian weighting) evaluation of the MID075 sphere-on-SiO_2 validation measurement, depending on weighting distribution width. 149
A.25. Estimated errors of single-fit (Gaussian weighting) evaluation of the MID074 sphere-on-Au validation measurement, depending on weighting distribution width. 150
A.26. SiO_2 Substrate layer thicknesses determined by SPRM and XRR. . . 151
A.27. Histograms of cell-substrate distances by BFP segment and by coating. 155
A.28. HEK293 Cell-substrate-distance and cytoplasm-RI distribution and correlation from raw data of the left and top BFP segment. 156
A.29. HEK293 Cell-substrate-distance and cytoplasm-RI distribution and correlation from raw data of the right and bottom BFP segment. . . . 157
A.30. Color plots of fitted cell-substrate distances from all 68 HEK293 measurements (color scale up to 300 nm). 158
A.31. Color plots of the fitted cytoplasmic RIs of all 68 HEK293 measurements. 159
A.32. Color plots of the determined SPR angles of all 68 HEK293 measurements. 160
A.33. Color plots of the determined SPR peak widths of all 68 HEK293 measurements. 161
A.34. All hand-drawn labels for all 68 HEK293 measurements, cell by cell and BFP segment by BFP segment. 162
A.35. Color plots of fitted cell-substrate distances from all 68 HEK293 measurements (color scale up to 500 nm). 163
A.36. SPRM widefield images of HEK293 cells before each SPRM area scan (100x TIRF objective). 164

A.37. Top camera images of the halogen-illuminated Human Embryonic Kidney 293 Cells (HEK293 cells) before each sprm area scan (20x air objective). 165
A.38. Superimposed top camera images of HEK293 cells before and after each SPRM area scan (20x air objective). 166
A.39. Overview of all neuron-substrate distance measurements on Au substrates: Brightfield, widefield SPRM, neuron-substrate distance & cytoplasm RI 168
A.40. Au substrate layer parameters and neuron medium RI, determined by SPRM and XRR / Abbe refractometer, as well as neuron-substrate distance and cytoplasmic RI distribution. 169

List of Tables

5.1. AFM measured layer thicknesses of Au substrates. 92
5.2. XRR determined layer thickness and RMS layer roughness by sample batch. 94
5.3. Stratified layer model of a HEK293 cell on a coated SiO_2 substrate. . 96
5.4. Stratified layer model of a neuron on a coated Au substrate. 96
5.5. Cell medium RI values measured with an Abbe refractometer. 97

A.1. Overview of presented SPRM measurements on HEK293. 170
A.2. Overview of various presented SPRM measurements. 172
A.3. Overview of presented SPRM measurements on neurons. 173

List of Acronyms

AFM Atomic Force Microscopy.

AIC Akaike Information Criterion.

ALD Atomic Layer Deposition.

AMPGO Adaptive Memory Programming for Global Optimization.

BFP Back-Focal Plane.

Con-A Concanavalin-A.

dSTORM Direct Stochastic Optical Reconstruction Microscopy.

EC Extinction Coefficient.

ECIS Electric Cell-Substrate Impedance Sensing.

ECM Extracellular Matrix Gel.

EM Electron Microscopy.

FIB Fibronectin.

FLIC Fluorescence Interference Contrast.

FOV Field of View.

FRET Förster Resonance Energy Transfer.

GIETM Graphene Induced Energy Transfer Microscopy.

GUV Giant Unilamellar Vesicle.

HEK293 cells Human Embryonic Kidney 293 Cells.

HNF Helmholtz Nano Facility.

IMI Insulator-Metal-Insulator.

ISCAT Interferometric Scattering.

LAM Laminin.

LED Light Emitting Diode.

MEA Micro Electrode Array.

MIET Metal Induced Energy Transfer.

NA Numerical Aperture.

OP Object Plane.

PBS Phosphate Buffer Solution.

PDL Poly(D)lysine.

PECVD Plasma-Enhanced Chemical Vapor Deposition.

PLL Poly(L)lysine.

PRP Perpendicular Reflection Pixel.

PS Penicillin-Streptomycin.

QCM Quartz Crystal Microbalance.

RI Refractive Index.

RICM Reflection Interference Contrast Microscopy.

RIM Refractive Index Microscopy.

RMS Root Mean Square.

ROI Region of Interest.

SLB Supported Lipid Bilayer.

SMLM Single Molecule Localization Microscopy.

SNR Signal-to-Noise Ratio.

SP Surface Plasmon.

SPP Surface Plasmon Polaritons.

SPR Surface Plasmon Resonance.

SPRHM Surface Plasmon Resonance Holographic Microscopy.

SPRM Surface Plasmon Resonance Microscopy.

TE Transverse Electric.

TEM Transmission Electron Microscopy.

TIRFM Total Internal Reflection Fluorescence Microscopy.

TM Transverse Magnetic.

TMM Transfer Matrix Method.

XRR X-ray Reflectometry.

List of Symbols

Symbol	Meaning	Unit
t	time	s
c	speed of light	m/s
c_0	speed of light in vacuum	m/s
ω	circular (optical) frequency	1/s
λ	wavelength	m
n	real-valued refractive index	1
$\tilde{n}$	complex refractive index	1
κ	extinction coefficient	1
ϵ_r	relative permittivity	1
ϵ_0	permittivity of free space	F/m
μ_r	relative permeability	1
μ_0	permeability of free space	H/m
σ	electrical conductivity	S/m
$\mathbf{E}$	electrical field vector	V/m
$\mathbf{H}$	magnetic field vector	A/m
$\mathbf{J}$	current density	$\mathrm{A/m^2}$
$\mathbf{D}$	electric flux density vector	$\mathrm{C\,m^{-2}}$
$\mathbf{P}$	electric polarization density vector	$\mathrm{C\,m^{-2}}$
ρ	charge volume density	$\mathrm{C/m^3}$
$\mathbf{k}$	wave vector	1/m
$\mathbf{k}_0$	wave vector in vacuum	1/m
$R_{p/s}$	sample reflectance for p/s-polarized light	1
$r_{p/s}$	Fresnel reflection coefficient for p/s-polarized light	1
I	intensity	$\mathrm{W/m^2}$
L	illumination	$\mathrm{W/m^2}$
NA	numerical aperture	1
$\theta_{\max}$	maximum aperture opening angle	rad

Symbol	Meaning	Unit
θ_{SPR}	surface plasmon resonance angle	rad
θ	angle of reflection	rad
x_0, y_0	coordinates of the BFP image center	pixels
r	radial coordinate in BFP images	pixels
r_{max}	BFP radial coordinate of a marginal ray	pixels
$n_{\mathrm{N\text{-}LAF21}}$	refractive index of substrate material N-LAF21	1
Δz	defocusing	m
Δi	defocusing index shift[1]	1
ϕ	angular coordinate within the BFP	rad
h	specimen-/cell-substrate distance	nm

[1] Width of the illuminated area on the sample in units of the scanning stage step size.

1 Introduction

1.1. General Introduction

The cell-substrate interface plays a crucial role in many aspects of biomedicine, for example: in the study of cancer cells [79]; in the question of cytotoxicity and cell morphology during drug development [51]; in the study of cell adhesion on e.g. vascular grafts [17]; in the understanding of collective cell migration in e.g. wound healing [122]; and in the evaluation of in vitro electrophysiological experiments for basic neuroscience research [143]. The latter one is especially relevant at this institute and plays a key role in the understanding and treatment of neurodegenerative diseases such as Alzheimer's, Parkinson's, Huntington's and ALS. [42]

To elaborate on the last example, when performing in vitro electrophysiological experiments using microelectrode arrays, knowledge of the cell-substrate distance is required for interpretation of the measured signal amplitudes. This requirement has its roots in modeling the electrical transfer function between the neuron and the probe electrode, usually by means of the point-contact model [16]. This model contains several free parameters to be determined, such as cell-electrode contact area, cell-surface area, electrical membrane capacitance, membrane resistance and the characteristic parameter of the seal resistance, which can be interpreted to quantify the overall electrical coupling between cell and electrode. However, the seal resistance is inversely proportional to the cell-substrate distance, so knowledge of the latter is essential for its estimation [34].

While there are a few non-optical approaches to cell-substrate interface studies, such as critical shear stress measurements [31], Quartz Crystal Microbalance (QCM) measurements [48] and Electric Cell-Substrate Impedance Sensing (ECIS) [20], only ECIS is able to provide an estimate of the average cell-substrate distance [105]. Optical methods, on the other hand, have been shown to map cell-substrate distances with nm precision and diffraction-limited lateral resolution, such as Total Internal Reflection Fluorescence Microscopy (TIRFM) [22], Fluorescence Interference Contrast (FLIC) [36], Reflection Interference Contrast Microscopy (RICM) [68], Electron Microscopy (EM) [65], Metal Induced Energy Transfer (MIET) [99] and SPRM [108].

However, a drawback of some of these methods is the reliance on knowledge of the intracellular RI, which can vary over a range of about 1.34-1.40 ($\lambda = 632.8\,\mathrm{nm}$) [97]. As shown by Kreysing et. al. [108], an assumed constant RI in SPRM can lead to measurement errors in the range of 100 nm, rendering accurate measurements impossible.

While the methods of EM and MIETM are intrinsically independent of assumptions about intracellular RI, Kreysing et al. presented a data analysis scheme for amplitude-scanning SPRM that allows the simultaneous co-determination of cytoplasmic RI. [108] While this adds SPRM to the leading methods for determining cell-substrate distances, SPRM has the advantage over EM and MIETM in that it operates both non-invasive and label-free.

1.2. Project History

The work on label-free cell-substrate distance measurements using SPRM was originally started at the Institute of Bioelectronics (IBI-3) by Koji Toma, a postdoctoral researcher who had previously worked on plasmonic sensing with Wolfgang Knoll, and who was trained in SPRM by Hiroshi Kano, the two inventors of objective-focused scanning SPRM. In its original configuration, the SPRM setup at IBI-3 was already a combined widefield and scanning setup, as inspired by Watanabe et al. [83]. Using a partially manual data analysis approach, HEK293 cell-substrate distances were the first to be published using this setup [89].

The project was later adopted by Eva Kreysing as a Ph.D. student, who continued the development through various design iterations, most notably the use of a projector light source instead of a laser to eliminate speckle noise, and the use of a liquid crystal radial polarizer instead of the four-plate ZPol approximate radial polarizer. [107] Most importantly, however, she recognized and communicated the importance of cytoplasmic RI in SPRM cell-substrate distance measurements, transforming the data analysis approach to incorporate simultaneous RI co-determination [108]. She investigated cell-substrate distances and RI variations in beating cardiomyocyte cells [108] and later compared cell-substrate distances of neurons between SPRM and EM measurements for investigating artifacts in EM sample preparation [121]. In doing so, she demonstrated the full potential and reliability of this method.

Hossein Hassani, who was introduced to SPRM as a master's student supervised by Eva Kreysing and assisted in the development of the data acquisition and analysis software, soon took over the project as a Ph.D. student. Some design iterations of the setup were introduced. A multi-angle widefield approach was introduced for increased lateral resolution. A laser illumination with reduced coherence and an

LED illumination were introduced to improve the Signal-to-Noise Ratio (SNR) of measurements. Other design choices were reversed. From projector illumination he returned back to a laser illumination for higher imaging speeds. From the liquid crystal radial polarizer he returned back to the original four-plate ZPol polarizer due to practical problems with the former. [123] Perhaps most importantly, he recognized and established new imaging modes of the present setup, such as a platinum substrate imaging mode for small angle imaging [120] and a RIM mode using bare glass substrates [123].

Having inherited the setup after Hossein Hassani left the institute, I, Justus Bednár, was given the opportunity to take SPRM imaging further at the Institute of Bioelectronics. Thanks to the dedication and co-supervision of Eva Kreysing, much of the original knowledge has been passed on. While some further design changes to the setup would be necessary for future projects, the focus of this work has been on the scalability of data acquisition and analysis. The capabilities of the setup had been demonstrated in previous projects. However, for the sensitive but delicate data analysis procedure, the majority of measurements had to be hand-picked from those that were too noisy and potentially defocused. In addition, the need for manual data analysis input at various steps of the analysis procedure made the results highly dependent on user expertise and less reproducible. [124]

1.3. Thesis Layout

This thesis begins with an overview of the scientific foundations of this work, providing the context and necessary background knowledge in chapter 2. A brief summary of the biology of cells and cell-substrate interfaces, necessary for later discussion, is given in section 2.1. A more comprehensive comparison of existing methods for investigating cell-substrate interfaces is provided in section 2.2. The brief and partial review of electromagnetism in section 2.3 builds up to the simplified derivation of the central Transfer Matrix Method (TMM) in section 2.3.3 for modeling reflectance data. The advantage of a simplified derivation of the TMM is that it provides a more transparent insight into the assumptions behind reflectance modeling, balancing generality with 'simplicity', as appropriate for this use case. On the other hand, the generalization of the TMM to metal layers is outlined in section 2.3.4, as it is central to the description of Surface Plasmon Resonance (SPR). SPR is then introduced and discussed from a more conventional perspective in section 2.4. In section 2.5, an overview of the various sub-branches of SPRM is given, with an emphasis on the historical perspective.

An overview of the materials and methods used, with the exception of SPRM, and an overview of complementary measurements is given in chapter 3. The topic of

SPRM substrate fabrication is addressed in section 3.1. The steps of sensor assembly from substrates and subsequent treatments are outlined in section 3.2. The cell culture protocols and steps that turn sensors into samples are discussed in section 3.3. Finally, remaining noteworthy supplementary experimental methods are specified in section 3.4.

Chapter 4 contains a description of the experimental SPRM setup, as inherited from Hossein Hassani, as well as an explanation of the main components of the data analysis. The latter is also a central result of my work. After a description of the setup in section 4.1, section 4.4 takes some space to reflect on a few assumptions. The data analysis algorithm consists of three main parts. Sections 4.2, 4.3 and 4.5 deal with each part, explaining the main ideas and principles behind each approach. Section 4.6 adds a description of the data analysis treatment for reference illumination intensity that is separate from the three main steps. While key design choices in the data analysis software are rationalized in this chapter, this should not obscure the fact that many decisions were made heuristically. In order to provide maximum transparency, the data analysis software is published and documented as "SPRManalysis-2" [144].

Chapter 5 provides an overview of the measurement results for the characterization of SPRM sensors (substrates). It includes results from brightfield microscopy (section 5.1), AFM (section 5.2), XRR (section 5.3) and SPRM (section 5.4). In addition, RI measurements by refractometer (section 5.5) are also listed. Sections 5.6 and 5.7 present and discuss test measurements to validate the RI and specimen-substrate distance results obtained by measurement and data analysis. Validation of specimen-substrate distance measurements is of particular importance. The quality of the results obtained allows, for the first time, a discussion of experimentally determined statistical and systematic measurement errors. The chapter concludes with section 5.8, a theoretical discussion of statistical and systematic measurement uncertainties. In both, sections 5.7 and 5.8, the performance of the two different SPRM sensor types (Au and SiO_2) is discussed in comparison.

Finally, chapter 6 contains the main body of experiment description and experimental data on cell-substrate distances. Discussed are results obtained for HEK293 cells (section 6.1) from an extensive series of 68 measurements, and for neurons (section 6.2) in an intermediate dataset of 26 measurements.

Chapter 7 summarizes the principle results of this work and looks at potential future directions for the project.

2 Review of Fundamentals

2.1. Cells and Cell Adhesion

This section reviews the biology of cells and cell interfaces to prepare for the interpretation of measurement results in chapter 6. Unless otherwise stated, the content of this section is based on the textbook "Molecular Biology of the Cell" by B. Alberts et al. [49].

Eukaryotic cells are among the smallest known forms of life and are also the smallest living components of larger forms of life such as mammals. They are enclosed and compartmentalized by membranes, have DNA-encoded program instructions, an independent metabolism in exchange with their environment, catalyze and regulate complex chemical reactions, grow and reproduce independently, and show evolutionary adaptation, thus exhibiting the key characteristics of life listed by the Max Planck Society. [139] A drawing of a eukaryotic cell is shown in fig. 2.1, showing some of the main structural elements and conveying some of the complexity within.

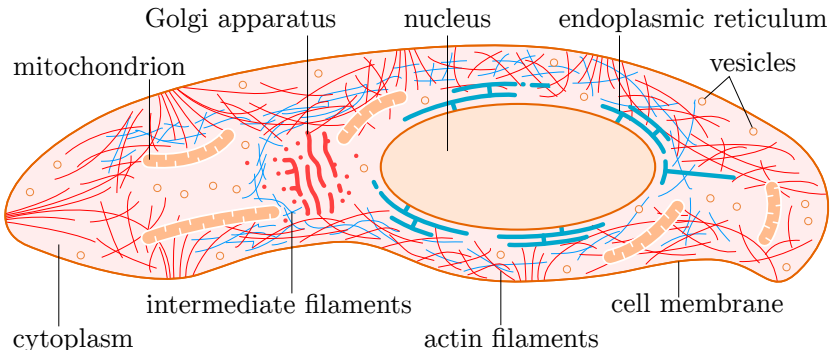


Figure 2.1.: Sketch of a eukaryotic cell with selected organelles to indicate the complexity of cellular organization. The diameter of a cell is about (10-15) µm in the case of Human Embryonic Kidney 293 Cells (HEK293 cells) and (10-30) µm in the case of neurons (soma). Sketch adapted from [49, Ch. 1].

The cell membrane, discussed in detail in section 2.1.3 and fig. 2.2, plays an important role in this work. And not only is the cell as a whole surrounded by a membrane - most organelles, including the nucleus, endoplasmic reticulum, Golgi apparatus and mitochondria, are separated from the rest of the cell by membranes. The density of proteins and nucleic acids gives the cell an increased optical Refractive Index (RI) (see section 2.3.1) relative to its surrounding medium. Depending on the organelle and the density and charge of the biomolecules enclosed within it, their RI differs from that of the cytoplasm, a fact that is exploited, for example, in differential interference contrast (DIC) microscopy.

Most cells in culture require the presence of a substrate. The properties of substrates, particularly physiochemical properties, influence the characteristics, health and proliferation of the cell. [73]

2.1.1. Neurons

Neurons (nerve cells) are the fundamental units of the nervous system, responsible for information processing in most animals. They are cells that specialize in processing and transmitting information in the form of electrical and chemical signals. In terms of structure, neurons can be roughly divided into three parts:

The soma (cell body) is responsible for basic cell functions and contains most cell organelles as well as the cell nucleus.

Dendrites are narrow, branched, long protrusions of the cell membrane that extend from the cell body. Their elongated and highly branched structure allows them to receive signals from up to 100 000 possibly distant neurons. They transmit them to the cell body.

The axon, normally a single one, also a protrusion of the cell membrane, carries signals from the cell body to other neurons. Axons can be less than 1 mm to over 1 m long and branch at their end. **Neurites** is an umbrella term for both dendrites and axons.

The generation and transmission of intracellular signals takes place via an electrical depolarization of the membrane, which is polarized to a certain resting potential in its resting state. Such membrane depolarization, whether spontaneous or externally induced, propagates through the cell across the membrane in either a passive or an amplified form, depending on the neuron. Regarding intercellular signaling, in most cases there is a chemical synapse at the interface between two neurons, which converts internal electrical signals of the presynaptic cell into chemical signals, which in turn may trigger electrical signals in the postsynaptic cell. Without going into detail, cascading activations of the cell membrane that cause large electrical signals

are referred to as action potentials.

Since neurons and their activation patterns are responsible for a wide range of control tasks in the human organism, there is also a wide range of severe neurodegenerative diseases, such as Alzheimer's, Parkinson's, Huntington's and amyotrophic lateral sclerosis (ALS). [42] Both neuroimplants and in vitro Micro Electrode Array (MEA) platforms are seen as promising route for the development of corresponding therapies. In both cases, the approach is to measure or selectively influence the activation patterns of neurons via electrode contacts. In the case of neuroimplants, cochlear implants for hearing restoration and deep brain implants for Parkinson's disease are two prime examples of therapeutic success. [42] While MEAs play an important role in the development of neuroimplants, they also enable the study of neurodegenerative diseases in vitro under controlled laboratory conditions. [85]

Since knowledge of cell-electrode distances is a prerequisite for the interpretation of extracellular MEA signals, this work plays a particularly important role in the case of neurons. The cell-substrate distance, influencing the sealing resistance parameter, is an important feature of the point contact model for modeling the electrical transfer function between a cell and an electrode. [16]

Primary cells are cells from an organism that have not been genetically modified. In the case of neurons, the interest in their natural behavior makes primary cells much more relevant than cell lines. Therefore, primary embryonic rat neurons are used in this work. As a widely used experimental animal in neuroscience, the Wistar rat provides neurons with maximum genetic uniformity in a standardized and reliable manner. [24]

2.1.2. HEK293 Cells

HEK293 cells are derived from human embryonic kidney cells, which were immortalized in the 1970s through genetic modification. [57] This means that the cells can divide indefinitely in culture. For this reason, but also because of their ease of handling, rapid growth, robustness and high (DNA) transfection efficiency, HEK293 cells are one of the most widely used cell lines. [57] Since these cells naturally express various receptors and ion channels, similar to neurons, they are often used to study neurobiological questions. As in the case of neurons, the measurement of the cell-substrate distance is essential for the evaluation of MEA measurements. The availability of Electron Microscopy (EM) cell-substrate distance measurements, published in 2008 by Wrobel et al. [65], provides a valuable comparison of methods.

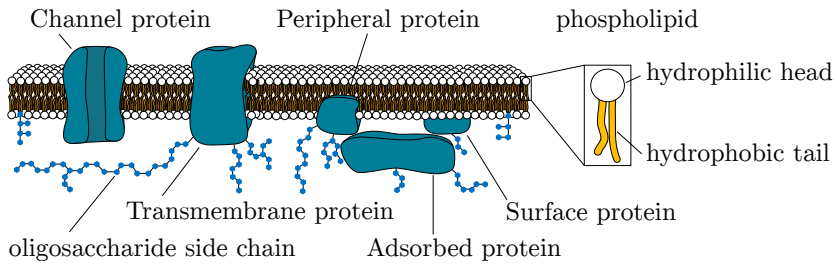


Figure 2.2.: Sketch of the cell membrane and some of its main components. The phospholipid bilayer provides the backbone. Integrated or associated are membrane proteins, of which some examples are shown. The carbohydrate-rich zone outside the cell membrane is called glycocalyx. The oligosaccharides that make up this layer can be anchored to lipids (glycolipids) or to proteins (glycoproteins). Sketch adapted from [49, Ch. 10] and [59].

2.1.3. Cell Membranes

The cell membrane separates the inside of a cell from the outside. It allows the cell to organize complex tasks such as metabolism, signaling and reproduction - in short, to stay alive - without violating the second law of thermodynamics (see [49, Ch. 2] for further reading). In addition, the membrane performs a whole range of specialized tasks that are beyond the scope of this section. An overview of membrane components and their influence on the cell-substrate distance is given below.

Lipid Bilayer

As shown in fig. 2.2, phospholipid molecules are the basic building block of the cell membrane. Their ambiphilic nature, consisting of hydrophilic heads and hydrophobic tails, allows them to self-assemble into lipid bilayers in an aqueous environment. This bilayer alone is approximately 5 nm thick [90, Sec. 12.5] and serves as a diffusion barrier. It is important to note that despite their organization, phospholipids retain a high degree of mobility, so we can think of a lipid bilayer as a two-dimensional liquid.

Membrane Proteins

Proteins are also components of the cell membrane; for example, they may be anchored only in the outer phospholipid layer (peripheral proteins), anchored through both phospholipid layers (transmembrane proteins), bound only to the lipid bilayer (surface proteins), or bound only to other proteins from the outside (adsorbed proteins).

Another category worth mentioning are channel protein, an example of how the cell membrane specifically controls molecular transport. As already discussed in [107], the extracellular part of some proteins, in particular integrins, measures around 20 nm, so that even in areas of close cell-substrate contact we should expect at least these molecular sizes as a cell-substrate distance.

Glycocalyx

At the outer edge of the cell membrane, cells usually have a carbohydrate layer thick enough to be visible on electron microscopy images. [66] This layer is called the glycocalyx and consists of oligosaccharide side chains of certain lipids (glycolipids) and proteins (glycoproteins). No literature was found on the thickness of the glycocalyx of HEK293 cells, and even for cell types where glycocalyx thickness has been reported, there is controversy on values depending on culture conditions, preparation and measurement methods. [66] For example, Chappell et al. [66], using EM, reported that the glycocalyx thickness of human umbilical vein endothelial cells averaged 878 nm ex vivo[1], but only 29.4 nm in vitro, and suggested that cell culture conditions were the reason for this difference. Human induced pluripotent stem cells (IPSCs) are considered a potential candidate for comparison with HEK283 cells due to their common human ancestry and early stage of development. An evaluation of the glycocalyx thickness of human IPSC-derived endothelial cells using super-resolution confocal Z-stack microscopy revealed mean values of around 2 µm under static cell culture conditions. [128] However, as these cells were cultured for 96 h and the glycocalyx thickness was only determined for the apical side, a comparison with HEK293 cells from this work may also not be very meaningful. Furthermore, the trypsin[2] used in the cell culture protocols could degrade the glycocalyx completely. However, HEK293 cells are fast growing cells. Therefore, we can only conclude at this point that the glycocalyx is expected to influence the measured cell substrate thickness, probably even more than extracellular parts of membrane proteins.

2.1.4. Cell Adhesion

A fundamental property of cells is their ability to interact adhesively. Among other functions, this gives organisms their mechanical stability. This fundamental interaction is mediated by junctions. Multiple relevant ways of categorizing junctions will be presented. Figure 2.3 provides an accompanying visual representation.

[1] Here: Tissue taken directly from human umbilical cords.
[2] Protein-degrading enzyme that also cleaves protein anchors of the glycocalyx.

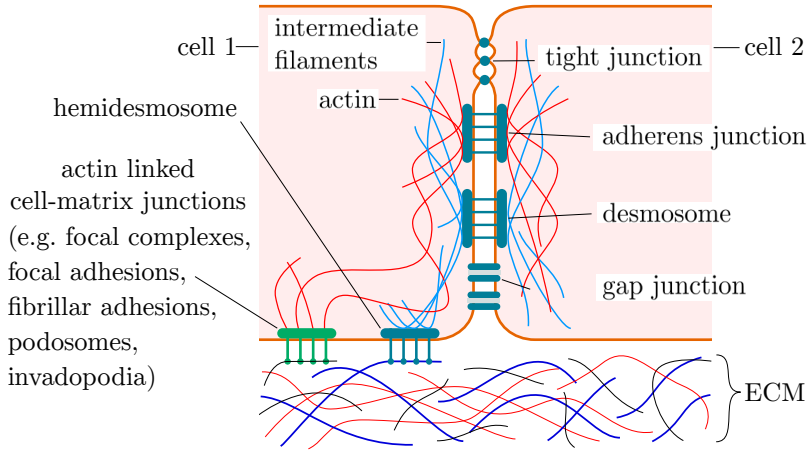


Figure 2.3.: Sketch of the cell-cell and cell-matrix interface, visualizing different types of adhesion junctions. Some actin fibers and intermediate filaments have been sketched to visualize the distinction between actin- and intermediate filament-linked junctions. The extracellular matrix (ECM) is shown in different colors to indicate its multi-component nature, with junction-anchoring components depending on the junction type. Sketch adapted from [49, Ch. 19].

Cell-Cell Adhesion vs. Cell-Matrix Adhesion

On the one hand, there are junctions for direct cell-cell adhesion, such as tight junctions, adherens junctions, desmosomes and gap junctions. On the other hand, there are junctions for (indirect) extracellular matrix (ECM)-mediated adhesion, such as hemidesmosomes, focal complexes [100], focal adhesions [100], fibrillar adhesions [100], podosomes [56] and invadopodia [56].

Functional Discrimination of Adhesive Junctions

Another axis of discrimination runs along functional roles. On the one hand, there are anchoring junctions, which primarily serve to mechanically anchor cells (e.g. adherens junctions, focal adhesions, desmosomes and hemidesmosomes); on the other hand, there are occluding junctions, which close diffusion pathways between cells (e.g. tight junctions); channel-forming junctions, which allow the exchange of small molecules across the cell membrane (e.g. gap junctions); and signaling junctions, such as the chemical synapses between neurons.

Actin-linked vs. Intermediate Filament-linked Junctions

The last axis of differentiation to be mentioned is the differentiation depending on the anchor point within the cell. In cell-cell adhesions, there are desmosomes, which connect the skeletons of the intermediate filaments of two cells, and adherens junctions, which connect the actin skeletons of two cells. In the case of cell-matrix adhesions, hemidesmosomes can be named in the case of intermediate filament-anchored binding, as well as focal complexes [100], focal adhesions [100], fibrillar adhesions [100], podosomes [56] and invadopodia [56] in the case of actin-anchored binding.

Cell-Matrix Junctions in HEK293 cells and neurons

Not all junctions are found in all cell types. For example, hemidesmosomes are mainly found in epithelial cells. Podosomes are typically found in cells of monocytic lineage [56] and invadopodia form in invasive cancer cells. [56]

Regarding HEK293 cells and cell-matrix adhesion sites, as these will be of interest for the interpretation of the results in this work, it can be expected to observe focal adhesions [58] and thus focal complexes as precursors of focal adhesions as well as fibrillar adhesions as a subsequent developmental stage of focal adhesions. [100]

In neurons, a type of junction similar to focal adhesions is reported. [115] These junctions locate at growth cones, which are characteristic protrusions of neurons that drive and steer the growth of neurites on their way to connect with other neurons.

Composition of Adhesive Junctions

Both cell-cell junctions and cell-matrix junctions are protein complexes composed of several intracellular and transmembrane proteins that together form a functional unit. Cadherins and integrins are two families of proteins that are particularly relevant here. Cadherins are proteins that are predominantly found in cell-cell junctions. Integrins are proteins that are predominantly found in cell-matrix junctions. As discussed by Kreysing [107], an integrin size of approximately 20 nm should be considered when discussing cell-substrate distances within cell-matrix junctions. This is also likely to be the minimum cell-substrate distance observed.

2.2. Characterizing Cell-Substrate-Interfaces

The study of cell-substrate-distances, cell-substrate-adhesion properties and cell motility on various materials is of interest to many biomedical applications like implants [17], wound healing [122], cancer therapy [79], drug development [51] and neuroelectronic applications [129, 143]. This section provides an overview of the methods available for this purpose. Presented methods are divided into optical and non-optical methods. Their advantages and disadvantages are compared. Figure 2.4 provides a graphical summary of this section. However, this overview is not exhaustive. Methods are considered quantitative here if they can predict the value of cell-substrate distance.

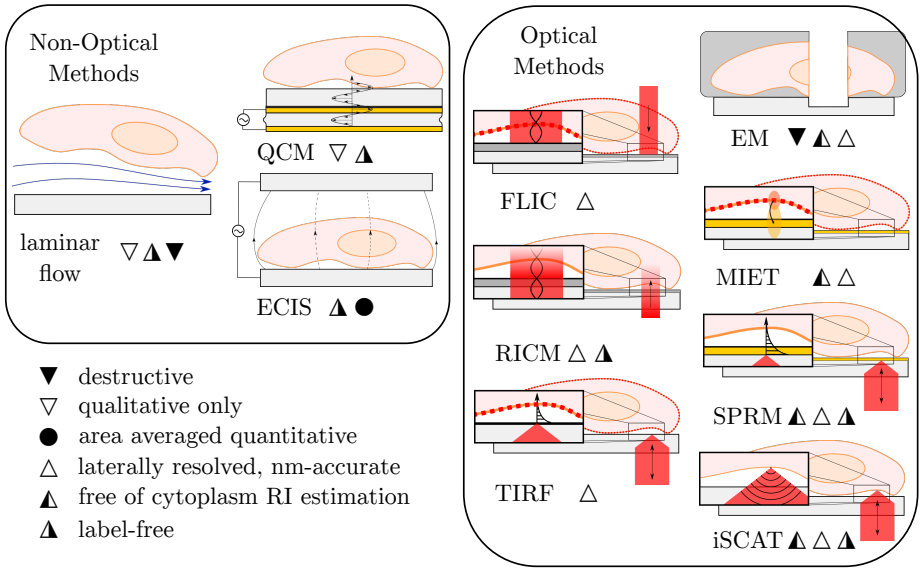


Figure 2.4.: Summarizing overview of methods for cell-substrate interface investigation with focus on methods for cell-substrate distance determination using a pictographic representation of methods.

2.2.1. Non-Optical Methods

Critical Shear Stress

A conceptually simple approach to analyzing cell-substrate adhesion is to determine the critical shear stress. The critical shear stress is defined as the hydrodynamic stress at which 50 % of all cells adhering to a surface detach. To determine this, a special flow chamber design is required, as in the work of Xiao and Truskey. [31] It

is therefore a purely mechanical method. As it detaches the cells from the surface, it is a destructive method. As it does not measure the cell-substrate distance, it is classified as non-quantitative.

QCM

Another mechanical, or more specifically acoustic, method is the use of a Quartz Crystal Microbalance (QCM). A QCM is a piezoelectrically driven acoustic resonator whose resonant frequency and bandwidth are sensitive to contact with an external mechanical impedance. While the method was originally used to determine the area density of thin deposited films in a vacuum, the current state of technology and theory allows for the investigation of cell-substrate contacts in liquid. [48, 90] While modeling the mechanical impedance allows certain quantitative statements to be made, these only represent an area average. [90] Furthermore, as no reported case of a modeled cell-substrate distance is known, this method is here only referred to as a qualitative method.

ECIS

With some similarity to the previous method, Electric Cell-Substrate Impedance Sensing (ECIS) can be used to examine the electrical impedance of a cell sample. [20, 105] Although the results of this method are usually also area-averaged, the method has previously been used to provide quantitative estimates of cell-substrate distances. For example, in 1991, Giaever and Keese reported an estimated average cell-substrate distance for fibroblast cell lines on Au of 113 nm. [20] And 2017, Zhang et al. reported an average value for bovine aortic endothelial cells on Au of 100 nm. [105] However, the modeling of ECIS data usually includes several assumptions. As Giaever and Keese described, the assumption of a different cellular shape resulted in alternative cell-substrate distance estimates of 32 nm or 285 nm. [20]

2.2.2. Optical Methods

TIRFM

Total Internal Reflection Fluorescence Microscopy (TIRFM) can determine cell-substrate distances by measuring the spatial distribution of fluorescence intensity across a fluorescently labeled basal cell membrane. When such a labeled membrane is placed in the exponentially decaying electric field coupled to a totally reflected beam, the fluorescence intensity also follows an exponential distance dependence [22]:

$$F(x, y, \theta) = K \cdot d_f \cdot T(\theta) \cdot \exp\left[-\frac{h(x, y)}{d_p(\theta)}\right]$$

In this equation, x and y are lateral image coordinates, θ is the angle of light incidence, $h(x, y)$ is the cell-substrate distance, K is an instrumental constant, d_f is the membrane thickness, $d_p(\theta)$ is the penetration depth of the evanescent field and $T(\theta)$ is the transmittance of the substrate, calculated from Fresnel's equations (see section 2.3.3). By inverting this equation, the fluorescence intensity can be mapped onto the cell-substrate distance. 1992, Truseky et al. presented cell-substrate distance profiles for bovine aortic endothelial cells, featuring cell-substrate distances in the range of (20-160) nm. [22]

FLICM

By placing a cell with fluorescently labeled membrane above a reflective silicon surface and evaluating the fluorescent intensity after excitation in a self-interfering (standing) light wave, Fluorescence Interference Contrast (FLIC) microscopy became one of the first methods to determine cell-substrate distances with nanometer resolution, and to map those for single cells with a diffraction limited lateral resolution. Due to light interference at the reflective silicon surface, fluorophore excitation- and emission-probabilities can be modeled as a function of substrate-distance. [32] Using this technique, in 1998, Braun and Fromherz measured cell-substrate distances of (105 ± 6) nm on laminin-coated silica surfaces and (62 ± 5) nm on fibronectin-coated silica surfaces. [36]

However, a drawback is that the method relies on technically demanding checkerboard-like step substrates to eliminate ambiguity in the modeling of the detected fluorescence intensities. [32]

RICM

Another interference-based technique for quantitative cell-substrate-interface monitoring with diffraction limited lateral resolution is Reflection Interference Contrast Microscopy (RICM). However, unlike FLIC microscopy, this technique works without fluorescent labeling and can therefore be classified as label-free. Furthermore, illumination and imaging is performed from the opposite side of the sample. [93]

In order to determine a sample substrate distance, a multi-layer reflection model has to be fitted against the observed reflected intensity. As with FLIC microscopy, this approach also faces an ambiguity in modeled intensities. However, in case of RICM, this ambiguity can be elevated with help of a dual-wavelength approach. 2009, Monzel et al. demonstrated this technique by measuring the distance between Giant Unilamellar Vesicles (GUVs) and a Supported Lipid Bilayer (SLB) as a model system. [68]

Cell-substrate distance measurements have been reported e.g. 1964 by Curtis [5] or

more recently by Biswas et al. [113]. However, these studies masked all cell interface areas that are subject to the aforementioned ambiguity. A systematic cell-substrate distance mapping that resolves this ambiguity, such as the dual-wavelength approach, is not known.

iSCAT

Introduced in 2004 by Sandoghdar et al, confocal Interferometric Scattering (ISCAT) microscopy is a relatively new interference-based technique capable of imaging 3D interfaces. [53, 137] Like RICM, it is label-free. However, it is based not only on reflection interference, but also on the interference between reflected and scattered light.

The experimental setup for iSCAT confocal microscopy is based on that of conventional confocal laser scanning microscopes. Laser light is focused through an objective. The same objective collects both reflected and scattered light. A pinhole provides spatial filtering and a photomultiplier tube detects the interference intensity. Galvanometric mirrors are used to scan the focus across the sample. An important step in the reconstruction of scanned images is background subtraction. To reconstruct height profiles in a sample, a z-stack is acquired, each image is background corrected, and a ridge-detection algorithm is applied to vertical slices through the z-stack. [137]

It appears that an ISCAT measurement of cell-substrate distances has not yet been published, but Küppers et al. [137] demonstrate the capabilities of the method in reconstructing the height profiles of basal and apical nuclear membranes. Using a nanofabricated staircase sample, the uncertainty of their height determination is determined to be 3.5 nm.

EM

With EM, leveraging the advantage of the short wavelength of high-energy electrons [1], the field of cell-substrate interface research can rely on an imaging technique with nanometer resolution. 2008, Wrobel et al. reported a Transmission Electron Microscopy (TEM) study of cell-substrate distance distributions for HEK293 cells on SiO_2 surfaces with various coatings. [65] This work demonstrated different distributions of the cell-substrate distances depending on coatings, all with their distribution maximum being in the range between a few tens of and 100 nm.

However, before cell-substrate distances could be imaged with TEM, cells have been chemically fixed, stained with heavy metals for contrast enhancement, embedded in resin and sectioned with a focused ion beam. [65] In addition to the considerable effort involved in these preparatory steps, the resin embedding step

is suspected of influencing the actual proportions of interest. [11, 33] The direct comparison with SPRM in [121] shows that preparation artifacts can be moderate with up to a few tens of nanometers. Cryo-fixation [95] may offer a preparation method with fewer artifacts.

MIETM

Metal Induced Energy Transfer (MIET) microscopy is a relatively new method for measuring cell-substrate distances that was developed in 2014. [87] It is based on the distance-dependent effect of energy transfer between a fluorophore and a nearby metal layer, similar to Förster Resonance Energy Transfer (FRET) [3] between two fluorophores:

$$\left(\frac{r}{R_0}\right)^6 = \frac{\Delta\tau}{\tau}$$

In this equation, r is the molecular distance and R_0 is the characteristic FRET radius of the dye pair, while τ is the unquenched fluorescence lifetime and $\Delta\tau$ is the measurable change in fluorescence lifetime. As presented by Berndt et al. 2010 [72], derived from the theory of electric dipoles, the distance between a fluorescent molecule of known (dipole) orientation and a metal layer can be predicted from its fluorescence lifetime. Thus, by measuring the local fluorescence lifetime of a fluorescently labeled membrane with known fluorophore dipole orientation, its distance to an underlying Au substrate can be determined with nanometer precision. [87]

Very potent MIET microscopy variations and hybrids with other methods exist, such as double-wavelength MIET microscopy [106], Graphene Induced Energy Transfer Microscopy (GIETM) microscopy [116] with even Ångström-precise fluorophore-substrate distance determination and an isotropic-super-resolution Single Molecule Localization Microscopy (SMLM) variant [130] as a hybrid between MIET microscopy and Direct Stochastic Optical Reconstruction Microscopy (dSTORM).

Among published results, cell-substrate-distance mean-values of MDCK-II cells, MDA-MB-231 cells and A549 cells on Au have been reported as (28 ± 5) nm, (54 ± 8) nm and (67 ± 7) nm respectively. [87] Epithelial NMuMG cells have been tracked through their epithelial-to-mesenchymal transition to undergo a cell-substrate distance adjustment from (110-120) nm towards (120-156) nm. [99] Cell-substrate distances of Dictyostelium discoideum cells on collagen-I-coated SiO_2 substrates were measured to be (47 ± 8) nm in a vegetative cell and (27 ± 3) nm in a developed cell. [134]

SPRM

A detailed introduction to SPRM follows in section 2.5 and chapter 4. Figure 4.2 shows a sketch of the experimental setup. Here, as with all the other methods, the

focus is on context and comparison of SPRM.

As the central topic and core method of this work, Surface Plasmon Resonance Microscopy (SPRM) is discussed last. In contrast to most of the optical methods presented here, SPRM is label-free, as it can map the vertical distribution of RI layers by modeling the angle dependence of the sample reflectance. [89] However, unlike RICM, it does so with nanometer precision and without interference-based ambiguity thanks to the sensitive interaction between Surface Plasmon Polaritons (SPPs) and the cell-substrate interface. As a consequence, in addition to its capability of mapping cell-substrate distances, the intracellular cytoplasmic RI can be determined in parallel, which offers the advantage of being independent of its error-prone estimation. [108]

The first SPRM-based estimate of a cell-substrate distance of (160 ± 10) nm was provided by Giebel et al. for the central lamellipodium of a goldfish glial cell on an Al-substrate. [40] In the first-known SPRM-based quantitative and laterally resolved cell-substrate distance mapping, Toma et al. determined distribution mean-values for Poly(L)lysine (PLL)-, Laminin (LAM)-, Fibronectin (FIB)- and non-coated Au surfaces to be at (49.6 ± 15.9) nm, (91.6 ± 24.2) nm, (77.0 ± 11.7) nm and (91.6 ± 30.3) nm respectively. [89] Son et al. determined the cell-substrate distance of a human aortic endothelial cell on Au to be in the range of (40-60) nm. [110] However, since these first quantitative SPRM measurements relied on the estimation of an intracellular cytoplasmic RI, which as shown by Kreysing et al. [108] can lead to errors of up to 100 nm, the results of more modern SPRM variants are of particular interest here. For example, Kreysing et al. measured cell-substrate distances of contracting cardiomyocytes on gold to be in the range of (40-100) nm. [108] For neurons on PLL-coated Au substrates, they reported values in the range of (10-100) nm. [121] Dai et al. measured distances for RAW264.7 cells on Au to be distributed around a mean value of 89 nm. [133] As presented in chapter 6, this work supplements this list with measurements for HEK293 cells on SiO_2 and neurons on Au, each with different cell-adhesive coatings.

2.3. Optics of Interfaces and Stratified Media

SPRM can be understood from a purely classical approach to optics. This section outlines how the equations used are derived from Maxwell's equations of electrodynamics. It is intended to provide a context within the established theory of electrodynamics. Furthermore, this basic approach aids in the derivation of the TMM formalism in section 2.3.3, which is essential to the data analysis described in section 4.5. The phenomenon of SPR is not explicitly discussed in this section, but will be in section 2.4.

2.3.1. Electromagnetic Waves in Dielectrics

If we take Maxwell's equations [63, p. 214] as a starting point and limit the discussion to *linear*, *isotropic*, *homogeneous*, *non-conductive* media, *without free (permanent) magnetization* ($M_0 = 0$) and *without free (permanent) polarization* ($P_0 = 0$), we can write:

$$\nabla \cdot \mathbf{E} = \frac{\rho}{\varepsilon_r \varepsilon_0} \tag{2.1}$$

$$\nabla \times \mathbf{E} = -\mu_r \mu_0 \frac{\partial \mathbf{H}}{\partial t} \tag{2.2}$$

$$\nabla \cdot \mathbf{H} = 0 \tag{2.3}$$

$$\nabla \times \mathbf{H} = \mathbf{J} + \varepsilon_r \varepsilon_0 \frac{\partial \mathbf{E}}{\partial t} \tag{2.4}$$

Here $\mathbf{E}$ and $\mathbf{H}$ are the electric and magnetic fields, respectively. $\mathbf{J}$ is the current density and ρ is the electric charge density. Constants ε_0 and μ_0 are the vacuum permittivity and vacuum permeability. Variables ε_r and μ_r are the relative permittivity and permeability in a given material. As this chapter is dedicated to (uncharged) dielectrics, we further assume the *absence of free charges* ($\rho = 0$) and the *absence of currents* ($\mathbf{J} = 0$). From eq. (2.2) and eq. (2.4), together with the general vector calculus relation $\nabla \times \nabla \times \mathbf{A} = \nabla(\nabla \cdot \mathbf{A}) - \nabla^2 \mathbf{A}$, the homogeneous wave equations (eq. (2.5)) can be derived. [63, p. 255–256]

$$\nabla^2 \mathbf{E} - \frac{1}{c^2} \frac{\partial^2 \mathbf{E}}{\partial t^2} = 0 \quad \text{and} \quad \nabla^2 \mathbf{H} - \frac{1}{c^2} \frac{\partial^2 \mathbf{H}}{\partial t^2} = 0 \quad \text{with} \quad c = \frac{1}{\sqrt{\varepsilon_r \varepsilon_0 \mu_r \mu_0}} \tag{2.5}$$

Here, the variable c is introduced and has the dimension of a velocity. For the frequencies ω of interest, the terms "electromagnetic wave" and "light" are used interchangeably to refer to the solutions of these equations. By adding the assumption of time-harmonic fields, the solutions can be expressed as follows:

$$\mathbf{E}(\mathbf{r}, t) = \mathbf{E}(\mathbf{r}) e^{-i\omega t} \qquad \text{and} \qquad \mathbf{H}(\mathbf{r}, t) = \mathbf{H}(\mathbf{r}) e^{-i\omega t} \tag{2.6}$$

Plane Waves

While a more detailed discussion of specific solutions to eq. (2.5), such as plane waves, spherical waves and wave packets, can be found in [63, Ch. 4.3], a few properties of plane waves shall be discussed here in conclusion. Looking at eq. (2.7), it might be intuitive to call this solution a plane wave:

$$\mathbf{E}(\mathbf{r}, t) = \mathbf{E}_0 e^{i(\mathbf{k}_E \cdot \mathbf{r} - \omega_E t)} \qquad \text{and} \qquad \mathbf{H}(\mathbf{r}, t) = \mathbf{H}_0 e^{i(\mathbf{k}_H \cdot \mathbf{r} - \omega_H t)} \tag{2.7}$$

And it can be seen that the wave vector $\mathbf{k}$ points in the direction of wave propagation. Since $\mathbf{E}$ and $\mathbf{H}$ do not only have to obey the wave equations, but are also coupled by Maxwell's equations, we can derive from eq. (2.2):

$$\mathbf{k} \times \mathbf{E}_0 e^{i(\mathbf{k}_E \cdot \mathbf{r} - \omega_E t)} = \omega \mu_r \mu_0 \mathbf{H}_0 e^{i(\mathbf{k}_H \cdot \mathbf{r} - \omega_H t)} \tag{2.8}$$

This shows firstly that we can define $\omega \coloneqq \omega_E = \omega_H$ and $\mathbf{k} \coloneqq \mathbf{k}_E = \mathbf{k}_H$, and secondly:

$$\mathbf{k} \times \mathbf{E}_0 = \omega \mu_r \mu_0 \mathbf{H}_0 \tag{2.9}$$

Remaining Maxwell's eqs. (2.1), (2.3) and (2.4) reveal that $\mathbf{k}$, $\mathbf{E}$ and $\mathbf{H}$ are orthogonal to each other:

$$\mathbf{k} \cdot \mathbf{E}_0 = 0 \qquad \text{and} \qquad \mathbf{k} \cdot \mathbf{H}_0 = 0 \qquad \text{and} \qquad \mathbf{k} \times \mathbf{H}_0 = -\omega \varepsilon_r \varepsilon_0 \mathbf{E} \tag{2.10}$$

Inserting the solution eq. (2.7) into the wave eq. (2.5) shows that the ratio between $k \coloneqq |\mathbf{k}|$ and ω is fixed:

$$c = \frac{\omega}{k} \tag{2.11}$$

With $\lambda = 2\pi/k$ as wavelength and $\tau = 2\pi/\omega$ as wave period, $c = \lambda/\tau$ is the speed of light in a given medium. The RI can be defined as the ratio between the speed of light in a medium and its value in vacuum c_0 (where $\mu_r = \varepsilon_r = 1$):

$$n \coloneqq \frac{c_0}{c} = \sqrt{\varepsilon_r \mu_r} \tag{2.12}$$

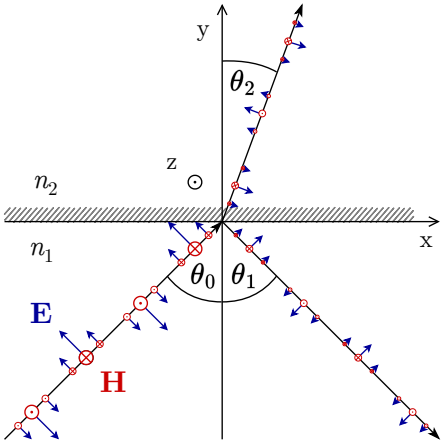
2.3.2. Reflection and Refraction at Interfaces

In this section the behavior of $\mathbf{E}$ and $\mathbf{H}$ fields at interfaces is discussed, followed by a consideration of light reflection and refraction in the case of plane waves at an ideal interface. The outline here is intended to give a sense of the relations and introduce equations, definitions and notation, further needed in section 2.3.3. A thorough derivation of the relationships can be found in [63, Chapter 2.1.4, 4.3.10.A, 4.3.10.B]

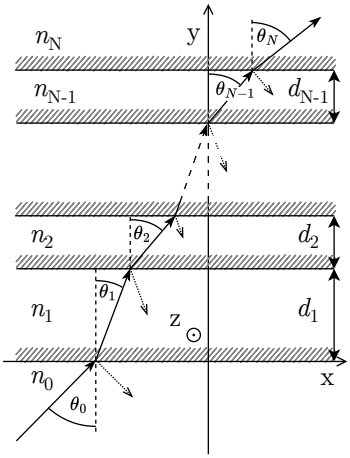
E and H Fields at Interfaces

Integrating Maxwell's eqs. (2.1) and (2.3) over a volume around the interface, and then letting the volume expansion approach 0 in direction of $\mathbf{n}$, the interface normal, we see that the normal field components behave as follows:

$$\mathbf{n} \cdot (\mathbf{E}_2 \varepsilon_{r,2} - \mathbf{E}_1 \varepsilon_{r,1}) = 0 \quad \text{and} \quad \mathbf{n} \cdot (\mathbf{H}_2 \mu_{r,2} - \mathbf{H}_1 \mu_{r,1}) = 0 \tag{2.13}$$



(a) Sketch of a p-polarized wave that is reflected and refracted at an interface between two media in the xz-plane.



(b) Simplified depiction of a plane electromagnetic wave traveling through a stratified medium. Arrows illustrate the direction of the k-vector in each layer.

Figure 2.5.: Reflection and transmission of electromagnetic plane waves at interfaces.

Integrating Maxwell's eqs. (2.2) and (2.4) over a closed rectangular path back and forth through the interface, and then letting the rectangle converge to a line at the interface, we see that the tangential field components behave as follows:

$$\mathbf{n} \times (\mathbf{E}_2 - \mathbf{E}_1) = 0 \quad \text{and} \quad \mathbf{n} \times (\mathbf{H}_2 - \mathbf{H}_1) = 0 \tag{2.14}$$

Reflection and Refraction of Electromagnetic Plane Waves

Let's assume the scenario of a plane wave, arriving at an interface between two media with material properties ε_1, μ_1 and ε_2, μ_2. Since the reflection and refraction of light are known phenomena [18], a reasonable approach to solving the linear wave eq. (2.5) splits the fields $\mathbf{E}$ and $\mathbf{H}$ into incident and reflected components within the first

medium and a refracted component within the second medium. Further assuming that all components can be described as plane waves, we can write:

$$\mathbf{E}_i = \mathbf{E}_{0,i} e^{i(\mathbf{k}_i \cdot \mathbf{r} - \omega_i t)} \quad \text{and} \quad \mathbf{H}_i = \frac{\mathbf{k} \times \mathbf{E}_i}{\omega \mu_{r,i} \mu_0}$$
$$\text{with} \quad \mu_{r,0} = \mu_{r,1}$$

for $i = 0$ (incoming wave in medium 1), $i = 1$ (reflected wave in medium 1) and $i = 2$ (refracted wave in medium 2).

There is a coordinate system in which the the xy-plane coincides with the interface between the two media. The angles between the normal of the plane $\mathbf{n} = \mathbf{e}_z$ and each wave vector $\mathbf{k}_i$ are now defined as θ_i. The angle between each wave vector $\mathbf{k}_i$ and the x-axis are named φ_i and the orientation of the x-axis is defined such that $\varphi_0 = 0$. From the interface behavior of fields (eqs. (2.13) and (2.14)) follows the identity of phases:

$$(\mathbf{k}_0 \cdot \mathbf{r} - \omega_0 \cdot t)_{z=0} = (\mathbf{k}_1 \cdot \mathbf{r} - \omega_1 \cdot t)_{z=0} = (\mathbf{k}_2 \cdot \mathbf{r} - \omega_2 \cdot t)_{z=0} \tag{2.15}$$

The equality of the wave frequencies ω_i follows from a consideration of the coordinate origin. The equality $\varphi_1 = \varphi_2 = 0$ follows from the comparison of x- and y- components of $\mathbf{k}_i$. This means that all wave vectors $\mathbf{k}_i$ lie within the plane of incidence, which is spanned by $\mathbf{k}_0$ and $\mathbf{n}$. The relation between wave vector magnitudes can also be obtained from a component-wise consideration of eq. (2.15):

$$k_0 \sin\theta_0 = k_1 \sin\theta_1 = k_2 \sin\theta_2 \tag{2.16}$$

Applying eqs. (2.11) and (2.12), we can now state the laws of reflection (eq. (2.17)) and refraction (eq. (2.18)):

$$\theta_0 = \theta_1 \tag{2.17}$$

$$\frac{\sin\theta_1}{\sin\theta_2} = \frac{n_2}{n_1} \tag{2.18}$$

Total Reflection

A medium that has a higher refractive index relative to another is referred to as optically denser. We can observe that in the case of a reflection from an optically denser medium (n_1) to an optically thinner medium (n_2), there is a critical angle $\theta_{0,C}$ (see eq. (2.19)) at which, and above which, no refracted wave propagates into

the thinner medium. This critical angle is called angle of total reflection and it is determined by the following equation:

$$\sin\theta_{0,C} = \frac{n_2}{n_1} \tag{2.19}$$

p- and s- polarized light

In order to consider reflection and refraction, a coordinate system is aligned with the plane of incidence (spanned by the wave vector $\mathbf{k}$ and interface normal $\mathbf{n}$). It will be helpful to introduce the distinction between p- and s-polarized light. While p-polarized light is an electromagnetic wave with its electrical component parallel to the plane of incidence (see fig. 2.5a), the electrical component of s-polarized light is perpendicular to the plane of incidence. Thanks to the linearity of eq. (2.5), a wave that is not purely p- or s-polarized can be divided into respective components. It should be noted that some authors, such as Born and Wolf [39], also refer to Transverse Magnetic (TM) and Transverse Electric (TE) waves instead of p- and s-polarized light.

2.3.3. Reflection at a Stratified Medium : Transfer-Matrix-Method

In this section, the Transfer Matrix Method (TMM) for the description of light in a stratified medium is introduced. It lies at the core of cell-substrate-distance- and cytoplasmic RI parameter-optimization. A thorough and general derivation of the formalism can be found in [39, Sec. 1.6]. This section presents an adaptation of that derivation in which all assumptions made are introduced as early as possible, so that the omission of generality allows for a few simplifications.

In order to approach the description of light reflection at a stratified medium, i.e. a series of successive media with parallel interfaces, we begin by considering a (plane) p-polarized light wave that moves within a medium towards the interface of the next medium. The choice of coordinate system corresponds to fig. 2.5a. This choice gives $H_x = H_y = E_z = 0$ and Maxwell's eqs. (2.2) to (2.4) can be written as component-wise equations:

$$\frac{\partial E_y}{\partial z} = 0 \tag{2.20a}$$

$$\frac{\partial E_x}{\partial z} = 0 \tag{2.20b}$$

$$\frac{\partial E_y}{\partial x} - \frac{\partial E_x}{\partial y} = i\omega\mu_r\mu_0 H_z \tag{2.20c}$$

$$\frac{\partial H_Z}{\partial z} = 0 \tag{2.21}$$

$$\frac{\partial H_z}{\partial y} = -i\omega\varepsilon_r\varepsilon_0 E_x \tag{2.22a}$$

$$-\frac{\partial H_z}{\partial x} = -i\omega\varepsilon_r\varepsilon_0 E_y \tag{2.22b}$$

First, we eliminate E_x and E_y from these equations by inserting eqs. (2.22a) and (2.22b) into eq. (2.20c). Using the wave equation definition for c (eq. (2.5)), and the relation in eq. (2.11), we condense the system of equations into the following partial differential equation:

$$\frac{\partial^2 H_z}{\partial x^2} + \frac{\partial^2 H_z}{\partial y^2} + k^2 H_z = 0 \tag{2.23}$$

Assuming a trial solution form of $H_z(x, y) = X(x)U(y)$ allows us to separate x- and y-dependent parts:

$$\frac{1}{X}\frac{d^2X}{dx^2} = -\frac{1}{U}\frac{d^2U}{dy^2} - k^2 \tag{2.24}$$

Since one side of the equation only depends on x, while the other side depends only on y, we can conclude that both sides equal a constant. It will be helpful to express this constant as $-k_x^2$. It follows that X can be expressed as $X(x) = X_0 \cdot exp(ik_x x)$. And therefore, H_z can be expressed as:

$$H_z = U(y)e^{i(k_x x - \omega t)} \tag{2.25}$$

Equations (2.22a) and (2.22b) give $E_x \propto \frac{\partial H_z}{\partial y}$ and $E_y \propto \frac{\partial H_z}{\partial x}$, which tells that E_x and E_y share the same x-dependence as H_z. We therefore write:

$$E_x = V(y)e^{i(k_x x - \omega t)} \tag{2.26}$$

$$E_y = W(y)e^{i(k_x x - \omega t)} \tag{2.27}$$

The Characteristic Matrix Formalism

Using Lagrange's notation for derivatives and eqs. (2.20c), (2.22a) and (2.22b) to express U' and V' in terms of U, V and W, then eliminating W, leads to the pair of coupled 1st order linear differential equations:

$$U' = \frac{k}{i}\sqrt{\frac{\varepsilon_r\varepsilon_0}{\mu_r\mu_0}}V \qquad \text{and} \qquad V' = \frac{i}{k}\sqrt{\frac{\mu_r\mu_0}{\varepsilon_r\varepsilon_0}}\left(k_x^2 - k^2\right)U \tag{2.28}$$

These can be decoupled into two 2nd order (ordinary) linear differential equations:

$$U'' = (k_x^2 - k^2)U \qquad \text{and} \qquad V'' = (k_x^2 - k^2)V \tag{2.29}$$

There are mathematical solutions (u_1, v_1) and (u_2, v_2) with eq. (2.30) as (mathematical) boundary condition. Thanks to the linearity of this problem, the particular phys-

ical solution (U, V) with (physical) boundary conditions $U(0) = U_0$ and $V(0) = V_0$ can be written in matrix notation as eq. (2.31):

$$u_1(0) = v_2(0) = 0 \quad \text{and} \quad u_2(0) = v_1(0) = 1 \tag{2.30}$$

$$\underbrace{\begin{bmatrix} U \\ V \end{bmatrix}}_{\mathbf{Q}} = \underbrace{\begin{bmatrix} u_2 & u_1 \\ v_2 & v_1 \end{bmatrix}}_{\underline{\mathbf{N}}} \underbrace{\begin{bmatrix} U_0 \\ V_0 \end{bmatrix}}_{\mathbf{Q_0}} \tag{2.31}$$

This representation shows that we can calculate the components of the E- and H-fields in any z-plane from the field strengths within the $z = 0$ plane. Since eq. (2.32) shows that the determinant of $\underline{\mathbf{N}}$ is constantly non-zero $\underline{\mathbf{N}}$ is invertible and we can therefore express eq. (2.31) in the way of eq. (2.33):

$$\frac{\mathrm{d}}{\mathrm{d}y} \det(\underline{\mathbf{N}}) = \frac{\mathrm{d}}{\mathrm{d}y}(u_2 v_1 - u_1 v_2) = 0 \quad \text{and} \quad \det(\underline{\mathbf{N}}(0)) = 1 - 0 = 1 \tag{2.32}$$

$$\mathbf{Q_0} = \underline{\mathbf{M}}\mathbf{Q} \quad \text{with} \quad \underline{\mathbf{M}} = \underline{\mathbf{N}}^{-1} = \begin{bmatrix} v_1 & -u_1 \\ -v_2 & u_2 \end{bmatrix} \tag{2.33}$$

With M as the characteristic matrix of the medium, this representation will be more practical.

The Characteristic Matrix of a Single Layer

Before discussing a stratified medium, we need to determine the specific structure of the characteristic matrix in the case where light travels through a single (homogeneous, laterally infinite) layer of material. We return to the decoupled 2nd order linear differential eq. (2.29) with the following ansatz:

$$U_i(y_i) = A_i \cos(k_i y_i \cos\theta_i) + B_i \sin(k_i y_i \cos\theta_i)$$

The indices i indicate that their variables are specific to one layer (the one with index i). In the case of the coordinate y_i for example, the beginning of (each) layer i is the reference point $y_{i,0} = 0$. Also, in this ansatz we have used the following relation that is motivated by fig. 2.5b, which reflects our choice of coordinate system:

$$k_{x,i} = k_i \sin\theta_i$$

θ_i denotes the angle between k-vector and y-axis for the i-th layer in a stratified layer system. Using Snell's law, this angle can be propagated through the layers to:

$$\theta_i = \arcsin\left(\frac{n_0}{n_i}\sin\theta_0\right) \tag{2.34}$$

Equation (2.28) gives the other component $V_i(y)$:

$$V_i(y_i) = i\sqrt{\frac{\mu_{r,i}\mu_0}{\varepsilon_{r,i}\varepsilon_0}}\cos\theta_i(B_i\cos(k_i y_i\cos\theta_i) - A_i\sin(k_i y_i\cos\theta_i))$$

Now, we can adjust A_i and B_i to meet the two boundary conditions from eq. (2.30) for $(u_{1,i}, v_{1,i})$ and $(u_{2,i}, v_{2,i})$, respectively:

$$u_{1,i}(y_i) = \frac{i}{\cos\theta_i}\sqrt{\frac{\varepsilon_{r,i}\varepsilon_0}{\mu_{r,i}\mu_0}}\sin(k_i y_i\cos\theta_i) \qquad v_{1,i}(y_i) = -\cos(k_i y_i\cos\theta_i)$$

$$v_{2,i}(y_i) = -i\sqrt{\frac{\mu_{r,i}\mu_0}{\varepsilon_{r,i}\varepsilon_0}}\cos\theta_i\sin(k_i y_i\cos\theta_i) \qquad u_{2,i}(y_i) = \cos(k_i y_i\cos\theta_i)$$

With these particular (mathematical) solutions, we can construct the characteristic matrix of a single layer:

$$\underline{\mathbf{M_i}} = \begin{bmatrix} -\cos(k_0 n_i d_i\cos\theta_i) & -\frac{i}{q_i}\sin(k_0 n_i d_i\cos\theta_i) \\ iq_i\sin(k_0 n_i d_i\cos\theta_i) & \cos(k_0 n_i d_i\cos\theta_i) \end{bmatrix} \quad \text{with} \quad q_i = \sqrt{\frac{\mu_{r,i}\mu_0}{\varepsilon_{r,i}\varepsilon_0}}\cos\theta_i \tag{2.35}$$

Here we have used $k_i = k_0 n_i$, which follows from eqs. (2.11) and (2.12). Also, we have set y_i to the thickness d_i of the layer, describing the transfer through the complete layer from $y_i = 0$ to $y_i = d_i$.

The Characteristic Matrix of a Stratified Layer System.

The description of a stratified layer system is not far from the characteristic matrix of a single layer. Assuming two adjacent layers along the y-axis of a coordinate system (see fig. 2.5b), where the fist one expands from $y = 0$ to $y = d_1$, and the second layer expands from $y = d_1$ to $y = d_1 + d_2$, we can use the matrix notation to express the field amplitudes $\mathbf{Q_0}$ at the beginning of the first layer relative to the field amplitudes $\mathbf{Q}(y = d_1)$ at the beginning of the second layer, which we can then express relative to the field amplitudes $\mathbf{Q}(y = d_1 + d_2)$ at the end of the second layer:

$$\mathbf{Q_0} = \underline{\mathbf{M_1}}(d_1)\mathbf{Q}(d_1) = \underline{\mathbf{M_1}}(d_1)\underline{\mathbf{M_2}}(d_2)\mathbf{Q}(d_1 + d_2) \tag{2.36}$$

This way, we can relate the field amplitudes at the beginning and end of any stack of (finite-thickness) layers, using the product of layer matrices as characteristic matrix of the stratified layer system $\underline{\mathbf{M_{SLS}}}$. For a stack of $N-1$ layers, that is:

$$\underline{\mathbf{M_{SLS}}} = \prod_{j=1}^{N-1} \underline{\mathbf{M_j}}(d_j) \tag{2.37}$$

Reflectance of a Stratified Layer System

The reflectance of a stratified layer system is obtained from its characteristic matrix. A stratified layer system is a stack of $N-1$ (finite-thickness) layers, embedded between a semi-infinite preceding medium (index $i = 0$) and a semi-infinite succeeding medium (index $i = N$), as depicted in fig. 2.5b. To obtain this reflectance, we compare the relation of the field amplitudes from the matrix elements with the relation from the concept of reflectance and transmittance. If we denote the amplitude of the incident and reflected H-field on one side of the stratified medium by A and R respectively, and the amplitude of the transmitted H-field on the other side of the stratified medium by T, we get the following relations:

$$\begin{bmatrix} U_0 \\ V_0 \end{bmatrix} = \begin{bmatrix} A+R \\ q_1(A-R) \end{bmatrix} = \underline{\mathbf{M}} \begin{bmatrix} U(z_N) \\ V(z_N) \end{bmatrix} = \underline{\mathbf{M}} \begin{bmatrix} T \\ -q_N T \end{bmatrix} \tag{2.38}$$

To express V_0 and $V(z_N)$, we have used eq. (2.10). Denoting elements of $\underline{\mathbf{M}}$ as m_{ij}, we can also write component-wise:

$$A + R = (m_{11} - q_N m_{12})T \tag{2.39}$$

$$q_0(A - R) = (m_{21} - q_N m_{22})T \tag{2.40}$$

Solving these equations, we can determine the stratified layer systems (amplitude) reflection coefficient r_p for p-polarized light:

$$r_p = \frac{R}{A} = \frac{(m_{21} - q_N m_{22}) - q_0(m_{11} - q_N m_{12})}{(m_{21} - q_N m_{22}) + q_0(m_{11} - q_N m_{12})} \tag{2.41}$$

The assumption of an s-polarized plane wave at the beginning of this derivation gives the reflection coefficient r_s for s-polarized light:

$$r_s = \frac{(m_{21} - p_N m_{22}) - p_0(m_{11} - p_N m_{12})}{(m_{21} - p_N m_{22}) + p_0(m_{11} - p_N m_{12})} \quad \text{with} \quad p_i = \sqrt{\frac{\varepsilon_r \varepsilon_0}{\mu_r \mu_0}} \cos\theta_i \tag{2.42}$$

The (power) reflectances R_p and R_s result from the (amplitude) reflection coefficients r_p and r_s as their square value:

$$R_p = r_p^2 \qquad \text{and} \qquad R_s = r_s^2 \tag{2.43}$$

In the same way, transmission coefficients and transmittances are determined. Finally, it should be noted that Fresnel's equations (see [63, p. 301]) for reflectance and transmittance between two media (with $\mu_{r,1} = \mu_{r,2}$) are retrieved as limit cases. The different signs compared to Born and Wolf [39, Sec. 1.6.3] are due to the choice of coordinate system and have no influence on the calculation of reflectance (and transmittance).

2.3.4. Absorption

So far, only electromagnetic waves in insulators have been considered. However, as we are particularly interested in the optical response of metals, as follows from section 2.4, the TMM derived in section 2.3.3 needs to be extended to conductive media.

As shown in [63, Ch. 4.3.9], eq. (2.44) follows from Maxwell's equations as a generalization of the homogeneous wave equation (eq. (2.5)), taking into account the electrically excited current density $\mathbf{J}$. Here, the current density $\mathbf{J} = \sigma\mathbf{E}$ was expressed by the electric field strength via the conductivity σ. Further, a harmonic time dependence $\exp(-i\omega t)$ of the E and B fields was assumed.

$$\left(\nabla^2 + \frac{\omega^2}{c^2} + i\omega\mu_r\mu_0\sigma\right)\mathbf{E} = 0 \quad \text{and} \quad \left(\nabla^2 + \frac{\omega^2}{c^2} + i\omega\mu_r\mu_0\sigma\right)\mathbf{H} = 0 \tag{2.44}$$

This equation can be reshaped into the familiar form of eq. (2.5) by defining a complex dielectric constant $\tilde{\varepsilon}_r = \varepsilon_r + i\sigma/(\varepsilon_0\omega)$. The implications of such a generalized dielectric constant also include a generalized complex RI $\tilde{n}$, the imaginary part of which, as motivated in section 2.4.1, is called the extinction coefficient and describes the absorption of electromagnetic waves in matter.

The TMM formalism can be extended to conductive materials via this definition of the complex properties $\tilde{\varepsilon}_r$ and $\tilde{n}$. For this, the following substitutions are needed in the presented formalism:

$$\begin{aligned} n &\longrightarrow \tilde{n} = n + i\kappa \\ \varepsilon_r &\longrightarrow \tilde{\varepsilon}_r = \varepsilon_{r,1} + i\varepsilon_{r,2} \end{aligned}$$

A simple transformation of the characteristic layer matrix for p-polarized light $\underline{\mathbf{M}}_{p,j}$ and s-polarized light $\underline{\mathbf{M}}_{s,j}$ as well as of expressions q_j and p_j from the last section, together with the introduction of a new term β_j allows for a more convenient expression of the TMM formalism, inspired by [114]:

$$\underline{\tilde{\mathbf{M}}}_{p,j} = \begin{bmatrix} \cos(\tilde{\beta}_j) & -\frac{i}{\tilde{q}_j}\sin(\tilde{\beta}_j) \\ -i\tilde{q}_j \sin(\tilde{\beta}_j) & \cos(\tilde{\beta}_j) \end{bmatrix} \quad (2.45a) \qquad \tilde{p}_j = \sqrt{\tilde{n}_j^2 - n_0^2 \sin^2(\theta_i)} \quad (2.45c)$$

$$\tilde{q}_j = \frac{p_j}{\tilde{n}_j^2} \quad (2.45d)$$

$$\underline{\tilde{\mathbf{M}}}_{s,j} = \begin{bmatrix} \cos(\tilde{\beta}_j) & -\frac{i}{\tilde{p}_j}\sin(\tilde{\beta}_j) \\ -i\tilde{p}_j \sin(\tilde{\beta}_j) & \cos(\tilde{\beta}_j) \end{bmatrix} \quad (2.45b) \qquad \tilde{\beta}_j = k_0 d_j p_j \quad (2.45e)$$

This expression has the advantage that it depends on the material constants n and κ, which can be found in conveniently prepared databases such as [142] for all relevant materials and optical wavelengths. All other equations from section 2.3.3 stay unchanged.

2.3.5. Scattering

Light scattering is a phenomenon that occurs when electromagnetic waves interact with structures of the same order of magnitude as the wavelength. This interaction depends on the properties of the scattering structure, such as size, shape and optical properties, and can change the properties of the scattered light, most importantly its direction. While we distinguish between scattering at volume defects and scattering at surfaces, the first one is more important for biological samples and the latter one is more important for high-reflective surfaces. [44, Ch. 1]

Neither case is accounted for by the TMM, so they are treated as noise. However, while volume scattering in biological samples (e.g. cells) cannot be reduced, surface scattering can be reduced. Substrate fabrication methods with low Root Mean Square (RMS) surface roughness are preferred. As derived from angle-resolved scattering (ARS) theory, eq. (2.46) expresses the relative scattered intensity for a light beam being reflected off a reflective surface with an incident angle θ_0, given that the RMS surface roughness δ is much less than the wavelength of light λ. [12]

$$TIS = \left(\frac{4\pi\delta\cos\theta_0}{\lambda}\right)^2 + \mathcal{O}\left(\frac{\delta^3}{\lambda^3}\right) \quad (2.46)$$

For a surface roughness of 1 nm (see chapter 5), this value is less than 0.0004.

2.4. Surface Plasmon Resonance

The theory of light reflection at a stratified layer system, derived for dielectrics in section 2.3.3 and generalized to metals in section 2.3.4, contains an implicit description of Surface Plasmon Resonance (SPR) for the analysis of measurements. However, this section provides an explicit introduction to Surface Plasmon Polaritons (SPPs), Surface Plasmons (SPs) and SPR to provide a deeper understanding of the observed and utilized phenomenon in general, to understand why SPR sensitivity is localized to interfaces, and to explain the need for a metal layer and high RI substrates.

2.4.1. Electromagnetic Waves in Metals

This section is a summary of the relevant background from S. A. Maier [62, Ch. 1.1].

As in section 2.3.1, an isotropic, linear medium with local and instantaneous responses to an electric field as assumed. For dielectrics, i.e. materials with bound electrons, the electric field strength $\mathbf{E}$ and the electric flux density $\mathbf{D}$ are related by eq. (2.47a) via the (induced) polarization $\mathbf{P}$ or equivalently via the scalar proportionality constant $\varepsilon_0\varepsilon_r$. In contrast, the corresponding material response for conductors, i.e. materials with free electrons, is associated with eq. (2.47b), in which the current density $\mathbf{J}$ is related to $\mathbf{E}$ via the conductivity σ.

$$\mathbf{D} = \varepsilon_0\mathbf{E} + \mathbf{P} = \varepsilon_0\varepsilon_r\mathbf{E} \qquad (2.47a) \qquad\qquad \mathbf{J} = \sigma\mathbf{E}. \qquad (2.47b)$$

However, as S. A. Maier further discusses, we can use either of these two equations to describe metals. This is expressed by eq. (2.49). The derivation of eq. (2.49) is outlined next.

Taking into account that optical properties of metals cannot be described solely through local and instantaneous responses, we extend eqs. (2.47a) and (2.47b) to integral expressions that include spatially and temporally distributed contributions from ε_r, $\mathbf{E}$ and σ. It turns out that the familiar compact representation is again obtained if these integral equations are Fourier transformed into the domain of frequency ω and wave vector $\mathbf{k}$:

$$\mathbf{D}(\mathbf{k},\omega) = \varepsilon_0\varepsilon_r(\mathbf{k},\omega)\mathbf{E}(\mathbf{k},\omega) \qquad (2.48a) \qquad \mathbf{J}(\mathbf{k},\omega) = \sigma(\mathbf{k},\omega)\mathbf{E}(\mathbf{k},\omega). \qquad (2.48b)$$

Taking the time derivative of eq. (2.47a) and expressing the current density in

terms of the time derivative of the polarization $\partial \mathbf{P}/\partial t = \mathbf{J}$, we obtain eq. (2.49)[3] as a link between eq. (2.48a) and eq. (2.48b) after a term transformation.

$$\varepsilon_r(\mathbf{k}, \omega) = 1 + \frac{i\sigma(\mathbf{k}, \omega)}{\varepsilon_0 \omega} \tag{2.49}$$

It should be noted that the imaginary unit in eq. (2.49) is a result of the time derivative of the electric field, which generally corresponds to a factor $-i\omega t$ in the Fourier domain. This suggests that $\sigma = \sigma_1 + i\sigma_2$ and $\varepsilon_r = \varepsilon_1 + i\varepsilon_2$ are complex quantities. As we have defined the RI via ε_r in eq. (2.12), we treat it as a complex quantity $\tilde{n} = n + i\kappa$ in this case. Using the complex variable $\tilde{n}$ in eq. (2.7) for plane waves, eq. (2.50), Beer's law, can be derived, describing the attenuation of light intensity I for a penetration depth x into a material.

$$I(x) = I_0 e^{-\alpha x} \qquad \text{with} \qquad \alpha(\omega) = \frac{2\kappa(\omega)\omega}{c} \tag{2.50}$$

While n continues to measure the reduction of the phase velocity of light in a medium, κ describes its absorption by the medium. The material property κ is the extinction coefficient.

For non-magnetic materials, assuming $\mu_r = 1$, we can simplify eq. (2.12) to $n = \sqrt{\varepsilon_r}$, which allows us to express the real part of ε_r as:

$$\varepsilon_1 = n^2 - \kappa^2 \tag{2.51}$$

This expression plausibilises that most dielectrics (non-absorbing, κ small) have a positive value of ε_1, while most metals (absorbing over many frequencies, κ large) have a negative value of ε_1. In section 2.4.3 this signifies the role of metals for SPR sensing.

2.4.2. Plasma Frequency of the Free Electron Gas

This section is a summary of the relevant background from S. A. Maier [62, Ch. 1.2]

To describe the dielectric function of metals $\varepsilon_r(\omega)$ in the context of this compact introduction to SPPs and SPR, and for the frequency ranges relevant here, the Drude model, an atomistic plasma model of free electrons will be sufficient. An electron distribution against a background of stationary, positively charged atomic nuclei is

[3] This equation differs from that in section 2.3.4. This difference arises from slightly different definitions of ε_r and σ in section 2.3.4 (W. Nolting, [63, Ch. 4.3.9]) and this section (S. A. Maier, [62, Ch. 1.1]). It is only due to convention that the same symbol is used for both cases.

assumed. In an external electric field $\mathbf{E}$, the motion of the electrons is described by the following equation [62, Ch. 1.2]:

$$m\ddot{\mathbf{x}} + m\gamma\dot{\mathbf{x}} = -e\mathbf{E} \tag{2.52}$$

The dot notation for time derivatives is used. The parameter m is the mass of an electron, e is its charge, $\mathbf{x}$ is its position, and γ is a damping parameter, being interpreted by this model as a collision frequency of electrons. [62, Ch. 1.2] For a harmonically driven system with $\mathbf{E}(t) = \mathbf{E}_0 \exp(-i\omega t)$, eq. (2.53) is a particular solution of this equation.

$$\mathbf{x}(t) = \frac{e}{m(\omega^2 + i\gamma\omega)}\mathbf{E}(t) \tag{2.53}$$

If the polarization is expressed as the displacement of electrons $\mathbf{P} = -n_e e\mathbf{x}$, with n_e being the electron density, a comparison with eq. (2.47a) gives the dielectric function for a free electron gas:

$$\varepsilon_{metal} = 1 - \frac{\omega_p^2}{\omega^2 + i\gamma\omega} \qquad \text{with} \qquad \omega_p = \frac{n_e e^2}{\varepsilon_0 m} \tag{2.54}$$

This dielectric function suggests the definition of the plasma frequency ω_p. For large frequencies ω or low damping γ, the limit of the undamped free electron plasma is obtained:

$$\varepsilon_{metal,undamped} = 1 - \frac{\omega_p^2}{\omega^2} \tag{2.55}$$

Again, metals possess a negative real part of the dielectric function for frequencies below the plasma frequency.

As discussed by S. A. Maier [62, Ch. 1.3], the plasma frequency is the natural frequency of a free-electron plasma oscillation. The quanta of these oscillations are called volume plasmons. However, surface plasmons are of interest here. These are introduced in the next section.

2.4.3. Surface Plasmon Polariton (SPP) and Surface Plasmon (SP)

This section is based on a description of SPPs by S. A. Maier [62, Ch. 2.2], but modified to build on the relations from section 2.3.3. In order to reconstruct this derivation in detail, it is recommended to compare both sources.

Compared to electromagnetic waves (see section 2.3.1), SPPs are an alternative solution to Maxwell's equations. A solution that can only be found at metal-

dielectric interfaces and that is characterized by interface confinement, making it an attractive probe for interfacial sensing.

Taking the approach to Maxwell equation solutions in eqs. (2.25) to (2.27) from section 2.3.3, we can express the definition of SPPs [62, Ch. 2.2] through eq. (2.56):

$$U(y) = \hat{U}e^{-\kappa y} \qquad \text{and} \qquad V(y) = \hat{V}e^{-\kappa y} \tag{2.56}$$

$\hat{U}$ and $\hat{V}$ are constant amplitudes of the magnetic and electric field components U and V. Be aware that the same coordinate system as in section 2.3.3 is chosen, therefore this solution is based on p-polarized light waves. It can be seen that U and V both comply with differential eq. (2.29) from section 2.3.3.

If we use this approach in Maxwell's eqs. (2.22a) and (2.22b), we obtain the following relationship:

$$H_z = \frac{i\omega\varepsilon_r\varepsilon_0}{\kappa}E_x \tag{2.57}$$

If we apply this solution at the interface of two media with dielectric constants ε_1 and ε_2, as shown in fig. 2.6a, the continuity of the tangential E and H field components (see eq. (2.14)) dictates the following equations:

$$\hat{U} = \hat{V} \qquad \text{and} \qquad k_{x,1} = k_{x,2} \qquad \text{and} \qquad \frac{\varepsilon_1}{\kappa_1} = \frac{\varepsilon_2}{\kappa_2} \tag{2.58}$$

Taking into account the coordinate system in fig. 2.6a with $y = 0$ at the interface, surface confined fields ($\kappa_1 < 0$ and $\kappa_2 > 0$) require ε_1 and ε_2 to have opposite signs. As discussed in section 2.4.1, this is the case for an interface between a metal and a dielectric.

Inserting eq. (2.56) into eq. (2.29) gives the relationship between κ, k and k_x:

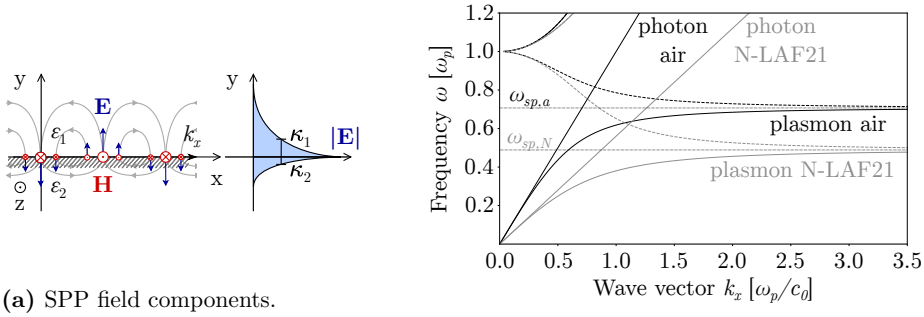
$$\kappa_1^2 = k_x^2 - k_0^2\varepsilon_1 \qquad \text{and} \qquad \kappa_2^2 = k_x^2 - k_0^2\varepsilon_2 \tag{2.59}$$

Combining eqs. (2.58) and (2.59), the dispersion relation of SPPs can be derived as:

$$k_x = \frac{\omega}{c_0}\sqrt{\frac{\varepsilon_1\varepsilon_2}{\varepsilon_1 + \varepsilon_2}} \tag{2.60}$$

Figure fig. 2.6b plots this dispersion relation for SPPs between a Drude metal with negligible damping (eq. (2.55)) and two dielectrica of approximately constant dielectric function ($\varepsilon_{air} = 1$, $\varepsilon_{N-LAF21} = 3.184$).

In relation to fig. 2.6b, a number of points require further elaboration. SPP excita-



(a) SPP field components. Inspired by [86].

(b) SPP dispersion relation

Figure 2.6.: SPP (excitation) at an interface. The orientation of E- and H-field components as well as E-field lines and the amplitude decay of the E-field in an SPP is shown in (a). The dispersion relation of SPPs at an interface between a Drude metal and an N-LAF21 glass substrate is shown in (b). Sections in which k_x has a real value are shown as a solid line. For frequencies in the dashed section, k_x only has an imaginary value.

tions correspond exclusively to the regions of the SPP dispersion curve that lie to the right of respective photon dispersion curves. For high values of k_x, the limit of a SP is obtained, which is a collective *uncoupled* interfacial electron oscillation with frequency ω_{sp}. The absence of a crossing between photon and SPP dispersion relations implies that a phase-matching technique is necessary for light-driven excitation of SPPs, which is discussed in the next section.

2.4.4. SPP Excitation and Surface Plasmon Resonance (SPR)

As the derivation of the SPP dispersion relation is based on the p-polarized light solution of Maxwell's equations, it could be hypothesized that SPPs are also excitable by s-polarized light. However, as demonstrated in [62, Ch. 2.2], no non-zero solution can be found in that case, meaning also that SPPs can only be excited through p-polarized light. Moreover, as stated in the last section, SPPs can only be excited at a metal-insulator-interface.

Excitation of SPPs using light presents a significant challenge, as illustrated in the dispersion relation depicted in fig. 2.6b. The discrepancy between the in-plane wavenumber k_x of SPPs and the wavenumber k of light, for any given medium and irrespective of wavelength, necessitates the utilization of special phase-matching approaches. [62, Ch. 2.2]

In this section, the approach of utilizing an Insulator-Metal-Insulator (IMI) config-

uration with a thin metal layer situated between two dielectrics of distinct optical density ($n_0 > n_2$) will be discussed. As outlined by S. A. Maier [62, Ch.3.2], the higher in-plane wavenumber $k_{x,0} = n_0 k_0 \sin\theta$ in the first dielectric together with the phenomenon of light tunneling through the metal layer allow for the excitation of SPPs at the interface between the metal and the second dielectric. The second dielectric needs to have a lower SPP wavenumber $k_{x,2} < k_{x,0}$ and incident light angles θ need to exceed the critical angle of total reflection θ_{crit} at the initial interface.

As argued by Kreysing [107], this approach can also be explained without invoking the quantum mechanical concept of tunneling. The phenomenon of total reflection causes the z-component of the complex wave number $k_{1,z}$ to be imaginary in the metal. This allows the wavenumber x-component $k_{1,x}$ to exceed the overall wave number $|k_1| = \sqrt{k_{1,x}^2 + k_{1,z}^2}$ in the metal.

Having discussed how SPPs are generated at interfaces, the question remains as to how SPPs can be used to analyze their environment. Firstly, influences that can modify the resonance condition, e.g. the effective RI of the sample, must be within the decay length of the evanescent field. This follows from the surface confinement of electric fields and makes SPP-based sensing intrinsically interfacial. As discussed by S. A. Maier [62, Ch. 10.2], the modification of a plasmonic interface and the resulting change in the resonance condition can be observed by either wavelength or angle interrogation:

- In case of wavelength interrogation, the change in the resonance wavelength of the light is informative. The response of the wavelength-reflectance spectrum of the sample is analyzed.

- In case of angle interrogation, which is relevant to SPRM, the change in the resonance wave vector component k_x is informative. Since $k_{1,x}$ of the light translates into a corresponding angle of light incidence, the response of the angle-reflectance spectrum is analyzed.

2.5. Surface Plasmon Resonance Microscopy (SPRM)

This section is designed to introduce the reader to the basic principles of SPRM through a historical lens. Based on an understanding of SPR from the previous section, the different SPRM variants are discussed in roughly chronological order. However, special emphasis is placed on amplitude response focused-objective SPRM (and furthermore on widefield-objective SPRM), as these are the techniques used in this work (see fig. 4.2). Figure 2.9 provides a visual overview of all SPRM variants discussed. A chronological overview of selected milestones can be seen in fig. 2.7.

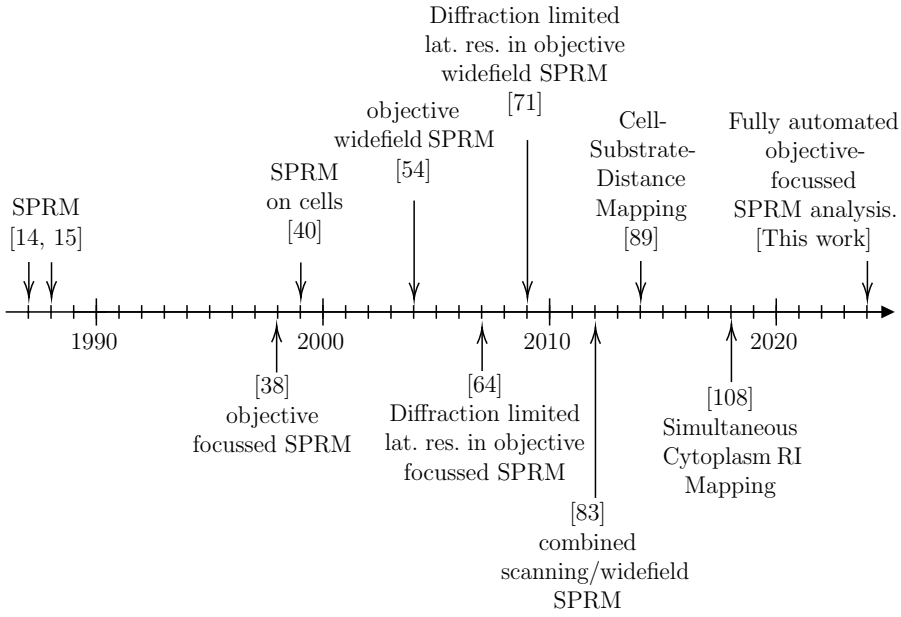


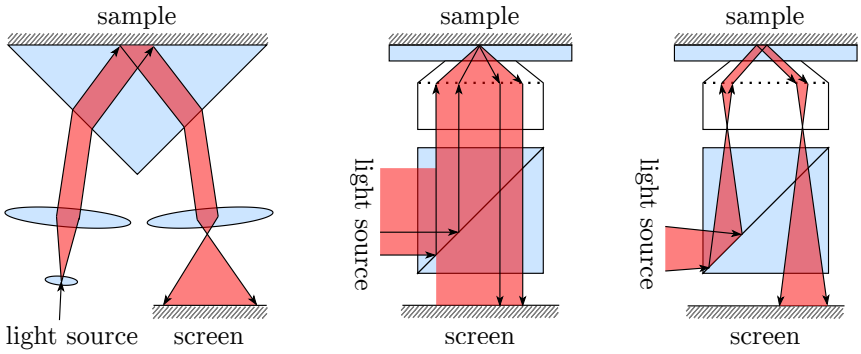
Figure 2.7.: Timeline of selected SPRM milestones, on which this work is based.

The technical details of (amplitude response) SPRM are covered in chapter 4. In particular, fig. 4.2 may be helpful for further understanding.

2.5.1. Prism Based SPRM

The first known SPRM configurations in 1987/88 [14, 15] were prism-based setups similar to the Otto- and Kretschmann- SPR configurations presented twenty years earlier. [7, 6] While Yeatman and Ash [14] already presented the possibility of a raster-scanning microscopy mode alongside with a widefield imaging mode, the setup of Rothenhäusler and Knoll [15] features the possibility of also measuring the transmitted light with a second camera. In both cases, the addition of imaging optics transforms a one-dimensional SPR configuration into an SPR measurement setup with lateral resolution, which will be our definition of an SPRM. While those prism configurations are sometimes separately referred to as SPR imaging (SPRI) systems [76, 111], the chosen definition here follows the original publications that coined the term of SPRM. [14, 15] A depiction of such a basic prism-SPRM configuration is given in fig. 2.8a.

Although higher resolution objective-coupled variants followed (see following sec-



(a) Prism SPRM **(b)** Focused Objective SPRM **(c)** Widefield Objective SPRM

Figure 2.8.: Sketch of an SPRM configuration with prism-coupling (a) and objective-coupling (b,c). For objective-coupled SPRM, there's a sketch of a focused(-scanning) mode (b) and a widefield mode (c).

tions), prism SPRM played a historical role in the study of cell-substrate distances. For example, the work of Giebel et al. [40] is believed to present the first reported estimation of cell-substrate distance using SPRM, and Peterson et al. [76] later provided a study of the developmental dynamics of cell-substrate interfaces.

2.5.2. Objective Based SPRM

It has been understood that the lateral resolution of SPRM can be limited by the SPP propagation length which is dependent on wavelength. [25] For wavelengths, needed for good SPR contrast, SPP propagation length is at the order of tens of µm. Therefore, 1998 it was shown by Kano et al. [37, 38] that SPPs can also be excited by a light coupling through an objective lens, which allows for several convenient ways of SPP localization, hence improving the lateral resolution. [64, 71, 119]

It should be noted that Kano et al. demonstrated such a setup in transmission mode (using 2 objectives) [38] as well as in reflection mode (using 1 objective) [37]. The latter one however is much more common in the literature at hand, and so this thesis refers to reflection-mode SPRM unless stated otherwise. The two sketches in figs. 2.8b and 2.8c feature such a setup. The important distinction between these two subtypes of objective SPRM will be outlined in the following two sections.

However, the maximum observable angle of reflection θ_{max} in such a configuration

is limited by the objective Numerical Aperture (NA) and the sample substrate RI through eq. (2.61). [147] It follows directly that objectives with high NA are required for samples with high SPR angles, such as biological cells in aqueous media. [54]

$$\mathrm{NA} = n \sin \theta_{max} \tag{2.61}$$

2.5.3. Objective Focused Scanning SPRM

Objective-coupled SPRM was first introduced as a focused(-scanning) microscopy technique where linearly or radially polarized light is focused onto a single spot or multiple scanning-spots sequentially. [38, 37] The focusing onto a single spot allows for a wide angle spectrum of reflected light to be captured. While the geometrical light path depiction in fig. 2.8b presents only two explicit angles of light incidence for illustrative reasons, the actually obtained angle spectrum is continuous from 0 to θ_{max}.

We could say that this technique offers the possibility of measuring a local reflectance-angle spectrum in a single shot, but therefore sacrifices the simplicity of lateral imaging previously achieved with prism SPRM. As for its locality, theoretical and experimental demonstration of reaching diffraction-limited resolution was provided by Watanabe et al. in 2007. [64] As for the reflectance-angle spectrum, its spot-wise evaluation allows for a quantitative, nm-resolved mapping of cell-substrate distances. [89] And as first demonstrated by Kreysing et al. [108], also the cytoplasmic RI of a cell can likewise be mapped simultaneously. Moreover, they have shown that this parallel determination of both parameters is a vital necessity, as determining only the cell-substrate distance under the assumption of a constant cytoplasmic RI leads to measurement errors of up to 100 nm. This is a reason why widefield SPRM methods are usually not suited for a precise quantitative analysis of cell-substrate distances.

Among the achievements of objective-focused SPRM are, for instance, measurements of spatio-temporally resolved membrane fluctuations in contracting cardiomyocytes [108] as well as the non-invasive measurement of RIs within cell organelles [117]. An important validation of the method lies in the successful direct comparison with SEM cell-substrate distance profiles. [121] A modification of the method, which improves its accessibility, is the use of platinum substrates as demonstrated by Hassani et al. which could replace the need for high-RI objectives in some applications. [120] The scope of application of objective-focused SPRM has developed in various directions since its inception, the investigation of photo-induced birefringence in azo-polymer thin films by Chakraborty and Kano being just one example. [125] With regard to the application for quantitative cell-substrate distance determination, however, it can be said that only a few pursue this approach, which may also be due to the relatively challenging and computationally intensive evaluation (see chapter 4), to which this work devotes a special focus.

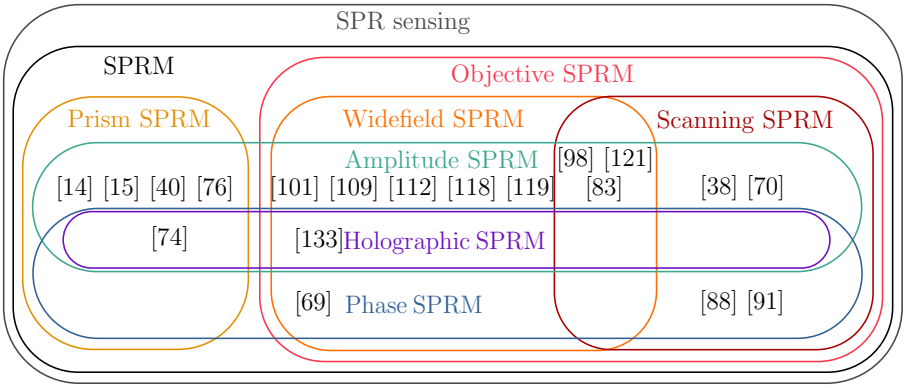


Figure 2.9.: Euler diagram of SPRM types and their relationship to each other. References to corresponding publications are given as examples; it is avoided to refer to more than one publication per research group in each setup type.

2.5.4. Objective Widefield Imaging SPRM

SPR can also be used more directly for imaging contrast if a larger area in the sample plane is illuminated and imaged. [54] However, in order to achieve sufficient contrast, the spectrum of incident illumination angles has to be restricted to a narrow range around expected SPR angles. This can either be achieved through a mask in a homogeneously illuminated Back-Focal Plane (BFP) while keeping the sample slightly out of focus [54, 69] or by a focused illumination in the BFP where also the sample is in focus [83, 89]. The second variant has the advantage of a relatively uncomplicated combination of scanning and widefield SPRM, as first shown by [83]. Since the present work also utilizes this approach to widefield SPRM, fig. 2.8c represents such a configuration.

Even though, widefield objective SPRM is closer related to the original variant of prism SPRM in that it brings back the simplicity and speed of single shot lateral imaging, it was first mentioned by Stabler et al. in 2004. [54] A theoretical and experimental demonstration of reaching diffraction-limited lateral resolution was provided by Watanabe et al. in 2009. [71] Furthermore, they succeeded in the widefield imaging of cell-substrate-interfaces in 2010. [77] In a remarkable widefield SPRM study 2017 by Liu et al. [101], it was even managed to create spatially and temporally resolved images of the propagation of electrical action potentials within individual neurons using this technique, thanks to its high sensitivity towards charge density fluctuations.

However, quantitative estimation of cell-substrate distances in the wide-field SPRM mode is usually not possible. Only a few variations such as angle-scanning wide-field

SPRM [98] or Surface Plasmon Resonance Holographic Microscopy (SPRHM) [133] provide this capability. Finally, among the numerous variations and improvements of this method, a multi-channel spatial light-switching approach should be mentioned here, which enables an improvement in lateral resolution through the localization of SPPs in widefield images. [71, 119, 123] A version of such an adaptation can also be found in the setup used here.

2.5.5. Amplitude Response SPRM

For the last three subsections on SPRM variants, let us take a look on the different contrast mechanisms that SPRM can be based on. The historically earliest mechanism, as well as the most common in the literature cited here, is amplitude contrast. Here, similar to classical variants of SPR sensing [7, 6], it is sufficient to capture the light intensity reflected from a sample. Either close to the angle of SPR in case of prism SPRM [14] or widefield objective SPRM [54], or angle-resolved in a wide spectrum in case of focused objective SPRM [38].

In the first two cases, the steep reflectance gradient around the SPR angle leads to a contrast-mapping of its local variation in the sample plane. In case of focused objective-SPRM, imaging is based on analyzing the entire angular reflectance spectrum at each point of the Region of Interest (ROI). The fitting of a reflectance model (see section 2.3.3) is finally what allows for the mentioned quantitative, nm-resolved mapping of cell-substrate distances alongside with cytoplasm RIs. [108].

2.5.6. Phase Response SPRM

Building on the results of Kano et al. [38], Somekh et al. established a different variant of focused objective-SPRM by integration into an interferometer. [46] This alternative variant uses the reflected light phase information instead of its amplitude information. Furthermore, it only requires a lock-in amplifier instead of a camera. By Berguiga et al., this approach was developed further to operate in an aqueaous environment. [60] By Somekh et al. it was later generalized to function also as a widefield method [69], borrowing the approach from Stabler et al. [54].

To the best of my knowledge, there has been no reported application of phase SPRM for a quantitative mapping of cell-substrate distances, although this should not imply that this would not be possible.

2.5.7. Holographic SPRM

Owing to the fact that neither intensity nor phase in widefield SPRM is a single-valued function of RI or of cell-substrate-distance, Hu et al. [74] proposed the technique

of SPRHM, which could be regarded as a hybrid between amplitude and phase SPRM. The potential of the method is particularly evident with Dai et al.[133], in whose work SPRHM is developed into a dynamic (real-time) wide-field technique for simultaneous monitoring of cell-substrate-distance and cytoplasm RI, using a wavelength- multiplexing approach.

3 Materials, Methods and Instrumentations

At the beginning of this chapter, a few terms are clarified in order to be able to differentiate as precisely as possible. The next sections in particular will make intensive use of these terms (see also fig. 3.1):

Cover glass The high RI glass foundation that is in direct contact with the SPRM immersion oil on top of the objective during a measurement.

Substrate The cover glass with all intended additional metal and passivation layers, also adhesive layers, which are themselves however not primary subject of an SPRM measurement.

Sensor The substrate, glued to a hole-in-the-bottom Petri dish.

Specimen The subject of an SPRM measurement, but explicitly without the sensor.

Sample The unity of specimen and sensor.

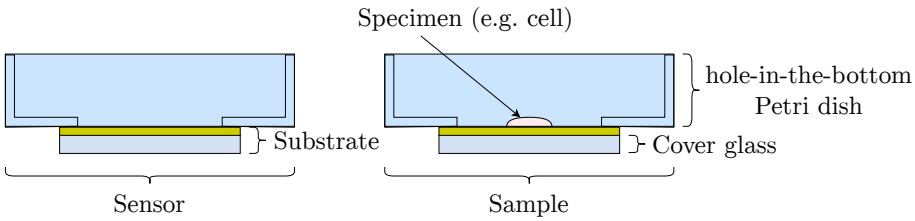


Figure 3.1.: Visualization of sensor and sample (cross section) to clarify related terminology.

3.1. Substrate Fabrication

3.1.1. N-LAF21 Cover Glass

For the choice of cover glass from possible candidates, the following factors were considered in the order listed: Optical properties, price and surface quality. As for the optical properties, the manufacturer of the objective sells matching cover glasses of a specific RI and Abbe number. Matching the RI at our Laser's wavelength is desired here for mainly two reasons:

- Working distance adjustment: Cover glasses can only be produced and handled with a finite minimum thickness. Since we want to focus Laser light under a very high angle onto the plasmonic layer, the cover glass needs to have a high enough RI to allow the focus to be outside its body, taking also into account a necessary finite film of immersion oil (see fig. A.1).
- Avoiding pre-layer-stack reflections: Since we are interested in the modeling of reflectances, unaccounted reflectance contributions and a loss of light intensity should be avoided. The plot in fig. A.2 shows reflectances for a tolerable range of mismatch between RIs (pre-layer-stack reflectance $< 0.000\,25$).

The Lanthanum Flint material N-LAF21 (SCHOTT AG, Mainz, Germany, Glass Code: 788475.428) turns out to be the closest match compared to the official manufacturer's cover glass, having an RI of $n_{632.8} = 1.78454$ at 632.8 nm wavelength. As for the price of the cover glasses, a large order of custom-cut N-LAF21 cover glasses resulted in a reduction of costs by a factor of about 20 per unit compared to the original manufacturer's offer.

The dimensions and agreed tolerances of ordered custom cut cover glasses are displayed in fig. 3.2. Unspecified tolerances were agreed to be within ISO 10110-11, which is sufficient to avoid unpleasant effects due to e.g. sample curvature or thickness gradients. Finally, optical surfaces were polished to yield a Scratch/Dig specification of 40/20.

3.1.2. Metal Coatings and Passivation

Protocol established and executed by Michael Prömpers.

The steps described in this section were carried out at the Helmholtz Nano Facility (HNF). All substrates are based on N-LAF21 cover glasses, as described in the previous section. For all types of substrates, the following cleaning steps are always performed first:

1. Cover glasses are cleaned in Ethanol, Acetone and Isopropanol for 5 min each.

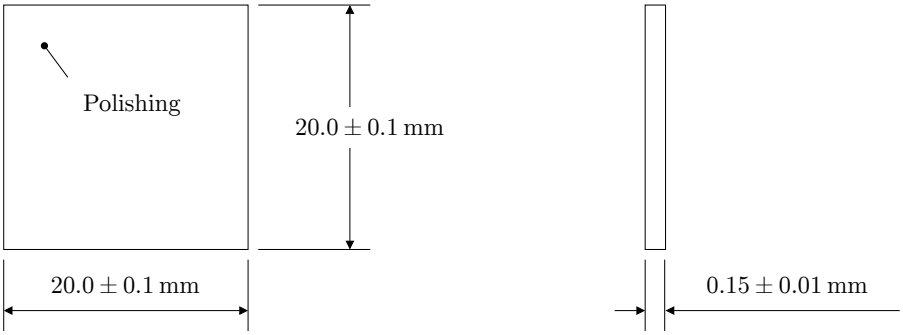


Figure 3.2.: Technical drawing of the substrate cover glass, including dimensions and tolerances.

2. They get O_2 plasma cleaned at 200 W with a 50 sccm flow rate for 5 min.

Depending on the substrate variant, the processes described next are used to produce thin layers (see fig. 3.3). For Au- and SiO_2 substrates (named after their uppermost layer):

3. A 3 nm Cr-layer is deposited by e-beam vapor deposition at 5×10^{-7} mbar and a deposition rate of 0.3 nm/s (Univex 400, Leybold).

4. A 47 nm Au-layer is deposited by e-beam vapor deposition, using the same parameters and the same machine.

The Cr-layer serves here as an adhesion layer. As indicated by table 5.1 and fig. A.5, the vacuum pressure has a significant impact on metalization results. The first substrates produced as part of this project experienced inconsistencies in vacuum pressure during fabrication. These substrates are not used in any of the reported measurements. Although a detailed investigation of the influence of vacuum pressure was not carried out, it is hypothesized that the thicker Cr layers observed with poorer vacuum pressure (table 5.1 and fig. A.5) are not necessarily caused by an increased deposition rate. Instead, if the vacuum pressure is too high, contaminants may be embedded in the film, oxide layers may form, or scattering effects may produce a less homogeneous, possibly porous, film.

The following two steps are only performed for SiO_2 coated substrates:

(5.) An adhesion layer of 2 nm Al_2O_3 is added by Atomic Layer Deposition (ALD) (FlexAL ALD, Oxford Instruments)

(6.) Before a passivating layer of 18 nm SiO_2 is applied by Plasma-Enhanced Chemical Vapor Deposition (PECVD) (Customized system, SENTECH Instruments GmbH)

For what will be called reference substrates (reference samples), a 300 nm Cr-layer is e-beam vapor deposited as the only layer on top of an N-LAF21 cover glass. Evaporation parameters are the same as for the 3 nm Cr-layers in Au- and SiO_2-substrates.

While Au- and SiO_2-substrates are used for plasmonic measurements, reference samples are effectively used as mirrors with their reflectance depending only on the two parameters of Cr RI and Cr Extinction Coefficient (EC), used to characterize the Laser's illumination intensity distribution.

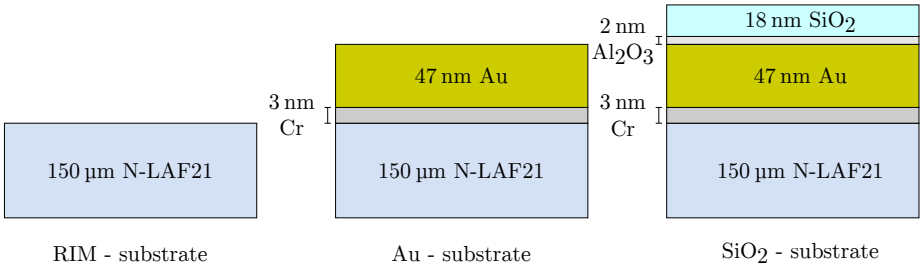


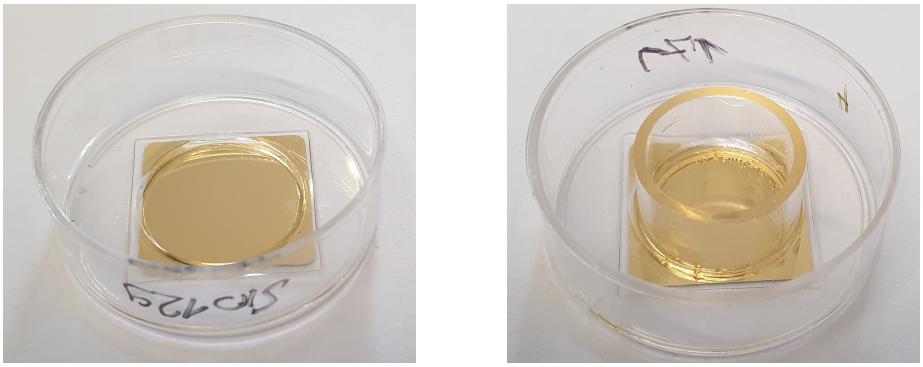
Figure 3.3.: Non-proportional representation of the different substrate types used in this work. Not shown are reference substrates and substrates for lateral resolution characterization. Refractive Index Microscopy (RIM) substrates are only used for the RI validation measurements in section 5.6.

3.2. Sample Preparation

3.2.1. Sensor Assembly

Protocol based on a protocol by Eva Kreysing, as described in [107]

To allow liquids and cell specimens in cell medium to interact with SPPs generated in the substrate, the sensor must be able to hold a volume of liquid for the duration of the measurement. For this, substrates are glued to the bottom of a 35 mm Petri dish (Cell E&G, Houston, Texas, USA), using a dual component optical epoxy (EPO-TEK 302-3M, Epoxy Technology, Inc., Billerica, Massachusetts, USA). The sensitive (plasmonic) surface faces into the volume of the Petri dish (see fig. 3.4a). The adhesive gets cured for at least 24 h at room temperature, which is stated as alternative curing protocol in the manufacturer's technical data sheet. As shown in fig. A.4, the primary curing protocol of 3 h at 65 C leads to a bending of substrates which makes it impossible later to retain focus in an area scanning measurement. Except for the curing parameters of the adhesive this protocol was adopted from [123] in order to avoid conflicts with material's chemical properties and biocompatibilities.



(a) Sensor w/o ring **(b)** Sensor with ring

Figure 3.4.: Photograph of two SPRM sensors (substrates glued to the bottom hole of Petri dishes). The left image shows the most commonly used variant without inner glass ring. The right image shows an adaptation with an inner glass ring used for some neuron cultures.

For a number of measurements with neuron cultures, an additional glass cylinder of (14.0 ± 0.5) mm inner diameter and with a height of (10.0 ± 0.5) mm gets glued onto the sensitive (plasmonic) surface inside of the Petri dish opening (see fig. 3.4b) to modify the contained liquids surface-to-volume ratio.

A flow chamber was designed as an alternative to Petri dish sensors for Joseph's work [135], theoretically allowing a controlled flow environment as well as a very rapid sensor assembly. However, induced pump vibration and the establishment of laminar flow within the chamber proved to be quite challenging issues and the flow chamber was not used for any of the results presented in this thesis.

3.2.2. Sensor Sterilization

Before sensors can be used in cell culture, they have to be sterilized to avoid contamination. Sterilization is performed in a two-step process:

1. Sensors get immersed into a mixture of 70 % EtOH and 30 % H_2O for (10-15) min.

2. They get exposed to at least 40 mWs/cm^2 UV light for 1 h.

After sterilization, (up to three) sensors are always kept within a larger Petri dish of 90 cm diameter, when not handled within a sterile bench. Until cells are seeded on those sensors, the outer Petri dish gets sealed with Parafilm®.

3.2.3. Cell-Adhesive Coatings on SiO_2

Coatings on SiO_2-substrates are applied to investigate their effect on cell-substrate-distances of HEK293 cells.

Adhesive coatings are applied by allowing sterilized substrate surfaces to soak in respective coating solutions for 30 min at room temperature. Afterwards, sensors are rinsed with 4 mL of Phosphate Buffer Solution (PBS), filled with 4 mL of HEK293 medium, and stored at 37 C in the incubator for up to 12 h until cell seeding.

In the following, coatings will be briefly discussed, roughly in order of their molecular complexity. For all coatings, apart from Extracellular Matrix Gel (ECM), the aim was to reproduce coatings from the work of Wrobel et al. [65].

PLL and PDL

PLL and Poly(D)lysine (PDL) are polymers of L-lysine and D-lysine that are used to engineer attachment and growth of in-vitro neuronal networks. [82] Due to their polar amine groups (see fig. 3.5a), they bind electrostatically and non-specifically to charged molecules, including many types of proteins. PLL however is also known for its cytotoxic and proinflammatory effects. [47] And similarly, also for PDL a cytotoxic effect has been demonstrated. [131]

The used variant of PLL has a molecular weight of (150-300) kDa. That of PDL has a molecular weight of (70-150) kDa. Both are of synthetic origin.

For coating with PLL, 4 mL of PLL-bidest solution (50 µg/mL PLL concentration) per sensor are used. For coating with PDL, 5 mL of PDL-PBS solution (100 µg/mL PDL concentration) per sensor are used.

Concanavalin-A

Concanavalin-A (Con-A) is a homotetrameric (consisting of four equal subunits) adhesion protein that stems from jack beans and can bind to carbohydrates. [26] Figure 3.5b provides an intuition of its size and complexity.

For coating, 2.5 mL of Con-A-bidest solution (100 µg/mL protein concentration) per sensor are used.

Fibronectin

FIB is a dimeric (consisting of two subunits) multi-role glycoprotein. The amino acid chain of each subunit exhibits mainly three different repetitive motives which

fold into three different kinds of domains. Different parts of this chain can bind to different kinds of other biomolecules, cell-surface receptors being one of them. [30] While the used variant of FIB was extracted from bovine plasma (see appendix C), fig. 3.5c (which is actually based on data from human FIB) gives an intuition of this molecule.

For coating, 4 mL of FIB-PBS solution (12.5 µg/mL protein concentration) per sensor are used.

Laminin

LAM is a heterotrimeric (consisting of three different subunits) cell-adhesive glycoprotein. Its subunits are termed α, β and γ. [103] While LAM strictly speaking refers to a family of different molecules, depending on the combination of subunits, we are referring just to the variant used here, being composed of subunits α_1, β_1 and γ_1 (LAM-111), and being isolated from a type of cancerous mouse cell (see appendix C). A sketch can be seen in fig. 3.5d.

For coating, 5 mL of LAM-Tris solution (2 µg/mL protein concentration) per sensor are used.

ECM

The extracellular matrix plays a vital and complex role for cells within multicellular organisms, functioning as a scaffold, providing cues for cell proliferation and differentiation, as well as supporting maintenance and repair of the cellular tissue. [52] ECM contains a mixture of different proteins and other components which can be used to mimic a natural environment of cells.

According to the manufacturer, the ECM used consists predominantly of laminin. Other main components are type-IV-collagen, heparan sulfate proteoglycan and entactin.

For coating, 350 µL of ECM-PDL-HBSS solution, consisting of 2.55 µL ECM gel (1 mg/mL) and 2.55 µL PDL (1 mg/mL), per sensor are applied to the 18 mm diameter opening above the substrate surface. Unlike with other coatings, ECM and PDL are thawed and kept on ice on the day of coating. Also substrates, pipette tips and HBSS were cooled to below 10 C before coating.

3.2.4. Cell-Adhesive Coatings on Au

Coatings on Au-substrates are applied to investigate their effect on cell-substrate-distances of primary rat neurons. Unlike for SiO_2-substrates, only two coatings for Au were investigated in this work.

PLL

PLL was selected as a coating because it is a commonly used surface modification at the institute for culturing neurons, as for example in the work of Cepkenovic et al. [132].

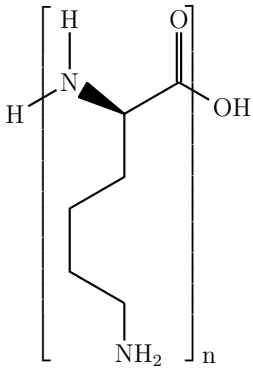
For coating, 2 mL of PLL-bidest solution (10 µg/mL PLL concentration) are applied per sensor. After 1 h at room temperature, the solution gets replaced by 4 mL HBSS and samples are sealed in Parafilm® and stored at 4 C for up to one week until seeding of neurons. It is taken care to not let the surface dry out after the application of PLL.

PDL-Laminin

As it is also a common surface modification for neuron culture, a two-step PDL-LAM coating is also investigated. The following protocol has been adapted from Kreysing et al. [136].

First, 1 mL of PDL-Penicillin-Streptomycin (PS)-PBS solution (10 µL PS and 10 µL PDL) is applied to the 18 mm diameter opening of each sensor. Confined in a Parafilm®-sealed container, sensors are kept in the fridge overnight, before the solution gets removed and surfaces get quickly washed two times with (2-3) mL of PBS. A third wash is performed for 20 min before the PBS is removed again.

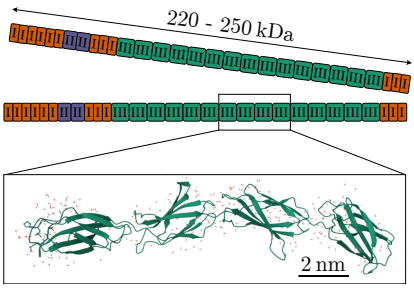
Second, 1 mL of LAM-PS-NB (Neurobasal Medium™) solution (10 µL PS and 1 µL LAM) is applied in the same way. However, in this second step, sensors are incubated for at least 4 h at 37 C. Finally, the coating solution gets replaced with neuron medium and sensors are stored in the incubator until neuron seeding.



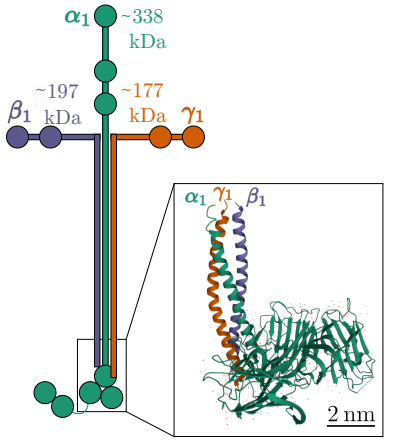
(a) The polymeric structure of (α) PLL and PDL, different only in their three-dimensional spatial arrangement. [141, 140]. The index n indicates the number of subunit-repetitions.



(b) Chrystallographic structure of metal-free Con-A. While only the metallized conformation of Con-A is relevant for carbohydrate-binding, this depiction provides an intuition on the overall size of the complex. [27, 26]



(c) Sketch of the dimeric structure of FIB. Its constituting domains FN-I, FN-II and FN-III are shown in different colors. A segment of four type III domains is shown in detail to illustrate structure and size. [29, 30]



(d) Sketch of the heterotrimeric structure of LAM-111. Its constituting parts α_1, β_1 and γ_1 are shown in different colors. Its integrin-binding region is shown in detail to illustrate structure and size. [102, 103]

Figure 3.5.: Illustration of the molecular structure of Poly-L-Lysine, Poly-D-Lysine, Concanavalin-A, Fibronectin and Laminin.

3.3. Cell Culture

Unless otherwise stated, all steps described in this section are performed under sterile conditions.

3.3.1. HEK293 Medium

The medium used throughout this work for cultivation, washing and experimentation with HEK293 cells is composed as follows:

- 90 % Dulbecco's modified Eagle's medium (DMEM)
- 9 % fetal bovine serum (FBS)
- 1 % PS

Catalog numbers are listed in appendix C. The medium gets prepared in volumes of 100 mL. It is kept sterile and stored between use at 4 C. Medium older than one month is only used for washing.

3.3.2. Thawing and Freezing of HEK293 Cells

HEK293 cells used throughout this work were originally provided to the Institute by Arnd Baumann.

To allow for easy transportation and storage, preventing changes in phenotype and genotype over extended periods of time, cell lines are typically stored in liquid nitrogen. [35]

Thawing

At the beginning of cell culture work, but also at later time points to obtain cells with a lower passage number, HEK293 cells are thawed from liquid nitrogen. From the liquid nitrogen storage, a cell-aliquot is moved quickly to a 37 C water bath. As soon as the aliquot is liquid, its content gets pipetted into a 15 mL centrifuge tube with 5 mL of pre-warmed media. The cell suspension gets centrifuged for 5 min at 1100 rpm. The supernatant gets aspirated and replaced by 1 mL of warm medium. Once the cell pellet has been dispersed using a (1 mL) micropipette tip (pipetting up and down approx. 10 times), the cell suspension is moved to a T25 flask with 5 mL of pre-warmed cell culture medium before quickly being moved to the incubator. The culture gets split on the next day. From there on, it is maintained as described in the next section.

Freezing

To replenish the supply of frozen HEK293 cells, a unit of cells gets thawed, grown in three T75 flasks (Th. Geyer GmbH & Co. KG, Cat. No. 7696782, 75 cm^2 growth area) to reach a confluency of (80-90) % and then re-frozen. For this, ten cryo-tubes with 100 µL DMSO are cooled in the gas phase above a container with 300 mL liquid nitrogen. Cells get separated from their substrates, centrifuged, and dissolved in 9 mL of medium. For each cryo tube, 900 µL of cell suspension is added. Cell suspension and DMSO are mixed by pipetting up and down twice (using a 1000 µL pipette tip). Tubes are quickly sealed and moved to the cold liquid nitrogen gas phase. After 4 h, frozen cells are moved into the liquid nitrogen cell bank.

3.3.3. Maintenance of HEK293 Cells

HEK293 cells are maintained in T25 cell culture flasks (Th. Geyer GmbH & Co. KG, Cat. No. 7696781, 25 cm^2 growth area) with cell medium in a humidified 5 % CO_2 atmosphere at 37 C. At a confluency of about (70-80) %, usually every (3-4) d, cells have to be split. Prior to splitting, however, cells get investigated under the EVOS M5000 light microscope, using at least the lowest- and highest magnification objectives. If cells appear healthy and ready for splitting, their medium gets exchanged for 1 mL of freshly-thawed warm trypsin/EDTA. For the purpose of washing, this volume gets removed again and cells are incubated in another (1-1.5) mL of Trypsin/EDTA for 5 min (humidified 5 % CO_2 atmosphere at 37 C). This step should loosen cell adhesions. If cells, after a gentle shaking of the flask, still appear clustered under the light microscope, they are shaken incrementally coarser until they appear separated. However, it is also aimed to deactivate again the Trypsin/EDTA as fast as possible by adding 5 mL of warm cell medium. The resulting (6-6.5) mL of cell suspension get transferred to a 15 mL centrifuge tube before centrifuging for 5 min at 1100 rpm. The supernatant gets removed and cells get re-suspended in 1 mL of warm medium. Once the cell pellet has been dispersed using a (1 mL) micropipette tip (pipetting up and down approx. 10 times), 100 µL of the cell suspension is added to a new T25 flask with 5 mL of pre-warmed cell culture medium before quickly moving cells back to the incubator.

In the last step, cells are also seeded onto prepared SPRM sensors with 3 mL of pre-warmed cell medium, if needed for a measurement. Those cells are kept in the incubator for (5-10) h.

3.3.4. Neuron Medium

The neuron medium used throughout this work for cultivation, washing and experimentation. The composition, optimized for neuron growth, and simultaneously for the inhibition of glial cells, is composed as follows:

- 10 mL Neurobasal Medium^{TM}
- 100 µL B-27^{TM} supplement
- 25 µL L-Glutamine
- 10 µL Gentamicin

Catalog numbers are listed in appendix C. The medium is prepared from shared supplies in the required quantities as needed.

3.3.5. Isolation of primary rat neurons

Protocol established and executed by Bettina Breuer.

Cortical neurons are isolated from E18 Wistar rats (RjHan:WI, supplied by Janvier). After a 10 min 0.05 % trypsin treatment, dissociated neurons are plated on prepared sensors. Seeding densities can be taken from table A.3.

3.3.6. Maintenance of primary rat neurons

Neurons are cultured for (3-5) d in a humidified 5 % CO_2 atmosphere at 37 C. Culture medium volume and surface, as well as other sample related details are listed in table A.3. The culture medium was not changed, but in some cases topped up to the original volume after (2-3) d.

3.3.7. Buffers

Buffers are prepared from listed components and distilled water under constant stirring. When components are dissolved, pH is adjusted to 7.4 at room temperature by adding HCl or NaOH. Buffers get filtered (0.2 µm pore size) autoclaved and kept sterile for use in cell culture.

PBS

- 137 mM NaCl
- 8.1 mM Na_2HPO_4
- 2.7 mM KCl
- 1.4 mM KH_2PO_4

Tris

- 150 mM NaCl
- 50 mM Tris

HBSS

Bought ready-to-use. (See appendix C)

3.4. Auxiliary Methods

3.4.1. Atomic Force Microscopy

Atomic Force Microscopy (AFM) is an Ångström-precise scanning probe microscopy method for the mapping of surface topographies. [43]

Substrate Layer Thickness Determination

Measurements performed by Anja Zaß at the HNF and Alex Winkel at the University of Cambridge

In a first attempt to monitor substrate layer thicknesses, AFM scans are performed across artificially separated layer steps. The fabrication of a stepped substrate, as shown in fig. A.6, is done by covering parts of the substrate in each metallization step with a rectangular prism[1]. Step size measurements are performed as area scans over all steps. Three measurements were carried out by Anja Zaß. These measurements are analyzed with Gwyddion [81]. Four additional measurements were performed and analyzed by Alex Winkel. The results are presented and discussed in section 5.2.

Substrate Layer Topography Measurements

Measurements performed by Kevin Rosenberger at the HNF.

In a later attempt to characterize thickness variations and surface defects of SPRM substrate layers, AFM topography measurements are carried out on three small areas ($5 \times 5\,\mu m$), one medium sized area ($50 \times 50\,\mu m^2$) and one large area ($100 \times 100\,\mu m^2$) for a Cr coated substrate and a Cr-Au coated substrate respectively. Scans are analyzed with Gwyddion [81] and Python.

[1] It was expected that photoresist residues may distort the measurement of the step heights in the case of a lithographic process.

3.4.2. X-Ray Reflectometry

X-ray Reflectometry (XRR) provides absolute measurements on area-averaged film thicknesses and their RMS roughness. Interference fringes in the observed angular reflectance spectrum have oscillation periods that are inversely proportional to film thicknesses. Oscillation amplitude decay is positively correlated with film roughness. These oscillations can be fitted by a stratified multilayer reflectance model (compare section 2.3.3) to extract Ångström-accurate layer thickness and RMS roughness values. [43]

In this work, a Bruker AXS D8 ADVANCE ($\lambda = 1.5406\,\text{Å}$) is used to stochastically monitor these two parameters for fabricated substrate layers, usually for every 10^{th} substrate of each batch. Reflectance data is fitted with a robust differential evolution optimizer, implemented in the open source software GenX. [126]

Measurements performed by Yifan Xu.

3.4.3. Refractometry of Liquids

An Abbe refractometer (Carl Zeiss AG, model G, see fig. 3.6a) is used to determine the RI values of cell media, as required for modeling the reflectance spectra of cell samples. Light from an Light Emitting Diode (LED) with a wavelength of 635 nm (LED635L, Thorlabs Inc., 15 nm FWHM) is attenuated and dispersed to an eye-safe intensity before it is coupled into the refractometer, using its mirror construction. The value of RI gets determined as described in the user manual. Holding a phone camera to the right eye-piece, the reticle is moved onto the observed angle of total reflection (see fig. 3.6c). An image is taken for digital re-evaluation. Then holding the phone camera to the left eye-piece, the value of RI is read and another image is taken (see fig. 3.6b). Measurements are carried out at room temperature, which is determined using the room thermostat. At the beginning of each series of measurements, the RI of H_2O gets determined as a control.

3.4.4. Compound Microscopes

The following compound microscopes were used for stated purposes.

Axio Vert

A digital inverted microscope from Carl Zeiss AG that is used to take phase-contrast (PC), differential interference contrast (DIC) and brightfield images of HEK293 cells

and SPRM substrate surfaces until May 2023. Its inverted design is convenient for the placement of cell culture samples and SPRM substrates.

EVOS™ M5000

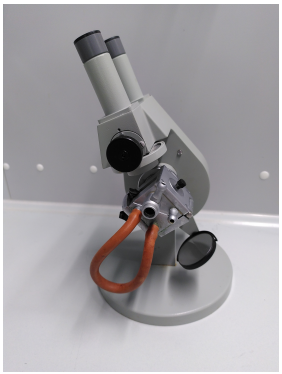
A fully integrated digital inverted benchtop microscope from Thermo Fisher Scientific Inc. that is used for transmitted-light imaging of HEK293 cells, neurons and SPRM substrate surfaces from May 2023 on. Air objectives with magnifications 1.25 x, 4 x, 10 x and 20 x are used.

Axiotech Vario

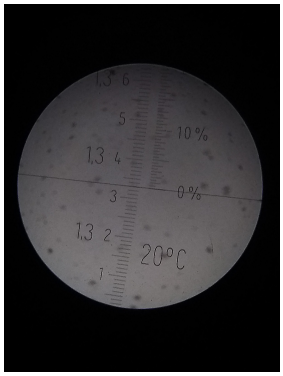
Integrated into the prototype SPRM setup (see section 4.1), this microscope is equipped with a HAL 100 (Carl Zeiss AG, Oberkochen, Germany) light source. A 20 x air objective is employed to take reflected light images of samples on the optical axis of the SPRM objective. Furthermore, the HAL 100 halogen light source is employed to take transmission mode (brightfield) images with the SPRM setup Object Plane (OP) camera. Halogen light paths for both imaging modes are depicted in fig. A.9. The HAL 100 light source has been aligned and focused according to the manufacturer's instructions.

3.4.5. Osmometry

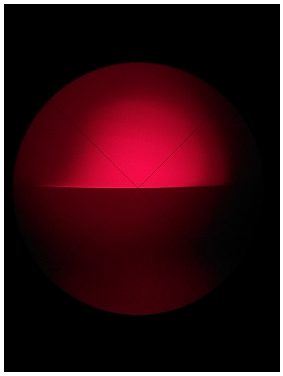
During the culturing of neurons, the stability of osmolarity was ensured by regular measurements with a Gonotec® Osmomat 3000 basic freezing point osmometer. Measurements are carried out as instructed by the device. Cleaning of the sensor with H_2O before and after measurements was performed to avoid cross-contaminations.



(a) Photograph of the refractometer.



(b) View through the left eye-piece.



(c) View through the right eye-piece.

Figure 3.6.: Picture of the Abbe refractometer used and photographs taken through the left and right eyepieces during the measurement of the H_2O refractive index.

4 Amplitude Response, Combined Scanning and Widefield SPRM

4.1. The Prototype Setup

Unlike in section 2.3 where we discussed properties of light in terms of wave optics, this chapter will consider light and its propagation from the point of view of geometrical optics in terms of rays. A derivation or discussion of this concept is not given here, but a thorough introduction can be found in [39, Ch. 6], where geometrical optics is derived from wave optics as the limit of zero wavelength.

The current SPRM setup is the iterative result of the work of Koji Toma [89], Eva Kreysing [107] and Hossein Hassani [123]. The version used was built by H. Hassani and its detailed construction can be found in [123]. The features of LED illumination kit and coherence removal kit were not used in the main part of this project, therefore a simplified setup sketch without these features is shown in fig. 4.1.

Optical paths in scanning and widefield SPRM

Independent of the imaging mode, a polarized 10 mW He-Ne laser (25-LHP-991-230, Melles Griot, Santa Ana, California, USA) with a wavelength of $\lambda = 632.8\,\text{nm}$ is used as the illumination light source. The laser is switched on for at least 10 min before use. The light intensity can be adjusted by neutral density filters, but these were not used in the present measurements. A linear polarizer defines the beam polarization relative to the optical table. A laser line filter ensures the spectral purity of the beam. The initial beam diameter of 0.65 mm is expanded to 21 mm by a beam expander. A subsequent iris is left at a maximum aperture of 25 mm to cut out stray light.

In the case of scanning SPRM, the beam is directed to the radial polarizer. Since the current version of the setup uses a ZPol (Micro Laser Systems, Inc., Garden Grove, California, USA) as the radial polarizer, the resulting beam polarization is only approximately radial. Two lenses are used to image the plane of the radial polarizer onto the BFP of the high NA objective (NA 1.7 APON100×HOTIRF, Olympus Corp., Tokyo, Japan). The objective focuses the beam onto the Au layer of the

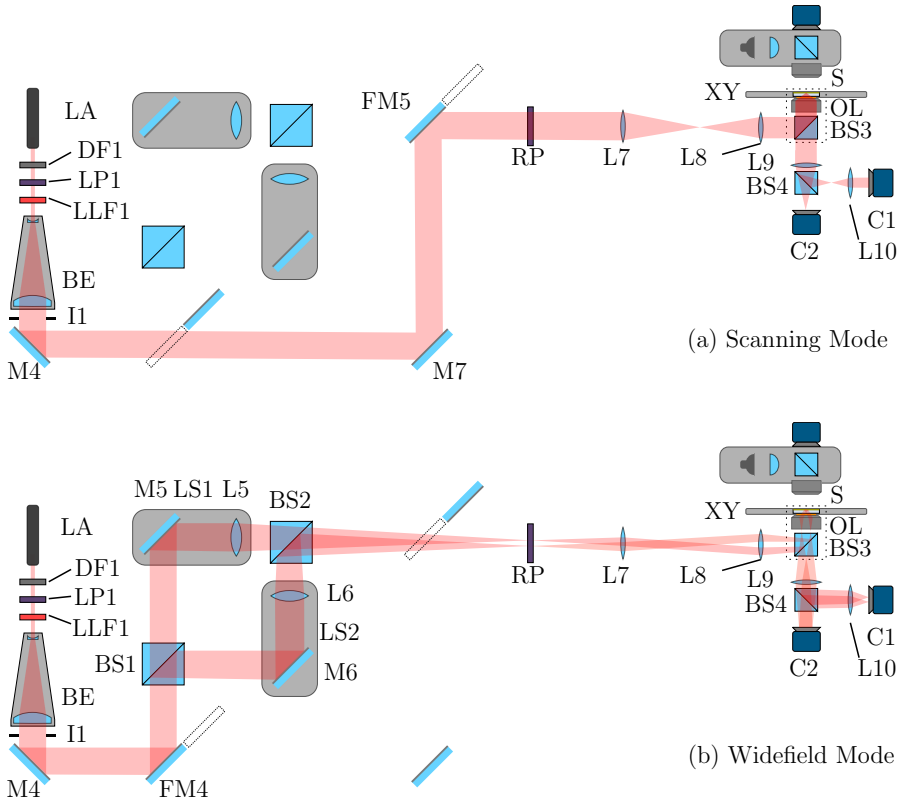


Figure 4.1.: Simplified sketch of relevant beam paths in the SPRM prototype setup used throughout this work. The configuration for objective focused scanning SPRM is shown in (a). The configuration for objective widefield imaging SPRM is shown in (b). While the physical setup also includes additional light paths for reduced coherence laser illumination and LED illumination, these were not used and are therefore not shown here, thus reducing the number of mirrors and lenses in this illustration. A sketch of the complete physical setup can be found in [123, Ch. 4]. The elements are labelled as lenses (L#), mirrors (M#), flippable mirrors (FM#), beam splitters (BS#), objective (OL), laser (L), neutral density filter (DF), linear polarizer (LP), radial polarizer (RP), laser line filter (LLF), beam expander (BE), irises (I#), linear stage (LS), sample (S), scanning stage (XY) and cameras (C#). Labelling and numbering correspond to [123, Ch. 4]. The dotted area around sample and objective is detailed in fig. 4.2. Halogen light transmission and reflection microscopy modes, also covered by the parts of the setup on the right of the sketch, are detailed in fig. A.9.

sample and collects the cone of reflected light, transforming it back into a parallel beam. Two beam splitters are used to direct this reflected beam to two cameras (Ximea MQ042MG-CM). The BFP camera images the cross sectional intensity distribution of the beam in the BFP. The OP camera images the focused spot in the OP.

In the case of the widefield SPRM, the beam is directed through the dual beam widefield kit[1] [123], resulting in two horizontally separated beams. Their horizontal positions are individually adjustable using the two linear stages of the dual beam widefield kit. Focusing these two beams onto two opposite segments of the ZPol results in two opposite linearly polarized beams. Two lenses focus these two beams onto the BFP of the high NA objective. The objective converts them into two parallel beams that meet at the OP. Similar to [119], a reduced SPP propagation length and thus improved lateral resolution is achieved. The objective focuses the parallel beams of reflected light into the BFP. The BFP camera images the focused light spots in the BFP. The OP camera images the reflected intensity distribution in the OP.

Contrast mechanisms in scanning and widefield SPRM

As introduced in section 2.5.3, scanning SPRM can produce topographic maps of the basal cell membrane or other structures close to a metallic surface by analyzing the local reflectance-angle-profile at each point of a raster scanning measurement. As shown in insets (a2) and (a3) of fig. 4.2, each angle of reflection in the light cone is mapped to a radial position in the beam cross section in the BFP. Captured by the BFP camera, these cross section images are analyzed in detail as described in the following sections of this chapter.

As introduced in section 2.5.4, widefield SPRM maps the distribution of reflectance values for a given angle of incidence in the OP. By adjusting the linear stages of the dual beam widefield kit, the angle of incidence can be set to match the SPR angle of the substrate, resulting in a minimum reflected intensity in the absence of a sample. As shown in inset (b1) of fig. 4.2, the presence of a cell, for example, increases the reflected light intensity in parts of the beam where the basal cell membrane is close to the plasmonic layer, effectively imaging cells as bright areas in the OP camera image plane. The reverse contrast mechanism, where the angle of light incidence is adjusted to the SPR angle in the presence of the sample, is of course also possible.

Sample holder

Samples are placed on a piezoelectric stage (M-687.UL, Physik Instrumente (PI), Karlsruhe, Germany), controlled by a C-867.262 controller (PI). To mount the samples on the piezoelectric stage, a tiltable sample holder was designed by *Johannes*

[1] The dual beam widefield kit consists of BS1, BS2, M5, M6, LS1, LS2, L5 and L6.

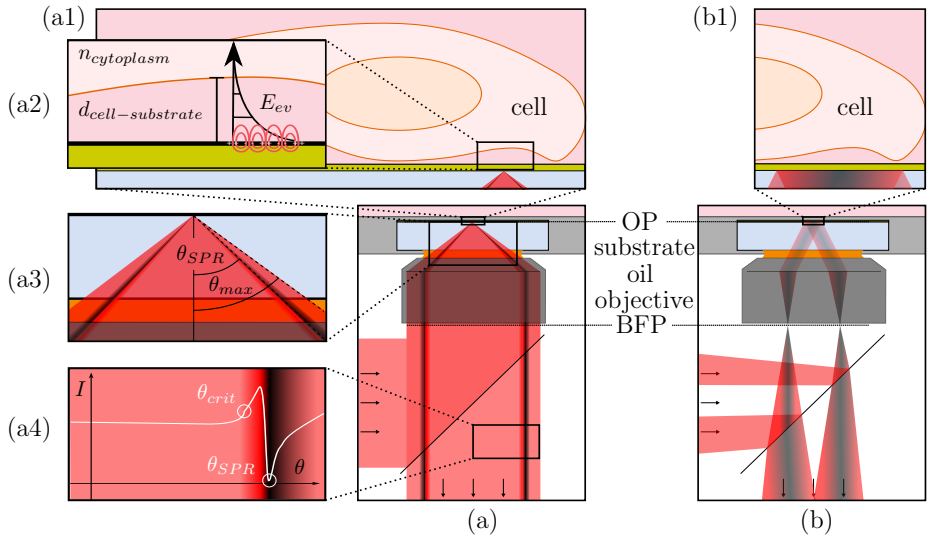


Figure 4.2.: Sketch of the light-sample interaction in the measurement setup. A magnified view of the dotted area in fig. 4.1 is given for scanning SPRM in (a) and for widefield SPRM in (b). Insets (a1) and (b1) show the different contrast mechanisms in scanning and widefield mode. SPPs and the coupled evanescent field E_{ev}, probing cell-substrate distance and cytoplasmic RI are shown in (a2). The SPR angle and the definition of θ_{max} are shown in (a3). The definition of the critical angle and the SPR angle are shown in (a4).

Pfennings and manufactured by the mechanical workshop. This tiltable sample holder has three micrometer screws as support points to the stage, allowing any tilt between the optical axis and the normal of the sample plane to be compensated. Unfortunately, as it turned out, the compensation procedure has to be repeated for each sample. Furthermore, the manual adjustment of the screws in an iterative process of moving the stage in x and y directions until the focus remains in the sample plane regardless of stage position is quite time consuming. As cell measurements are considered time critical, only a coarse adjustment of the tilting stage has been performed. However, for scanning measurements of a few tens of µm, the loss of focus observed in the OP was considered negligible.

Before mounting a sample, the objective is gently[2] cleaned with an optical grade cotton swab[3] soaked in isopropanol. The top camera (see section 3.4.4) is used to

[2]No pressure applied.

[3]A lens cleaning tissue should be sufficient if there are no oil residues on the lens. This reduces the possibility of damaging the lens.

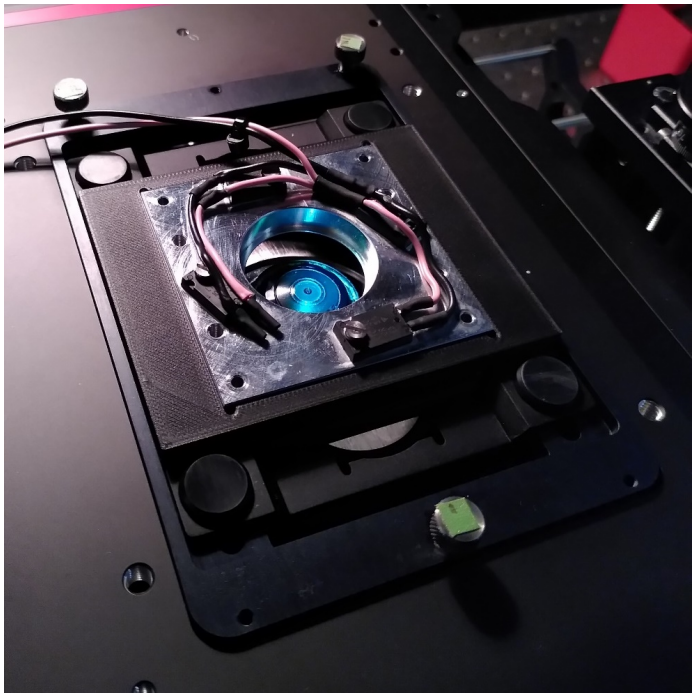


Figure 4.3.: Photo of the tiltable sample holder mounted in the piezo xy stage. The heating module is mounted in the center of the tiltable sample holder using a 3D printed adapter. The objective can be seen through the opening at the center of the heating module. The markings 'I', 'II' and 'III' on micrometer screws of the tilting stage also serve to track the orientation of the screws.

check that the objective surface is free of dust and oil residues (see fig. A.3). The gap between the high NA objective and the sample substrate is bridged by a high NA immersion oil (n=1.7800, Cargille Refractive Index Liquid Series M, Cedar Grove, New Jersey, USA) as depicted in fig. A.1. 3-6 drops are applied using a needle-tip syringe prior to mounting the sample. Sample mounting is considered a time critical step due to the crystallization of the immersion oil on contact with air. [123, Ch. 4]

For cell-substrate measurements, a heating module is added to the sample holder. The heating module has no temperature control mechanism, but the supply voltage is adjusted using a manual thermometer so that the temperature of a liquid-filled sample with a closed lid reaches $(34 \pm 2)\,\mathrm{C}$. When used, the heating module is switched on at least one hour before measurements. The heating module together with the tilting sample holder is shown in fig. 4.3.

Data acquisition software

The cameras and sample stage are controlled centrally by Python software. This software was developed by *Dijo Moonnukandathil Joseph* as part of his master's thesis. [135]

For area scans, a snake path scan pattern with a specified step size in the x- and y-directions can be generated automatically. One way is to specify the start and stop coordinates directly in the diagonal corners of an ROI. However, the most commonly used mechanism is to first move one corner of the rectangular ROI into the visible transmitted part of the laser beam using the top camera view of the brightfield microscope (see section 4), thereby setting the stop coordinate of the stage. Then the opposite corner of the ROI is moved into the visible part of the laser beam, setting the start coordinate for the scan. Exposure time is set using an exposure histogram. For Au and SiO_2 sensors, 1 ms is always used as the setting.

4.2. Analysis Step I : Back-Focal Plane (BFP) Parametrization

The following three sections (sections 4.2, 4.3 and 4.5) provide an overview of the key components and considerations of the data analysis software developed as part of this project. While the Matlab data analysis software previously developed by Hossein Hassani is an important contribution to this project, it became clear early on that important changes were needed to make the data analysis more robust and reproducible. The robustness now achieved is due to the implementation of a least squares optimization approach (see section 4.5). Reproducibility is achieved through the use of parameter json files that are stored with the data analysis results. In this way, any analysis can be reproduced using the corresponding set of software version and parameter files. An additional benefit of the new data analysis software is that it is written entirely in Python, an open source (non-commercial) programming language, removing barriers to accessibility. All code is documented using the PEP 257 docstring conventions. The decision not to use an object-oriented programming structure is a conscious one in favor of code readability. The complete software is published as `SPRManalysis-2` *[144]. Although the entire software was developed by me, the data analysis approaches of Koji Toma [89], Eva Kreysing [107] and Hossein Hassani [123] certainly served as a starting point.*

The first step in SPRM data analysis is committed to the extraction of parameters x_0, y_0 and r_{max} from eq. (4.2), needed in the second step (section 4.3). The parameters x_0 and y_0 represent the center coordinates of the BFP image, which correspond to the location where the beam's partial ray, reflected perpendicularly

from the sample, is imaged. The parameter r_{max} denotes the projected size of the objective aperture (see fig. 4.7).

The procedure is as follows: First, the outer edge of the beam cross section (the aperture) and the SPR minimum are detected in BFP images, using a custom edge detection algorithm (section 4.2.1). Then the aperture edge (beam outline) is fitted to determine r_{max} (section 4.2.2) and the SPR minimum (dark inner "circle") is fitted to determine (x_0,y_0) (section 4.2.3).

The described operations are implemented in the `extract_bfp_img_features` function of the `extract_bfp_img_features.py` module of `SPRManalysis-2` [144].

4.2.1. Edge Detection

The analysis of BFP images begins with an edge-detection procedure, which is employed to discriminate between pixels of the SPR minimum, the beam outline (aperture projection), and everything else, particularly ignoring noise and artifacts.

It was not possible to identify one parameter set that could be used to detect relevant BFP image edges in a robust manner using standard edge detection algorithms, such as the Canny algorithm [13]. A common issue observed was the varying sharpness of relevant edges. For instance, the edges surrounding the SPR minimum can be more or less pronounced, depending on the sharpness of the substrate's SPR peak. Conversely, the beam-outline edge can be blurred to varying degrees when the sample defocuses over the course of a measurement (see section 4.3.4).

For this reason, a custom edge detection algorithm has been developed, drawing upon prior knowledge about the problem at hand, including its radial symmetry and the approximate position of expected edges. The edge-detection procedure is comprised of six steps. Using the example BFP image from fig. 4.4, these steps will be now explained:

Figure 4.4a A BFP image of 2048x2048 pixels, each pixel represented by an 8-bit unsigned integer, is loaded into the working memory.

Figure 4.4b Intensity gradients are calculated. For this purpose, the image is convolved with a Sobel operator [8], which enables the calculation of the gradient magnitude and gradient orientation angle. These will be employed in the subsequent two stages.

Figure 4.4c The radial symmetry of relevant edges is leveraged to filter pixel-wise gradient orientations, constraining them to lie within a window around that pixel's polar coordinate.

Figure 4.4d Gradient magnitudes are filtered using a constant threshold, binarizing the image and providing a first step in noise reduction.

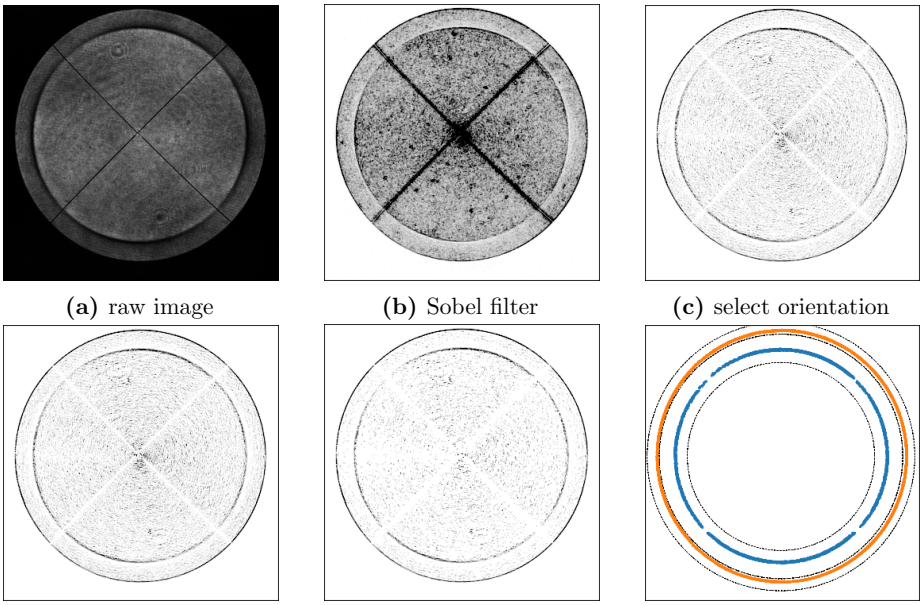
Figure 4.4e A second step of noise reduction is achieved through the application of a binary opening operation [67, Sec. 9.3], which effectively removes unconnected single-pixel edges.

Figure 4.4f As a consequence of the aforementioned variability in edge sharpness, edges are described by gradients of variable widths. However, due to the radial symmetry of the problem, it is possible to identify clusters in the radial coordinates of the edge pixels. The lack of sufficient knowledge regarding the center (x_0,y_0) of radial symmetry represents a minor challenge. This issue can be circumvented by dividing the image into smaller angular segments around the expected radial position of the SPR minimum (see fig. A.10) and aperture (see fig. A.11). In each angular segment, the artificial widening of radial clusters due to the error in the guessed center (x_0,y_0) of polar coordinates can be neglected. Therefore, pixels can be attributed to the SPR minimum edge (blue) or to the aperture edge (orange), if they are distributed within n_σ standard deviations around the center of a fitted Gaussian radius distribution. This last step can be seen as a further measure of noise reduction.

The code implementation of this edge-detection procedure can be found in the function designated as `__custom_edge_detector` within the `edge_detection.py` module of `SPRManalysis-2` [144].

4.2.2. Aperture Fitting

As previously stated at the beginning of section 4.2, one of the parameters that we aim to determine is the projected size of the aperture, which we will refer to as r_{max}. In order to retrieve this parameter, a geometrical shape is fitted to the detected edges (section 4.2.1) of the aperture (orange dots in fig. 4.4f). However, a preliminary attempt to use the Hough transform for circle detection [9] or the more generalized version of the Hough transform for ellipse detection [50] did not yield satisfactory precision. Consequently, an alternative approach is employed, whereby the parameterized outline of geometrical shapes is fitted in a least-squares manner. The shapes used for fitting are discussed in the following:



(a) raw image **(b)** Sobel filter **(c)** select orientation

(d) thresholding **(e)** (binary) opening **(f)** radial clustering

Figure 4.4.: Visualized steps during BFP image edge-detection. For steps 2-5, contrast is enhanced for better visibility. For step 6, classified edges are scatter-plotted in blue (SPR-minimum) and orange (aperture) with larger-than-pixel marker size. Black-dotted circles in step 6 represent user-specified classification boundaries.

Circle Fit

The initial attempt was to extract x_0 and y_0, the coordinates of the Perpendicular Reflection Pixel (PRP), as the center of a circle fit (dotted line in fig. 4.5).

Ellipse Fit

However, the residuals of such a fit indicate that a circle is not an appropriate description. Given the inevitable alignment imperfections between the optical axis and the planes of sample, lenses and camera, it is reasonable to posit that an ellipse, rather than a circle, is a more appropriate description (dash-dotted line in fig. 4.5). This is due to the fact that the cross-section between a cylindrical or conical surface (such as the beam outline) and a plane at a near-perpendicular angle (such as the camera screen) is always an ellipse. [78, pp. 6-8]

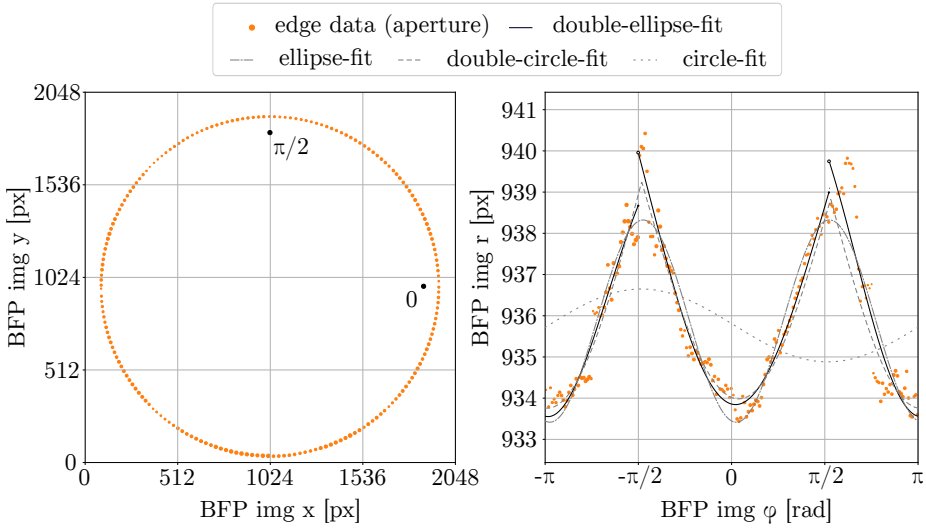


Figure 4.5.: Compressed representation of detected (aperture) edges in Cartesian (left) and polar coordinates (right) together with a fit (right plot only). The magnitude of discrete data points is indicative of the weighting of associated edge points, which is proportional to the number of detected (uncompressed) edge pixels. The double ellipse fit is represented by the solid black line within the polar coordinate plot (right). It is displayed with two discontinuities, which are not actual discontinuities but serve to demonstrate the (vertical) association between data points and the two ellipses.

Double Circle Fit

Another issue that arises from an imperfect alignment between the objective and the sample plane is the shadow cast by the objective's aperture, which is applied twice to the double-passing beam. Consequently, the imaged beam outline projection can be more accurately described as a two-circle overlap (dashed line in fig. 4.5) area rather than a single circle area.

Double Ellipse Fit

In light of the two aforementioned objections, a plausible model for the shape of the projected beam outline would be the cross-section of two overlapping ellipses (solid line in fig. 4.5). The two ellipses would therefore describe the projection of the objective aperture along the beam path onto the BFP camera. This path includes the reflection at the sample plane in case of ellipse 1 (but not in case of ellipse 2).

Although the example data and fit in fig. 4.5 provide an initial impression of the

suitability of the four described models, a systematic comparison can be achieved through the Akaike Information Criterion (AIC). A comparison of AIC values for the different models across all BFP images from the HEK293 measurement series in section 6.1 (table A.1) is presented in fig. A.12. As can be seen from the figure, this criterion consistently favors the double ellipse model across all measurements in table A.1.

One of the semi-minor ellipse axis parameters of the double ellipse fit is therefore used as a prediction of r_{max}. Figure A.13 shows the distribution of values obtained throughout the analysis of all measurements from table A.1. Although r_{max} should be independent of sample tilt and positioning, as confirmed by ray geometry simulations, and therefore consistent between different measurements, fig. A.13 shows large variations in the fitted values of r_{max}.

The observed variation in interference patterns at the edge of the beam cross-section in BFP images provides one plausible source of these variations. A layer of hardened oil residues at the edge of the lens, which is wider or narrower depending on the cleaning, as shown in fig. A.3, provides another plausible explanation. A third possible source of variation would be sample-related differences in the overall intensity of the reflected light, resulting in different radii of edge detection. However, a definitive explanation remains open. Nevertheless, as confirmed by the RI measurement validation in section 5.6, assuming the rounded median of the median values in fig. A.13 (935 px) as r_{max}, an acceptably small systematic error is achieved.

The code implementation of the aperture fitting functions can be found in the functions designated `fit_circle`, `fit_ellipse`, `fit_two_circles_intersection` and `fit_two_ellipses_intersection` within the `geometric_fitting.py` module of `SPRManalysis-2` [144].

4.2.3. Center Detection

As mentioned above, the center of the BFP x_0, y_0 is the pair of image coordinates corresponding to the ray with perpendicular reflection. They are therefore also called Perpendicular Reflection Pixel (PRP) coordinates. These coordinates should not be confused with the center of the beam cross section (obtained from the fits described in the previous section), the center of the radial polarizer (visible dark cross in BFP images) or simply the center coordinates of the image (1024, 1024).

Firstly, it is important to note that the coordinates of interest are constant throughout a measurement, as long as the sample is not repositioned, which would change its inclination with respect to the optical axis. A geometrical construction of the light rays between the objective and the sample (as shown in fig. A.14) shows that

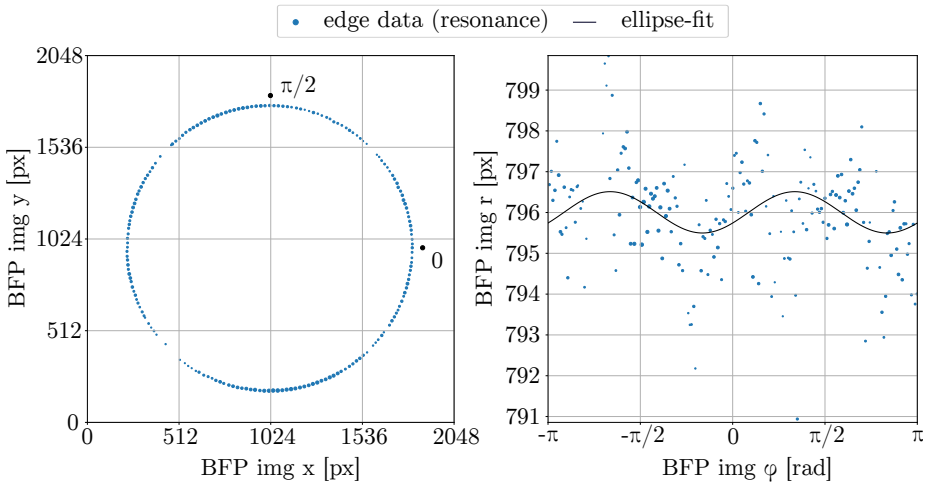


Figure 4.6.: Compressed representation of detected (resonance) edges in Cartesian (left) and polar coordinates (right) together with a fit (right plot only).

the center coordinates x_0, y_0 are unaffected by the loss of focus, which is the only parameter in fig. A.14 that could change during a measurement.[4]

A first idea to detect the center coordinates was to fit an ellipse to the detected edge of the SPR minimum (blue in fig. 4.4f), as it seems intuitive that the pixel with zero reflection angle lies in the center of any ring with constant reflection angle. However, as will be discussed later, the assumption that the SPR minimum corresponds to a constant SPR angle in all directions of the BFP is prone to error. As can be seen in fig. A.15, the detected centers of the fitted SPR ellipses are widely scattered and follow systematic patterns over the course of a measurement. Therefore, while an ellipse fit to the SPR minimum is still performed to obtain an initial guess of the center coordinates, a refinement procedure (see section 4.3.3) with at least one iteration is used to refine the median center coordinates of all ellipse fits within a measurement. (The refined coordinates are also shown in fig. A.15 for that particular example measurement.)

The code implementation of the center fitting function can be found in the function designated `fit_ellipse` within the `geometric_fitting.py` module of `SPRManalysis-2` [144].

[4] If it is not intuitive that the perpendicular ray is reflected on itself regardless of the sample-focus distance, the following website is a great tool to explore: https://phydemo.app/ray-optics/

4.3. Analysis Step II : Intensity-Angle-Profile Extraction

The second step in SPRM data analysis aims to extract the intensity angle profile reflected from the sample substrate location in focus. This is done by superimposing a radial coordinate system on the BFP image and binning pixels along the radial coordinate (section 4.3.1). The radial coordinate axis must then be mapped to the corresponding angle of incidence (reflection) values in the sample plane, also called OP (section 4.3.2). As these two steps depend on, and are sensitive to, the center coordinate of the chosen polar coordinate system (x_0,y_0), a statistical analysis of the extracted BFP profiles can be fed back to refine this determined PRP coordinate (x_0,y_0) (section 4.3.3). Finally, some effects of defocusing and how to deal with them are discussed (section 4.3.4).

The operations described are implemented in the `extract_bfp_intensity_profile` function of the `extract_bfp_profiles.py` module of `SPRManalysis-2` [144].

4.3.1. Radial Binning

After placing a polar coordinate system around the PRP (x_0,y_0) on a BFP image, effective intensity values and their distribution are calculated for bins of radial coordinates, thus eliminating any dependence on the angular coordinate ϕ.

Effective Values

In this step, "effective values" can be either mean values or median values. In these cases the distribution of values would be characterized by either a standard deviation or an interquartile range. Due to the noisy nature of BFP profiles, the presence of ripples and airy discs, all evaluations are based on medians and interquartile ranges.

Eliminated ϕ Dependence

When calculating effective intensity values, we have to exclude those pixels with ϕ coordinates around the angular positions of radial ZPol shadows (black cross in fig. 4.4a). Four different profiles, termed 'left', 'top', 'right' and 'bottom', are calculated independently from the four segments of the ZPol polarizer, using only angles within ± 2.5 rad around the horizontal and vertical directions. The reason for this split profile calculation and the narrow choice of 'opening angle' will become clear in section 4.3.4 on defocusing. An example of resulting BFP profiles is shown in fig. 4.8. Furthermore, since the ZPol polarizer does not produce perfect radial polarization, we need to consider the s-polarized intensity component that is contained in the (predominantly p-polarized) calculated BFP intensity profiles. However, this

consideration will be postponed until section 4.5.1 of analysis step 3.

Angle of incidence (AOI) binning, mean profile calculation and median profile calculation are implemented in the functions designated `get_bin_aois`, `mean_std_profile` and `median_p_quantile_profile` within the `extract_bfp_profiles.py` module of `SPRManalysis-2` [144].

4.3.2. Radius-to-Angle Mapping

To describe the relationship between the angle of reflection (incidence) θ in the OP and the corresponding radial position of the partial ray in the BFP, we must apply the sine condition for "stigmatic imaging with wide-angle pencils". [39, Sec. 4.5] Equation (4.1) represents our limit of the sine condition, where all rays in the BFP are parallel: [39, Sec. 4.5.1]

$$\frac{r}{\sin\theta} = \frac{r_{max}}{\sin\theta_{max}} \tag{4.1}$$

Using the definition of the NA in eq. (2.61), we can calculate angles θ from the BFP radial coordinate r through eq. (4.2):

$$\theta(r) = \arcsin\left(\frac{r \cdot NA}{r_{max} \cdot n_{N-LAF21}}\right) \quad \text{with} \quad r = \sqrt{(x-x_0)^2 + (y-y_0)^2} \tag{4.2}$$

As shown in fig. 4.7, r is the BFP radial coordinate of an arbitrary ray, r_{max} is the BFP radial coordinate of a marginal ray, NA is the numerical aperture of the objective and n is the RI of the N-LAF21 substrate within which the light is focused.

In fig. 4.8, the calculated angles theta are given together (upper x-axis) with corresponding BFP radial coordinates r (lower x-axis).

Radius-to-angle mapping is implemented in the `radius_2_angle` function of the `coordinate_transforms.py` module of `SPRManalysis-2` [144].

4.3.3. Center Refinement

Unfortunately, the described method of determining the BFP center (x_0,y_0) results in unexpectedly high variances in the PRP coordinates. For example, determined PRP coordinates of measurement MID007 are shown in fig. A.15. It can be seen that the determined PRP coordinates are distributed over an area of approximately 10 px by 10 px. Several clusters are visually identifiable. However, as can be taken from figs. 5.13 and A.18, a PRP coordinate misclassified by 1 px already leads to a systematic cell-substrate distance measurement error of up to 20 nm, depending on

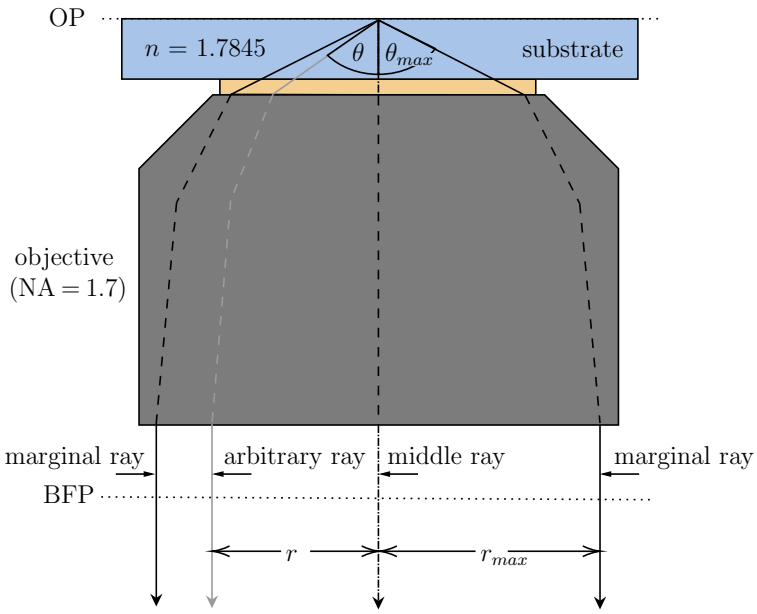


Figure 4.7.: Sketch of the beam path from the OP through the objective to the BFP. Dashed light paths through the objective are purely hypothetical and for visualisation. The actual paths may be more complex due to the unknown design of the objective, but we know that the angles θ_{max} and θ and the radial positions r and r_{max} follow the sine condition. [39, Sec. 4.5.1]

cell-substrate distance, cytoplasm RI and substrate type.

As indicated by ray geometry simulations, PRP coordinates should remain unchanged as long as the angle between the beam and the optical axis and the sample tilt (α and β in fig. A.14) don't change within a scanning measurement. However, as will be discussed in section 4.3.4, a defocused sample can cause the mixing of different Fields of View (FOVs) within a single BFP image, distorting the ellipse of the SPR minima in multiple directions and thus affecting the apparent PRP obtained from the ellipse fit.

Therefore, a strategy for refining PRP detection has been implemented. If it cannot be assumed that all segments in the BFP (left, top, right, bottom) 'see' the same part of the sample (see next section), then it cannot be assumed that the elliptical shape of the SPR minimum is centered around the PRP. However, if the scan areas are large enough, it can be assumed that over the course of an entire measurement, all segments of the BFP will 'see' parts of the sample that are free of specimen. If the

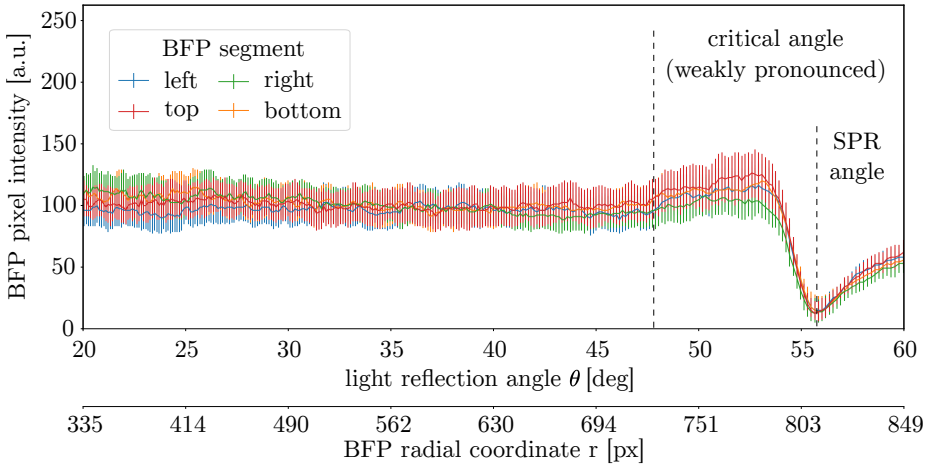


Figure 4.8.: Plot of segment-wise extracted BFP intensity profiles. Error bars represent the distribution of the aggregated intensity values as interquartile range, not the uncertainty on the effective (median) values. The x-axis is given in both BFP image radial coordinates and reflected light incidence angles. As an example BFP intensity profile, the faint expression of the critical angle is representative for most measurements on SiO_2 substrates (table A.1). Even weaker pronunciations of the critical angle have also been observed.

SPR profiles are analyzed separately by segment (left, top, right, bottom), we can use this assumption to estimate the difference between the assumed PRP coordinate and the true PRP coordinate from a segment comparison of the determined SPR angle distributions.

Figure 4.9 shows the segment-wise distribution of determined SPR angles[5] as a violin plot. The first percentile is marked as a horizontal line for each segment. As all samples used in this work have a higher RI than the surrounding medium, the first percentile SPR angles of all segments are expected to belong to specimen-free measurement points. Therefore, the first percentiles in SPR angle distributions should be the same for all analyzed BFP segments. Assuming that determined differences in first percentile SPR angles are only due to PRP detection error[6], half of the difference between the left and right segments is equal to the error Δx_0 of the horizontal PRP coordinate, and half of the difference between the top and bottom

[5] Actually fig. 4.9 shows the distribution of SPR radii before radii are converted to angles of light incidence. Angles of incidence are not practical for this approach due to the non-linearity in eq. (4.2).

[6] Ignoring the effects of e.g. laterally inhomogeneous substrate layers or a potential unisotropic warping of the BFP due to optical aberration.

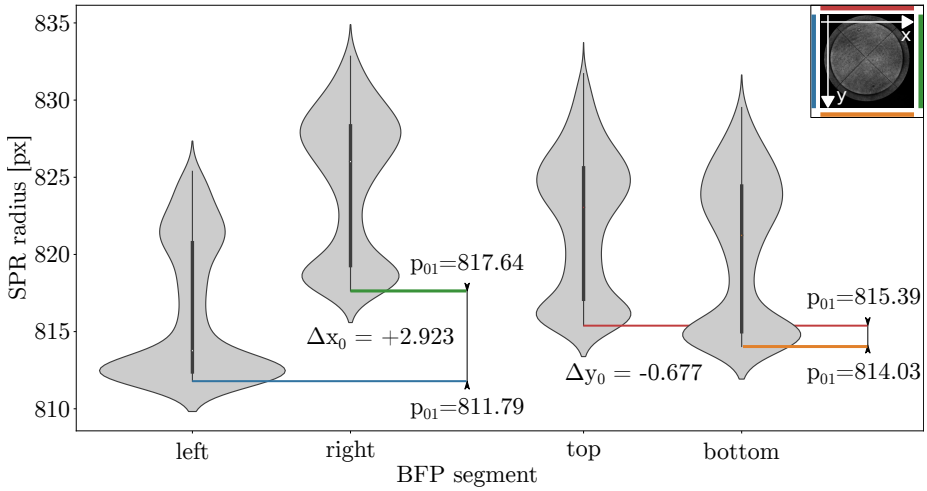


Figure 4.9.: Violin plot with distributions of evaluated SPR positions in each BFP segment for example measurement MID007. The two peaks in the bimodal distributions can be attributed to cell-free sample areas with lower SPR angles and cell-covered sample areas with higher SPR angles (compare fig. 4.10). The discrepancy in vertical violin positions indicates a poorly defined PRP (center) of BFPs. First percentiles (scan points not affected by a cell) are compared to obtain a correction for PRP coordinates as half of the first percentile difference in each direction. Differences in violin proportions are caused by a segment-dependent field of view (FOV), an effect of defocusing (see section 4.3.4).

segments is equal to the error Δy_0 of the vertical PRP coordinate.

Center refinement is implemented in the `resonance_angle_segment_comparison` function of the `bfp_profile_statistics.py` module of `SPRManalysis-2` [144].

4.3.4. Handling of Defocusing

This section discusses the causes, effects and handling of defocusing.

While a lateral self-focusing mechanism has been claimed for phase-response SPRM [45], it turns out that the lateral and axial resolution of the present amplitude-response SPRM deteriorates substantially when focus is lost. The BFP segment-dependent FOVs shown in figs. A.30 to A.33 demonstrate the extent of defocusing. An explanation of segment-dependent FOVs will follow shortly.

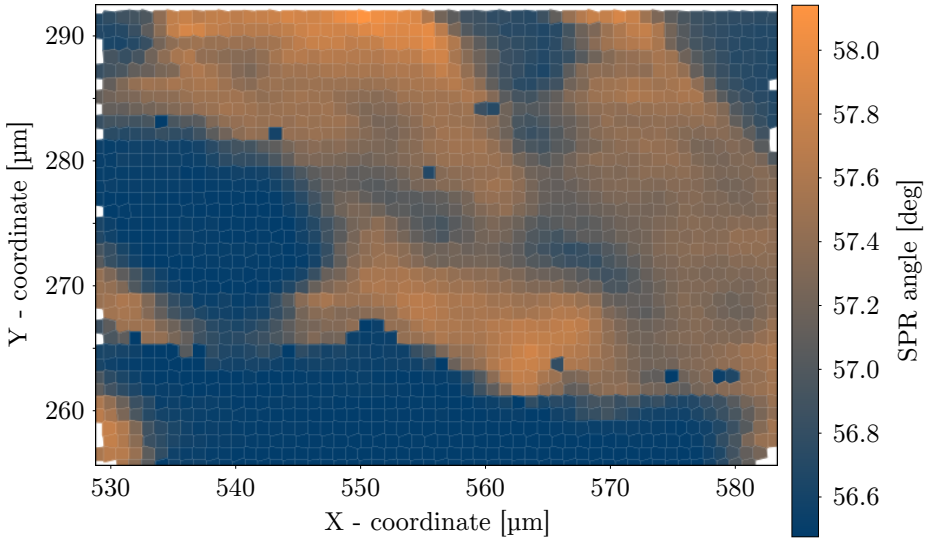


Figure 4.10.: Spatial mapping of (top BFP segment) SPR angles for example measurement MID007. The outline of three HEK293 cells can be identified as regions with higher SPR angles. A relatively large part of the scan area with lower SPR angles is free of the cell specimen. This part corresponds to the lower peak in SPR angle distributions (compare fig. 4.9).

Causes of Defocusing

It is assumed that underfocus occurs when the stage descends towards the objective due to the interplay of gravity and acoustic vibrations. Over- or under-focusing can occur if the temperature of the substrate rises[7] or falls[8]. A tilt or curvature[9] of the sample substrates can also cause defocusing from the lateral movement of the sample during a scan. Sun et al. [146] also list all three of these causes of defocus in their publication of a novel auto-focus SPRM approach. They report average underfocus values Δz of (0-6) µm for their setup.

The short working distance of the objective is a factor that makes the microscope more sensitive towards defocusing. A given sample displacement out of focus Δz causes a proportionally higher increase in the pre-focal beam diameter Δd at the OP:

$$\Delta d = 2 \cdot \tan\left(\arcsin\left(\frac{\mathrm{NA}}{n_{N-LAF21}}\right)\right)\Delta z \approx 6.27\Delta z \tag{4.3}$$

[7] e.g. due to laser illumination
[8] e.g. if samples from the incubator are not in thermal equilibrium with the heating stage
[9] only observed when samples are cured with the optical adhesive at 65 C, as seen in fig. A.4

Effects of Defocusing

Figure 4.11 shows the laser beam geometry in the vicinity of the objective from BFP to OP in sections through three different planes. The left half of fig. 4.11 sketches an almost focused setup. The right half of fig. 4.11 sketches an exaggeratedly defocused setup. Sketches in the middle row are intended to show the relationship between the defocus Δz and the pre-focal beam diameter Δd in the OP, thus visualizing eq. (4.3). The two sketches in the top row show the circular illuminated area of diameter Δd on the sample. This is also the area from which light is reflected. The right sketch implies that the measurement result has to represent an average or a convolution across this area. The two sketches in the bottom row display the cross section of the beam in the BFP being imaged, which is the basic unit of raw data. Although it would look identical to sketch this beam cross-section in real space, it is done so in reciprocal space[10] in order to highlight the mapping between the coordinates in this image and the angles of incidence at the OP. The dark circle in both BFP images corresponds to the SPR angle of the sample. The two dashed black circles correspond to the minimum and maximum evaluated angles of the BFP profile. As this annulus of relevant data in the BFP corresponds to an annulus of reflected light in the OP (marked ring in the top row of images), it is referred to as the 'sensitive' region in both the OP and BFP.

This is where a key problem with defocused measurement data becomes apparent. A BFP image from a defocused scanning measurement contains reflectance information over the entire 'sensitive' region. When an entire BFP image is compressed into a single BFP profile, the reflectance information from laterally distributed parts of the sample is averaged. However, if the sample is not laterally homogeneous, there is no guarantee that the average of contained SPR reflectance profiles will again result in a valid and physically meaningful SPR reflectance profile. Even if it did, the lateral resolution of SPRM scanning measurements would still be limited to the diameter (slightly less than Δd) of the sensitive region.

The second consequence of defocus to be discussed is the distortion of the apparent BFP center coordinates (PRP coordinates) x_0, y_0 when determined from ellipse fits to SPR angles as discussed in section 4.2.3. Unless we can assume that all points on the fitted SPR ellipse actually correspond to the same SPR angle, its center cannot be assumed to correspond to the PRP. Figure A.16 clearly shows how the apparent PRP coordinates (which should be constant or at least without systematic deviations) are distorted by the presence of the cell specimen.

Finally, the possibility of a defocus-dependent scaling of r_{max} should be briefly discussed, as this can also be hypothesized from fig. 4.11. And indeed, as shown

[10] or Fourier space, to borrow the terminology of Kano and Knoll [37]

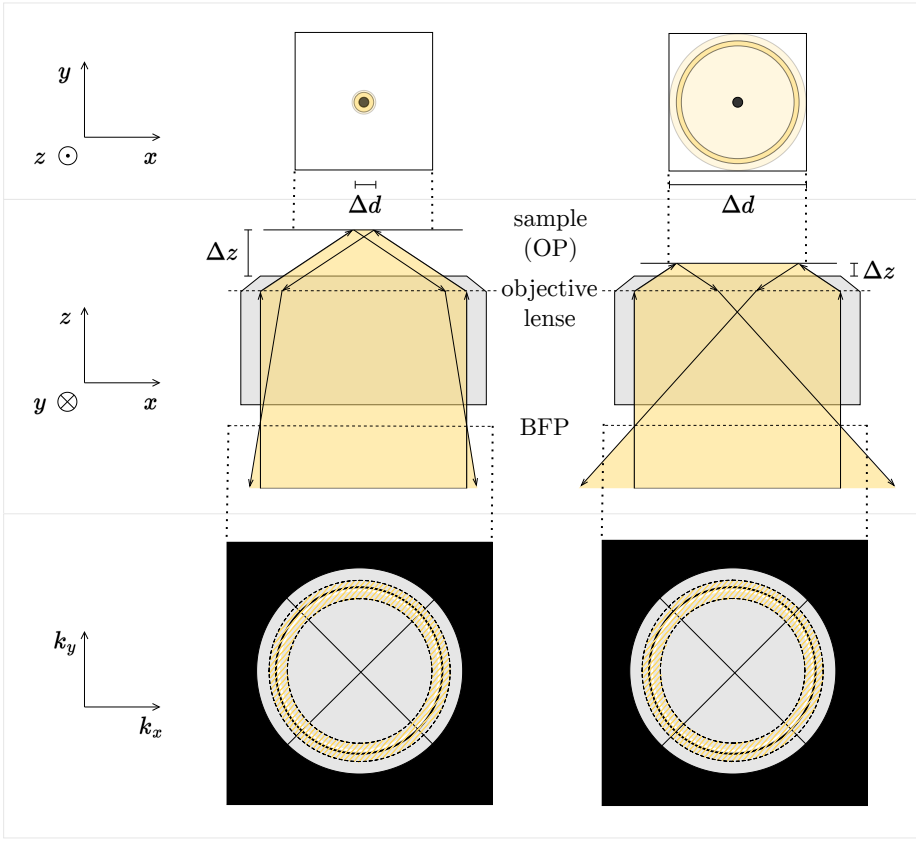


Figure 4.11.: Illustration of the relationship between (real-space) beam cross-section reflected by the sample and (reciprocal space) BFP beam cross-section. On the left, the case is shown where the sample is almost in focus. On the right, the case for an exaggeratedly defocused sample is shown. For both cases, the path of outermost light rays are drawn as arrows. The 'sensitive' (annulus) region of the BFP data is hatched yellow. The corresponding 'sensitive' (annulus) region in real-space is displayed with higher color saturation.

in fig. A.13, the distribution of r_{max} values shows quite large variances. If these variances were due to a defocus-related scaling of the BFP, the assumed value of r_{max} would have to be determined and updated from measurement to measurement, or even within a measurement. However, since any approach to such data evaluation has led to large systematic errors and obvious artifacts, it is assumed that the reasons described in section 4.2.2 dominate the variation of r_{max}.

Handling of Defocusing

The problem and severity of defocusing only became apparent at a late stage in this project, experimental solutions will be discussed in section 7.2.

The center refinement procedure in section 4.3.3 optimizes the PRP coordinates (x_0,y_0) unaffected by defocusing effects. It is therefore a compensation mechanism for defocusing.

As a direct consequence of the defocus-induced distribution of information across the BFP, BFP segments are analyzed separately[11] (left, top, right, bottom). Furthermore, BFP segments are only evaluated within narrow angular segments of $\pm 2.5\,\mathrm{rad}$ opening angle (see section 4.3.1), obviously trading off Signal-to-Noise Ratio (SNR).

In the remainder of this section, a computational method is presented that allows the combined analysis of BFP segments, even in the presence of defocus:

Figure 4.12 illustrates the idea of this approach, making two assumptions:

- Defocus Δz is stationary or progresses slowly, so that it can be assumed stationary within a single scan line.
- The SPR angle at any sample coordinate between two adjacent scan points can be interpolated.

In short, information is not lost due to defocusing, it is just distributed in an awkward way. However, by making a comparison[12] between the SPR angles of different BFP segments across a scan line, matching pieces of information (i.e. matching intensity profiles) can be brought back together. Similar to the comparison of SPR angles within a scan line (as in fig. 4.12), a pairwise comparison between scan lines[13] allows a re-matching of distributed BFP intensity profiles in the opposite direction

[11] if the sample is not homogeneous as in section 5.6

[12] Technically, this is the calculation of a cross-correlation between arrays of SPR angles from within the same scan line.

[13] Technically, this is the calculation and comparison of pairwise correlation coefficients between arrays of SPR angle values, corresponding to scan lines.

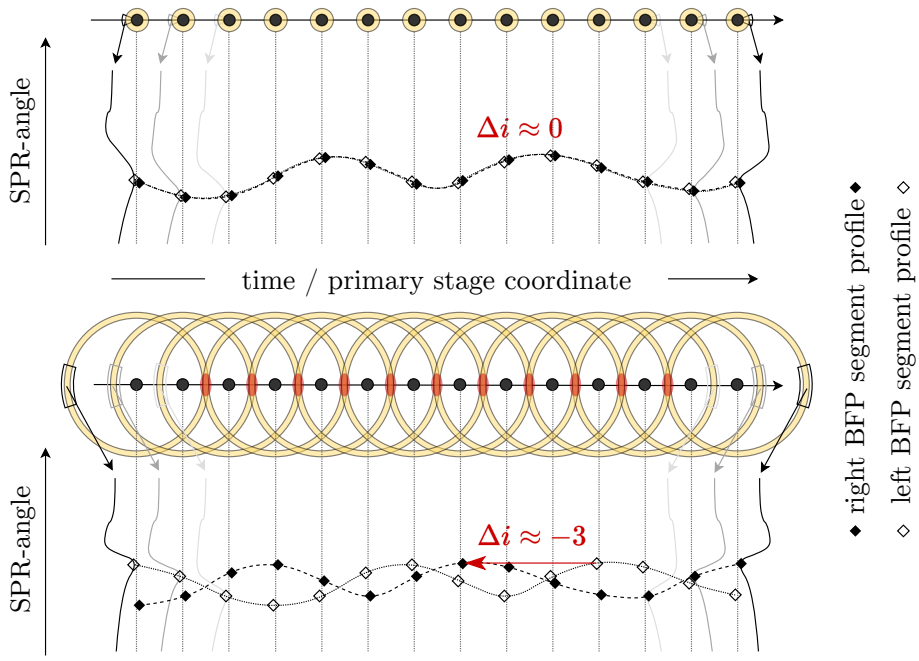


Figure 4.12.: Illustration of a concept to compensate for defocus effects after BFP intensity profile extraction. At the top and bottom, 'sensitive' regions (annuli) of the laser beam on the sample are illustrated for the sequence of scan points in a horizontal scan line (left to right). The top sketch shows a measurement in focus, the bottom sketch a measurement with high defocus. Below the sketch of sequential 'sensitive' regions is a sketched graph of a possible corresponding SPR angle sequence, taken from both the left and right BFP segments. The axis from left to right can be interpreted as either a time axis or a sample coordinate axis. While the SPR angles of the left and right BFP segments are almost identical in the focused measurement (top), they differ substantially, but also systematically, in the unfocused measurement (bottom). This systematic offset allows a theoretical rearrangement between left and right BFP profiles, simply by shifting their sequences against each other, to recover pairs of BFP profiles with (better) matching intensity distributions. The (scanning point) index shift Δi that would match left- and right BFP segments (SPR angles) is drawn into both parts. While the dark gray bullets indicate the original coordinates of the scan, the regions marked in red would be the corresponding updated set of coordinates after this procedure. These regions are drawn here on the overlaps of matching parts from different 'sensitive' regions, but even if the overlaps don't match as smoothly as in this sketch, a remaining distance smaller than Δd would still represent an improvement in the defocus-limited lateral resolution of the scan.

(between upper and lower BFP segment profiles). Pairwise comparison allows to take into account the different degrees of defocus between scan lines. As important as finding matching intensity profiles is determining the corresponding effective sample coordinates. Effective sample coordinates are calculated as the average of stage coordinates belonging to matched BFP segment profiles. As can be seen in fig. 4.12, the location of reported stage coordinates (dark gray bullets) and the location of effective sample coordinates (red marked areas) are different. This correction to lateral stage coordinates is particularly important for the analysis of the sphere-substrate distance validation measurement in section 5.7.

At the end of section 5.7, fig. 5.11 demonstrates the impact of this defocus compensation routine. Overall, this approach to defocus compensation is applied to the evaluation of measurements with measurement IDs MID074, MID075 (sphere validation measurements) and MID082 to MID106 (neuron-substrate distance measurements).

The details and implementation of this approach can be found in the `digital_refocusing` function of the `bfp_profile_statistics.py` module of `SPRManalysis-2` [144]

4.4. Necessary assumptions and simplifications

Before discussing the application of reflectance models, some necessary assumptions are highlighted. In the case of cell-substrate distance measurements, these assumptions become simplifications. Examples are given where the validity of each assumption becomes questionable:

- RIs within sample layers are "well defined"[14] and homogeneous: This assumption is questionable in the case of biological layers such as the cell membrane. Proteins and oligosaccharides associated with the cell membrane, for example, can extend up to tens of nm (see section 2.1.3) into neighboring layers, affecting their interaction with light as well.
- The temporal stability of the layer RI values is a related assumption: laser-induced temperature fluctuations, cell metabolism and water evaporation are examples of causes that break this assumption.
- Another assumption, linked to the stratified layer system assumption, is the number of relevant layers. Since the evanescent wave of SPs has a limited reach into the interface of interest, the last sample layer with relevant interaction is

[14] Since RI is a property of bulk materials (see eq. (2.12)), RI values of nm-thick layers are conceptually useful but not necessarily meaningful by their strict definition.

modeled as semi-infinite. In the case of cell-substrate samples, the cytoplasm is assumed to be the last layer: This assumption breaks down in cases where thin protrusions of the cell or organelles within the cell are imaged.

- The parallelism of the layers is another assumption that may occasionally fail: Membrane curvatures or the curvature of the spherical specimen in section 5.7 are not taken into account.

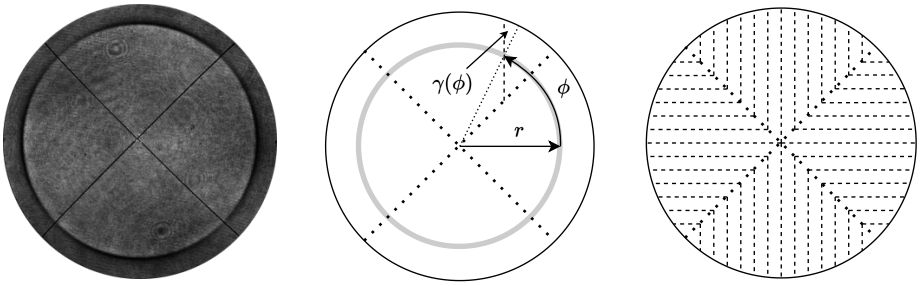
4.5. Analysis Step III : Layer Model Parameter Optimization

Previously, cell-substrate-distance and cytoplasmic RI have been inferred from intensity profiles in a semi-automatic way. First, the parameters of substrate layers (e.g. Cr and Au) were selected manually to reproduce measured intensity profiles without cells. Then, the SPR angle and the critical angle of total reflection were extracted from intensity profiles of cell measurements. Through a simulated calibration curve, the cytoplasmic RI was determined from the critical angle. The cell-substrate distance was then determined from the SPR angle. This approach effectively separates the determination of the cell-substrate distance and cytoplasmic RI. It exploits the fact that the critical angle of total reflection is only sensitive to the RI of the last sample layer within the evanescent field. [123]

Unfortunately, this approach has a few weaknesses. Firstly, the manual determination of substrate layer parameters introduces a degree of arbitrariness. Second, the determination of a critical angle may fail due to poor SNR, especially for substrates where this angle only correlates with a weak peak in intensity derivative. In particular, these two weaknesses caused serious problems in the analysis of the SiO_2 sensor based measurements in section 6.1. Therefore, an alternative, robust intensity profile analysis scheme is presented in this section. The return to a least squares approach with the presented use of optimization and weighting methods allows a decoupling of cell-substrate distance and cytoplasm RI that has previously not been achieved (see section 5.7).

4.5.1. Objective Function

This section explains the procedure used to determine the free parameters of the stratified layer model (table 5.3 and table 5.4), including the cell-substrate distance and the cytoplasmic RI, by optimizing the reflectance model from section 2.3.3. For this purpose, it is important to clarify the following terms and to avoid their confusion.



(a) Intensity in the BFP beam cross section

(b) polar coordinate system of the BFP

(c) light polarization in the BFP

Figure 4.13.: Illustrations of the intensity distribution of the BFP beam cross section (a), the BFP polar coordinate system (b) and the distribution of light polarization in the BFP (c). Also shown in (b) is the angle γ between the polarization angle and the angular pixel coordinate ϕ.

Intensity I The light intensity of the reflected beam within the BFP (see fig. 4.13a). It can be expressed as a function of polar BFP coordinates r and ϕ (see fig. 4.13b). Considering both polarization components p- and s-, the intensity can be expressed as the sum of these component intensities at every point (r, ϕ): $I(r, \phi) = I_p(r, \phi) + I_s(r, \phi)$.

Illumination L The light intensity of the incoming beam within the BFP can be expressed in the same way: $L(r, \phi) = L_p(r, \phi) + L_s(r, \phi)$. Keep in mind, that the illumination can not be measured directly with this setup, so it has to be measured indirectly (see section 4.6).

Reflectance R The ratio between Intensity and Illumination, defined for each polarization component: $R_{p/s}(r) = I_{p/s}(r, \phi)/L_{p/s}(r, \phi)$. It is independent from the polar BFP coordinate ϕ.

It should be noted that when radial polarization is used, intensity and illumination are exclusively p-polarized. However, the radial polarizer (ZPol) produces only quasi-radial polarization and the actual ϕ-dependent polarization of intensity and illumination is visualized in fig. 4.13c. Therefore, depending on ϕ, we have to deal with components of s-polarized light, resulting for example in non-vanishing profile intensities at the SPR angle. Expressing the difference between ϕ and the angle of polarization as γ (see fig. 4.13b), the relative amount of p-polarization can be expressed as $\cos^2(\gamma)$ and the relative amount of s-polarization can be expressed as $\sin^2(\gamma)$.

Given a BFP profile with n angles of incidence $\theta_{1..n}$, intensities $I_{1..n}$ and weights

$w_{1..n}$, we can optimize the model parameters for $R_{p/s}$ by minimizing the term for χ^2 in eq. (4.4), following the standard least-squares approach for parameter optimization [21].

$$\chi^2 = \sum_{i=1}^{n} w_i \cdot \epsilon_i^2 = \sum_{i=1}^{n} w_i \cdot (I_i - \underbrace{L_p(r_i) \cdot R_p(r_i) - L_s(r_i) \cdot R_s(r_i)}_{I_{model,i}})^2 \tag{4.4}$$

Equation (A.1) expresses model- and illumination-based intensities $I_{model,i}$. Residuals are denoted by ϵ_i. Radii r_i have been mapped to angles, using the function $\theta(r_i)$ from section 4.3.2, to calculate angle-dependent reflectances (see section 2.3.3).

4.5.2. Optimization Algorithms

Before attempting to optimize the model parameters of cell-substrate distance and cytoplasm RI, the substrate layer model parameters must be fixed. Attempts to optimize all parameters at once have resulted in high (|correlation coefficient|>0.9) parameter correlations between cell-substrate distance and other parameters, leading to unreliable results for all parameters. [41].

Substrate Parameter Optimization

To determine substrate layer parameters (light gray in tables 5.3 and 5.4), the substrate reflectance in the absence of any specimen is evaluated. If a separate scan of a specimen-free area has been taken, this first step can be carried out on a median intensity profile of that scan. Otherwise, if the scanning measurement of interest also covers regions without a specimen, this first step of optimization can be carried out on a median intensity profile from specimen-free regions. The scan measurement locations (measurement spots) used for this substrate layer parameter determination are referred to here as the "control measurement" (spots). Figure A.17 shows an automated selection of control measurement spots from specimen-free regions.

Since substrate layers can have up to four free parameters (see table 5.3) and local optimizers tend to find local suboptimal solutions, the method of Adaptive Memory Programming for Global Optimization (AMPGO)[75] is used[15] here. This optimization algorithm is comparatively slow, but since the intensity profiles of the control measurement spots are combined into a median profile, only a single optimizer run is required per control measurement. The results of the substrate parameter optimization are discussed in section 5.4.

[15]The available implementation in the lmfit [94] library, based on the SciPy [127] library, is used.

Cell Parameter Optimization

Once the substrate layer parameters have been determined for the present measurement, the remaining two parameters, cell-substrate distance and cytoplasm RI, are determined together. As both parameters affect the position of the SPR angle (see fig. 4.14), optimizer algorithms tend to report high parameter correlations (|correlation coefficient|>0.9) which makes both parameter estimates unreliable. [41] A key challenge in cell parameter optimization is therefore the decoupling of cell-substrate distance and cytoplasmic RI.

A previous approach by Hassani [123] used the unique dependence between cytoplasmic RI and critical angle (see fig. 4.14) to first determine the cytoplasmic RI independently and then determine the cell-substrate distance with the resulting direct mapping from the SPR angle. However, the determination of the critical angle is quite challenging in many cases (see for example fig. A.21) due to interference patterns in the BFP. Therefore, a more robust approach is used here to be able to analyze all cell measurements performed in this work.

As expected from the addition of a $\sim$20 nm thick SiO_2 layer, which moves the sample further out of the evanescent field, SiO_2 coated substrates give a lower SNR than bare Au substrates. For this reason, a slightly less accurate but still more robust method is used for measurements on SiO_2 substrates. The optimization methods for measurements on Au and SiO_2 substrates are now presented in succession.

The Levenberg-Marquardt algorithm [2, 4] is used[16] in all optimization steps, unless otherwise specified.

- Au substrates : A least squares optimization is performed on all angles in a range of θ_1 to θ_3, estimating cell-substrate distance and the cytoplasm RI. Then, using only data from the part of the intensity profile around the critical angle (all angles between θ_1 and the maximum reflection angle θ_2), the cytoplasm RI value is optimized separately, starting from the previous parameter estimates. In a third optimization step, using only data around the SPR angle (all angles θ_2 and θ_3), the cell-substrate distance value is refined using the optimized fixed cytoplasm RI value. All three optimization steps use a uniform weight distribution. An example is given in fig. A.22.

- SiO_2 substrates : A single least squares optimization is performed on all angles between θ_1 and θ_3 to determine the cell-substrate distance and the cytoplasm RI in parallel. However, in contrast to Au substrates, a Gaussian weight distribution around the SPR angle is used. An example is given in fig. A.21.

[16] The available implementation in the lmfit [94] library, based on the SciPy [127] library, is used.

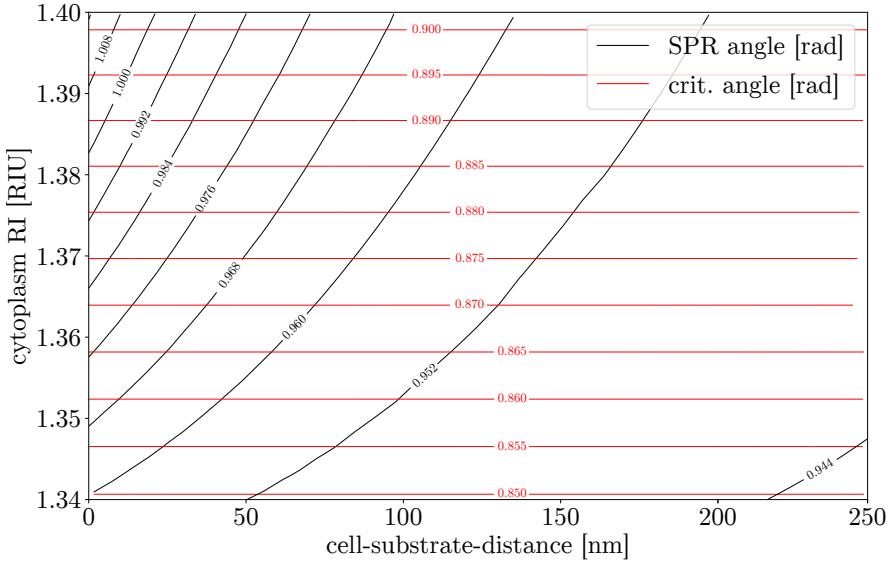


Figure 4.14.: Contour plot of SPR angle and critical angle as a function of cell-substrate distance and cytoplasm RI. It is evident that cytoplasmic RI can be determined from the critical angle value alone, suggesting why the previous approach to SPRM analysis relied on determining the critical angle from the reflectance spectrum. With the cytoplasmic RI determined, the SPR angle can be mapped directly onto the cell-substrate distance. The only drawback to this approach is the challenge of determining the critical angle, especially for intensity profiles such as the one shown in fig. 4.8. The plot is based on a simulation of 40x20 reflectance profiles with 634 data points per radian.

The results of the validation measurement in section 5.7 support the use of two different optimization approaches. As shown in fig. A.23, the presented method for Au substrates performs better in the validation measurement MID074 (on Au) and the presented method for SiO_2 substrates performs better in the validation measurement MID075 (on SiO_2).

The advantage of the first optimization method on Au substrates can also be explained by comparing the overall 3-step parameter optimization with the approach of Hassani [123]. The positions of the critical angle and the SPR angle allow a decoupling of cytoplasm RI and cell-substrate distance (see fig. 4.14) if the SNR around the critical angle is sufficient. The evaluation of simulated (zero noise) BFP images shows that uniform weights outperform Gaussian weights in an ideal scenario (see fig. A.20)

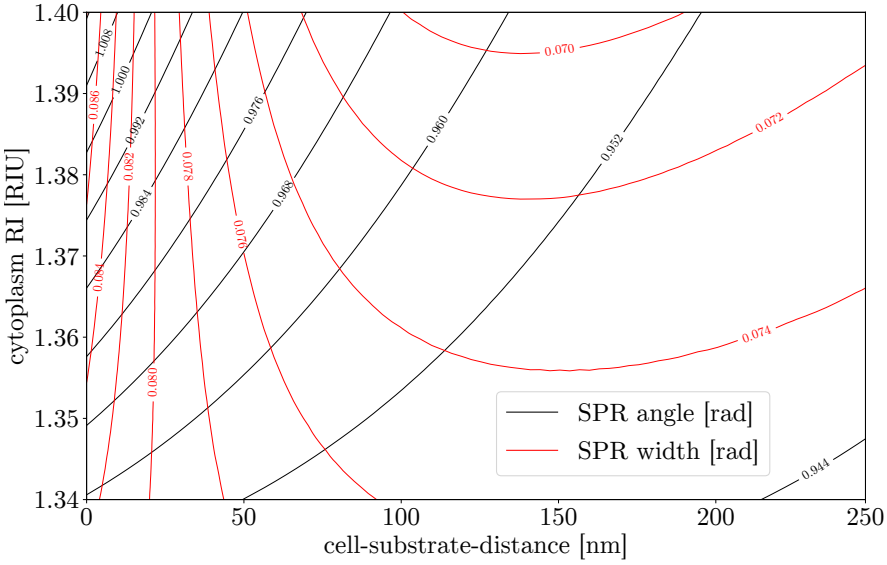


Figure 4.15.: Contour plot of SPR angle and SPR width as a function of cell-substrate distance and cytoplasm RI. Regions with almost perpendicular contour line crossings indicate excellent decoupling of cell-substrate-distance and cytoplasm RI when analyzing SPR angle and SPR width. The plot is based on a simulation of 80x80 reflectance profiles with 2536 data points per radian.

The advantage of the second optimization method on SiO_2 substrates can also be explained. The information conveyed by the SPR peak width (SPR width, see fig. 4.15) is key to the robustness of Gaussian weights. The significant role that resonance widths play in other resonator methods, such as QCM [90], suggests to emphasize parts of the reflectance profile around the SPR angle, as done by Gaussian weights. The disadvantage of Gaussian weights in the case of ideal data, as seen in fig. A.20, should not come as a surprise due to the neglect of valuable (available) information around the critical angle.

While it was originally expected that the emphasis on SPR angle and SPR width alone could make the measurements susceptible to artifacts from local substrate layer variations (compare AFM measurements, section 3.4.1), the analysis of cell measurements revealed only negligible variations in SPR angle and SPR width in bare substrate areas of the samples (see figs. A.32 and A.33).

Weighting choices

As discussed above, the following two weighting choices are used in least squares optimization:

- Gaussian weighting sets weights that follow the shape of a Gaussian around the SPR angle with a preset width σ. The set width of the Gaussian weight distribution is determined from a comparison of the estimated errors in a validation measurement (see fig. A.24).
- Uniform weighting applies the same weight to all profile intensity values. These weights are used for Au substrate measurements. A comparison with Gaussian weights over a wide range of distribution widths σ gave the best results for uniform weighting (see fig. A.25.

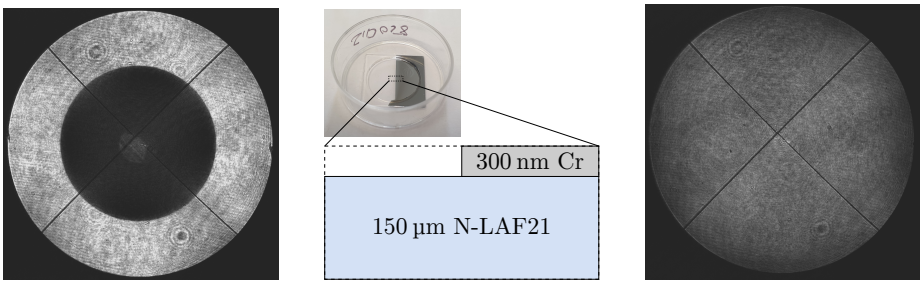
The code implementation of parameter optimization can be found in the `lm_fit_layer_model` function within the `layer_model_optimizer.py` module of `SPRManalysis-2` [144].

4.6. Reference Intensity Measurements

The concept of illumination was introduced in section 4.5.1 and relates measured intensity values I to the reflectance values R of the stratified layer model via eq. (4.4). Therefore, before measured intensities can be analyzed, the illumination L of the setup must be determined.

L was originally defined in section 4.5.1 as the intensity distribution incident on the BFP prior to reflection at the sample. This intensity distribution results from the original intensity distribution in the (Gaussian) laser beam cross section being modified by all optical components (i.e. filters, polarizers, mirrors, beam splitters, lenses and apertures) within the beam path. However, for practical purposes, it is considered to be the measured intensity in the hypothetical case of an ideal mirror sample with 100 % reflectance. This is a slightly different definition than before, as it includes optical components between the BFP and the BFP camera screen. However, since the actual measured intensities are always modified by these components, this redefinition doesn't change the previous considerations. Still, it is an important one.

As no ideal mirror with 100 % reflectance was at hand, an N-LAF21 substrate was coated with 300 nm of Cr to obtain a highly reflective sample whose reflectance is not dependent on the choice of surrounding medium or possible layers of condensed water or oxide on top. Such a two-layer mirror sample has the advantage of being well defined, assuming that the evaporated Cr layer shares the optical constants n and k with literature values [10] ((40-50) nm thick Cr layers evaporated on fused



(a) BFP image with total reflection edge for center detection

(b) Dual-domain substrate for reference intensity measurements

(c) BFP image of reference intensity for illumination reconstruction

Figure 4.16.: Reference intensity measurement substrates, as shown in (b), are half coated with a 300 nm thick Cr layer. The other half of these substrates is left blank to allow determination of the BFP image center coordinates x_0, y_0. This can be easily done using the clear edge at the total reflection angle as shown in the example BFP image (a). The image in (a) is deliberately overexposed, as no intensity analysis is performed on it, only edge detection (center detection). The information of x_0, y_0 is needed for the analysis of the actual reference intensity measurement, an example BFP image of which is shown in (c).

silica). However, there is no indication of sample orientation (PRP coordinates x_0, y_0) in the reflected intensity distributions I_0 (see fig. 4.16c). This poses a challenge for the calculation of angle-resolved reflectances from such a sample. Therefore, as sketched in fig. 4.16b, only half of the substrate is coated with Cr. The other half is left blank for PRP detection.

The reference intensity measurement used to analyze cell-substrate distance measurements consists of 5 individual measurements. One scan (MID069, table A.2) is performed on the Cr-free part of the sample (20 µm x 20 µm with steps of 2 µm x 2 µm), producing BFP images as shown in fig. 4.16a, to determine the PRP coordinate in the BFP as an average across 100 scan points. Four further scans (MID070-MID073, table A.2) are performed on the Cr coated part of the sample (same area and step size) for the actual illumination characterization, producing BFP images as shown in fig. 4.16c. From all reference intensity scans (MID070-MID073), BFP images are superimposed and the median intensity image $I_0(r, \phi)$ is calculated pixel by pixel. Using the known polarization distribution in the BFP (see fig. 4.13c), images of bare p- and s-polarized illumination intensity $L_p(r, \phi)$ and $L_s(r, \phi)$ are calculated from the median intensity image through eq. (4.5) (top plot in fig. 4.17 shows the median intensity profile $I_0(r)$). Using the PRP coordinates (x_0, y_0) extracted from

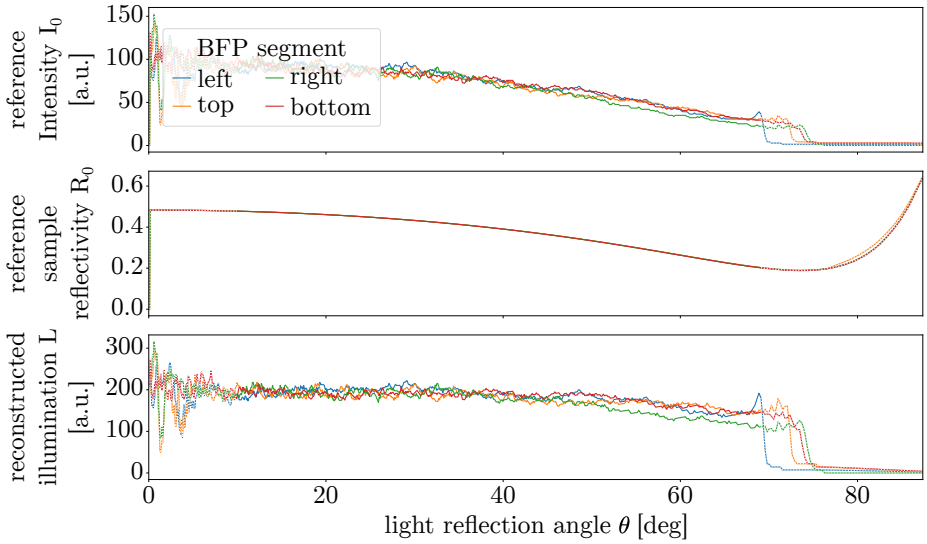


Figure 4.17.: Evaluation of reference intensity measurements for illumination reconstruction. All plots show intensities and reflectances by BFP segment (see legend). The top plot shows the total (p- and s-polarized) intensity I_0 extracted from a pixel-wise median reference intensity BFP. The middle plot shows the calculated total reflectance R_0 of the 300 nm Cr sample. The bottom plot shows the total setup illumination, reconstructed as the ratio between I_0 and R_0.

the MID069 measurement, the illumination intensity profiles $L_p(r)$ and $L_s(r)$ are then calculated from the illumination image of each polarization (bottom plot in fig. 4.17 shows the sum illumination profile $L_p(r) + L_s(r)$). Employing the TMM (section 2.3.3), the reflectance of the Cr mirror sample for p- and s-polarized light $R_p(r)$ and $R_s(r)$ (middle plot in fig. 4.17 showing the sum reflectance $R_p(r) + R_s(r)$) has been calculated for use in eq. (4.5).

$$\begin{aligned} L_p(r,\phi) &= L(r,\phi) \cdot \cos^2\gamma(\phi) \qquad \text{and} \qquad L_s(r,\phi) = L(r,\phi) \cdot \sin^2\gamma(\phi) \\ L(r,\phi) &= \frac{I_0(r,\phi)}{R_0(r,\phi)} \qquad \text{and} \qquad R_0(r,\phi) = \cos^2\gamma(\phi) \cdot R_p(r) + \sin^2\gamma(\phi) \cdot R_s(r) \end{aligned} \tag{4.5}$$

Illumination profiles are evaluated segment-wise, as shown in fig. 4.17. This has two reasons: BFP intensity profiles are also evaluated segment-wise, as argued in section 4.3; and different segments exhibit differences in illumination (visible in fig. 4.16c).

While it was originally hoped that interference patterns in BFP images could be compensated as a by-product of the reference intensity measurement, it turns out that interference patterns in BFP images are not stationary and therefore cannot be removed by simple background characterization. For this reason, illumination profiles are fitted with a piecewise polynomial function to remove interference patterns before use.

The code implementation of reference intensity evaluation can be found in the `extract_bfp_illumination_profile` function within the `extract_bfp_illumination.py` module of `SPRManalysis-2` [144].

5 Sensor Characterization Results

This chapter provides an overview of the measurement results for the characterization of SPRM sensors (substrates). It includes results from brightfield microscopy (section 5.1), AFM (section 5.2), XRR (section 5.3) and SPRM (section 5.4). In addition, RI measurements by refractometer (section 5.5) are also listed. Sections 5.6 and 5.7 present and discuss test measurements to validate the RI and specimen-substrate distance results obtained by measurement and data analysis. Particular emphasis is placed on the validation of specimen-substrate distance measurements, as the quality of the results obtained allows, for the first time, a discussion of experimentally determined statistical and systematic measurement errors. This chapter concludes with section 5.8, a theoretical discussion of statistical and systematic measurement uncertainties. In both, sections 5.7 and 5.8, the performance of the two different SPRM sensor types (Au and SiO_2) is discussed in comparison.

5.1. Brightfield Characterization

After sensor assembly (section 3.2.1) and before sensor sterilization (section 3.2.2), all substrate surfaces were visually inspected on either the Axio Vert (Carl Zeiss AG) with phase-contrast (PC) or differential interference contrast (DIC) or on the EVOS^{TM} M5000 in brightfield imaging mode. As depicted on the left image of fig. 5.1, even substrates without visible defects appear to exhibit a lateral inhomogeneity. As depicted in the right image of fig. 5.1, some substrates also exhibited visible local defects. However, as discussed in section 5.4, artifacts from these defects are excluded from the final meta-analysis of scans.

5.2. AFM Characterization

Substrate Layer Thickness Determination

- Measurements by Anja Zaß: Determined layer thicknesses are displayed in table 5.1 in columns for substrate 1-3. The edges of most layers are stretched too far to determine their heights unambiguously. The application of different background correction schemes leads to incompatibly large differences in de-

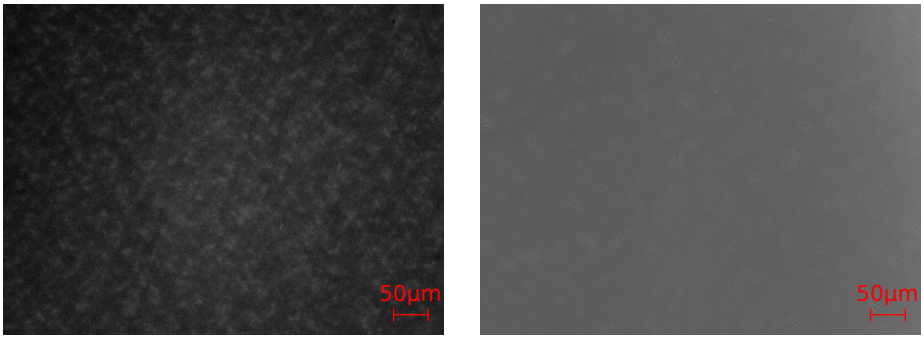


Figure 5.1.: EVOS^{TM} M5000 brightfield images of SiO_2 sensor substrates SID100 (left) and SID138 (right). The left image depicts a substrate with minimum visible defects under strong contrast enhancement. The right image depicts a substrate with maximum visible defects (tiny black dots and lines) at normal contrast.

termined step heights (see fig. A.6). These are therefore given as intervals in table 5.1.

- Measurements by Alex Winkel: Determined layer thicknesses are displayed in table 5.1 in columns for substrate 4-7.

Table 5.1.: AFM measured layer thicknesses of Au substrates in nm. Target thicknesses are 3 nm for Cr and 47 nm for Au. Missing values represent layer thicknesses that could not be determined. Values marked in lightgray belong to substrates that have not been metallized at the target vacuum pressure of 5×10^{-7} mbar.

layer	subst. 1	subst. 2	subst. 3	subst. 4	subst. 5	subst. 6	subst. 7
Au	30.1-35.1	31.7-50.9	17.5-37.3	31.0-33.0	29.0-31.0	59.0-61.0	-
Cr	5.3-5.9	1.0-5.3	-	1.5-3.0	-	8-10	10-15

The unexpected values for substrates 3, 6 and 7 can possibly be explained by the fact that these substrates belong to a batch in which the vacuum of 5×10^{-7} mbar specified in section 3.1.2 was not reached.

The reason for step samples with poorly defined steps probably lies in the chosen method of masking during e-beam vapor deposition. At the relevant size scale, the mask outline and edge are probably not sharp enough. XRR proves to be a

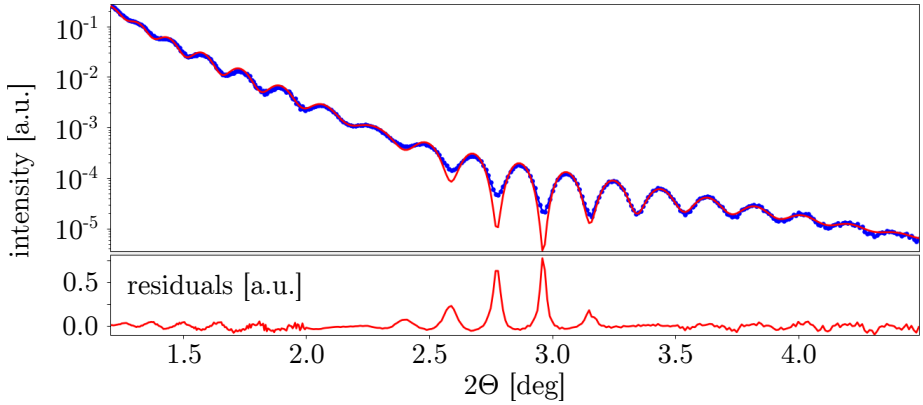


Figure 5.2.: Angular XRR spectrum of a Au substrate and its fit. Fit residuals are presented in the bottom plot.

better suited method, not only in theory, but also in terms of more consistent film thickness measurements[1].

Substrate Layer Topography Measurements

The topography of Cr and Au surfaces has been studied using AFM measurements of two substrates, as shown in figs. A.7, A.8a and A.8b. AFM measurements in fig. A.7 have the highest lateral resolution but some (Au - AFM scan 1/2) appear to have relatively high noise levels. The visible defects in all AFM measurements confirm the presence of localized layer defects as suggested by brightfield images (see fig. 5.1). Furthermore, figs. A.8a and A.8b show that the brightness variations visible in brightfield images (also fig. 5.1) are indeed due to variations in the thickness of the Cr- (and Au-) layer. It is unclear whether observed sensor height variations on Au surfaces are caused by thickness variations in the Au layer or by thickness variations in the underlying Cr layer. AFM sensor height variations (figs. A.8a and A.8b) appear to be more pronounced on Cr surfaces than on Au surfaces.

5.3. XRR Characterization

Figure 5.2 displays a typical measured and fitted intensity spectrum for a Au-substrate. The visible deviations between measurement and fit, being limited to the intensity minima, indicates an inhomogeneous thickness of the layer stack, leading

[1] All measured layer thicknesses are within the expected range and in agreement with SPRM measurements, as shown in fig. A.26

to a "washing out" of the sharp minima in the intensity spectrum. This observation is consistent with the AFM scans shown in figs. A.8a and A.8b.

Table 5.2.: XRR determined layer thickness d and RMS layer roughness σ_{RMS} by sample batch in units of nm. RMS layer roughness σ_{RMS} is not the thickness parameter uncertainty but a separate parameter. The uncertainty of the thickness parameters is estimated[a] as 0.2 nm. [138]

Variable	SID100-108	SID109-117	SID118-126	SID131-139	SID175-183
SiO_2 d	14.22	21.15	16.78	20.17	-
SiO_2 σ_{RMS}	2.10	2.52	2.06	2.00	-
Al_2O_3 d	1.25	1.41	0.98	1.41	-
Al_2O_3 σ_{RMS}	0.96	0.69	0.86	1.27	-
Au d	41.79	43.68	44.56	45.85	44.20
Au σ_{RMS}	1.26	0.98	1.06	1.00	1.42
Cr d	2.38	2.22	3.02	1.16	3.23
Cr σ_{RMS}	0.86	1.00	0.82	0.58	1.01

[a] An unresolved issue in the open source software prevented the χ^2-based estimation of parameter uncertainties. When comparing XRR data with SPRM data, RMS roughness values are more important than mean value uncertainties. Therefore, fixing this problem has not been prioritized.

The measured layer thicknesses and RMS roughness values for the sample batches used in the results published here are given in table 5.2. The measured layer thicknesses compared with the SPRM measured layer thicknesses of the substrates used in the MID000-MID068 measurements are visualized in fig. A.26.

5.4. SPRM Characterization

As discussed in section 4.5.2, Substrate Parameter Optimization, the sensor substrate layer parameters (dark gray in tables 5.3 and 5.4) of the reflectance model must be optimized in advance before cell-substrate distances and cytoplasm RI values (light gray in tables 5.3 and 5.4) can be determined. This is done by first analyzing the cell-free substrate "control" spots (see fig. A.17) of each sample.

SiO_2 substrates (HEK293 cell measurements)

The results of the determined substrate layer thickness parameters evaluated by BFP segment and for all HEK293 cell measurements (MID001-MID068) are shown in fig. A.26 and compared with XRR layer thickness measurements. It should be

noted that the XRR measurements represent average film thicknesses in only a single substrate per batch, whereas the SPRM values are taken from multiple localized spots on all other substrates in each batch.

The determined Au layer thickness is the most important parameter in terms of reflectance profiles. A similar positive trend in thicknesses from batch 1 to 4 can be seen in both SPRM and XRR values. However, it is notable that the SPRM values from the left and top BFP segments are systematically higher ($\sim$2 nm) than those from the right and bottom BFP segments. It is suggested that unaccounted for variations in the illumination distribution may have led to this systematic difference.

For the Cr layer thickness, SPRM gives a distribution of values that are all (1-2) nm higher than XRR values. A possible explanation could be that the assumed optical parameters of Cr are not accurate enough. Given that Cr optical parameters of thin films are dependent on film thickness [10], this explanation is not unlikely.

Looking at the Al_2O_3 thicknesses determined by SPRM, it is noticeable that all the values determined are well below 1 nm, whereas the values determined by XRR are between 1 nm and 1.5 nm. Again, inaccurate optical constants are a plausible explanation, not only because a certain degree of mixing between Al_2O_3 and neighboring layers cannot be ruled out.

The SiO2 thickness values measured by SPRM are systematically higher than those measured by XRR, especially in the first batch of substrates. As the properties of PECVD grown SiO_2 layers are known to show impurities and incomplete SiO_2 bonding depending on deposition parameters [23], inaccurate assumptions of optical parameters are again suspected as the cause of this deviation.

Au substrates (neuron measurements)

The results of the determined substrate layer thickness parameters evaluated for all BFP segments simultaneously and for all neuron measurements (MID082-MID106) are shown in fig. A.40a and compared with XRR and reflectometry data. A notable difference from the HEK293 measurements on SiO_2 is the observation that substrate layers could not be fitted from the SPRM data without simultaneous fitting of the cell medium RI. As shown in fig. A.40a, the fitted values for cell medium RI are consistently higher than the RI measured (for fresh medium) by refractometer. However, taking into account the incubation period of (3.5 ± 1.0) d, during which a certain amount of liquid evaporated from the cell culture dishes, higher observed RI values become plausible.

Table 5.3.: Stratified layer model of a HEK293 cell on a coated SiO_2 substrate. Original values of layer thickness d_j, RI (real component) n_j and extinction coefficient κ_j before optimization, together with their origins. Parameters optimized globally in a first fit are highlighted in light gray. Parameters optimized for each scan point are highlighted in dark gray.

layer	d_j [nm]	n_j	κ_j	ref. for d_j	ref. for n_j	ref. for κ_j
cytoplasm	-	1.3720	0.0000	-	[123][b]	[123]
membrane	8.0	1.500	0.0000	[123]	[123]	[123]
medium	10.0	1.3350	0.0000	guess[b]	section 3.4.3	guess[c]
coating	1.78	1.4000	0.0000	[65][a]	[55]	guess[c]
SiO_2	18.0	1.4761	0.0000	target value[b]	[84]	guess[c]
Al_2O_3	2.0	1.1677	6.4833	target value[b]	[92]	guess[c]
Au	47.0	0.1943	3.5921	target value[b]	[108]	[108]
Cr	3.0	3.3000	4.2731	target value[b]	[108]	[108]
N-LAF21	-	1.7845	0.0000	-	[104]	guess[c]

[a] The inverse-variance-weighted mean of reported coating layer thicknesses is used.
[b] Only an initial guess for the optimizer.
[c] Absorption of non-metallic layers is neglected.

Table 5.4.: Stratified layer model of a neuron on a coated Au substrate. Original values of layer thickness d_j, RI (real component) n_j and extinction coefficient κ_j before optimization, together with their origins. Parameters optimized globally in a first fit are highlighted in light gray. Parameters optimized for each scan point are highlighted in dark gray.

layer	d_j [nm]	n_j	κ_j	ref. for d_j	ref. for n_j	ref. for κ_j
cytoplasm	-	1.3720	0.0000	-	[123][b]	[123]
membrane	8.0	1.500	0.0000	[123]	[123]	[123]
medium	10.0	1.3340	0.0000	guess[b]	section 3.4.3	guess[c]
coating	1.78	1.4000	0.0000	[65][a]	[55]	guess[c]
Au	47.0	0.1943	3.5921	target value[b]	[108]	[108]
Cr	3.0	3.3000	4.2731	target value[b]	[108]	[108]
N-LAF21	-	1.7845	0.0000	-	[104]	guess[c]

[a] The inverse-variance-weighted mean of reported coating layer thicknesses is used.
[b] Only an initial guess for the optimizer.
[c] Absorption of non-metallic layers is neglected.

Substrate Defects

Brightfield microscopy images (section 5.1) and AFM topography scans (section 5.2) both reveal substrate layer defects and lateral substrate layer thickness inhomogeneities in SPRM sensors: Substrate layer defects raise the concern of discrete cell-substrate distance artifacts. Gradual lateral substrate layer thickness variations raise the concern of continuous cell-substrate distance artifacts, knowing that the SPRM width, to which cell-substrate distance determination is sensitive (see section 4.5.2), is also theoretically affected by substrate layer thicknesses.

As can be seen in some of the area scans in figs. A.30 and A.31 (e.g. MID045, MID051 and MID052), layer defects appear as local outliers in the measured cell-substrate distances and cytoplasm RI values. Because these outliers are sparse and represent parameter boundary values, they can be treated by masking (conditions specified in section 6.1). This way, they do not affect the meta-analysis of cell-substrate distance distributions.

As can be seen in figs. A.32 and A.33, the effect of substrate thickness variations on SPR angle and SPR width is negligible.

5.5. Refractometry of Liquids

An overview of the RI values obtained for both types of cell medium, together with the measured RI values of the double distilled water used as a control, is given in table 5.5.

Table 5.5.: Cell medium RI values measured with an Abbe refractometer. The scale marks are spaced far enough apart (see fig. 3.6b) to estimate the fourth digit of the RI. The measurement uncertainty is estimated to be 0.0005.

Measurement Date	Room Temperature	Medium Type	H2O RI	Medium RI
2023.12.04	25.5 C	HEK293 (fresh)	1.3328	1.3362
2024.04.10	25.5 C	Neuron (fresh)	1.3330	1.3350

A temperature coefficient of $-0.0001\,\mathrm{K}^{-1}$ is assumed for the RI of cell media, as estimated for water from Table 7 in [19] between 20 C and 30 C at atmospheric pressure. This temperature coefficient is used to estimate the RI values of cell media in SPRM measurements (34 C). It is noteworthy that the measured RI values for H_2O are systematically about 0.001 above the literature value for H_2O of 1.3319 [80] (20 C), not even taking into account the temperature difference. Since SPRM measurements of H_2O also gave a higher RI of 1.3333 ± 0.0001, it was decided not to assume a

small systematic error of the refractometer. Instead, a slightly higher RI is assumed for the bottled double distilled water in the laboratory, compared to pure H_2O.

5.6. SPRM Refractive Index Validation Measurements

As presented by Hassani [123], Refractive Index Microscopy (RIM) allows the measurement of isotropic and birefringent refractive indices with higher resolution than SPRM. RIM uses bare high RI substrates (without metal coating) on the same setup as described in section 4.1. The improvement in RI resolution is due to the unobstructed critical angle and the sharp edge of total reflection that dominates the reflectance profile in a RIM sample (as shown in fig. 4.16a).

One aspect that makes RIM attractive for the evaluation of the presented data analysis procedure, in particular for the evaluation of the determined r_{max} parameter, is the minimalism of the substrates used. Without the presence of potentially incorrectly characterized substrate layer thicknesses or optical constants, the modeling of reflectance profiles relies on far fewer assumptions when using only a two-layer model of substrate and liquid[2]. Therefore, RIM measurements of EtOH, H_2O and air were performed in areas of 40 µm x 40 µm (20x20 scan points), as listed in table A.2 (measurement IDs MID076-MID078).

Since the RI values determined in this way depend directly on the observed critical angle of total reflection via eq. (2.19), and the observed angle of total reflection depends directly on the specified value r_{max} via eq. (4.2), a systematic error in r_{max} would lead directly to a one-sided systematic error in all measured RI values.

While the measured RI values in 5.3, which cover the range of about half of the RI values measurable with this setup, do indeed appear to show higher precision than accuracy and thus systematic errors, the observed systematic errors are not one-sided. The magnitudes of the estimated systematic errors, also shown in fig. 5.3, are at maximum 0.1 %. With regard to the systematic error in the H_2O RI, it should be noted that the Abbe refractometer measurements (see table 5.5) also gave a value closer to 1.333, suggesting that the laboratory bottled double distilled water used for both measurements may have a slightly higher RI than pure H_2O.

It is possible that systematic errors are due to the distribution of noise or to optical aberrations in the BFP. In retrospect it is noted that no temperature (plus pressure and humidity in the case of air) measurements were made in the media

[2] Additional substrate layers would not change the apparent angle of total reflection, but the angle of total reflection would appear less pronounced. The least-squares approach to profile fitting also correlates the RI values determined with the properties of other substrate layers.

σ_{stat} :	0.00003	0.00013	0.00009
σ_{syst} :	-0.00029	0.00139	0.00006

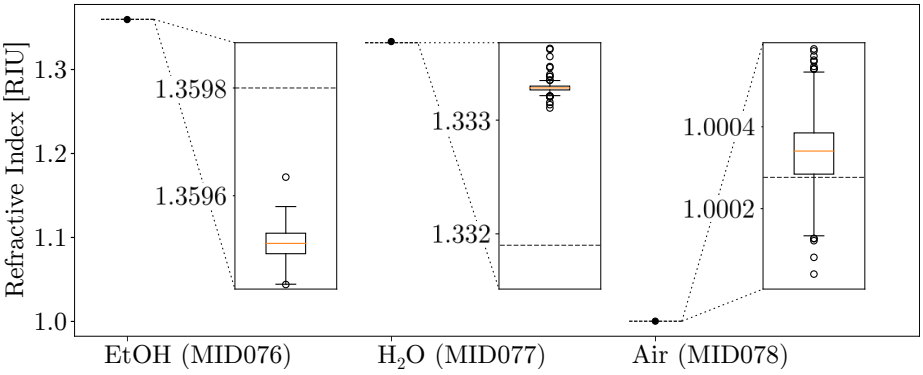
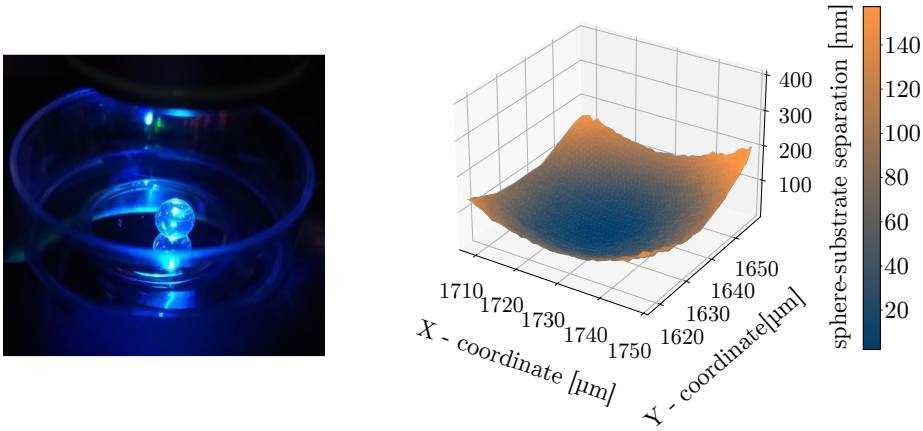


Figure 5.3.: Refractive indices of EtOH, H_2O (MilliQ) and air determined by RIM at room temperature (∼20 C). The distribution of values is shown by box plots (IQR ± 1.5 IQR, see matplotlib [61] documentation for version 3.6.2) in zoomed views. Literature values of EtOH [96] ("room temperature"), H_2O [80] (20 C) and air [28] (15 C, 101 325 Pa, dry) are shown as dashed lines. Statistical errors are estimated as sample standard deviations. Systematic errors are estimated as the difference between the median measured value and the literature value. The mean statistical error estimate is 0.000 08 and the mean absolute systematic error estimate is 0.000 58.

involved. In order to be able to make further statements, this measurement has to be repeated with exact temperature values or alternatively RI measurements on a dilution series as done by Kreysing [107].

5.7. SPRM Specimen-Substrate-Distance Validation Measurements

One of the key results of this work is the successful performance and analysis of a specimen-substrate distance validation measurement. Such a measurement allows to evaluate the overall performance of the setup and data analysis pipeline, as well as to estimate statistical and systematic measurement errors. For this measurement, a SiO_2 ball lens ((5000.0 ± 2.5) µm diameter, Edmund optics, #67-386) is used as specimen. One measurement (MID074) is carried out on an Au substrate, another measurement (MID075) is carried out on a SiO_2 substrate. Figure 5.4 gives a three-dimensional view of the sample arrangement and a first insight into the analysis results obtained.



(a) SiO_2 ball lens sample photo

(b) 3D plot of sphere-substrate distance

Figure 5.4.: Photo of the SPRM sample of SiO_2 ball lens and Au substrate, mounted in the stage of the microscope (a) and 3D plot of the SPRM measured sphere-substrate distance in measurement MID074 (b).

In contrast to previous approaches, as in [107], a larger diameter of the ball lens was chosen (5000 µm instead of 500 µm) in order to obtain more analyzable data points from a larger fraction of the substrate. Furthermore, the surrounding medium was chosen to be isopropanol instead of EtOH to reduce the RI difference between medium and sphere from 0.097 to 0.081, closer to the range of expected RI differences between cell medium and cytoplasm of 0.005-0.065, thus reducing the artificial contrast enhancement in this validation measurement.

Sphere-Substrate Distances: Sphere on Au

As can be visually confirmed in fig. 5.4b, the evaluated sphere-substrate distance values from MID074 (see table A.2) clearly follow the expected outline of a sphere. A further quantitative evaluation, visualized in fig. 5.5, confirms the expected spherical shape. The slight systematic deviation will be discussed in the following. To produce this plot, the coordinates of the sphere-substrate contact point are determined by fitting the equation of a sphere (eq. (5.1)) to the available data points. The lateral stage coordinates around this contact point are then transformed into polar coordinates r and ϕ. Plotting the sphere-substrate distances against the calculated radial coordinates r produces fig. 5.5. The residuals shown at the top of fig. 5.5 are

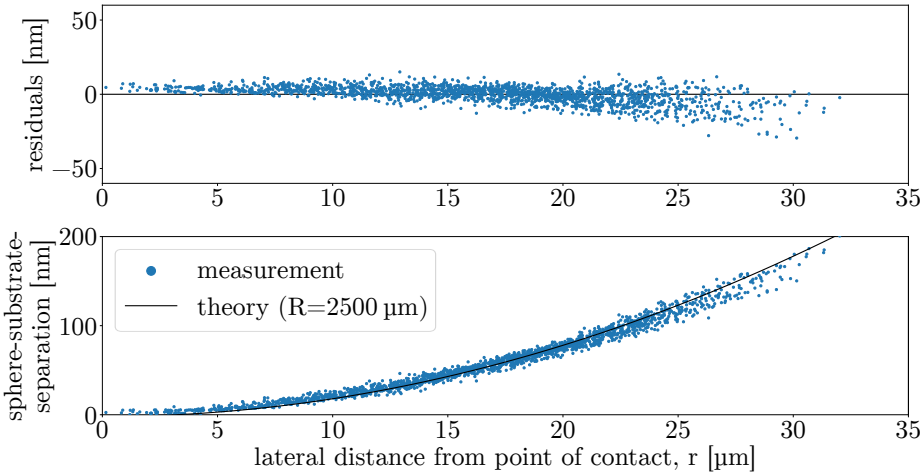


Figure 5.5.: Evaluation of sphere-substrate distance validation measurement with SiO_2 sphere on Au substrate. Evaluated sphere-substrate distances from measurement MID074 (see fig. 5.4b) are plotted against radial distance between measurement point and sphere contact point in the lower plot. The geometric expectation of values (assuming a 2500 µm sphere radius) is shown as black curve. The difference between measurement and expectation is shown in the upper plot.

the difference between evaluated sphere-substrate distances h and $h_{model}(r)$ from eq. (5.1).

$$h_{model}(r) = R - \sqrt{R^2 - r^2} \qquad \text{with} \qquad R = 2500\,\mu\text{m} \tag{5.1}$$

Discussion of Errors: Sphere on Au

The observed systematic deviation between the measured sphere-substrate distance values and the theoretical sphere shape is discussed next. One of the first possible explanations that comes to mind is a deviation of the sphere radius R from the stated manufacturing radius. And indeed, a sphere radius of 2700 µm would describe the data without any systematic deviation. However, the manufacturer stated a tolerance of only ±2.5 µm on their sphere radius. A diameter deviation of 200 µm was also not detected by a caliper measurement. Therefore, a significant deviation of the sphere radius is not accepted as an explanation.

Figure 5.6 shows the manufacturer's stated RI value on top of measured RI values. It can be seen that RI values follow a similar systematic deviation from expected values (compared to sphere-substrate distances). This further supports the idea that it is not the lateral coordinates but the actual values of sphere-substrate distances that deviate from the expectation. From the point of view of the least squares

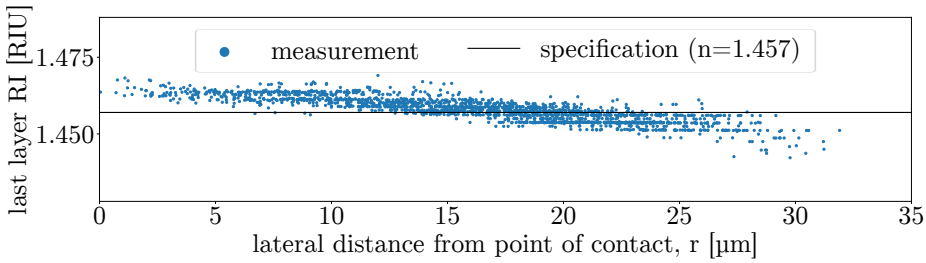


Figure 5.6.: RIs of the SiO_2 sphere determined with a Au sensor around the sphere-substrate contact in evaluation of measurement MID074. RI values are shown in blue, the manufacturer's RI specification is marked in black. The x-axis coincides with the x-axis in fig. 5.5.

optimizer, the effect on χ^2 of reducing the sphere-substrate distance can be partially compensated for by increasing the refractive index of the sphere. Both changes cause an increase in SPR angle, leading to a correlation between these two parameters. A reliable distinction between these two model constellations can be made in the region around the critical angle, but it is assumed that insufficient SNR in this region prevented the optimizer from disentangling the two parameters.

Figure 5.7 evaluates the residuals from fig. 5.5 as a function of sphere-substrate distance. The systematic error resulting from the discussed parameter correlation becomes visible together with the increasing measurement variance with increasing sphere-substrate distance, expressed as statistical error. Both measurement errors appear to have a linear relationship with measurement values. The fitted linear model of statistical errors will be regarded as prediction for statistical uncertainties of cell-substrate distances on Au substrates.

Sphere-Substrate Distances: Sphere on SiO_2

Figure 5.8 visualizes evaluated sphere-substrate distances of measurement MID075 (see table A.2). As for measurement MID074, they reproduce the expected spherical shape. However, measurement MID075 exhibits stronger systematic deviations.

Discussion of Errors: Sphere on SiO_2

A comparison between fig. 5.8 and fig. 5.9[3] reveals a correlation between determined parameters of sphere RI and sphere-substrate distance. In places where the sphere RI was determined to be higher than the manufacturer's specification, the sphere-substrate distance values obtained are also higher than expected. Figure 5.10 shows

[3]Note that fig. 5.8 has been cropped to the same extent as fig. 5.5.

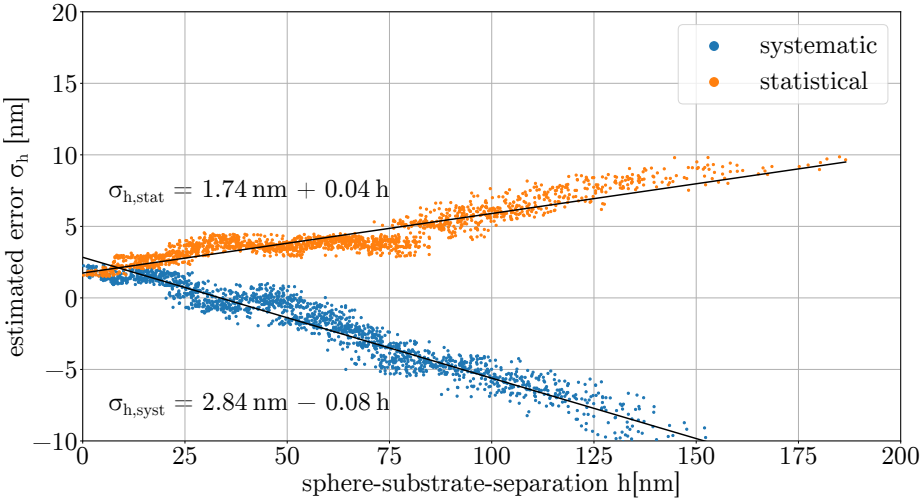


Figure 5.7.: Estimation of specimen-substrate separation measurement statistical and systematic error, using the SiO_2 sphere on Au substrate validation measurement. Statistical errors are estimated as the running sample standard deviation (window size of 40 data points) from the residuals shown in fig. 5.5. Systematic errors are estimated as the running average of these residuals (same window size). For both kinds or error estimates a linear fit is shown as black line.

residuals as a function of sphere-substrate distance. In contrast to fig. 5.7, systematic deviations do not follow a straight line. Instead, they behave fundamentally different compared to measurement MID074 on Au.

Without further measurements, it's not possible to say whether the difference in the observed systematic deviations between measurements is due to the type of substrates used (Au or SiO_2), the difference in parameter optimization algorithms (3-step fit with uniform weights vs. 1-step fit with Gaussian weights) or due to defects on sphere or substrate in measurement MID075. However, for the forthcoming discussion of cell-substrate distance measurements, systematic errors of Au and SiO_2 substrates will be estimated differently. A linear model is used to describe the specimen-to-substrate distance uncertainty in all subsequent measurements on Au substrates. The available sphere-substrate measurement on SiO_2 doesn't allow us to assume a linear relationship between measurement value and measurement error. Instead, the mean systematic error is calculated and regarded as experimental predictor of systematic uncertainties for measurements on SiO_2 substrates.

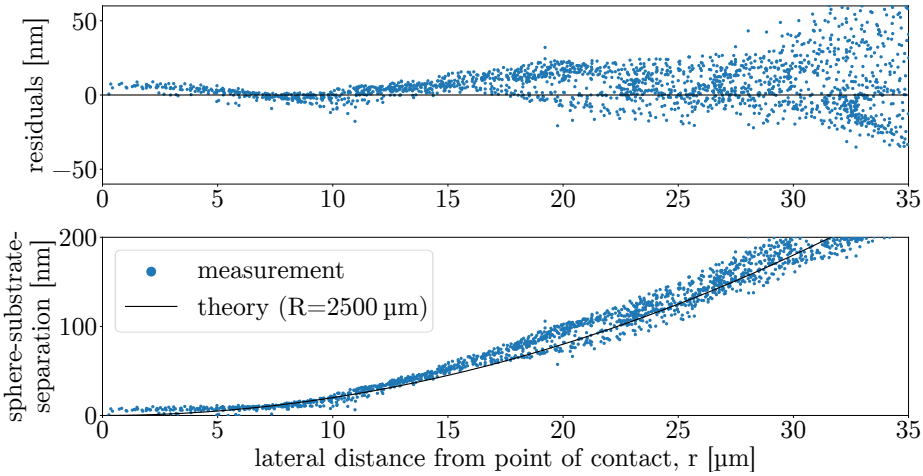


Figure 5.8.: Evaluation of sphere-substrate distance validation measurement with SiO_2 sphere on SiO_2 substrate. Evaluated sphere-substrate distances from measurement MID075 are plotted against radial distance between measurement point and sphere contact point in the lower plot. The geometric expectation of values (assuming a 2500 µm sphere radius) is shown as black curve. The difference between measurement and expectation is shown in the upper plot.

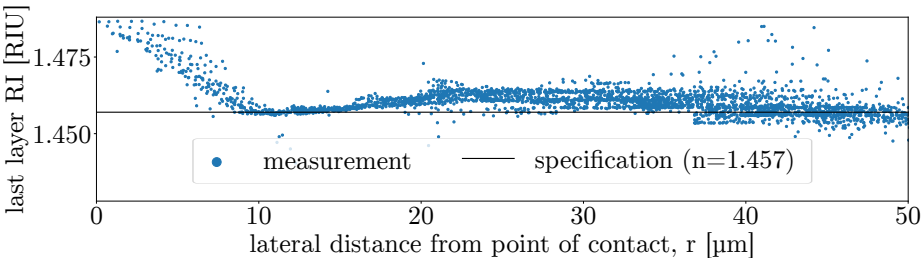


Figure 5.9.: RIs of the SiO_2 sphere determined with a SiO_2 sensor around the sphere-substrate contact in evaluation of measurement MID075. RI values are shown in the blue, the manufacturer's RI specification is marked in black. The x-axis coincides with the x-axis in fig. 5.8.

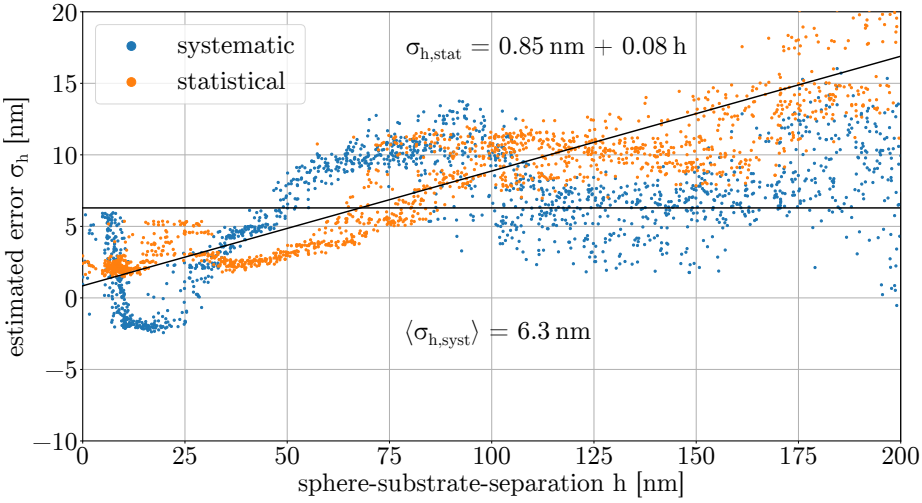


Figure 5.10.: Estimation of specimen-substrate separation measurement statistical and systematic error, using the SiO_2 sphere on SiO_2 substrate validation measurement. Statistical errors are estimated as the running sample standard deviation (window size of 40 data points) from the residuals shown in fig. 5.8. Systematic errors are estimated as the running average of these residuals (same window size). For statistical error estimates a linear fit is shown as black line. For systematic error estimates, a mean systematic error of 6.3 nm has been calculated.

For the estimation of the statistical errors (also shown in fig. 5.10), a linear model is used, as for the statistical errors on Au. The increased statistical error in the case of SiO_2, which follows a linear dependence with twice the slope, is consistent with the expectation that the additional SiO_2 substrate layer negatively affects the axial resolution of the microscope.

Compensation of Defocusing

An important factor in the successful analysis of these two measurements is the application of the defocus compensation procedure discussed at the end of section 4.3.4. In the case of measurement MID074, where only a slight defocus of Δi in the range 4-6 was evaluated, all four BFP segments could be analyzed together even without defocus compensation. However, when defocus compensation is applied, a reduction in the residual distribution can be seen, as shown in the upper part of fig. 5.11. In the case of measurement MID075, due to a significant defocus of Δi in the range of 4-45, only single segments could be analyzed without defocus compensation. With defocus compensation, the left and right BFP segments could be analyzed together.

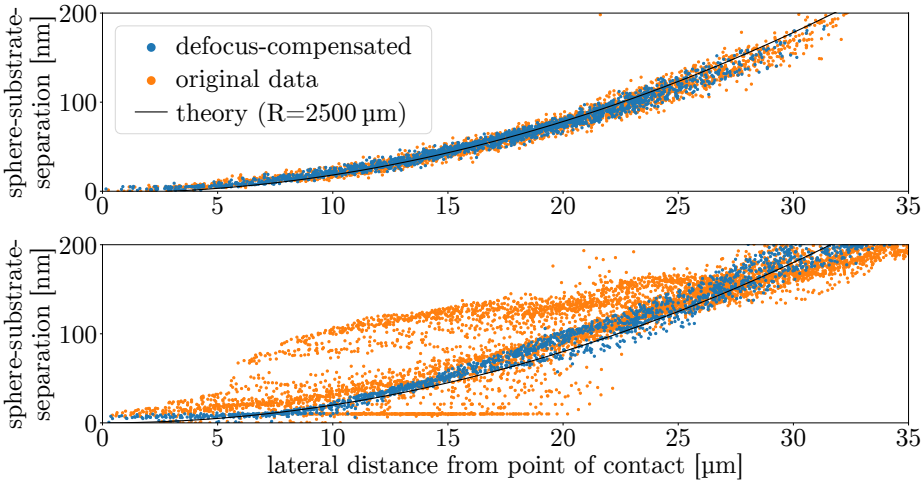


Figure 5.11.: Evaluation of both sphere-substrate distance validation measurements with and without defocus compensation. Sphere-substrate distances from measurement MID074 (top) and MID075 (bottom) were determined with and without defocus compensation, in both cases from the same selection of BFP segments and with otherwise identical analysis parameters.

A comparison of this two-segment analysis with and without defocus compensation is shown in the lower part of fig. 5.11.

5.8. SPRM Statistical and Systematic Uncertainty Estimation

At the heart of method evaluation is the discussion of statistical and systematic uncertainties. These quantify the reliability of measured values. For the SPRM-based determination of specimen-substrate distance h, this discussion must take into account that statistical and systematic uncertainties scale as a function of the underlying ground-truth specimen-substrate distance h_{true}. The reason for this lies in the nature of the measurement probe used, the evanescent field in the interface of interest. As h increases, the coupling between the evanescent field and the specimen gets weaker. A quantification of this effect can be seen in fig. 5.12, which shows the relationship between SPR radius r_{SPR} and h. For all the sensor and specimen-RI combinations shown, the dependence (derivative) of SPR angle with respect to h decreases for large values of h.

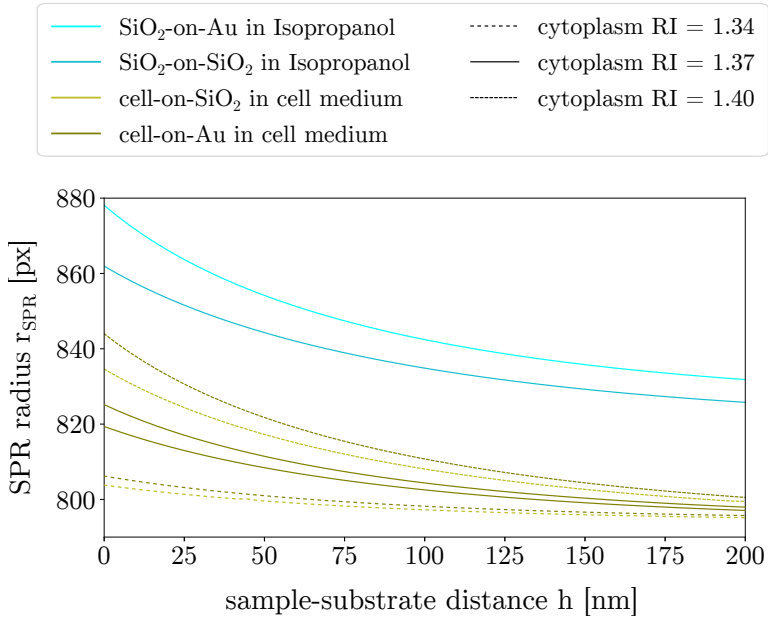


Figure 5.12.: Relationship between SPR radius and specimen-substrate distance h for Au and SiO_2 sensors with given specimen RI values. The dependencies shown are extracted from simulated SPR profiles. SPR angles are expressed as SPR radii (see eq. (4.2) for conversion to SPR angles) as changes in SPR radii are a linear measure of detectable changes in raw data BFP images and this plot is intended to visualize h-dependent sensitivity changes.

Statistical Uncertainties

A standard approach to determining the statistical uncertainties of parameters from least squares optimization, such as h, is based on the estimation of a parameter covariance matrix [21]. This is usually done in a subsequent step of the parameter optimization. However, this approach assumes that the optimization weights are set to the inverse variances of the fitted data, which is not the case for the weights applied in the described fit (see section 4.5.2).

The results of the h-validation measurement performed (see section 5.7, figs. 5.7 and 5.10) provide an experimental assessment of the h-dependent statistical uncertainties for both types of substrates and corresponding optimization algorithms. For

both substrate types, the observed statistical uncertainties show a linear dependence on h:

$$\sigma_{h,stat,\mathrm{Au}}(h) = 1.74\,\mathrm{nm} + 0.04 \cdot h \tag{5.2}$$

$$\sigma_{h,stat,\mathrm{SiO_2}}(h) = 0.85\,\mathrm{nm} + 0.08 \cdot h \tag{5.3}$$

For the SiO_2 substrate, a higher linear coefficient is observed, as expected, due to the additional SiO_2 layer moving the sample further out of the (sensitive) evanescent field. However, it is expected that confidence intervals calculated from these uncertainties will be too small. This is because of the relatively lower sensitivity for cell-substrate interfaces due to smaller RI differences between medium and specimen.

Systematic Uncertainties

In terms of systematic uncertainties, any incorrect assumption (e.g. sample geometry, sample composition, optical parameters of sample layers, illumination profile, wavelength) as well as the particular arrangement of interference patterns in the BFP can cause systematic measurement uncertainties of h. The set of BFP parameters x_0, y_0 and r_{max} is identified as a particularly sensitive source of systematic measurement uncertainties, since they determine the mapping from pixel coordinates to assumed reflection angles θ (see eq. (4.2)). The parameter optimization procedure doesn't allow a direct uncertainty propagation from parameter uncertainties σ_{x_0}, σ_{y_0} and $\sigma_{r_{max}}$ to $\sigma_{h,syst}$. Yet it is possible to formulate an approximate linear relationship between these uncertainties, for which the coefficients can be determined numerically:

$$\sigma_{h,syst}(h) = \sigma_{h,syst,0}(h) + \frac{\partial \sigma_{h,syst}}{\partial \sigma_{x_0}}(h) \cdot \sigma_{x_0} + \frac{\partial \sigma_{h,syst}}{\partial \sigma_{r_{max}}}(h) \cdot \sigma_{r_{max}} \tag{5.4}$$

To test the validity of a linear description and to determine the coefficients, a simulated data set with known parameter deviations from ground truth values $\Delta x_0 = x_0 - x_{0,true}$ and $\Delta r_{max} = r_{max} - r_{max,true}$ is evaluated as shown in fig. A.18 (cell-on-SiO_2 sample). The determined median h-dependent coefficients are summarized in fig. 5.13. Note that eq. (5.4) only includes a coefficient for the center x-coordinate uncertainty σ_{x_0} and not for the center y-coordinate uncertainty σ_{y_0}. The reason for this is that when analyzing a single BFP segment, one of these two coefficients becomes negligible (σ_{y_0} for horizontal BFP segments and σ_{x_0} for vertical BFP segments) while both contributions are symmetrical. Furthermore, simulations have shown that when opposite BFP segments are analyzed together, the contributions of σ_{x_0} (σ_{y_0}) cancel each other out. BFP parameter uncertainties

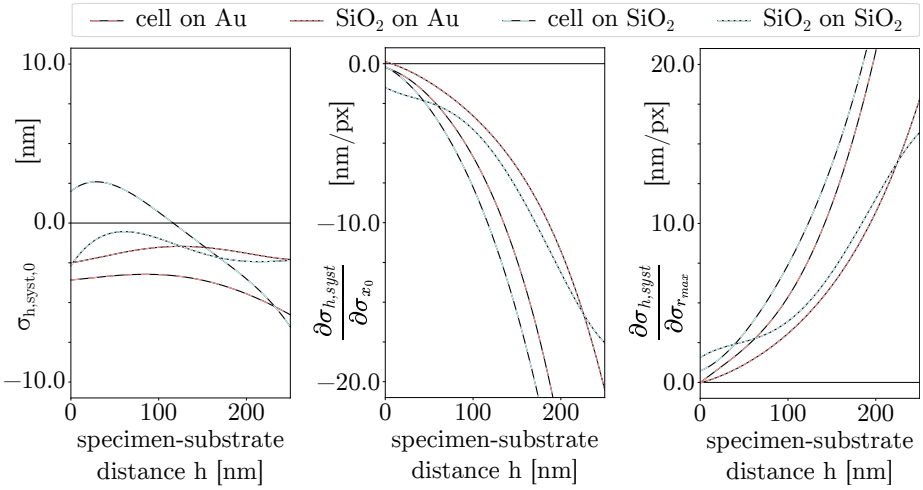


Figure 5.13.: Distance dependent factors for uncertainty propagation. Up to linear contributions to the median systematic specimen-substrate distance uncertainties, depending on the uncertainties in the BFP parameters x_0 and r_{max}, when evaluating simulated (noise-free) data sets for all 4 main sample types. The left plot shows the systematic uncertainty contribution, which is independent of the uncertainties σ_{x_0} and $\sigma_{r_{max}}$. For "cell on SiO_2" it corresponds to the polynomial fit of the middle plot in fig. A.18. The middle plot shows the linear uncertainty contribution from uncertainties on detected BFP image centers x_0. For "cell on SiO_2" it is half the difference between the polynomial fits in the center right and center left plots in fig. A.18. The right plot shows the linear uncertainty contributions from uncertainties on the assumed aperture size r_{mac}. For "cell on SiO_2" it is half the difference between the center bottom and center top plots in fig. A.18.

are assumed to be $\sigma_{r_{max}} \approx 1\,\mathrm{px}$ (see fig. A.13) and $\sigma_{x_0} < 0.5\,\mathrm{px}$ (values reported from the refinement procedure described in section 4.3.3). σ_{x_0} varies between measurements. The systematic uncertainties observed in the h-validation measurement (see section 5.7, figs. 5.7 and 5.10) are of the same order of magnitude and can therefore be explained as a consequence of the uncertainties $\sigma_{h,syst,0}$, σ_{x_0} and $\sigma_{r_{max}}$. The independent contribution $\sigma_{h,syst,0}$ is assumed to be an artifact of the analysis algorithm (profile discretization, weighting function, minimization algorithm, etc.).

6 SPRM Cell-Substrate-Distance Measurements

6.1. HEK293-Substrate-Distance Measurements

This section contains research also published in [145].

This section summarizes experimental cell-substrate distance (scanning) measurements collected from a series of 68 measurements (see table A.1), including 146 cell-substrate interfaces across 33 cell culture dishes with 6 standard cell-adhesive coatings as well as uncoated substrates. As a cell type, HEK293 cells are used for several reasons. Firstly, HEK293 cells are a popular cell line for many types of biological questions and in particular for electrophysiological measurements, making the investigation of cell-substrate distances a relevant question. [57] In addition, HEK293 cells are relatively easy to handle and grow quickly, allowing a high throughput of cells after a relatively short time in culture. Finally, a previous study [65] of HEK293 cell-substrate distances measured by TEM has been published at this institute, allowing for a direct comparison of methods.

The substrates used are SiO_2 substrates (see fig. 3.3) to approximate as closely as possible the culture conditions of Wrobel et. al [65]. The same substrate coatings and protocols are also used, with coating concentrations scaled by surface area (see section 3.2.3). ECM coating is an exception because the coating protocol has been updated due to the problem of non-uniform coating layers in [65]. However, the main difference in culture conditions between [65] and the measurements presented here is the time in culture. While Wrobel et. al [65] kept the cells in culture for 1-3 days, the cells in this work were cultured for about (5-9) h (with a few exceptions, see table A.1). The reason for this shorter time in culture is the attempt to avoid the observation of cell cycle dependent variations in cell-substrate distance. The time frame of (5-9) h after seeding is considered an appropriate window for measurements in which cells are expected to have developed adhesion to the substrate, but have not yet begun to divide. Furthermore, previously encountered problems of Au layer delamination during long substrate culture periods are conveniently avoided. Care was taken to minimize the difference in average culture duration between different coatings (see

table A.1). This was done to further minimize the risk of culture-duration dependent cell-substrate distance artifacts between different cell-adhesive coatings.

Cells are plated on substrates a maximum of 24 h after substrate coating, during which time the sensors are kept filled with medium at 37 C. At the time of measurement, cells are rapidly transferred from the 37 C incubator to the heating module (see fig. 4.3) of the SPRM setup. The SPRM setup is in the adjacent laboratory, so samples are covered to minimize temperature shock. The temperature of the HEK293 cell medium is stochastically measured after the measurements to be (34 ± 2) C. The reason for the mean temperature difference (compared to the incubator temperature) is an experimental error. The heating module has no feedback control system, so the temperature can only be adjusted by adjusting the input voltage. The SPRM measurement setup itself is described in section 4.1.

Only cells with a well-spread morphology, as assessed by widefield SPRM, are included in the measurements. An overview of all 68 (except one) widefield SPRM images taken prior to scanning measurements is shown in fig. A.36. A snake path scan pattern is generated for the ROI as described in section 4.1. Brightfield microscopy images are taken before and after each scan to detect cases of cell migration or changes in adhesion during a scan measurement. Figure A.37 shows brightfield images before all 68 scanning measurements, labeled by measurement ID and showing the rectangular ROI of successive scans. Figure A.38 shows the same view, but overlaid with images after each scan to detect changes in cell position and shape, as seen in measurement MID034.

A total of 271 256 BFP images are recorded over all 68 measurements, with an average measurement size of approximately 4000 images, corresponding to 1.035 TB of raw data. In the analysis of these measurements, each individual BFP image is subjected to the analysis steps described in sections 4.2, 4.3 and 4.5, with the exception of defocus compensation (section 4.3.4). Defocus compensation didn't work[1], for all measurements, therefore it was omitted for all measurements. Instead, each BFP segment is analyzed separately in the final analysis step (section 4.5) and the final results are compared between BFP segments.

Figures A.30 and A.31 show spatial mappings of cell-substrate distances and cytoplasm RI as determined by the optimizer for all scanning points of each measurement. Both figures provide four plots per scan, visualizing the results of all four BFP segments separately. No masks are applied to the data shown.

[1] The results of the cross-correlation calculation seem to indicate that some measurements were too defocused to find index shifts Δi for compensation. Although it cannot be excluded that the scan step sizes were simply too large to assume that changes in cell-substrate distance could be interpolated between them.

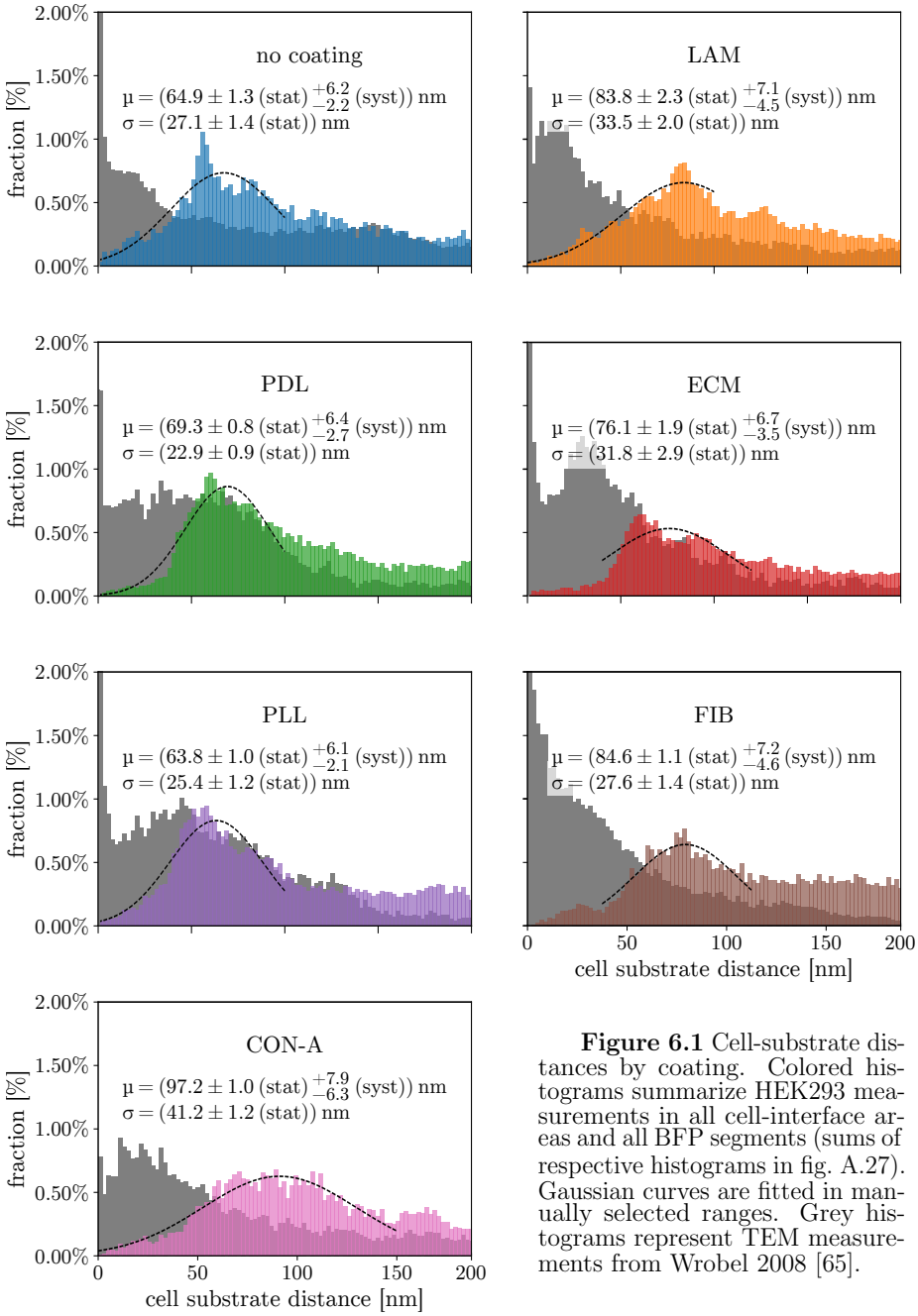


Figure 6.1 Cell-substrate distances by coating. Colored histograms summarize HEK293 measurements in all cell-interface areas and all BFP segments (sums of respective histograms in fig. A.27). Gaussian curves are fitted in manually selected ranges. Grey histograms represent TEM measurements from Wrobel 2008 [65].

Figure 6.1 shows histograms of all measured cell-substrate distances for each substrate coating. These histograms contain the sum of segment-wise histograms in figs. A.27a to A.27d. The data shown corresponds to cell-substrate distances h in fig. A.35, but masked with the following conditions: 1 nm <h $\leq$ 200 nm; 1.340 05 <RI <1.399 95; and coordinates lie within hand-drawn outlines of cell-substrate interfaces (see fig. A.34). The weighting of individual scan points is set so that histograms of different scanning measurements are weighted by the area of unmasked scanning regions, regardless of the scan resolution[2]. All histograms show a right-skewed, heavy-tailed distribution with only few close cell-substrate contacts. Gaussian fits[3] have peaks at (64-97) nm and widths of (23-41) nm. The statistical uncertainties shown are uncertainties of peak positions. These are taken from an estimate of the parameter covariance matrix of the Gaussian fit. Systematic uncertainties are estimated by eq. (5.4), assuming $\sigma_{r_{max}} = \pm 1$ and a negligible effect of σ_{x_0}. While some histograms, particularly for ECM gel coated substrates, show a second peak at higher cell-substrate distances (see figs. A.27a to A.27d), these peaks are not visible in evaluations of all four BFP segments. Also, as SPRM sensing is limited by the penetration depth of the evanescent field (see section 2.4.3) and sensitivity is critically reduced above 200 nm (see fig. 5.12), it is assumed that the observed peaks at cell-substrate distances above 200 nm are artifacts.

Figures A.28 and A.29 show the distribution of cell-substrate distances versus determined cytoplasm RI values for all data visualized in figure 6.1. The same color coding as in figure 6.1 is used to indicate substrate coatings. It can be seen that the cytoplasm RI values are spread over the whole range of allowed values (1.34 to 1.40), but cluster between 1.345 and 1.39. Values close to the optimization bounds (<1.345 or >1.395) are not trusted. Overall, both parameters show a weak correlation (0.15-0.30). It is assumed that this correlation results from the imperfect decoupling of both parameters by the optimization algorithm. As the absolute correlation is even lower than that of the sphere validation measurement on SiO_2 (-0.46), the systematic distance errors introduced are also expected to be lower. Clustering around lines of constant RI is considered to be an artifact of the optimization procedure. A region without data can be identified for high cytoplasm RI values and close cell-substrate contacts. A biological explanation for this could be a low optical density of close cell-substrate contacts. However, as close cell-substrate contacts are rarely observed, this observation should not be over-interpreted.

Histograms from TEM-based cell-substrate distance measurements by Wrobel et

[2]Different piezo stage step sizes of (0.7 ± 0.2) µm were chosen for each scan.

[3]Following the histogram analysis by Wrobel et al.[65], a fit is performed within ranges where the distribution can be approximated by a Gaussian probability density function. The purpose of these fits is to provide a simplified description of each distribution.

al. [65] are shown as gray histograms in the background of figure 6.1. The observation that close ($< 50\,\mathrm{nm}$) cell-substrate distances are rarely measured (8.9 % of the SPRM data) compared to the TEM values reported by Wrobel et al. (44.5 % of the data, gray in figure 6.1) is the most striking observation in the direct comparison. Considering that cells surround themselves with a glycocalyx (see section 2.1.3), larger cell-substrate distances measured by SPRM seem more plausible than predominantly tight cell-substrate contacts seen in TEM images. However, a few important differences between SPRM and TEM should be addressed at this point. Most importantly, SPRM measurements are carried out in vitro, whereas TEM measurements require multiple invasive steps to prepare the sample. In the case of Wrobel et al. [65], the following steps were performed: chemical fixation with glutaraldehyde; staining with osmium tetroxide (OsO_4) and uranyl acetate; resin embedding; and focused ion beam sectioning. Each[4] of these steps has the potential to alter the observed cell-substrate distance. Another difference between SPRM and TEM is the higher lateral resolution of TEM[5], due to its smaller wavelength, but also due to the chosen SPRM scan step size. Scan step sizes of $(0.7 \pm 0.2)\,\mu\mathrm{m}$ (varying between measurements) are the limiting factor for the lateral resolution of SPRM measurements. Another important difference between TEM and SPRM, when comparing the results of both methods, is that SPRM maps cell-substrate interfaces in two dimensions, whereas TEM images only show a cross section of a given vertical slice through the cell. A two-dimensional cell-substrate distance map has the advantage of capturing all locally resolvable distance variations. For example, local minima of cell-substrate distance can be seen at protrusions of HEK293 cells in SPRM scans, likely at sites of focal adhesions. A prominent example can be seen in measurement MID026 in fig. A.30.

Finally, there are a few reservations about the cell-substrate distances presented. First, cell-substrate spacing in this study should not be confused with an indicator of cell health or coating biocompatibility. As can be seen in the brightfield, widefield and scan images (see Figures figs. A.30, A.36 and A.37), different numbers and morphologies of cells are observed for different coatings. However, only cells with an elongated morphology were selected for the scan measurements. The few dead cells that appear in the scan images, for example in MID024 in fig. A.30, are excluded by masking (see fig. A.34). This naturally introduces a selection bias (survivorship bias) in cell-substrate distances. Another bias comes from the equal weighting of scan areas, which gives more weight to cells with large cell-substrate interfaces. Another caveat that should be mentioned is the use of FBS within the cell culture medium.

[4] Kreysing et al. presented a comparison in which the chemical fixation step did not introduce systematic changes to the cell-substrate distance, measured using SPRM. [121] However, they used a different sample preparation protocol to Wrobel et al. [65], and only selected cells with good SPRM contrast.

[5] The specified electron microscope is capable of sub-nm resolution images.

FBS contains large proteins that are assumed[6] to promote adhesion on uncoated SiO_2 substrates, but are also likely to alter the interaction between cells and compared substrate coatings. Finally, an effect of as yet unknown magnitude may be due to a cell medium RI within the cell-substrate interface that does not match the measured RI of fresh HEK293 medium. As cells secrete charged molecules into the narrow cell-substrate gap, a higher medium RI and thus a lower cell-substrate distance could be the result. The same effect can be caused by evaporation[7] of liquid from the sensor. As the laser light deposits energy in the cell-substrate gap for a prolonged period, the resulting temperature increase could compensate or overcompensate for this effect. Equation (A.2) and fig. A.19 are an extension of the systematic error estimation from section 5.8. However, in the absence of data on actual RI value deviations from within the cell-substrate cleft, the relevance of this extension is speculative.

6.2. Neuron-Substrate-Distance Measurements

Following the main body of HEK293 cell-substrate distance measurements, a second set of cell-substrate distance measurements is performed on primary neurons.

In contrast to SiO_2 substrates used for HEK293 measurements, neurons are cultured on Au sensors, either bare or with one of two commonly used coatings (PLL and PDL-Lam, see section 3.2.4). SPRM measurements are taken after (3.5 ± 1.0) DIV. All measurements, together with sample-specific details of neuron culture, are listed in table A.3. The measurement and analysis protocol are almost the same as for HEK293 cell-substrate distance measurements: The only difference in the measurement protocol lies in the acquisition of an additional brightfield image before each SPRM scanning measurement. The first difference in the analysis protocol is the Au-substrate specific optimization method (multi-step optimization with uniform weighting function, see section 4.5.2). The second difference in the analysis protocol is the successful application of defocus compensation (see section 4.3.4). An application to all measurements allows for a combined analysis of all BFP segments in each case.

An overview of the pre-scan brightfield and SPRM widefield images, as well as the corresponding neuron-substrate distance and cytoplasm RI maps, is shown in fig. A.39.

Figure 6.2 shows histograms of all neuron-substrate distances for each substrate coating. The data shown correspond to cell-substrate distances h in fig. A.39, masked

[6] Although specific interactions with integrins are not expected, electrostatic interactions with the substrate and cell membrane proteins are likely.

[7] To prevent this, culture dishes are covered most of the time and throughout the measurement.

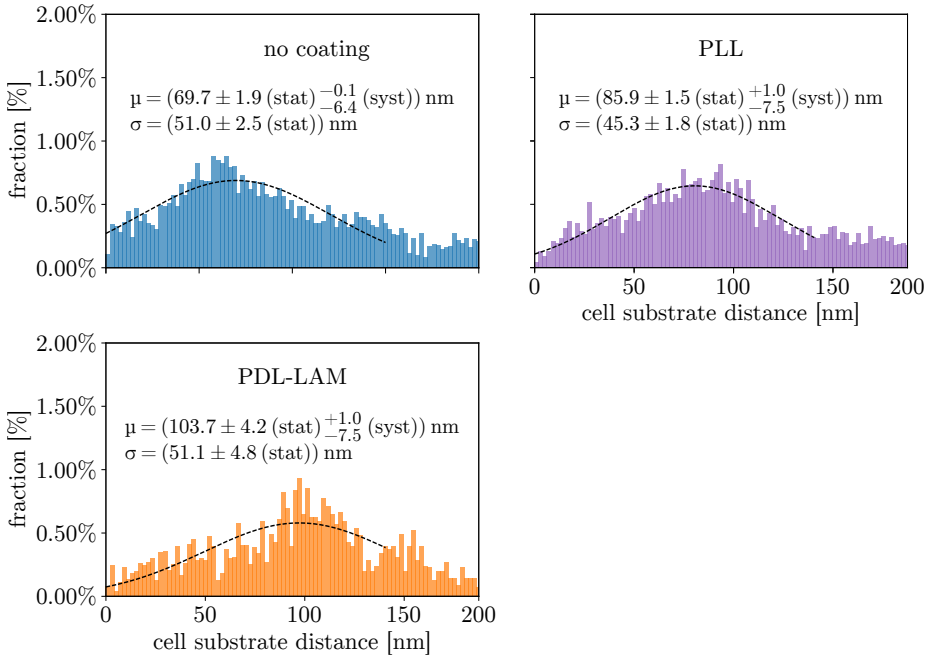


Figure 6.2.: Neuron-substrate distances by substrate coating. Colored histograms summarize SPRM measurements from all cell-interface areas. Gaussian curves are fitted in the range of (0-150) nm.

the same way as cell-substrate distances in figure 6.1. The weighting of individual scan points is set so that histograms of different scanning measurements are weighted by the area of unmasked scanning regions, regardless of the scan resolution[8]. The statistical uncertainties shown are taken from an estimate of the parameter covariance matrix of the Gaussian fit. Systematic uncertainties are estimated by eq. (5.4), assuming $\sigma_{r_{max}} = \pm 1$ and a negligible effect of σ_{x_0}. Distributions look comparable to those of HEK293 cell-substrate spacing on SiO_2 (see figure 6.1). Despite the relatively small number of measurements (25), especially for PDL-Lam coated substrates (5 measurements, see table A.3), all histograms show an approximate Gaussian distribution with peaks at (70-104) nm and widths of (45-51) nm.

Figure A.40b show the distribution of cell-substrate distances versus determined cytoplasm RI values for all data visualized in fig. 6.2. The same color coding as in fig. 6.2 is used to indicate substrate coatings. It can be seen that the cytoplasmic

[8]Different piezo stage step sizes of (0.60 ± 0.14) μm were chosen for each scan.

RI values, clustering between 1.34 and 1.37, tend to be smaller than for HEK293 measurements. Neuron-substrate distance and cytoplasm RI values show only a weak correlation of -0.167.

The same caveats listed at the end of section 6.1 apply here. Although the neuron medium does not contain serum, the B27$^{\text{TM}}$ supplement also contains proteins that may affect adhesion. Still, the effect of selection bias (survivorship bias) is expected to be even stronger for neurons on uncoated Au substrates. Bare Au surfaces make cell adhesion very difficult. This is manifested by a tendency for cells to cluster with neighboring cells and to detach from Au surfaces during network maturation (typically from DIV 4 onward).

7 Summary and Outlook

7.1. Summary

Cell-substrate distances are of interest for a number of research questions and biomedical applications. At the same time, they are challenging to measure. One obvious challenge is their size scale of tens of nanometers to 200 nm. Another challenge is that cell-substrate distances are, by definition, hidden between a cell and a substrate. Destructive measurements run the risk of influencing cell-substrate distances. Furthermore, since cells are sensitive to their environment, measurements should be taken directly in the environment of interest. And because the geometry of the basal cell membrane is curved, measurements should be laterally resolved, at least at the micron level.

This work presents advances in amplitude-scanning SPRM for specimen-substrate distance measurements with parallel specimen RI measurements. A novel SPRM data analysis software has been developed and published under a GPLv3 license. Key aspects of this data analysis routine are motivated and described in this thesis. The following elements shall be highlighted: A fully automated implementation focused on reproducibility, with all user inputs and measurement parameters condensed into a set of json files; A refinement procedure for the detection of the perpendicularly reflected ray, necessary for the calibration of reflection angles; A compensation procedure for progressive sample defocusing during measurements; and a robust least-squares based parameter optimization procedure. A particular advantage in the analysis of substrates with low SNR is the weighting method, which emphasizes not only the SPR peak but also the SPR width within the angular reflectance spectrum.

SPRM sensors are characterized using brightfield microscopy, AFM, XRR and SPRM measurements. With substrate inhomogeneities visible in brightfield microscopy images, AFM measurements on a single fabrication batch (2 substrates measured) found RMS roughness values below 1 nm for Cr and Au. XRR measurements show slightly higher RMS roughnesses of (1.1 ± 0.2) nm and (0.9 ± 0.2) nm over 5 fabrication batches (5 substrates measured). SPRM measurements show that these thickness variations do not cause significant artifacts in SPR angle and SPR width. Presented RI validation measurements using the SPRM setup (RI measurement only) result in

a statistical measurement error of less than 0.000 15 and a mean absolute systematic error of 0.000 58 for 3 measurements over a RI range of 1.0003-1.3598. Two sphere-on-substrate validation measurements of the SPRM setup and data analysis software are presented, one for a Au sensor and one for a SiO_2 sensor (SiO_2 coated Au sensor). The achieved quality of the validation measurement allows for the first time an experimental estimation of measurement errors. Statistical measurement errors at a relevant measurement value of 100 nm are 5.8 nm and 8.9 nm for Au and SiO_2 sensors respectively. Systematic errors at the same sphere-substrate distance are -5.2 nm for Au sensors and 6.3 nm for SiO_2 sensors. A theoretical discussion of statistical and systematic error sources is presented afterwards.

HEK293 cell-substrate distance measurements and neuron-substrate distance measurements both show cell-substrate distance distributions with peaks in the range between 64 nm and 104 nm. For HEK293 cells, cell-substrate distance distributions are compared between 6 different cell-adhesive coatings and uncoated SiO_2 substrates (68 measurements in total). For neurons, cell-substrate distance distributions are compared between 2 different cell-adhesive coatings and uncoated Au substrates (26 measurements in total). The HEK293 measurements are directly compared with TEM measurements from a previous publication. While 44.5 % of the cell-substrate distances measured in the TEM study were in the range up to 50 nm, only 8.9 % of the cell-substrate distances in the SPRM measured HEK293 cell-substrate distances are in this range.

7.2. Outlook

The following ideas for method improvements and measurements did not fit within the timeframe of this project, but may be of interest to future scientists working on amplitude-scanning SPRM.

- The effects of sample defocusing became apparent at a late stage in this project. Even if a sample is carefully brought into focus at the start of a measurement, the focus is often gradually lost over the course of a measurement ((1-2) h). A solution to this problem could be an autofocus procedure that minimizes the apparent size of the focus spot in the OP camera using a vertical nanopositioning stage in a feedback loop. However, in order not to limit the BFP image acquisition speed, I would recommend one of the following options: Upgrade the hardware of the current computer; or operate the OP camera and nanopositioning stage from a second computer.

- To improve control over the cellular environment, proper temperature control with a feedback loop is required. The redesign of a flow chamber with integrated temperature control would be an ideal solution. The new flow chamber design

would need to be validated with hydrodynamic simulations to avoid dead zones (pockets without liquid exchange). Such a flow chamber would be particularly useful for all types of ligand binding experiments and for supported lipid bilayer measurements.

- As suggested by Hossein Hassani at the end of his thesis [123], the installation of the XYZ piezo positioner with nanometer positioning accuracy (already available at the institute) would allow high-resolution cell scans. As Hassani argued, the positioner has a very limited lateral range (30µm), so it would have to be used in synchronous mode with the current micropositioning stage. This upgrade would not only allow high-resolution scans, but could also be combined with an autofocus function, as first suggested in this list.

- SiO_2 substrate layers show the greatest variability in film thickness. PECVD grown SiO_2 layers are also known to have different optical properties depending on the deposition parameters [23]. Therefore, switching to atomic layer deposition of SiO_2 would greatly improve the controllability of SiO_2 sensor properties.

- Hassani's coherence reduction kit significantly improves the SNR in BFP images by suppressing interference patterns. Unfortunately, it introduces temporal fluctuations in the intensity distribution. While these could be eliminated by using a faster rotating motor, such a strong motor created two new problems: Vibration from the motor caused blurring of the BFP images; and one of the glass diffusers broke apart due to radial forces at high rotation frequency. Finding a solution to fix the coherence reduction kit without introducing other artifacts or working hazards could enable sample-substrate measurements with sub-nanometer precision.

- As the current data analysis does not evaluate intensities at reflection angles below 34.1°, it would be possible to determine illumination profiles much more simply (compared to section 4.6) when performing a reference measurement on an N-LAF21 substrate in air for angles above the critical angle of total reflection (34.1°).

- As the neuron-substrate distance measurements were carried out at the very end of this project, the amount of data collected is too limited to draw any robust conclusions. Continuing this series of measurements and extending it to other substrate coatings would provide valuable information for the interpretation of MEA-based electrophysiological measurements. A combined SPRM and MEA measurement would indeed be a very interesting study, allowing a test of area contact models against the established but rather simplistic point contact model.

Acknowledgments

I am deeply grateful to **Prof. Dr. Andreas Offenhäusser** for giving me this once-in-a-lifetime opportunity that comes with this doctoral research project, the kind of experience that every curious mind, and especially every physics student, dreams of, for the chance to ask questions at the edge of what is known, and for the wisdom and experience that comes with it. Offering both, his professional experience and valuable insights into possible future directions of this work, his guidance through each milestone has been invaluable. Importantly, despite the economic realities that often dictate where we can focus our intellectual energies, he stood by me until the very end and trusted me to complete this project.

My heartfelt thanks go to **Dr. Eva Kreysing**, my mentor and scientific supervisor, who has been a constant source of support throughout this project. Her genuine interest in not only the project but also in me as a person, and her investment in my well-being, have meant more to me than I can express. Often, she was the only one who could truly understand my thoughts, even from a single sentence, providing me with a sense of shared language in times when I felt like a "foreigner" among my peers at the institute. The many hours she spent discussing every detail and reminding me of the significance of achieved milestones were crucial, especially when I struggled to see the bigger picture.

I would also like to extend my deepest gratitude to **Johanna Meyer**, who has to me been a role model and a gentle reminder of the importance of respecting and protecting my personal boundaries. In moments when I lost sight of myself in the depths of this project, she was there to pull me back to reality, enduring my oversights with patience and understanding, and holding the other end of the rope to ensure I didn't lose myself completely.

A special thanks to **Dijo Moonnukandathil Joseph** for being a curious, dedicated, and warm-hearted companion throughout the third year of this journey. His work in developing the current version of the Python control and data acquisition software has been indispensable.

Michael Prömpers deserves special recognition for producing all the substrates used for samples, calibration, and reference, as well as for our collaborative search for technical solutions. But furthermore, for being the kind of office neighbor one

looks forward to seeing every morning.

I extend my appreciation to **Dr. Vanessa Maybeck** and **Tina Breuer**, whose expertise and patience keep the institute—and especially the biolabs—running smoothly. Without their help, none of the measurements presented here would have been possible. Many thanks for the unwavering support, and for the invaluable work in isolating neurons.

Thanks also to **Dr. Ulrich Rücker** for guiding me through the introduction to XRR, overseeing the X-ray laboratory, and discussing measurement results with me. His expertise has been greatly appreciated.

I am grateful to **Yifan Xu** for performing the vast majority of XRR measurements after the setup I was using failed. Her assistance was critical to the completion of this project.

I would like to thank **Dr. Ferenc Bednár** for repeatedly listening to my challenges, providing perspective, and offering thoughtful feedback. Also, his support for my curiosity from an early stage in my life and his belief in my decision to study physics.

A big thank you to **Johannes Pfennings** and **Ruben Stüttgen** for their work in developing and designing various constructions, such as the tiltable sample holder (JP), the adapter module for the sample heater (JP), various motor mounts (JP), the design of the SPRM Flow-Chamber in its multiple versions (RS), as well as for the help in specifying the tolerances for the ordering of N-LAF21 sample substrates (JP).

I would like to express my sincere thanks to **Simon Hauser** and **Lisa Granville-Dirker** for their invaluable assistance in proofreading this thesis. Their careful attention to detail and insightful feedback has greatly helped to improve the clarity and quality of my work.

I would like to thank **Regina Stockmann** for designing and fabricating the grid samples used to calibrate the microscope stage, for contributing to discussions on SPR substrates, and for being the warm-hearted office neighbor that she is.

Thanks also to **Hossein (Erfan) Hassani** for introducing me to the SPRM setup, sharing insights into the existing data analysis software, and providing his preliminary dissertation.

I would like to thank **Alex Winkel**, **Anja Zaß**, and **Kevin Rosenberger** for performing the AFM measurements on my sample substrates. Their expertise was

instrumental in the assessment of sample quality.

I extend my sincere thanks to the **mechanical workshop team at IBI-3** for reliably bringing Johannes and Ruben's designs to life. Their feedback on feasibility and their availability to revise designs as needed were invaluable to the project's success.

I also want to thank the **IT department at IBI-3** for their consistent support with day-to-day IT issues, especially regarding data storage and the hardware of the SPR computer. Their quick assistance prevented frustrations and kept my work on track.

To **my fellows at IBI-3**, both past and present, thanks for making me feel like part of a lively and supportive community, even when I struggled to contribute as much as I would have liked during the latter half of this project.

Finally, I want to express my deepest gratitude to **Annette and Gerd Bungert**, who have nurtured me from kindergarten through to university. Their unwavering motivation, encouragement, and support have shaped the values I hold dear today, enabling me to become someone others can enjoy working with. Thanks for always standing by my side and for significantly contributing to the person I am today.

Although I have not carried out any animal experiments, some of the materials used are of animal origin, the most essential FBS. Although it is often considered a "by-product", it is derived from fetal bovine blood. It would not be appropriate to thank these animals, as they did not have a say, but I would like to mention them here.

A Appendix

$$
\begin{aligned}
\langle I(r,\phi)\rangle_\phi &\equiv \frac{1}{2\pi}\int_0^{2\pi} I(r,\phi)d\phi \\
&= \frac{1}{2\pi}\int_0^{2\pi} I_p(r,\phi) + I_s(r,\phi)d\phi \\
&= \frac{1}{2\pi}\int_0^{2\pi} L_p(r,\phi)\cdot R_p(r) + L_s(r,\phi)\cdot R_s(r)d\phi \\
&= \frac{1}{2\pi}\int_0^{2\pi} L(r,\phi)\cdot \cos^2(\gamma(\phi))\cdot R_p(r)d\phi \\
&+ \frac{1}{2\pi}\int_0^{2\pi} L(r,\phi)\cdot \sin^2(\gamma(\phi))\cdot R_s(r)d\phi \\
&= \langle L(r,\phi)\cdot \cos^2(\gamma(\phi))\rangle_\phi \cdot R_p(r) \\
&+ \langle L(r,\phi)\cdot \sin^2(\gamma(\phi))\rangle_\phi \cdot R_s(r) \\
&= L_p(r)\cdot R_p(r) + L_s(r)\cdot R_s(r)
\end{aligned} \tag{A.1}
$$

$$
\sigma_{h,syst}(h) = \sigma_{h,syst,0}(h) + \frac{\partial\sigma_{h,syst}}{\partial\sigma_{x_0}}(h)\cdot\sigma_{x_0} + \frac{\partial\sigma_{h,syst}}{\partial\sigma_{r_{max}}}(h)\cdot\sigma_{r_{max}} + \frac{\partial\sigma_{h,syst}}{\partial\sigma_{n_{medium}}}(h)\cdot\sigma_{n_{medium}} \tag{A.2}
$$

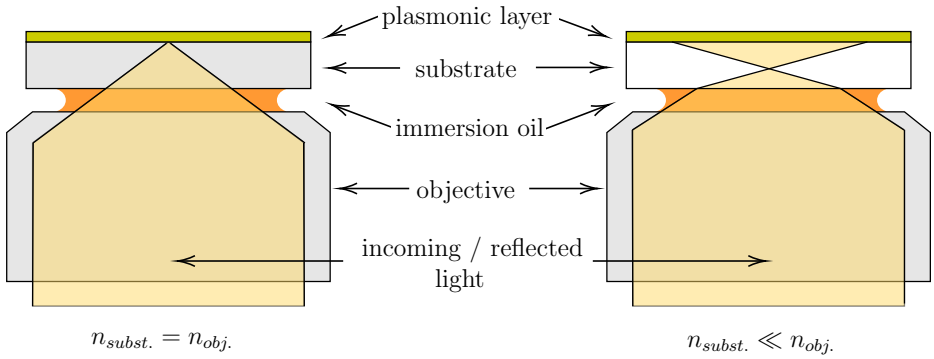


Figure A.1.: Illustration of the working distance adjusting role of cover glass and immersion oil. The case of index-matched objective, cover glass and immersion oil is shown on the left. The effect of a cover glass with lower RI is shown on the right.

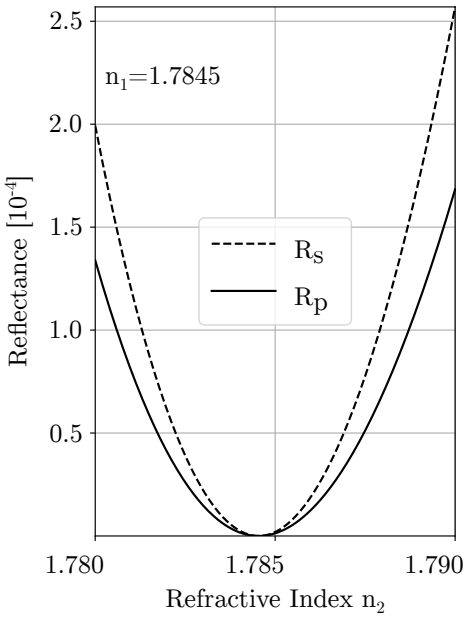
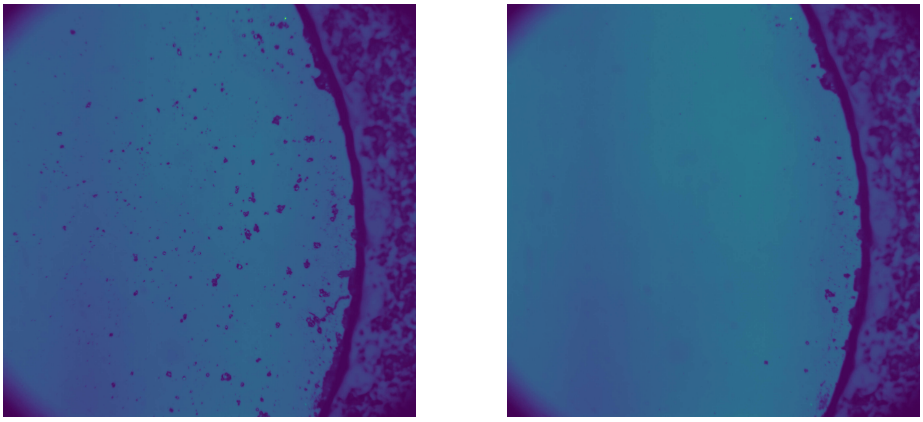
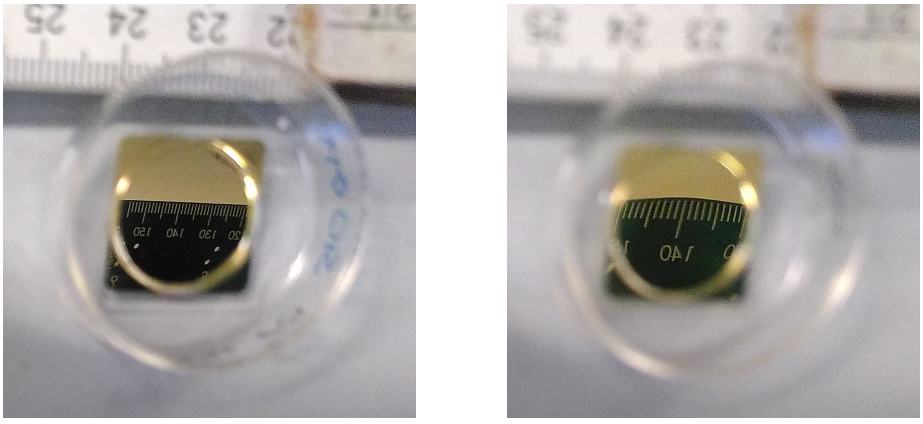


Figure A.2.: Plot of remaining reflectance between objective and cover glass, depending on RI matching, for p- and s-polarized light. Ideal RI matching ($n_1 = n_2$) results in zero reflectance. Curves were calculated using Fresnel equations.



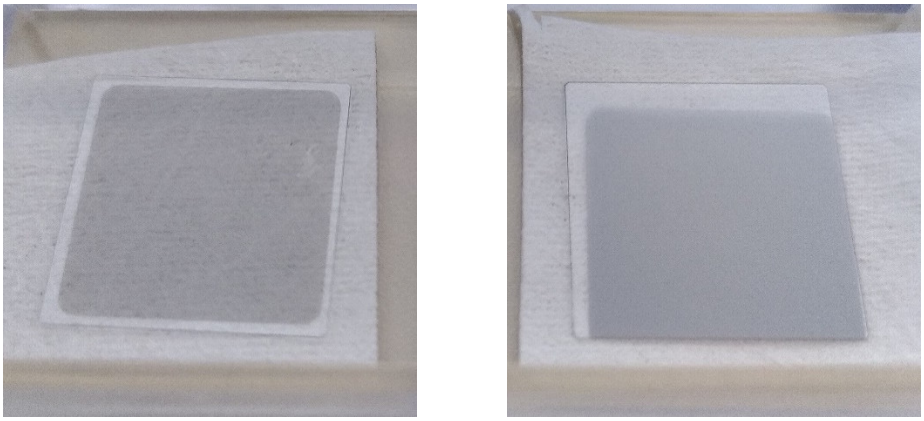
(a) Objective before cleaning **(b)** Objective after cleaning

Figure A.3.: Top camera view of the objective before and after cleaning. Part of a rather dirty lens surface is shown in (a). The same part is much cleaner in (b) after a single gentle cleaning with a cotton swab soaked in isopropanol.



(a) no visible substrate curvature **(b)** significant substrate curvature

Figure A.4.: Image of two Au substrate SPRM sensors, with and without thermally induced substrate curvature. A sensor assembled using the alternative room temperature curing protocol for the optical adhesive is shown in (a). A sensor cured at the recommended 60 C curing protocol with significant substrate curvature is shown in (b). It is assumed that the plastic Petri dish deforms at the higher temperature.



(a) high quality vacuum Cr layer **(b)** low quality vacuum Cr layer

Figure A.5.: Photographs showing the visible thickness difference between two Cr coatings produced at different vacuum qualities. For the sample in (a), vacuum was generated for over 2 h. For the sample in (b) vacuum was generated for less than 1 h. AFM determined Cr layer thicknesses discussed in section 3.4.1 also indicate that insufficient vacuum quality might cause an increase in Cr layer thickness.

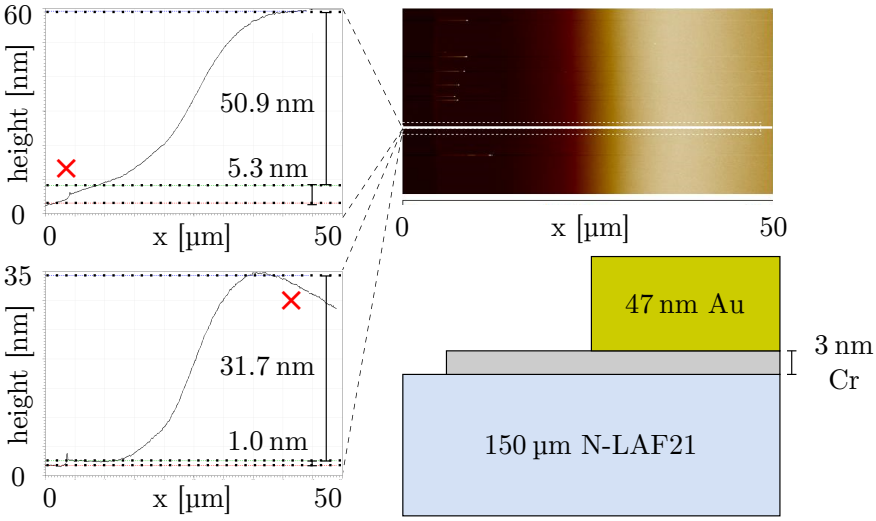


Figure A.6.: AFM measurement of substrate layer thickness. A sketch of the stepped substrate sample for thickness measurements is shown in the lower right. An example scan (subst. 2) is shown above. On the left, two profiles through the scan area are compared after alternative polynomial background subtraction results, leading to unacceptably large differences in the resulting layer thicknesses. It can be seen that both profiles still show a residual (background) height gradient after background subtraction, either on the far left (N-LAF21) or on the far right (Au), as marked by the red cross. Therefore, it was decided to specify the range between the respective layer thickness values in table 5.1.

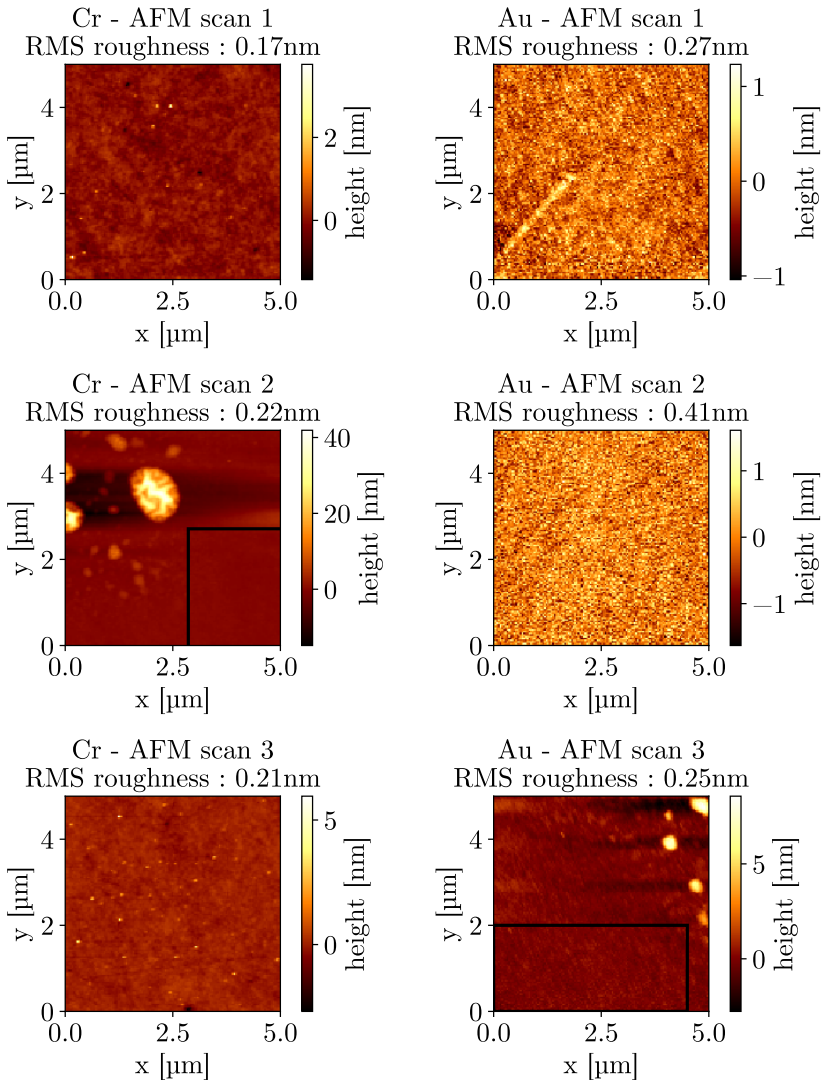
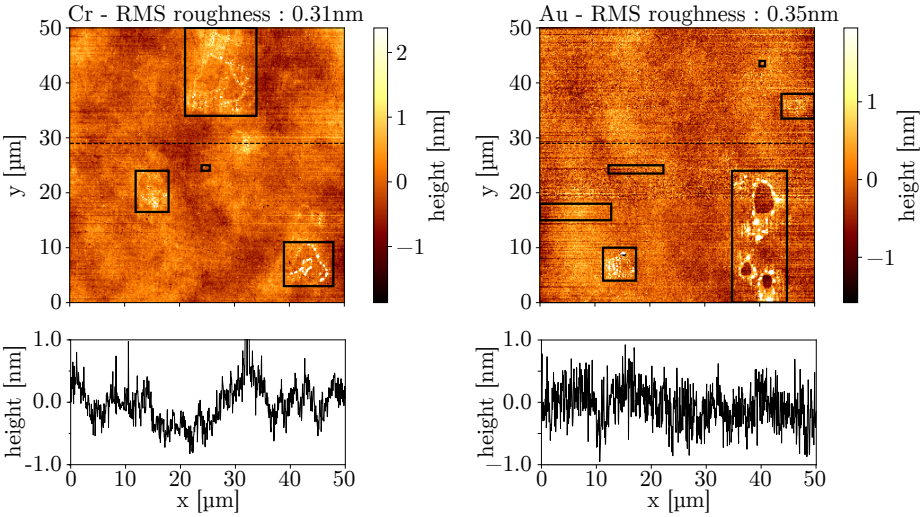
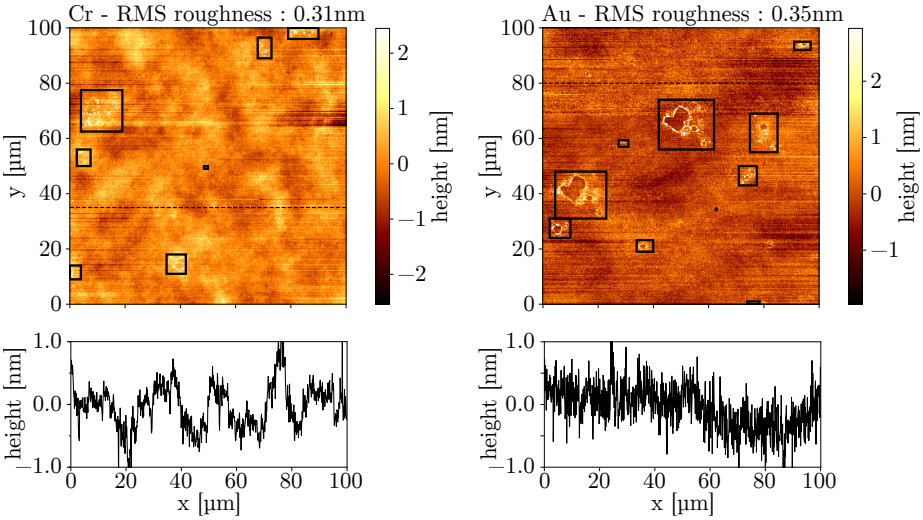


Figure A.7.: AFM measurements (5 µm x 5 µm) of Cr- and Au-layer topography. The measurements in the left column were taken at three different locations on a Cr-coated substrate. The measurements in the right column were taken at three different locations on a Cr-,Au-coated substrate. The RMS roughness was determined for each scan. Cr-scan 2 and Au-scan 3 show some artifacts, therefore the RMS roughness was determined only in the black outlined rectangular areas.



(a) 50 µm x 50 µm, Cr (left) and Au (right)



(b) 100 µm x 100 µm, Cr (left) and Au (right)

Figure A.8.: AFM measurements over 50 µm x 50 µm (top) and 100 µm x 100 µm (bottom) of Cr- (left) and Au- (right) layer topography. Measurements depict the same substrates as in fig. A.8a, but at different locations. The RMS roughness is given for all scans, calculated in visible areas, excluding black outlined rectangular regions. The color scale is clipped to height fluctuations of interest. Height profiles along dashed black lines are shown in respective plots below.

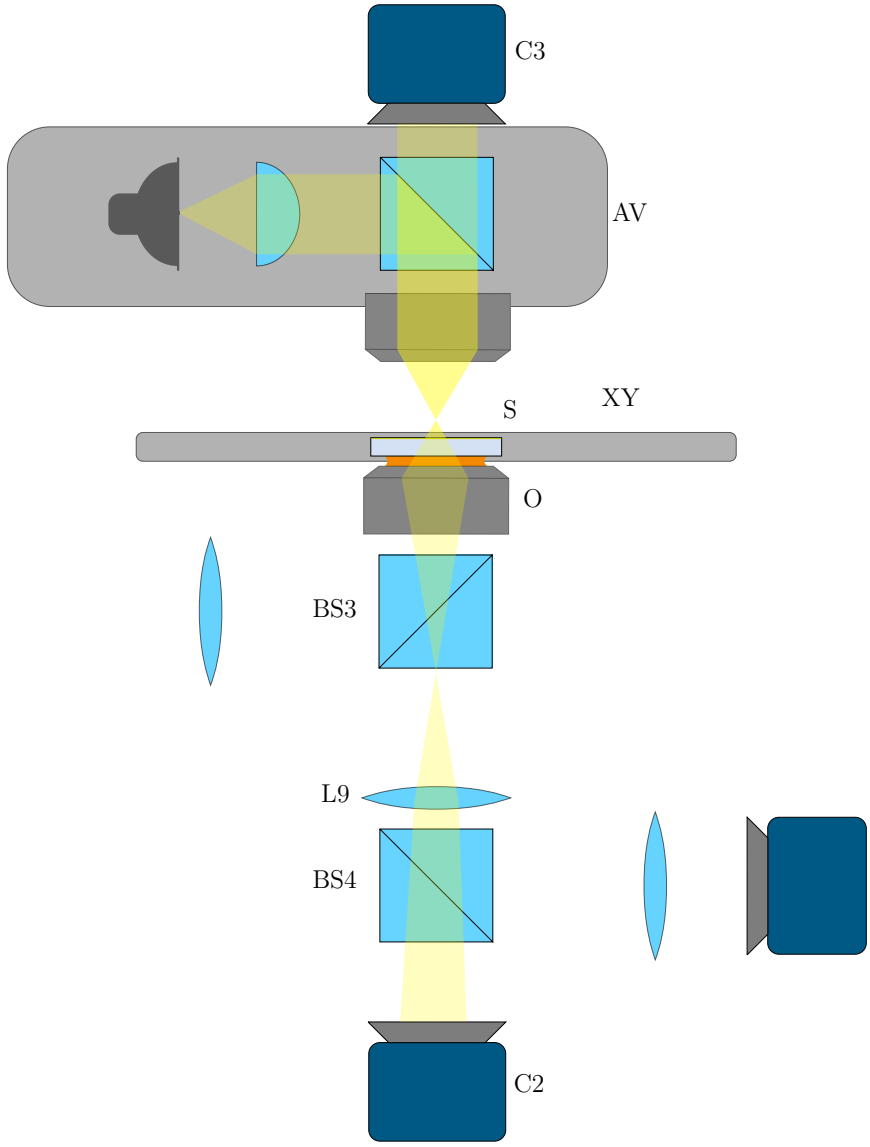


Figure A.9.: Sketch of halogen illumination light paths for top camera reflection mode imaging and OP camera transmission mode (brightfield) imaging. Elements are labelled as lenses (L#), beam splitters (BS#), cameras (C#), objective (OL), sample (S), scanning stage (XY) and Axiotech Vario (AV). Labelling and numbering correspond to fig. 4.1 and [123, Ch. 4].

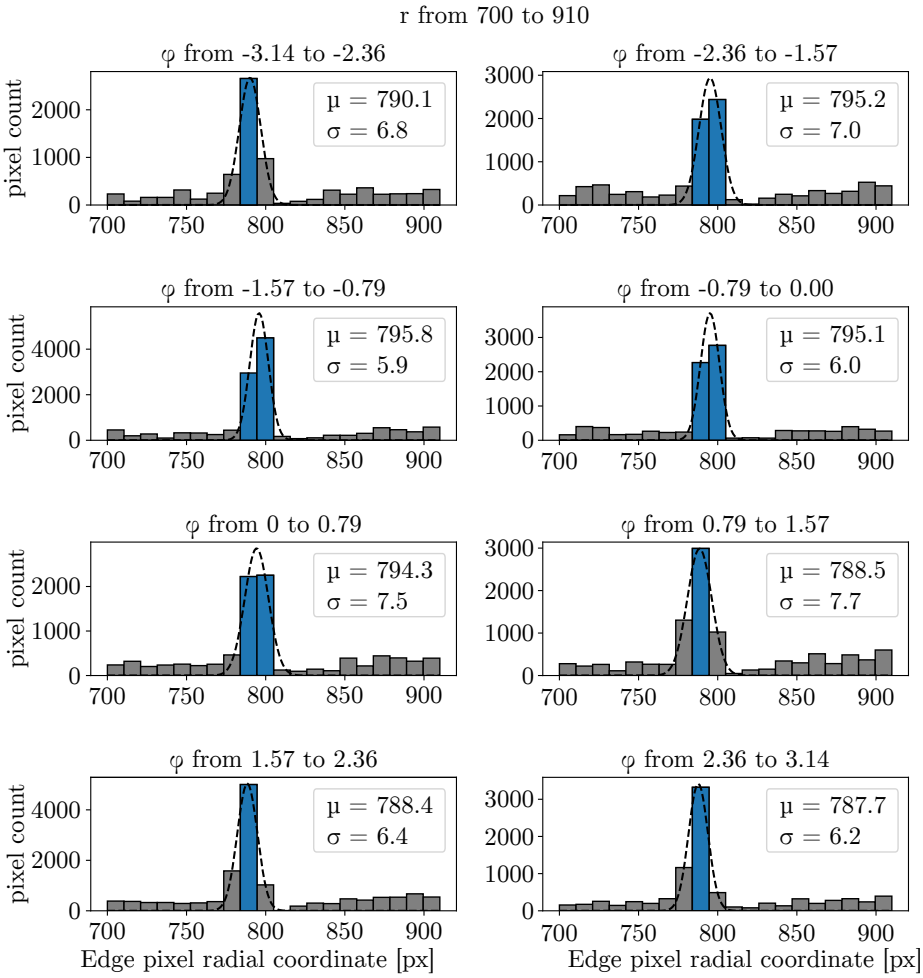


Figure A.10.: Radial coordinate distribution of detected edge pixels (see fig. 4.4e) around the radial position of SPR minimum in multiple angular segments. A Gaussian fit is performed on each segment distribution and helps to classify edges as SPR-minimum (blue) or noise (grey). Using these colors, the classification of pixels from fig. 4.4e is also shown in fig. 4.4f. *The classification boundaries do not coincide with the histogram binning. The use of color in histogram bars is merely a visual aid to illustrate the concept.*

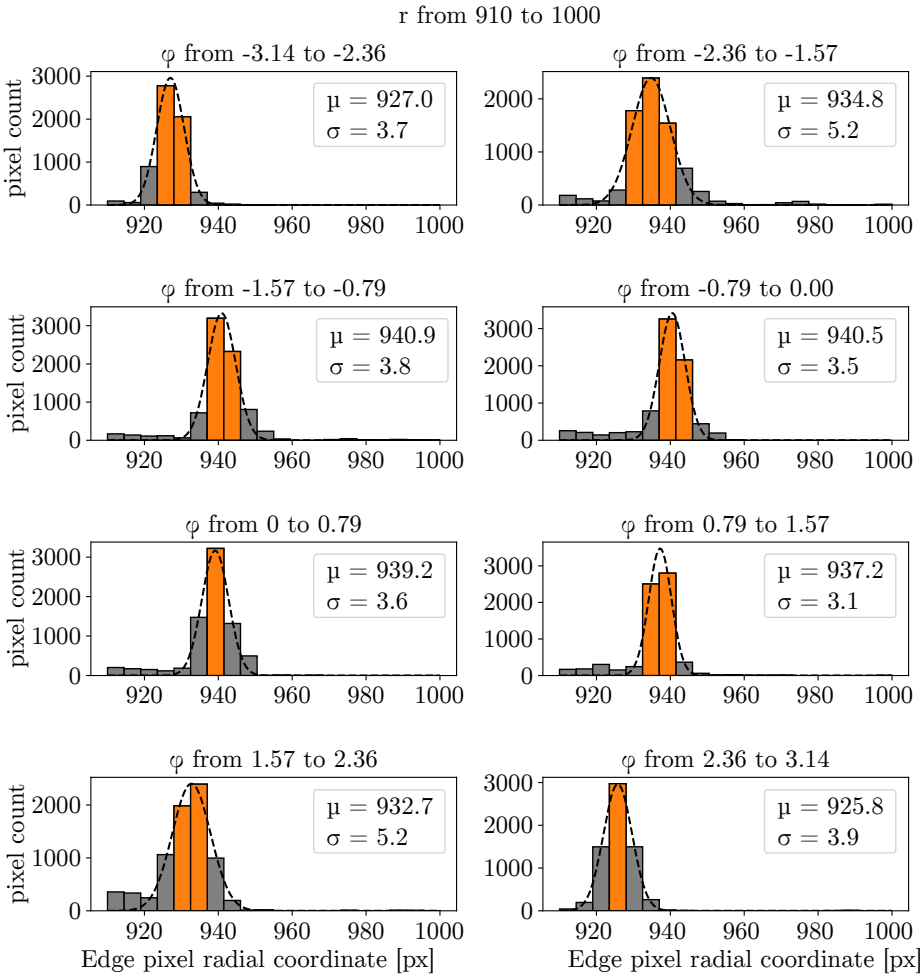


Figure A.11.: Radial coordinate distribution of detected edge pixels (see fig. 4.4e) around the radial position of aperture in multiple angular segments. A Gaussian fit is performed on each segment distribution and helps to classify edges as aperture (orange) or noise (grey). Using these colors, the classification of pixels from fig. 4.4e is also shown in fig. 4.4f. *The classification boundaries do not coincide with the histogram binning. The use of color in histogram bars is merely a visual aid to illustrate the concept.*

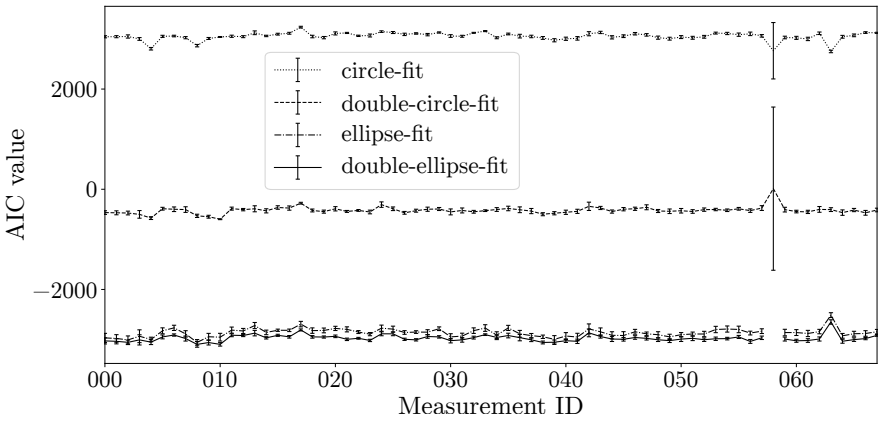


Figure A.12.: Distribution of AIC values for the four BFP image aperture fitting models compared. As lower AIC values indicate better fits, taking into account the trade-off between model accuracy and model complexity, the double ellipse model is regarded as the best model among candidates. The measurement IDs over which AIC values have been calculated are plotted on the x-axis and listed in table A.1.

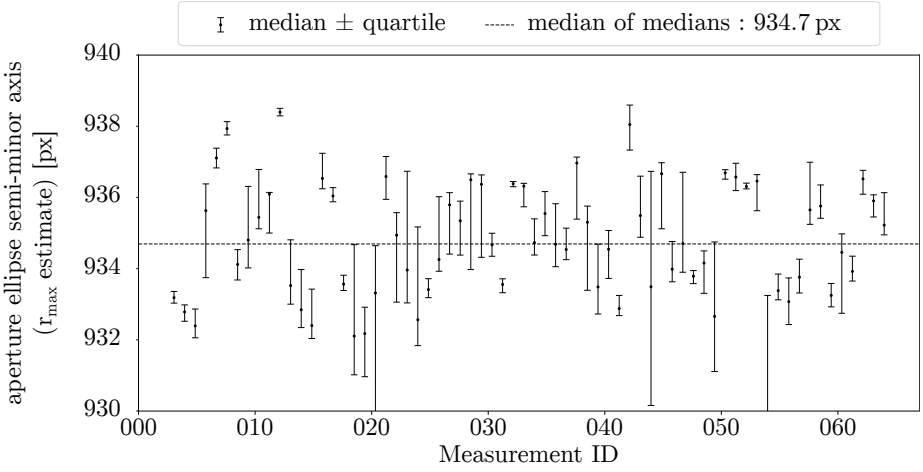


Figure A.13.: Distribution of the aperture size parameter r_{max}, extracted as semi-minor ellipse axis from the double ellipse model. Median values are represented by dot markers, upper and lower error bar caps represent first and third quartiles. The median of median values is drawn as dashed horizontal line. The measurement IDs over which r_{max} has been calculated are plotted on the x-axis and listed in table A.1.

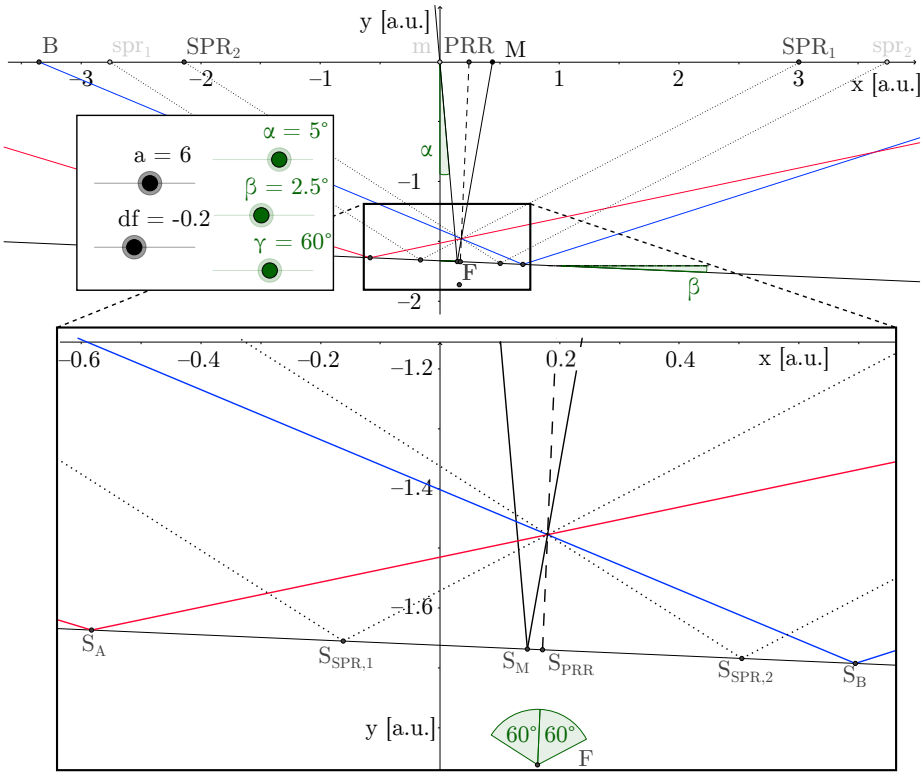


Figure A.14.: A geometrical construction of relevant light rays at the sample interface. It is assumed that the objective is an ideal lens aligned with the x-axis, with its center located at the origin (0,0). The width of the objective aperture is set to a value of a=6, expressed in an unspecified unit of measurement. An incident parallel beam of light (wider than the aperture) enters from above at an angle of α=5° and is focused towards the spot F. The sample plane at which the beam is reflected has an angle of β=2.5° to the horizontal. In this hypothetical scenario, the SPR angle is set to γ=60°. The unitless vertical distance between the sample plane and the focal plane is set to be df=-0.2. The blue and red lines represent the leftmost and rightmost beams that pass through the aperture, respectively. The black dotted lines represent partial rays that are reflected under the SPR angle. The solid black line represents the partial ray that initially passes through the middle of the lens. The black dashed line represents the beam that is perpendicularly reflected.

Figure A.15.: Overview of all determined PRP coordinates in example measurement MID007 together with possible aggregate values. The main plot on the top left visualizes both coordinates together. The secondary plots to the right and bottom visualize one coordinate each in sequential order, revealing oscillations in sync with the oscillatory snake scan pattern. Black markers represent individual PRP coordinates determined as ellipse centers from SPR ellipse fits (see section 4.2.3). Colored markers represent different ways of aggregation, as indicated in the lower right legend. The "optimized" aggregation refers to the refined PRP coordinates, as explained in section 4.3.3

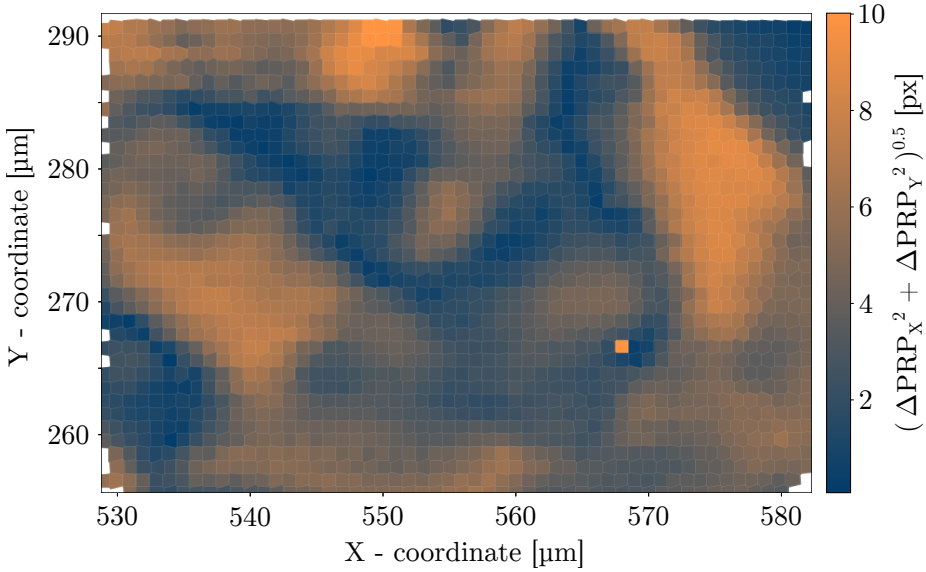


Figure A.16.: Spatial mapping of PRP coordinate deviation from mean values for example measurement MID007.

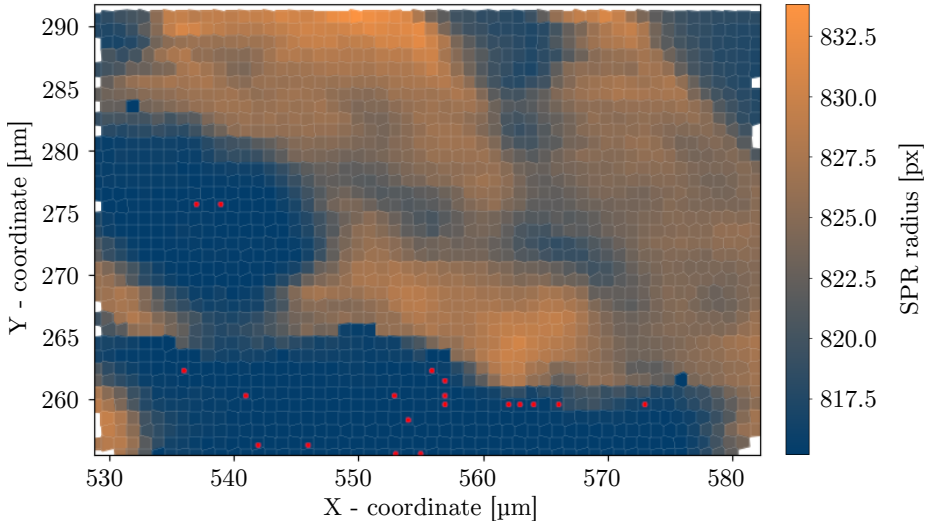


Figure A.17.: Spatial mapping of (top BFP segment) SPR radii, visualizing the selection of control measurement spots to find substrate parameters. Spots with a predicted SPR radius below the first percentile are marked in red. A median intensity profile is generated from these spots for substrate parameter optimization.

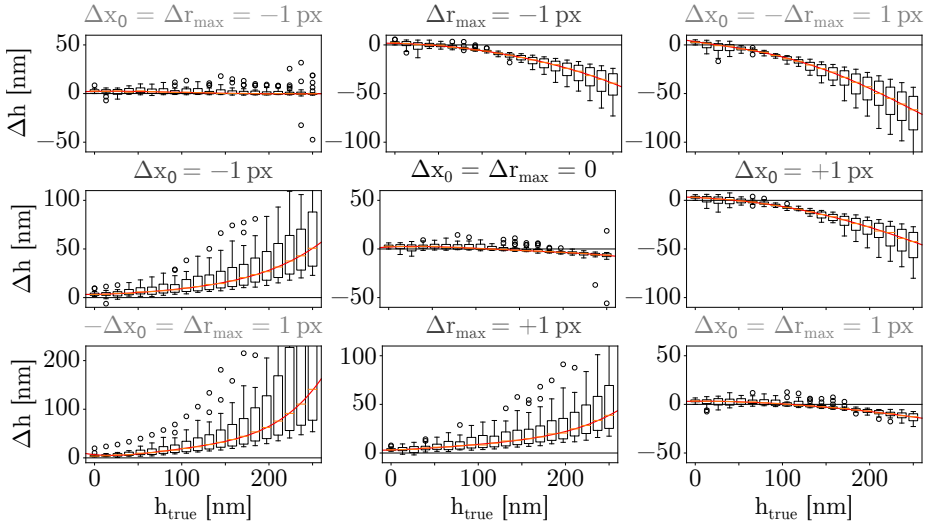


Figure A.18.: Overview of cell-substrate distance errors in the evaluation of a simulated data set (cell on SiO_2 sensor), showing the error propagation of the BFP parameters x_0 and r_{max}. The data is simulated and evaluated for a grid of 20 cell-substrate distances (h_{true}) and 20 cytoplasm RI values, as shown in fig. A.20. Such a simulated grid is then projected onto the h_{true}-axis, showing the cytoplasm RI dependent distribution of $\Delta h = h - h_{true}$ as a box plot. A polynomial fit of the median values is plotted on top as a red line. Each of the 3x3 plots visualizes a pair of x_0 error ($\Delta x_0 = x_{0,true} - x_0$) and r_{max} error ($\Delta r_{max} = r_{max,true} - r_{max}$) present in the corresponding analysis. The middle plot corresponds to an evaluation without error in x_0 and r_{max}. It can be seen that the effects of Δx_0 and Δr_{max} cancel when they have the same sign. Figure 5.13 gives an overview of the median error contributions for the four main sample types used in this work. It is noteworthy that these analyses are performed on a single BFP segment only (in the positive x direction within the BFP). Performing these analyses on a segment in y-direction yields much smaller Δx_0-dependent errors. Performing these analyses on all 4 segments combined eliminates Δx_0 (and Δy_0) dependent error contributions altogether ($|\Delta h/\Delta x_0| < 0.1\,\mathrm{nm\,px^{-1}}$).

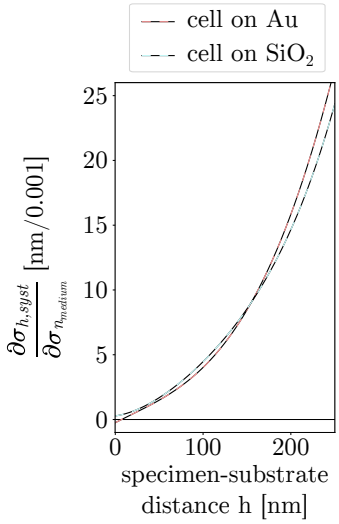


Figure A.19.: Up to linear contribution to the median systematic cell-substrate distance error, depending on the error in cell medium RI, when evaluating simulated (noise-free) data sets for both substrate types (Au/SiO_2).

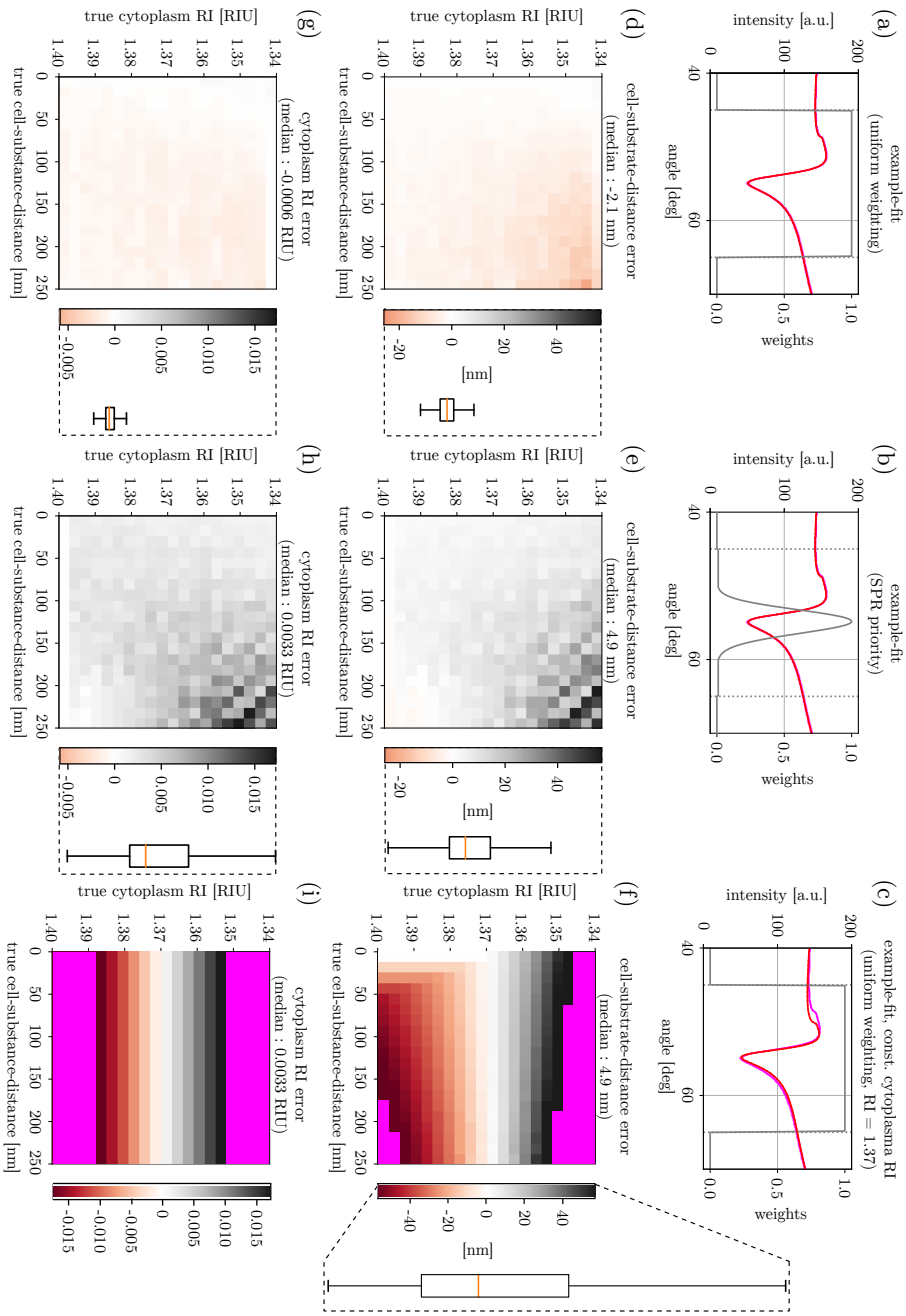

(a)
example-fit
(uniform weighting)
intensity [a.u.]
angle [deg]
weights
(b)
example-fit
(SPR priority)
(c)
example-fit, const. cytoplasma RI
(uniform weighting, RI = 1.37)
(d)
cell-substrate-distance error
(median : -2.1 nm)
true cytoplasm RI [RIU]
true cell-substance-distance [nm]
[nm]
(e)
cell-substrate-distance error
(median : 4.9 nm)
(f)
cell-substrate-distance error
(median : 4.9 nm)
(g)
cytoplasm RI error
(median : -0.0006 RIU)
(h)
cytoplasm RI error
(median : 0.0033 RIU)
(i)
cytoplasm RI error
(median : 0.0033 RIU)

Figure A.20.: Visualization of deviations from ground truth cell-substrate interface parameters for different weighting and fitting methods, using a simulated noise-free dataset (Cell on SiO_2 sensor). Example SPR reflectance curves and weighting functions are shown in (a) for uniform weighting and (b) for Gaussian weighting. The deviation between the analysis output and ground truth cell-substrate distance values is color coded in the 2D plot in (d) for uniform weighting and (e) for Gaussian weighting. The simulated dataset contains cell-substrate distances from 0 to 250 nm and cytoplasmic RI values from 1.34 to 1.40, arranged in a grid as indicated on all 2D plot axes. Box plots (IQR $\pm$ 1.5 IQR, see matplotlib [61] documentation for version 3.6.2) next to the color scale visualize the corresponding distributions. Similarly, the deviation between the analysis output and ground truth cytoplasm RI values is shown in (g) for uniform weighting and (h) for Gaussian weighting. The example of a uniform weighting fit assuming a constant cytoplasmic RI value of 1.37 is shown in (c). The obtained differences between the analysis output and ground truth cell-substrate distance values up to 100 nm are color coded (for consistency only up to 50) in (f), these deviations result from ignored deviations in the cytoplasm RI shown in (i).

It is evident that uniform weighting fits are better at predicting cell-substrate-interface parameters when noise-free data are available. The resulting parameters from Gaussian weighting fits are less accurate due to the lack of reflectance information around the critical angle of total reflection. However, both weighting methods show the largest absolute deviations from ground truth values only for the largest cell-substrate distances paired with the largest cytoplasmic RI values. The analysis of the simulated data set assuming a constant cytoplasmic RI highlights the critical role of considering cytoplasmic RI variations within cells, as previously argued by Kreysing et al. 2018 [108].

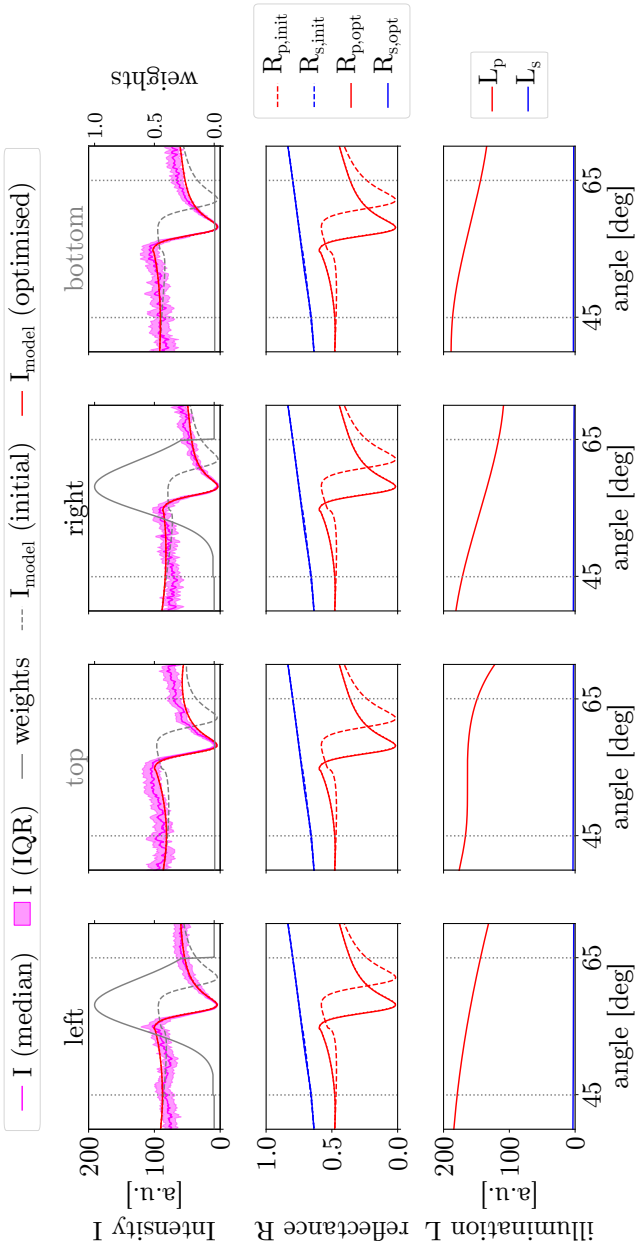


Figure A.21.: Example fit of SPRM reflectance data with Gaussian weighting. Displayed data and fit belong to a single scan point from measurement MID075. Each column corresponds to a BFP image segment as labeled above. The first row shows the measured and modeled light intensity together with a plot of the Gaussian weight distribution. Since only data from the left and right segments were fitted, weights for the top and bottom segments are zero. The second row displays model reflectance values for p- and s-polarized light before and after data fitting. The third row displays p- and s-polarized reference illumination, as determined from a reference intensity measurement. As is typical for SiO_2 sensors, the critical angle of total reflection cannot be determined from the intensity and reflectance curves.

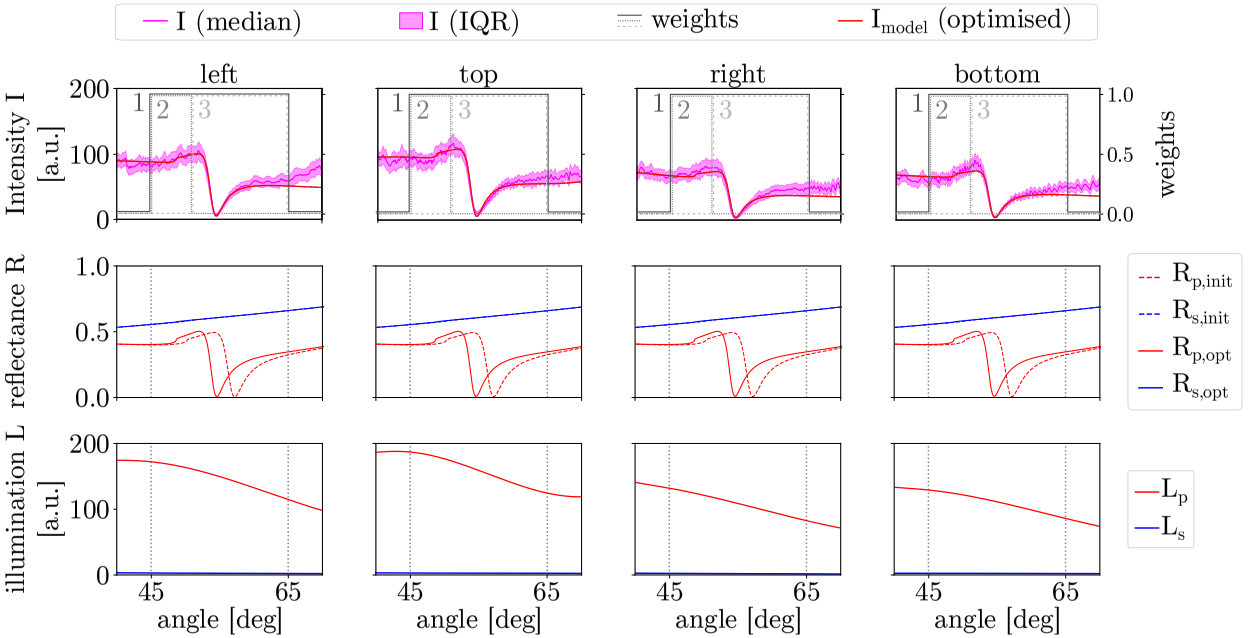


Figure A.22.: Example fit of SPRM reflectance data with uniform weighting carried out in three steps. Displayed data and fit belong to a single scan point from measurement MID090. Each column corresponds to a BFP image segment as labeled above. The first row shows the measured and modeled light intensity, along with a plot of the uniform weighting distribution in each of the three steps. The second row displays model reflectance values for p- and s-polarized light before and after data fitting. The third row displays p- and s-polarized reference illumination, as determined from a reference intensity measurement. As is typical for Au sensors, the critical angle of total reflection can be seen in the intensity and reflectance curves (peak in the first derivative of reflectance at approximately 50 deg angle).

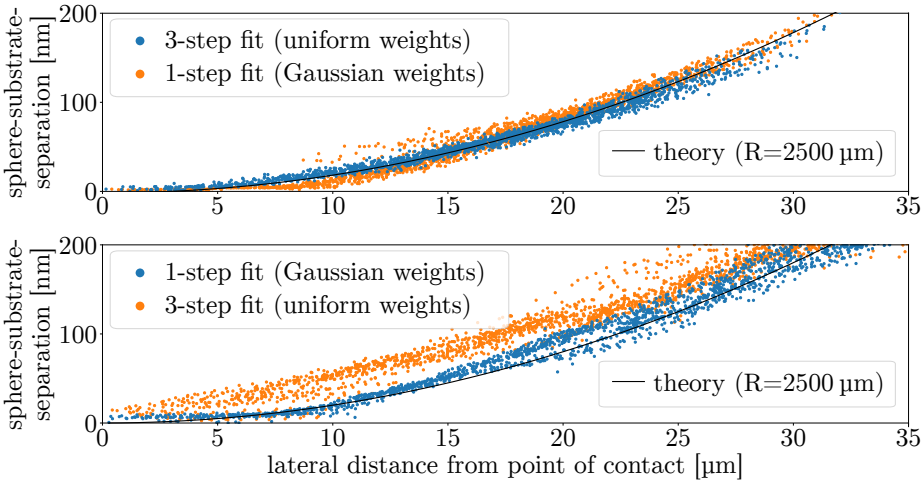


Figure A.23.: Evaluation of both sphere-to-substrate distance validation measurements with comparison of both fit algorithms on each. Whilst it can be seen that the MID074 measurement (above) can be evaluated by both algorithms, the 3-step (uniform weights) algorithm performs better, particularly in determining small sphere-substrate distances. For measurement MID075 (bottom) it can be seen that a meaningful analysis is not possible with the 3-step (uniform weights) algorithm, but therefore with the 1-step (Gaussian weights) algorithm.

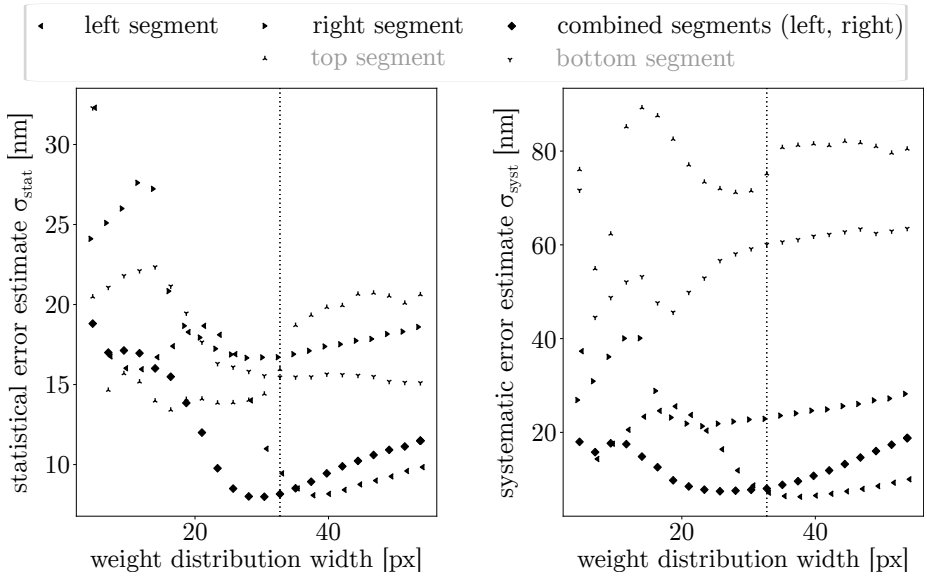


Figure A.24.: Estimated errors of single-fit (Gaussian weighting) evaluation of the MID075 sphere-on-SiO_2 validation measurement, depending on weighting distribution width. Mean statistical errors (left plot) and mean absolute systematic errors (right plot) are calculated as compact indicators of sphere-substrate distance dependent error estimates (shown in fig. 5.10). The widths of the Gaussian weighting distributions are given on the x-axis. Different markers indicate the analyzed BFP segment(s). The dotted vertical line indicates the selected distribution width in the analysis of measurements MID001-MID068.

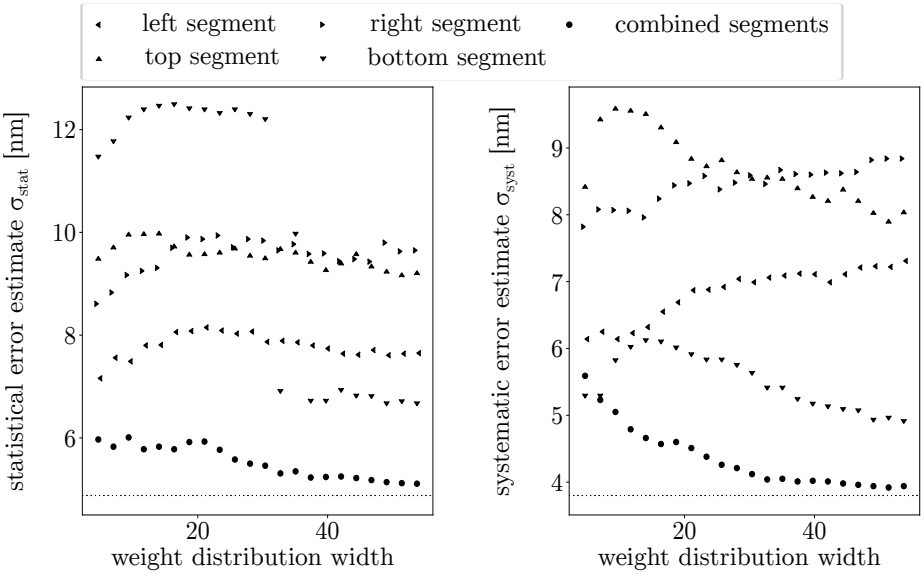


Figure A.25.: Estimated errors of single-fit (Gaussian weighting) evaluation of the MID074 sphere-on-Au validation measurement, depending on weighting distribution width. Mean statistical errors (left plot) and mean absolute systematic errors (right plot) are calculated as compact indicators of sphere-substrate distance dependent error estimates (shown in fig. 5.7). The widths of the Gaussian weighting distributions are given on the x-axis. Different markers indicate the analyzed BFP segment(s). The dotted horizontal line indicates the calculated error estimate in the case of a combined segment analysis with uniform weighting (infinite distribution width).

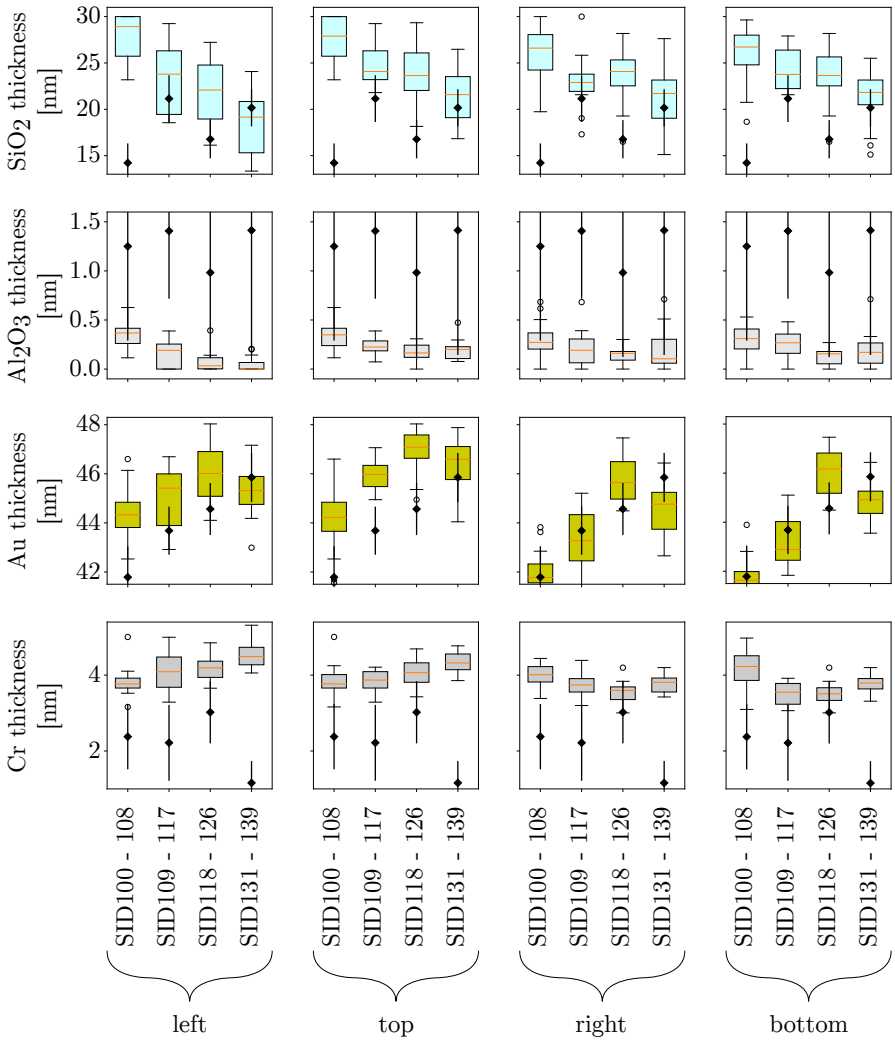
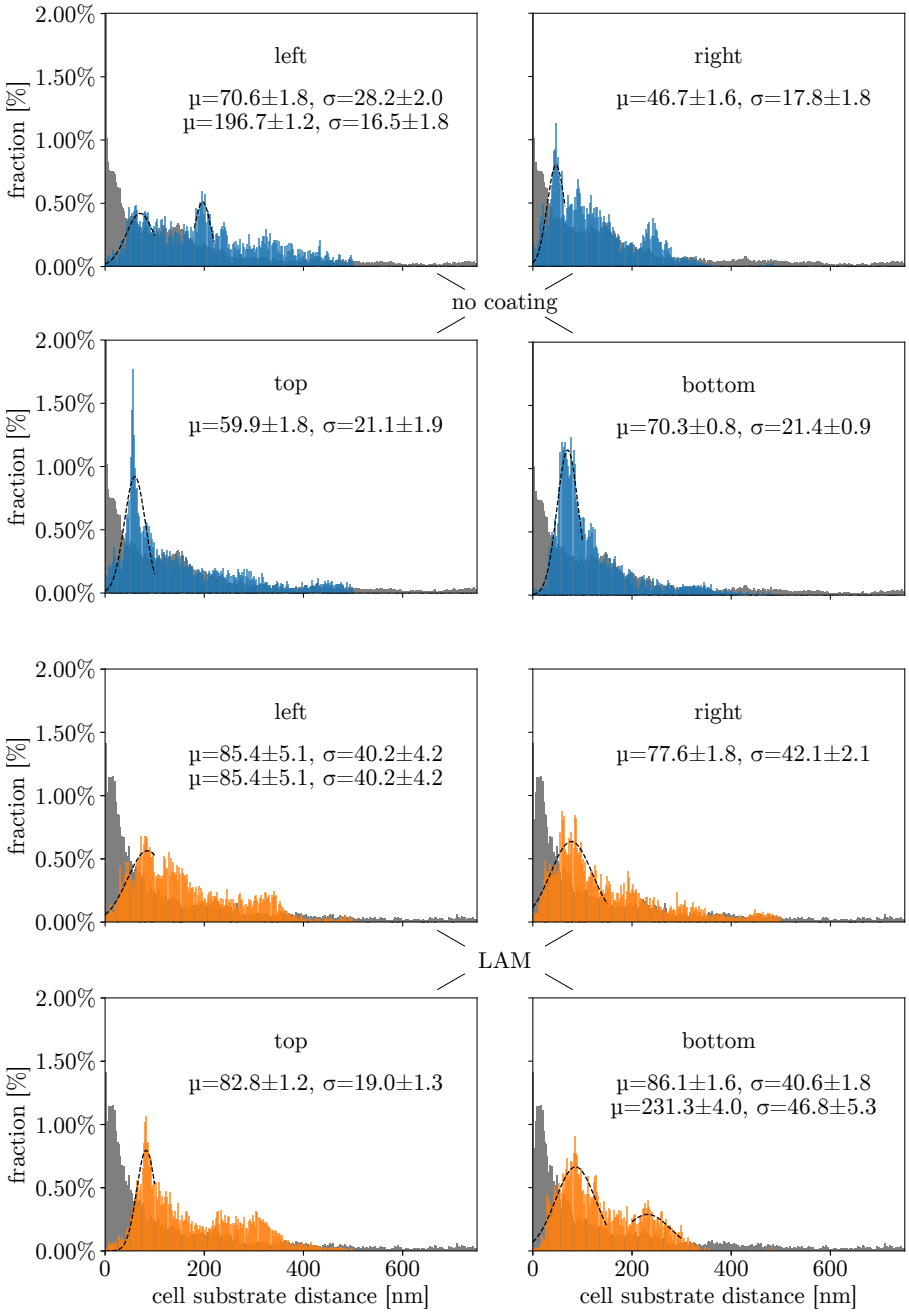
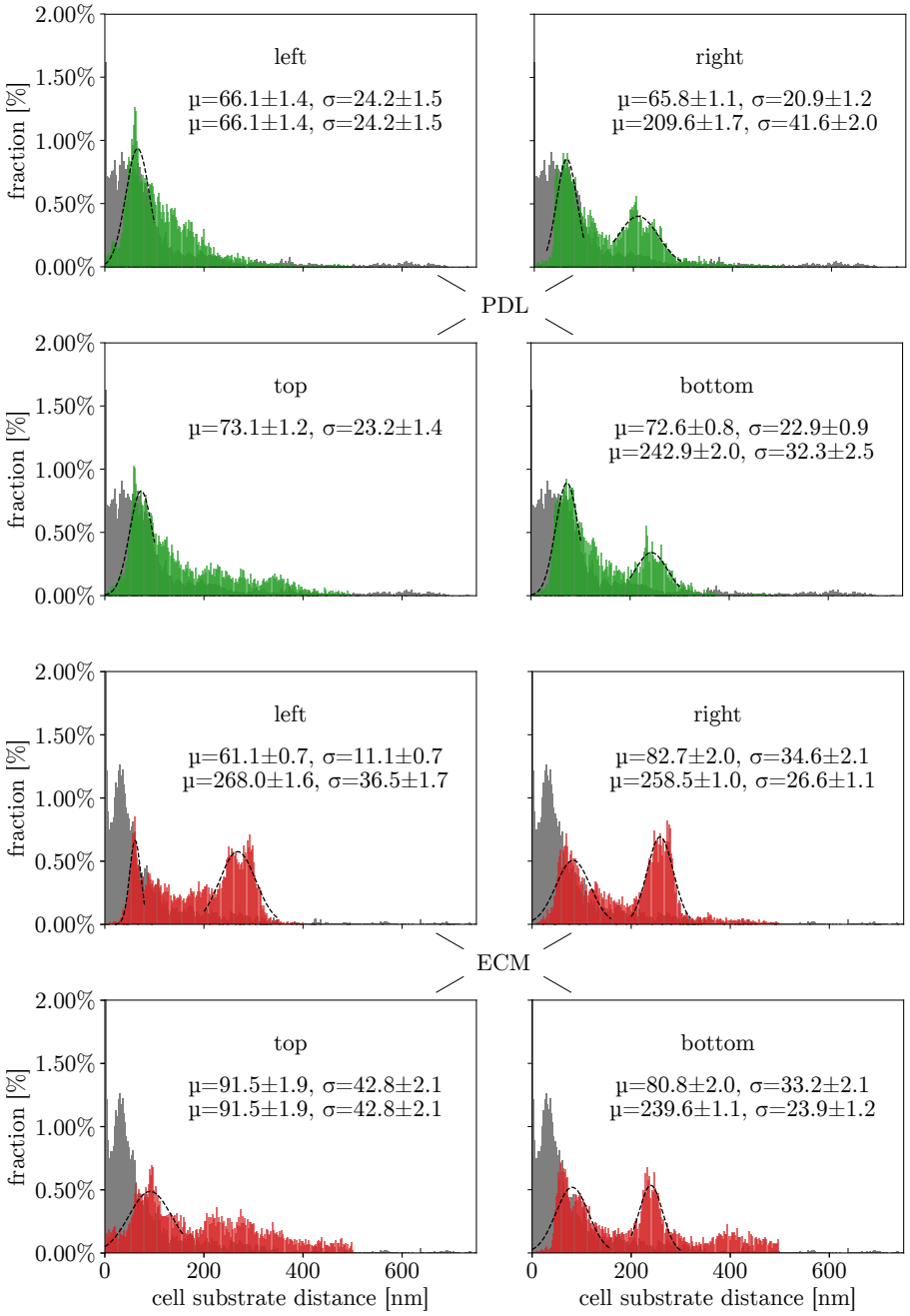


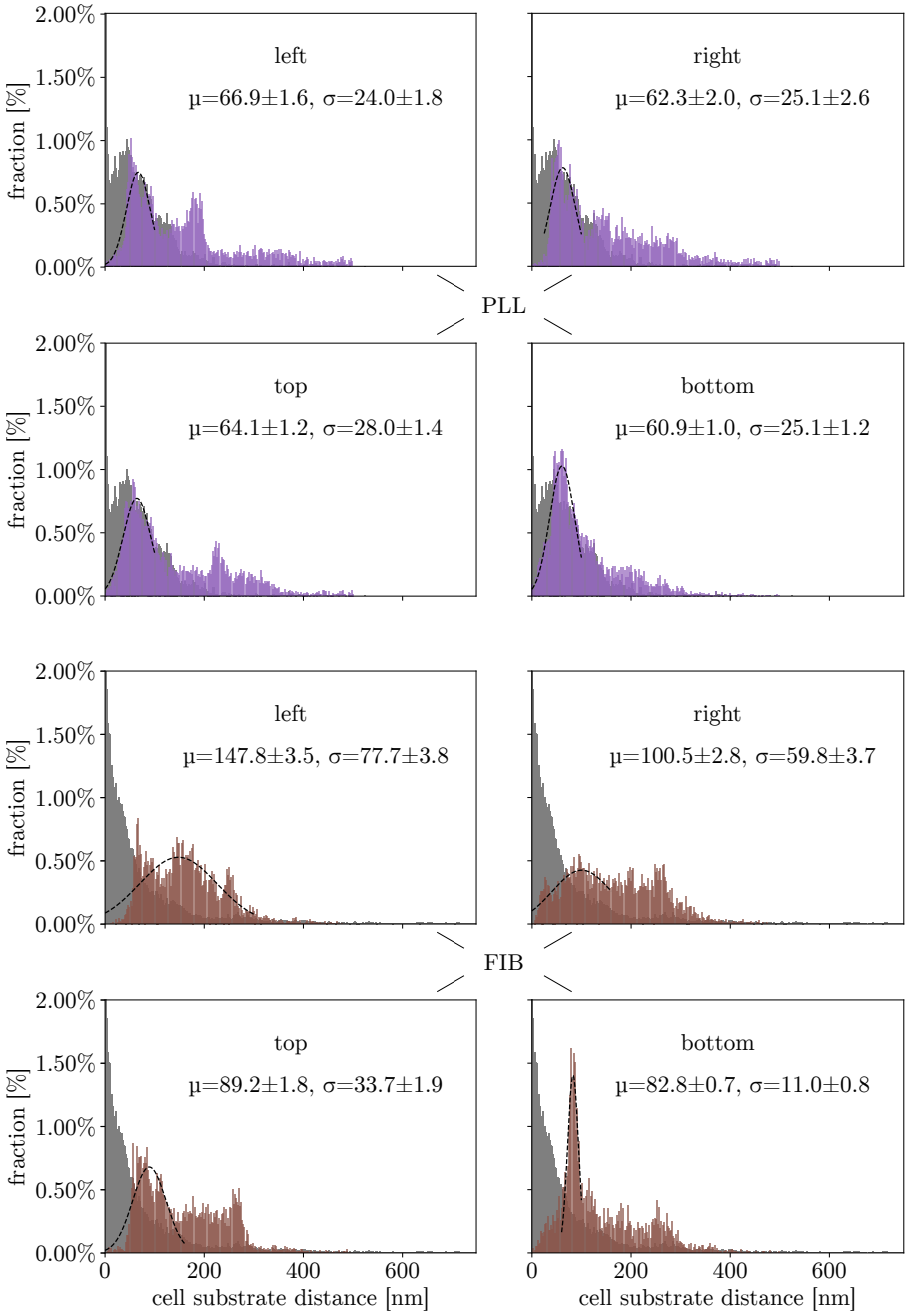
Figure A.26.: SiO_2 Substrate layer thicknesses determined by SPRM and XRR. Each row of plots corresponds to one of the substrate layers Cr, Au, Al_2O_3 and SiO_2. Each column of plots corresponds to the BFP segment (left, top, right, bottom) in which the SPRM analysis is performed. For each measurement in table A.1, an SPRM analysis of the substrate layer thicknesses is performed from automatically determined 'control' measurement spots. The distribution of these values is represented by box plots (IQR $\pm$ 1.5 IQR, see matplotlib [61] documentation for version 3.6.2). For each batch of substrates (substrate ids indicated on the x-axis) one substrate was used for XRR characterization. The XRR determined mean layer thicknesses and RMS roughness values are indicated by the black diamond markers and corresponding error bars.



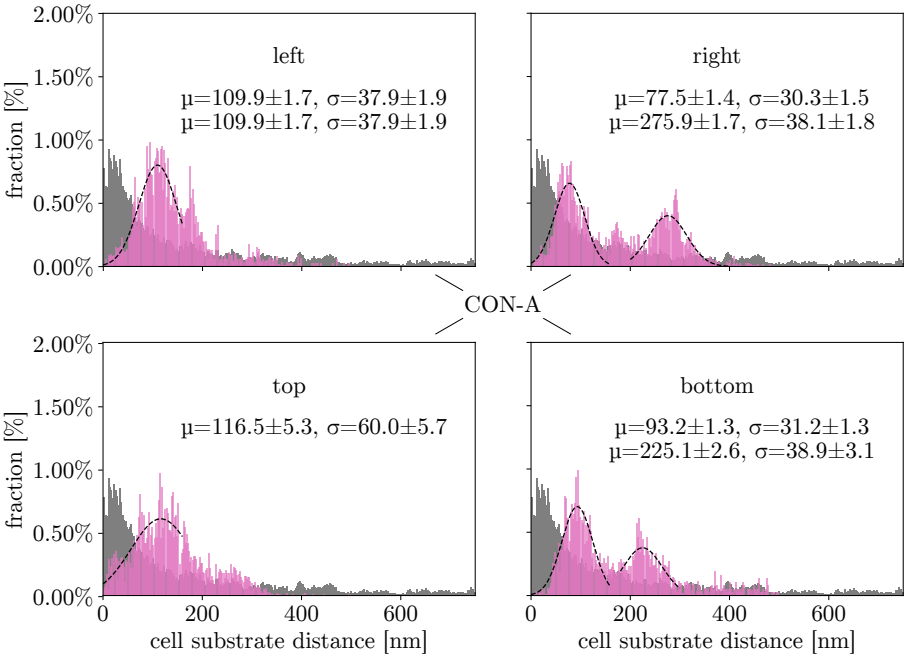
(a) Cell-substrate distances by BFP segment. (no coating, laminin)



(b) Cell-substrate distances by BFP segment. (PDL, ECM gel)

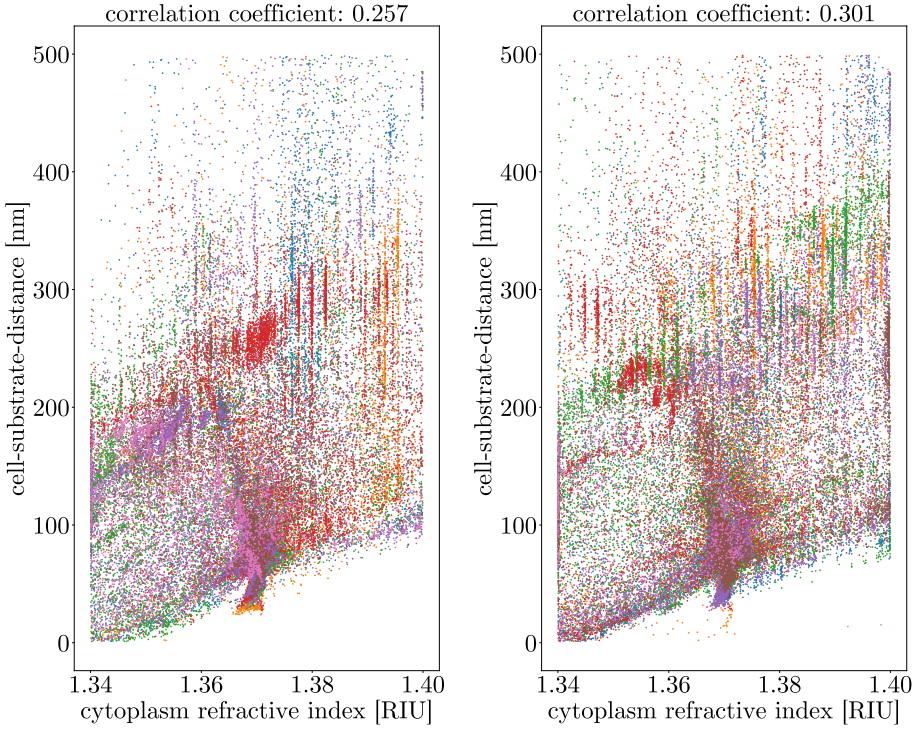


(c) Cell-substrate distances by BFP segment. (PLL, fibronectin)



(d) Cell-substrate distances by BFP segment. (concanavalin-A)

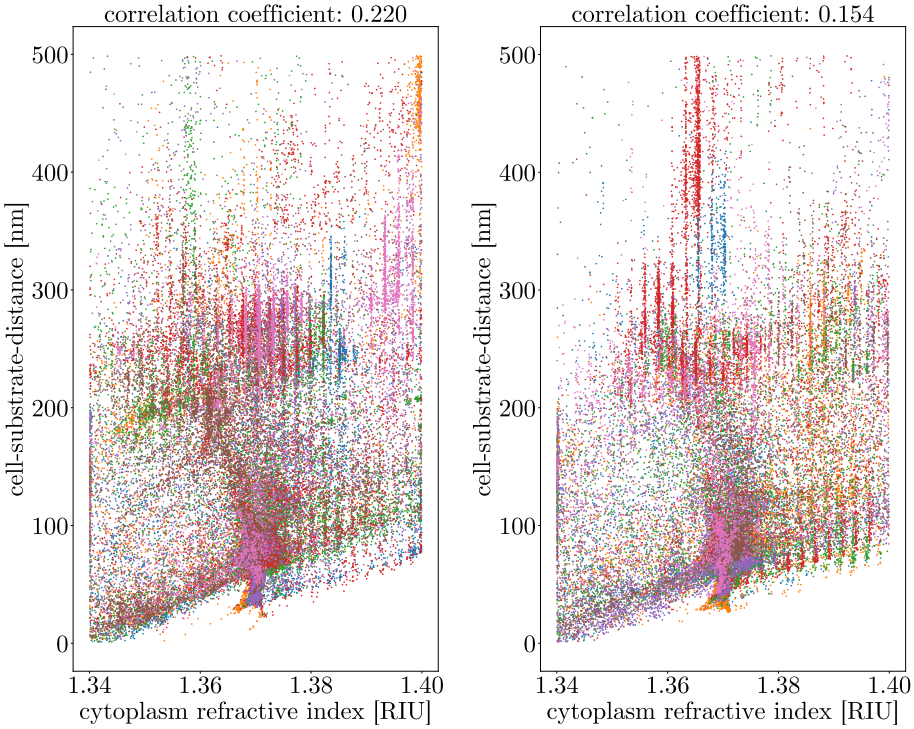
Figure A.27.: Histograms of cell-substrate distances by BFP segment and by coating. Colored bars summarize HEK293 measurements in non-masked areas. Data points from different cell measurements are weighted by scanned pixel areas to ensure uniform weighting of all imaged cell areas, unbiased by scan resolution. Gaussian curves are fitted in manually selected ranges. Mean values μ and widths σ of fitted peaks are given in the graphs. Grey histograms in the background summarize TEM measurements from Wrobel 2008 [65].



(a) Evaluation of left BFP segments.

(b) Evaluation of top BFP segments.

Figure A.28.: Scatter plots of all determined but unmasked HEK293 cell-substrate-distance - cytoplasm-RI pairs to visualize the parameter distribution from raw data of the left and top BFP segment. The correlation coefficient has been calculated and is shown above each plot.



(a) Evaluation of right BFP segments.

(b) Evaluation of bottom BFP segments.

Figure A.29.: Same visualization as in fig. A.28, but for parameters from the raw data of the right and bottom BFP segments. It is noticeable that in all BFP segment analyses (left, top, right, bottom) no close cell-substrate-contacts with high refractive index are detected.

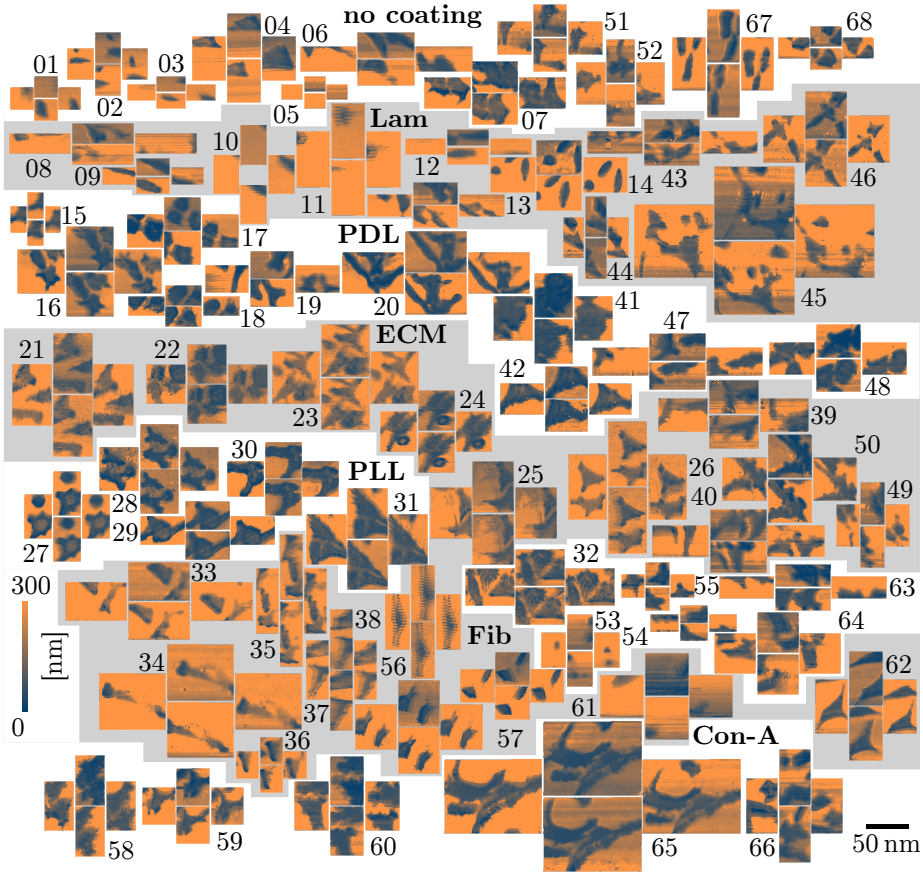


Figure A.30.: Color plots of cell-substrate distances from all 68 HEK293 measurements (color scale up to 300 nm). There are four plots for each measurement, representing the results of the analysis of the left, top, right and bottom BFP segments. The plots are grouped by surface coating. The measurements are numbered from MID001 (01) to MID068 (68). The color scale at the bottom left and the scale at the bottom right are applicable to all plots. It can be seen that the cell-substrate distance reaches the upper limit of the color scale in areas outside any cell. Cell-substrate distances of (300-500) nm were allowed in the parameter optimization, but are not resolved in the color scale, as such high values cannot be reliably determined by SPRM, and also to allow a higher resolution in the range (0-300) nm. An illustration of the full color coding of the optimization results from (0-500) nm is shown in fig. A.35.

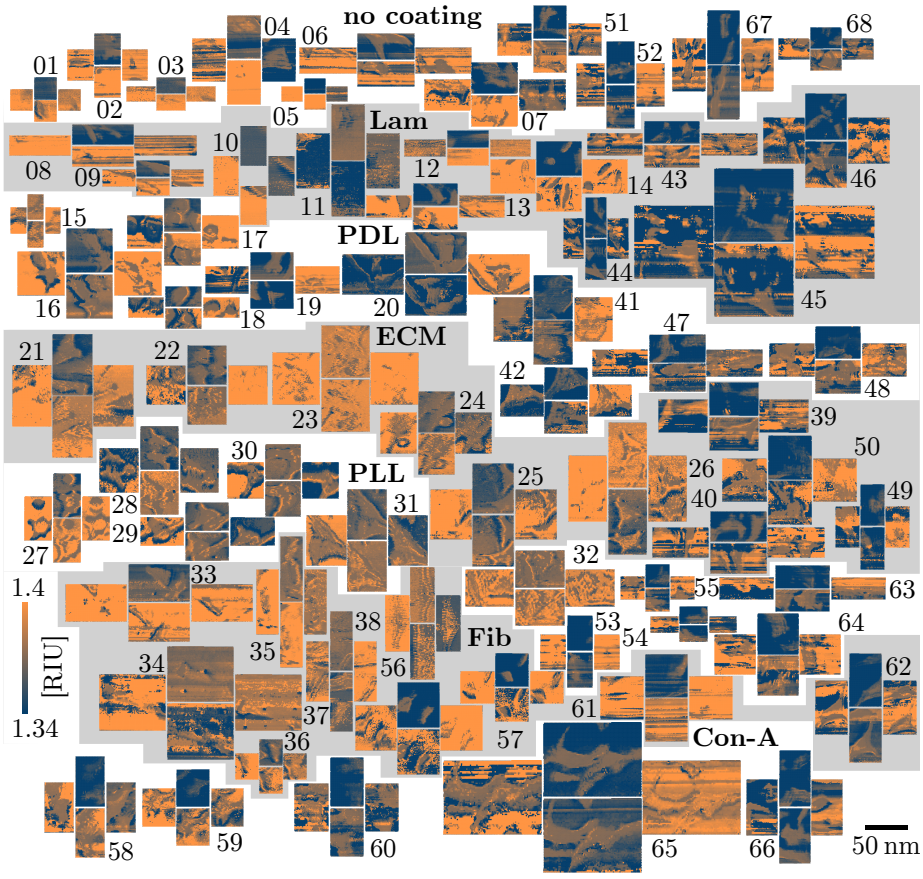


Figure A.31.: Color plots of the fitted cytoplasmic RIs of all 68 HEK293 measurements. The color scale at the bottom left and the scale at the bottom right are applicable to all plots. Color plots of the fitted cytoplasmic RIs of all 68 HEK293 measurements. The organization of the plots corresponds to that shown in fig. A.30. While it can be seen that the cytoplasmic RI of cells lies somewhere in the middle between the two limits of the color scale (which were also parameter limits of the optimizer), the values for "cytoplasmic RI" in areas without cells are predominantly at either the lower or the upper limit of the parameter space. This is related to the weak dependence of the fit residuals on cytoplasmic RI for large values of cell-substrate-separation.

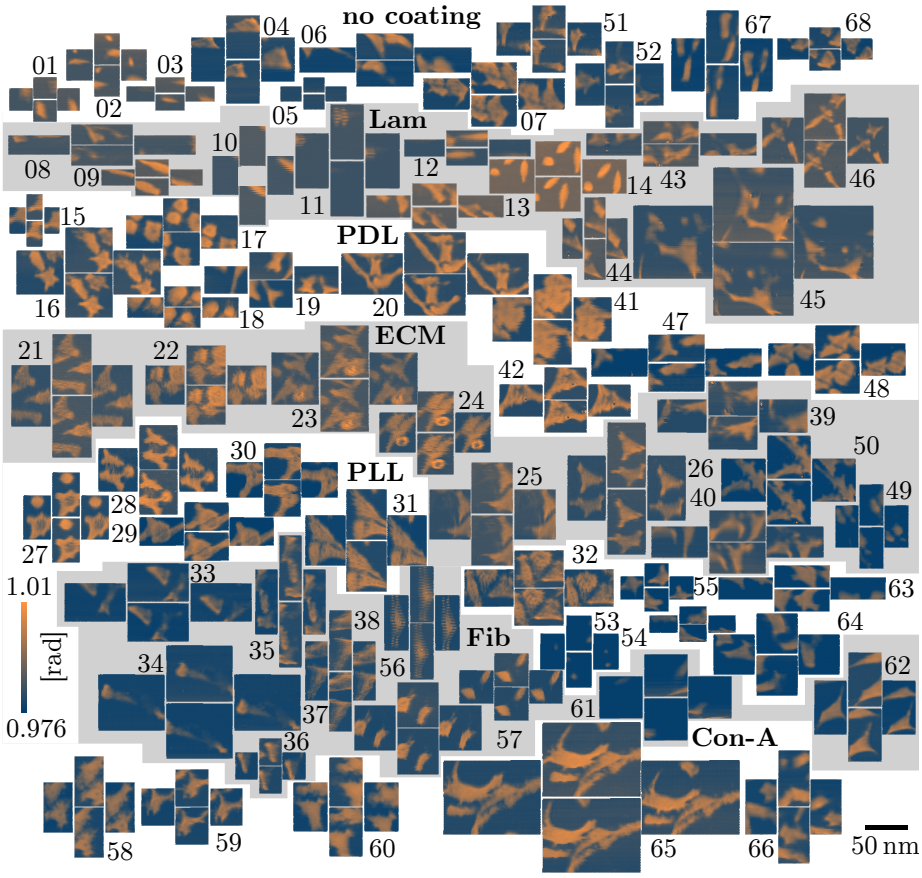


Figure A.32.: Color plots of the determined SPR angles of all 68 HEK293 measurements. There are four plots for each measurement, representing the results of the analysis of the left, top, right and bottom BFP segments. The plots are grouped by surface coating. The measurements are numbered from MID001 (01) to MID068 (68). The color scale at the bottom left and the scale at the bottom right are applicable to all plots. The contours of the imaged cells are clearly visible in the SPR angle distribution, demonstrating the sensitivity of SPR.

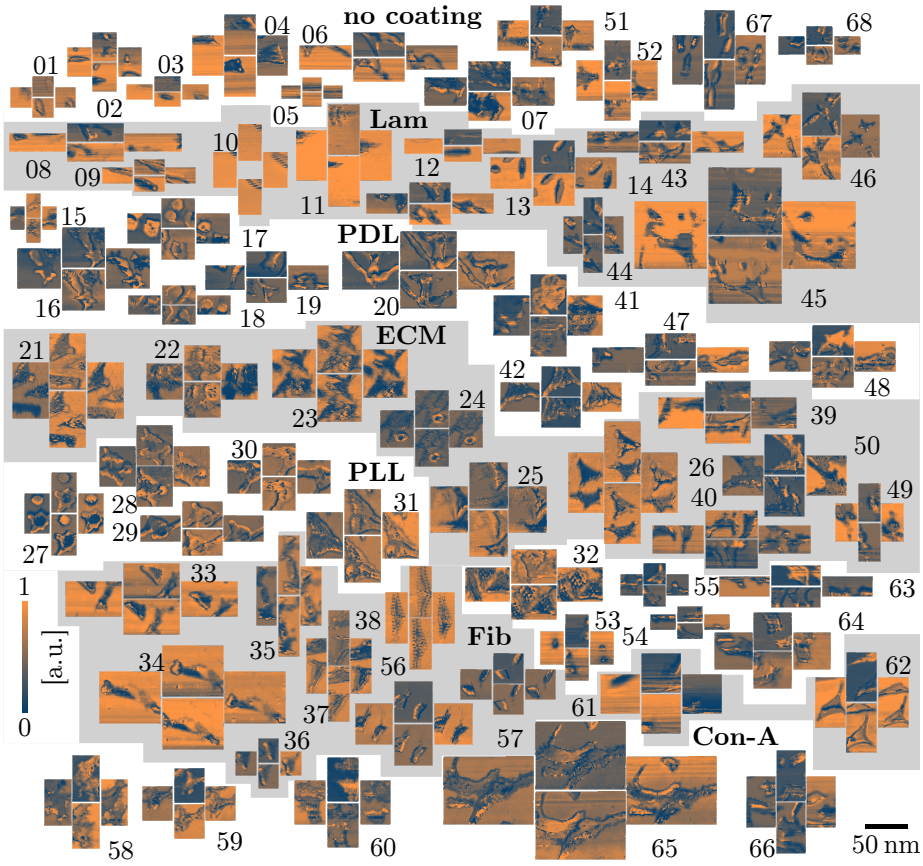


Figure A.33.: Color plots of the determined SPR peak widths of all 68 HEK293 measurements. The organization of the plots corresponds to that shown in fig. A.32. The color scale at the bottom left and the scale at the bottom right are applicable to all plots. For optimal contrast, SPR peak widths are displayed in arbitrary units (a.u.). This is necessary due to systematic (artificial) differences between BFP segments. These differences result from the implementation of SPR width determination together with an overall brightness variation between BFP segments. As this figure is only intended to confirm the negligibility of substrate-induced SPR width variations, a display in arbitrary units is sufficient.

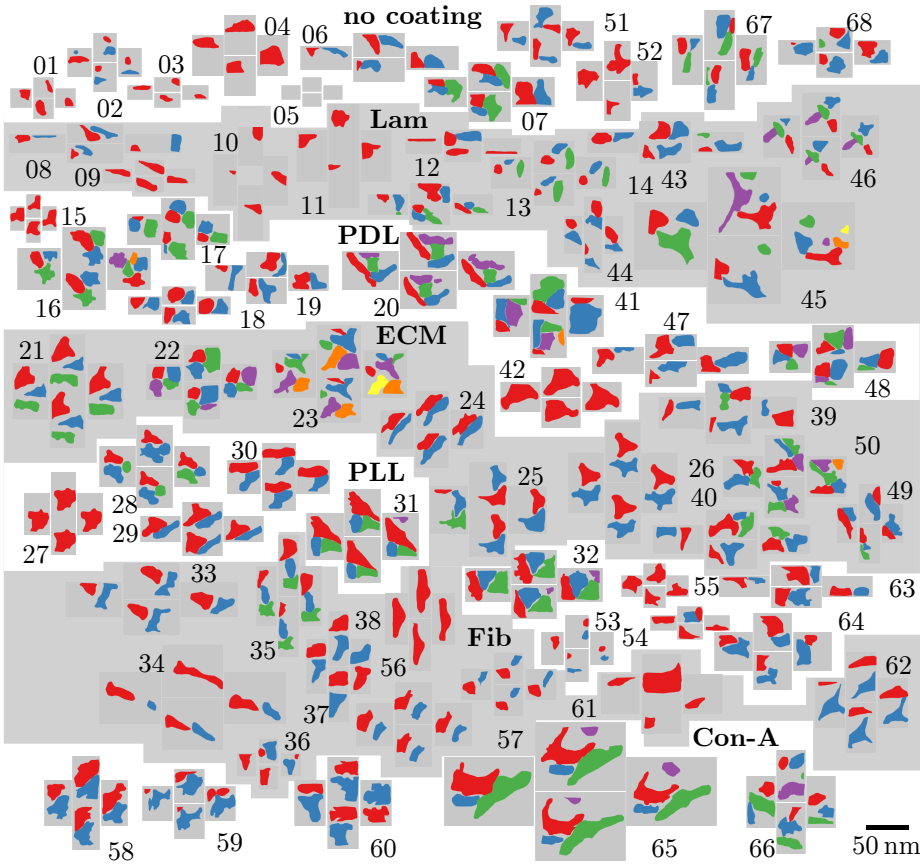


Figure A.34.: All hand-drawn labels for all 68 HEK293 measurements, cell by cell and BFP segment by BFP segment. The organization of the plots corresponds to that shown in fig. A.30. The scale at the bottom right is applicable to all plots. Different cells are represented by different colors. In some cases, the same cells were colored differently depending on BFP segment.

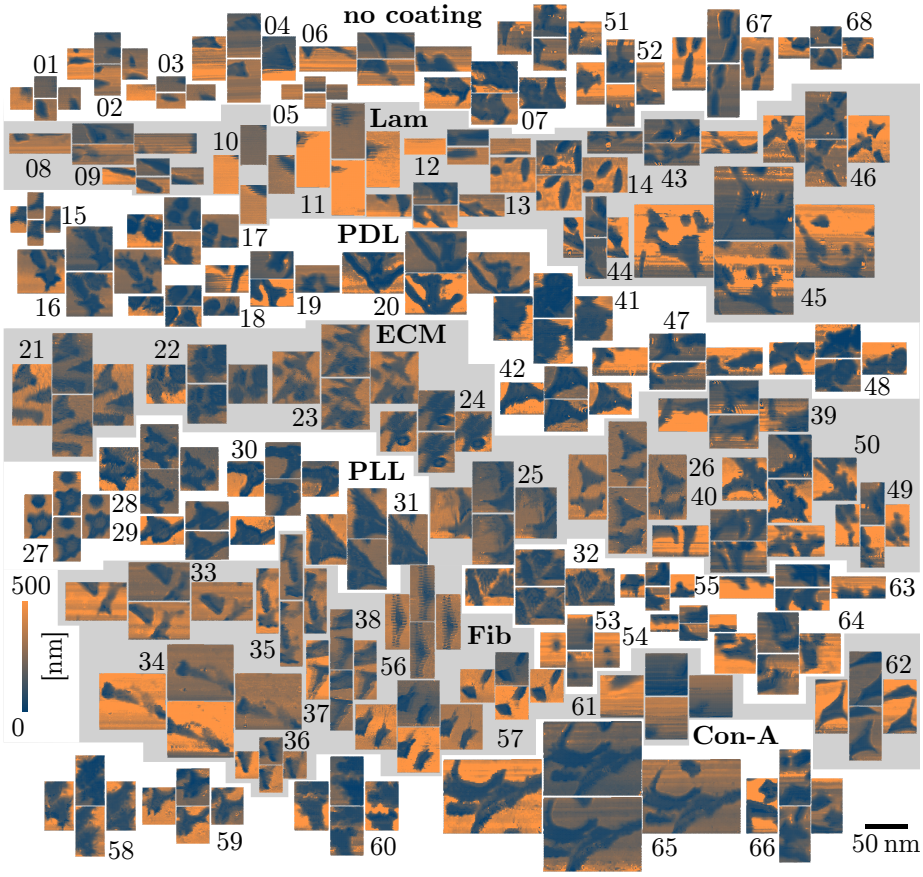


Figure A.35.: Color plots of cell-substrate distances from all 68 HEK293 measurements (color scale up to 500 nm). The organization of the plots corresponds to that shown in fig. A.30. The color scale at the bottom left and the scale at the bottom right are applicable to all plots. It should be noted that cell-substrate distances of (0-300) nm (at the given SNR) cannot be reliably resolved with SPRM. These values were only allowed in the optimization to avoid the bias observed when the optimization limits were too narrow. fig. A.35 shows the color coding of the same plots in the range (0-300) nm.

Figure A.36.: SPRM widefield images of HEK293 cells before each SPRM area scan (100x TIRF objective). The numbering of the measurements corresponds to the images in fig. A.37. No image is available for measurement MID008. The scale in the bottom right corner of each image is 20 µm.

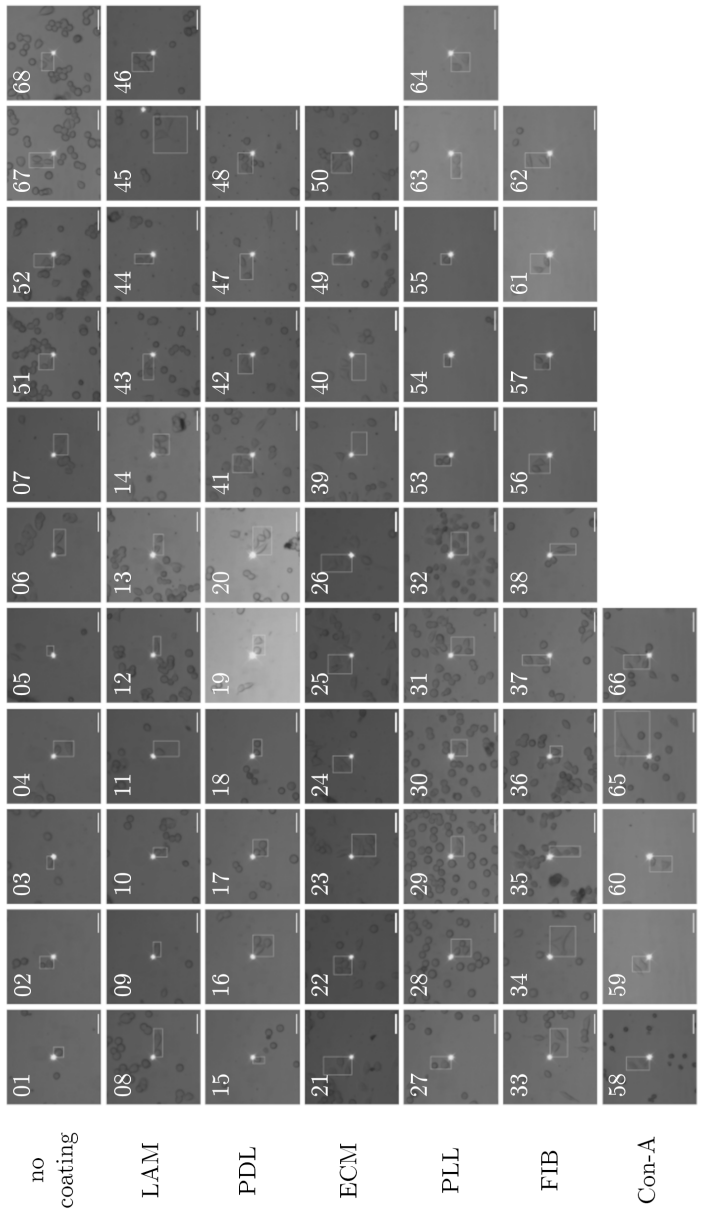


Figure A.37.: Top camera images of the halogen-illuminated HEK293 cells before each SPRM area scan (20x air objective). The images are labeled with measurement ids from MID001 (01) to MID068 (68). The scale in the bottom right corner of each image is 50 µm. The white rectangles represent the area of the subsequent SPRM scans. The overexposed spot in the center of each image corresponds to the transmitted part of the laser beam.

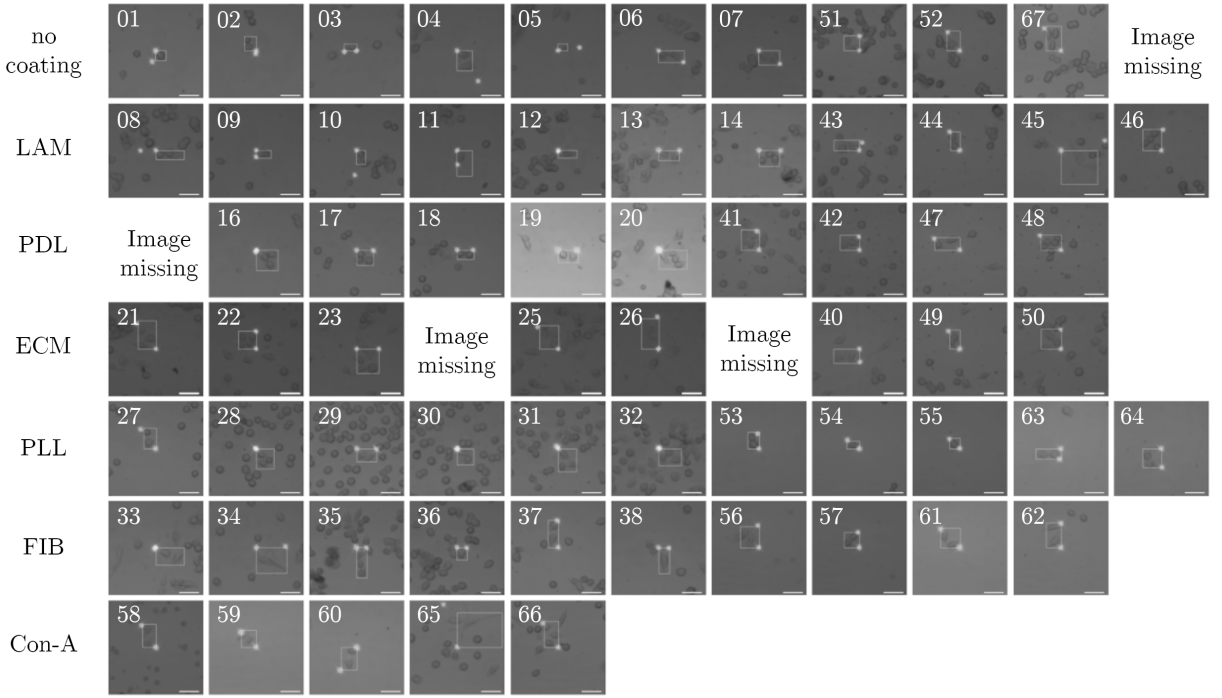
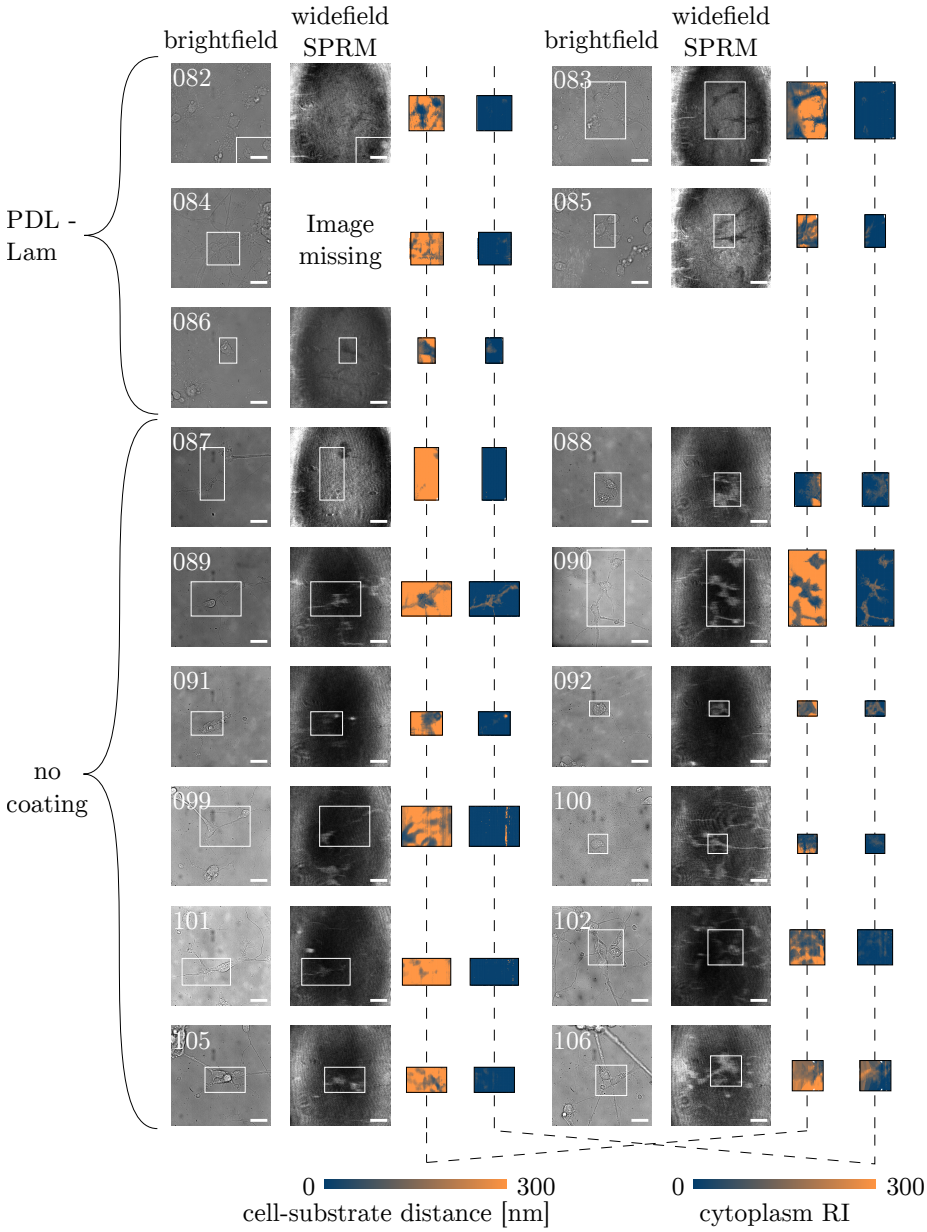


Figure A.38.: Superimposed top camera images of HEK293 cells before and after each SPRM area scan (20x air objective). The scale and the marked scan area as well as the numbering of the measurements correspond to the images in fig. A.37. In 4 cases an image after the scan is missing. Due to the blending, the laser beam is visible at two points in most of the images, as the start and end coordinates of the scans are usually different.


brightfield
widefield SPRM
brightfield
widefield SPRM
PDL - Lam
no coating
082
083
084
085
086
087
088
089
090
091
092
099
100
101
102
105
106
Image missing
0
300
cell-substrate distance [nm]
0
300
cytoplasm RI

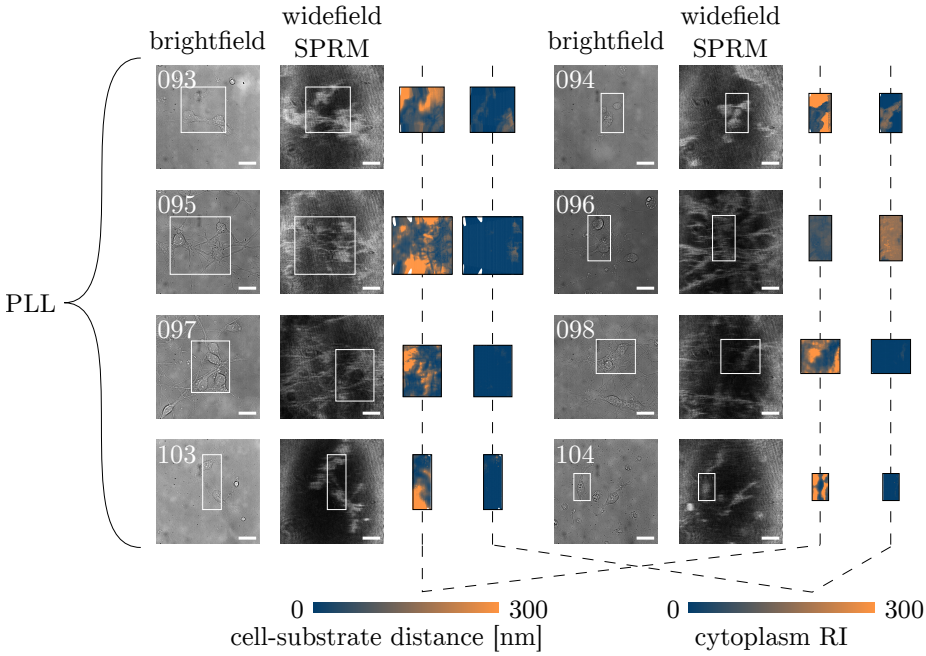
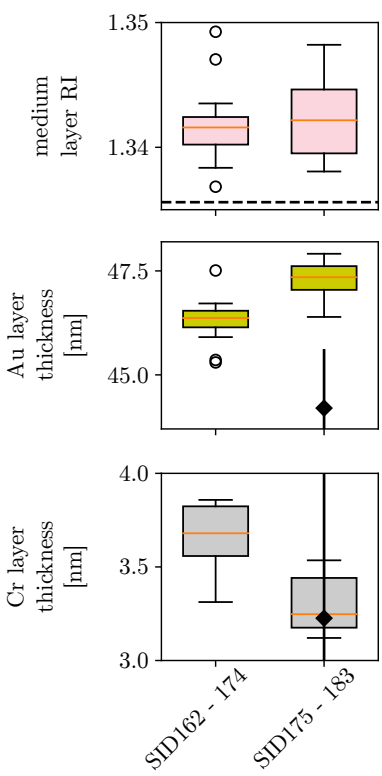
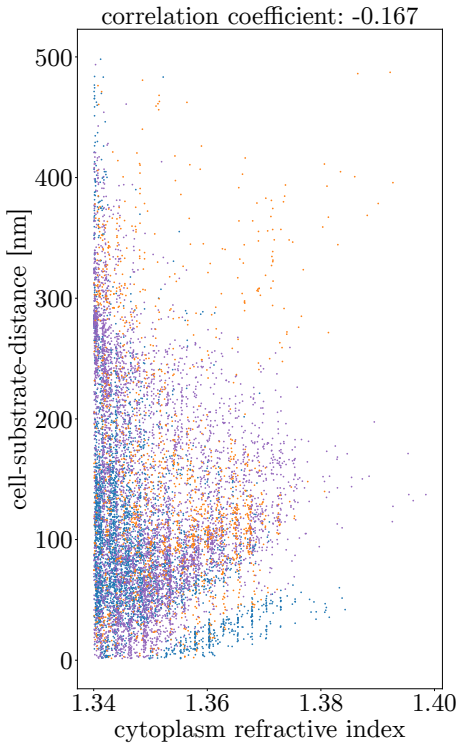


Figure A.39.: Overview of all neuron-substrate distance measurements on Au substrates. For each measurement, the three digits of the measurement ID are displayed in the corresponding brightfield image taken before the scanning measurement. Next to each brightfield image is the corresponding widefield SPRM image, also taken before the scanning measurement. Both images share the rectangular marking of the scan measurement area as well as a 20µm scale bar. Next to this are color plots of the fitted cell-substrate distances and cytoplasm RI values obtained from the scan measurement analysis.



(a) Substrate layer thicknesses and medium RI, determined for each measurement in table A.3 from automatically determined 'control' measurement spots. The distribution of these values is represented by box plots (IQR $\pm$ 1.5 IQR, see matplotlib [61] documentation for version 3.6.2). From the second batch of substrates (SID175-183) one substrate was used for XRR characterization (diamond markers, as in fig. A.26). The horizontal dashed line in the medium layer RI plot indicates an Abbe refractometer measurement (see table 5.5).



(b) Scatter plot of all unmasked neuron-substrate-distance and cytoplasm-RI pairs to visualize the parameter distribution and correlation obtained from the analysis of scanning SPRM measurements. The correlation coefficient has been calculated and is displayed above the plot. Colors indicate substrate coating, color coding corresponds to that in fig. 6.2.

Figure A.40.: Au substrate layer parameters and neuron medium RI, determined by SPRM and XRR / Abbe refractometer, as well as neuron-substrate distance and cytoplasmic RI distribution.

Table A.1.: Overview of presented SPRM measurements on HEK293. The 'Cell Splitting' column contains the coded number of freeze-thaw cycles and passages. For example, "Fx+5aPx+29a" indicates a number of 5 freeze-thaw cycles (Fx) and 29 passages (Px), where letters ('a', 'b', 'c') indicate different parent flasks from which cells were derived.

Measurement id	Measurement Date	hours in vitro	Sample id	Cell Splitting	Surface Coating
MID001	2023.07.19	4 h 22 min	SID100	Fx+5aPx+29a	-
MID002	2023.07.19	5 h 03 min	SID100	Fx+5aPx+29a	-
MID003	2023.07.19	6 h 03 min	SID100	Fx+5aPx+29a	-
MID004	2023.07.20	24 h 24 min	SID101	Fx+5aPx+29a	-
MID005	2023.07.20	25 h 39 min	SID101	Fx+5aPx+29a	-
MID006	2023.07.20	26 h 11 min	SID102	Fx+5aPx+29a	-
MID007	2023.07.20	27 h 22 min	SID102	Fx+5aPx+29a	-
MID008	2023.07.20	3 h 59 min	SID103	Fx+5aPx+29b	LAM
MID009	2023.07.20	5 h 25 min	SID103	Fx+5aPx+29b	LAM
MID010	2023.07.20	6 h 30 min	SID104	Fx+5aPx+29b	LAM
MID011	2023.07.20	7 h 23 min	SID104	Fx+5aPx+29b	LAM
MID012	2023.07.20	8 h 30 min	SID105	Fx+5aPx+29b	LAM
MID013	2023.07.20	9 h 45 min	SID105	Fx+5aPx+29b	LAM
MID014	2023.07.20	11 h 14 min	SID105	Fx+5aPx+29b	LAM
MID015	2023.07.21	5 h 16 min	SID106	Fx+5aPx+29c	PDL
MID016	2023.07.21	5 h 50 min	SID106	Fx+5aPx+29c	PDL
MID017	2023.07.21	7 h 32 min	SID107	Fx+5aPx+29c	PDL
MID018	2023.07.21	10 h 20 min	SID107	Fx+5aPx+29c	PDL
MID019	2023.07.21	11 h 23 min	SID108	Fx+5aPx+29c	PDL
MID020	2023.07.21	12 h 33 min	SID108	Fx+5aPx+29c	PDL
MID021	2023.07.26	5 h 06 min	SID109	Fx+5aPx+31a	ECM
MID022	2023.07.26	6 h 26 min	SID109	Fx+5aPx+31a	ECM
MID023	2023.07.26	7 h 20 min	SID110	Fx+5aPx+31a	ECM
MID024	2023.07.26	8 h 14 min	SID110	Fx+5aPx+31a	ECM
MID025	2023.07.26	9 h 00 min	SID111	Fx+5aPx+31a	ECM
MID026	2023.07.26	9 h 54 min	SID111	Fx+5aPx+31a	ECM
MID027	2023.07.27	5 h 33 min	SID112	Fx+5aPx+31b	PLL

Measurement id	Measurement Date	hours in vitro	Sample id	Cell Splitting	Surface Coating
MID028	2023.07.27	6 h 52 min	SID112	Fx+5aPx+31b	PLL
MID029	2023.07.27	7 h 48 min	SID113	Fx+5aPx+31b	PLL
MID030	2023.07.27	8 h 40 min	SID113	Fx+5aPx+31b	PLL
MID031	2023.07.27	9 h 25 min	SID114	Fx+5aPx+31b	PLL
MID032	2023.07.27	11 h 03 min	SID114	Fx+5aPx+31b	PLL
MID033	2023.07.27	5 h 37 min	SID115	Fx+5aPx+31c	FIB
MID034	2023.07.27	6 h 44 min	SID115	Fx+5aPx+31c	FIB
MID035	2023.07.27	8 h 05 min	SID116	Fx+5aPx+31c	FIB
MID036	2023.07.27	9 h 06 min	SID116	Fx+5aPx+31c	FIB
MID037	2023.07.27	9 h 47 min	SID117	Fx+5aPx+31c	FIB
MID038	2023.07.27	10 h 38 min	SID117	Fx+5aPx+31c	FIB
MID039	2023.09.28	4 h 41 min	SID118	Fx+5bPx+28a	ECM
MID040	2023.09.28	5 h 39 min	SID118	Fx+5bPx+28a	ECM
MID041	2023.09.28	6 h 35 min	SID119	Fx+5bPx+28a	PDL
MID042	2023.09.28	7 h 25 min	SID119	Fx+5bPx+28a	PDL
MID043	2023.09.28	8 h 12 min	SID120	Fx+5bPx+28a	LAM
MID044	2023.09.28	8 h 57 min	SID120	Fx+5bPx+28a	LAM
MID045	2023.09.29	28 h 25 min	SID121	Fx+5bPx+28b	LAM
MID046	2023.09.29	29 h 29 min	SID121	Fx+5bPx+28b	LAM
MID047	2023.09.29	30 h 40 min	SID122	Fx+5bPx+28b	PDL
MID048	2023.09.29	31 h 22 min	SID122	Fx+5bPx+28b	PDL
MID049	2023.09.29	32 h 08 min	SID123	Fx+5bPx+28b	ECM
MID050	2023.09.29	32 h 35 min	SID123	Fx+5bPx+28b	ECM
MID051	2023.10.05	4 h 37 min	SID124	Fx+5bPx+29	-
MID052	2023.10.05	5 h 17 min	SID124	Fx+5bPx+29	-
MID053	2023.10.12	4 h 48 min	SID131	Fx+5bPx+31	PLL
MID054	2023.10.12	5 h 22 min	SID131	Fx+5bPx+31	PLL
MID055	2023.10.12	5 h 45 min	SID131	Fx+5bPx+31	PLL
MID056	2023.10.12	6 h 15 min	SID132	Fx+5bPx+31	FIB
MID057	2023.10.12	7 h 06 min	SID132	Fx+5bPx+31	FIB
MID058	2023.10.12	7 h 53 min	SID133	Fx+5bPx+31	Con-A
MID059	2023.10.13	4 h 45 min	SID134	Fx+5bPx+32	Con-A

Measurement id	Measurement Date	hours in vitro	Sample id	Cell Splitting	Surface Coating
MID060	2023.10.13	5 h 35 min	SID134	Fx+5bPx+32	Con-A
MID061	2023.10.13	6 h 29 min	SID135	Fx+5bPx+32	FIB
MID062	2023.10.13	7 h 19 min	SID135	Fx+5bPx+32	FIB
MID063	2023.10.13	8 h 05 min	SID136	Fx+5bPx+32	PLL
MID064	2023.10.13	8 h 44 min	SID136	Fx+5bPx+32	PLL
MID065	2023.10.18	6 h 09 min	SID137	Fx+5bPx+33	Con-A
MID066	2023.10.18	7 h 08 min	SID137	Fx+5bPx+33	Con-A
MID067	2023.10.18	8 h 07 min	SID138	Fx+5bPx+33	-
MID068	2023.10.18	9 h 01 min	SID138	Fx+5bPx+33	-

Table A.2.: Overview of various presented SPRM measurements.

Measurement id	Measurement Date	Specimen Type	Ambient Medium	Substrate Type	Sample id
MID069	2023.02.02	reference	air	N-LAF21	SID058
MID070	2023.02.02	reference	air	300 nm Cr	SID058
MID071	2023.02.02	reference	air	300 nm Cr	SID058
MID072	2023.02.02	reference	air	300 nm Cr	SID058
MID073	2023.02.02	reference	air	300 nm Cr	SID058
MID074	2023.02.06	SiO_2 sphere	2-propanol	Au	SID048
MID075	2023.07.10	SiO_2 sphere	2-propanol	SiO_2	SID092
MID076	2024.04.26	bulk medium	ethanol	N-LAF21	SID168b
MID077	2024.04.26	bulk medium	water	N-LAF21	SID168b
MID078	2024.04.26	bulk medium	air	N-LAF21	SID168b

Table A.3.: Overview of presented SPRM measurements on neurons.

Measurement id	Measurement Date	rounded DIV	Sample id	Surface Diameter	Surface Coating	Cell Count	Medium Volume	From Hibernate
MID082–083	2024.04.08	4	SID162	14 mm	PDL-Lam	200k	1.5 mL	yes
MID084–086	2024.04.08	4	SID163	14 mm	PDL-Lam	200k	1.5 mL	yes
MID087–088	2024.04.11	3	SID168	14 mm	-	30k	1.5 mL	no
MID089–090	2024.04.11	3	SID169	14 mm	-	50k	1.5 mL	no
MID091–092	2024.04.12	4	SID170	14 mm	-	60k	1.5 mL	no
MID093–094	2024.04.12	2	SID173	14 mm	PLL	60k	1.5 mL	yes
MID095–096	2024.04.15	5	SID172	14 mm	PLL	60k	1.5 mL	yes
MID097–098	2024.04.15	5	SID171	14 mm	PLL	60k	1.5 mL	yes
MID099–100	2024.04.17	3	SID182	35 mm	-	150k	2.5 mL	no
MID101–102	2024.04.18	2	SID181	35 mm	-	150k	2.5 mL	no
MID103–104	2024.04.18	4	SID180	35 mm	PLL	150k	2.5 mL	no
MID105–106	2024.04.19	4	SID183	35 mm	-	150k	2.5 mL	no

B Bibliography

[1] Max Knoll and Ernst Ruska. „Das elektronenmikroskop“. In: *Zeitschrift für physik* 78 (1932), pp. 318–339.

[2] Kenneth Levenberg. „A method for the solution of certain non-linear problems in least squares“. In: *Quarterly of applied mathematics* 2.2 (1944), pp. 164–168.

[3] Th Förster. „Zwischenmolekulare energiewanderung und fluoreszenz“. In: *Annalen der physik* 437.1-2 (1948), pp. 55–75.

[4] Donald W Marquardt. „An algorithm for least-squares estimation of nonlinear parameters“. In: *Journal of the society for Industrial and Applied Mathematics* 11.2 (1963), pp. 431–441.

[5] ASG Curtis. „The mechanism of adhesion of cells to glass: a study by interference reflection microscopy“. In: *The Journal of cell biology* 20.2 (1964), p. 199.

[6] Erwin Kretschmann and Heinz Raether. „Radiative decay of non radiative surface plasmons excited by light“. In: *Zeitschrift für Naturforschung A* 23.12 (1968), pp. 2135–2136.

[7] Andreas Otto. „Excitation of nonradiative surface plasma waves in silver by the method of frustrated total reflection“. In: *Zeitschrift für Physik A Hadrons and nuclei* 216.4 (1968), pp. 398–410.

[8] Irwin Sobel, Gary Feldman, et al. „A 3x3 isotropic gradient operator for image processing“. In: *a talk at the Stanford Artificial Project in* 1968 (1968), pp. 271–272.

[9] Richard O Duda and Peter E Hart. „Use of the Hough transformation to detect lines and curves in pictures“. In: *Communications of the ACM* 15.1 (1972), pp. 11–15.

[10] PB Johnson and RW Christy. „Optical constants of transition metals: Ti, v, cr, mn, fe, co, ni, and pd“. In: *Physical review B* 9.12 (1974), p. 5056.

[11] VP Collins, B Arborgh, and U Brunk. „A COMPARISON OF THE EFFECTS OF THREE WIDELY USED GLUTARALDEHYDE FIXATIVES ON CELLULAR VOLUME AND STRUCTURE: A TEM, SEM, Volumetric and Cytochemical Study“. In: *Acta Pathologica Microbiologica Scandinavica Section A Pathology* 85.2 (1977), pp. 157–168.

[12] JM Elson, JP Rahn, and JM Bennett. „Relationship of the total integrated scattering from multilayer-coated optics to angle of incidence, polarization, correlation length, and roughness cross-correlation properties“. In: *Applied Optics* 22.20 (1983), pp. 3207–3219.

[13] John Canny. „A computational approach to edge detection“. In: *IEEE Transactions on pattern analysis and machine intelligence* 6 (1986), pp. 679–698.

[14] E Yeatman and EA Ash. „Surface plasmon microscopy“. In: *Electronics letters* 20.23 (1987), pp. 1091–1092. DOI: 10.1049/el:19870762.

[15] Benno Rothenhäusler and Wolfgang Knoll. „Surface–plasmon microscopy“. In: *Nature* 332.6165 (1988), pp. 615–617.

[16] Wade G Regehr et al. „Sealing cultured invertebrate neurons to embedded dish electrodes facilitates long-term stimulation and recording“. In: *Journal of neuroscience methods* 30.2 (1989), pp. 91–106.

[17] MA Rupnick et al. „Endothelialization of vascular prosthetic surfaces following seeding or sodding techniques using human microvessel endothelial cells“. In: *J Vasc Surg* 9 (1989), pp. 788–795.

[18] Roshdi Rashed. „A pioneer in anaclastics: Ibn Sahl on burning mirrors and lenses“. In: *Isis* 81.3 (1990), pp. 464–491.

[19] JMH Levelt Sengers and JS Gallagher. „Wavelength, Temperature and Density“. In: *J. Phys. Chem. Ref. Data* 19.3 (1990).

[20] Ivar Giaever and Charles R Keese. „Micromotion of mammalian cells measured electrically.“ In: *Proceedings of the National Academy of Sciences* 88.17 (1991), pp. 7896–7900.

[21] Michael L Johnson and Lindsay M Faunt. „[1] Parameter estimation by least-squares methods“. In: *Methods in enzymology*. Vol. 210. Elsevier, 1992, pp. 1–37.

[22] George A Truskey et al. „Total internal reflection fluorescence microscopy (TIRFM): II.* Topographical mapping of relative cell/substratum separation distances“. In: *Journal of cell science* 103.2 (1992), pp. 491–499.

[23] MF Ceiler Jr et al. „THE EFFECTS OF THE DEPOSITION CONDITIONS ON THE COMPOSITION AND PROPERTIES OF PECVD SILICON DIOXIDE FILMS“. In: *Proceedings of the Second International Symposium on Electrochemical Processing of Tailored Materials*. Vol. 93. 12. Electrochemical Society. 1993, p. 265.

[24] Bonnie Tocher Clause. „The Wistar rat as a right choice: Establishing mammalian standards and the ideal of a standardized mammal“. In: *Journal of the History of Biology* 26.2 (1993), pp. 329–349.

[25] Charles EH Berger, Rob PH Kooyman, and Jan Greve. „Resolution in surface plasmon microscopy“. In: *Review of scientific instruments* 65.9 (1994), pp. 2829–2836.

[26] Julie Bouckaert et al. „Crystallographic structure of metal-free concanavalin A at 2.5 Å resolution“. In: *Proteins: Structure, Function, and Bioinformatics* 23.4 (1995), pp. 510–524.

[27] J. Bouckaert et al. *Image from the RCSB PDB (RCSB.org) of PDB ID 1APN (The Crystallographic Structure of Metal-Free Concanavalin A at 2.5 Angstroms Resolution)*. Initial deposition on 28 July 1995, released on 3 April 1996, latest revision on 7 February 2024, accessed on 16 June 2024, corresponding publication DOI: https://doi.org/10.1107/S0907444996009237. 1996. DOI: `https://doi.org/10.2210/pdb1apn/pdb`.

[28] Philip E Ciddor. „Refractive index of air: new equations for the visible and near infrared“. In: *Applied optics* 35.9 (1996), pp. 1566–1573.

[29] D.J. Leahy, I. Aukhil, and H.P. Erickson. *Image from the RCSB PDB (RCSB.org) of PDB ID 1FNF (Fragment of human fibronectin encompassing type-III repeats 7 through 10)*. Initial deposition on 30 September 1995, released on 29 January 1996, latest revision on 7 February 2024, accessed on 17 June 2024, corresponding publication DOI: https://doi.org/10.1016/S0092-8674(00)81002-8. 1996. DOI: `https://doi.org/10.2210/pdb1fnf/pdb`.

[30] Daniel J Leahy, Ikramuddin Aukhil, and Harold P Erickson. „2.0 Å crystal structure of a four-domain segment of human fibronectin encompassing the RGD loop and synergy region“. In: *Cell* 84.1 (1996), pp. 155–164.

[31] Yao Xiao and George A Truskey. „Effect of receptor-ligand affinity on the strength of endothelial cell adhesion“. In: *Biophysical journal* 71.5 (1996), pp. 2869–2884.

[32] Dieter Braun and P Fromherz. „Fluorescence interference-contrast microscopy of cell adhesion on oxidized silicon.“ In: *Applied Physics A: Materials Science & Processing* 65 (1997).

[33] MJ Doughty, JPG Bergmanson, and Y Blocker. „Shrinkage and distortion of the rabbit corneal endothelial cell mosaic caused by a high osmolality glutaraldehyde-formaldehyde fixative compared to glutaraldehyde“. In: *Tissue and Cell* 29.5 (1997), pp. 533–547.

[34] Martin Jenkner and Peter Fromherz. „Bistability of membrane conductance in cell adhesion observed in a neuron transistor“. In: *Physical review letters* 79.23 (1997), p. 4705.

[35] Wayne M. Yokoyama. „Cryopreservation of Cells“. In: *Current Protocols in Immunology* 21.1 (1997), A.3G.1–A.3G.3. DOI: 10.1002/0471142735.ima03gs21. eprint: https://currentprotocols.onlinelibrary.wiley.com/doi/pdf/10.1002/0471142735.ima03gs21. URL: https://currentprotocols.onlinelibrary.wiley.com/doi/abs/10.1002/0471142735.ima03gs21.

[36] Dieter Braun and Peter Fromherz. „Fluorescence interferometry of neuronal cell adhesion on microstructured silicon“. In: *Physical review letters* 81.23 (1998), p. 5241.

[37] Hiroshi Kano and Wolfgang Knoll. „Locally excited surface-plasmon-polaritons for thickness measurement of LBK films“. In: *Optics Communications* 153.4-6 (1998), pp. 235–239.

[38] Hiroshi Kano, Seiji Mizuguchi, and Satoshi Kawata. „Excitation of surface-plasmon polaritons by a focused laser beam“. In: *JOSA B* 15.4 (1998), pp. 1381–1386.

[39] Max Born and Emil Wolf. *Principles of optics: Electromagnetic theory of propagation, interference and diffraction of light*. Cambridge, UK: Cambridge University Press, 1999, 55 ff. ISBN: 0521642221.

[40] K-F Giebel et al. „Imaging of cell/substrate contacts of living cells with surface plasmon resonance microscopy“. In: *Biophysical journal* 76.1 (1999), pp. 509–516.

[41] Michael L Johnson. „Parameter correlations while curve fitting“. In: *Methods in enzymology*. Vol. 321. Elsevier, 2000, pp. 424–446.

[42] Eric R Kandel et al. *Principles of neural science*. Vol. 4. McGraw-hill New York, 2000.

[43] C Mathew Mate et al. „New methodologies for measuring film thickness, coverage, and topography“. In: *IEEE transactions on magnetics* 36.1 (2000), pp. 110–114.

[44] Fernando Moreno and Francisco González, eds. *Light Scattering from Microstructures. Lectures of the Summer School of Laredo, University of Cantabria, Held at Laredo, Spain, Sept. 11-13, 1998*. 1st ed. Lecture Notes in Physics. Springer Book Archive, Published: 20 November 2013, Copyright: Springer-Verlag Berlin Heidelberg 2000, eBook Published: 11 January 2008. Springer Berlin, Heidelberg, 2000. ISBN: 978-3-662-14274-5. DOI: 10.1007/3-540-46614-2. URL: https://doi.org/10.1007/3-540-46614-2.

[45] Michael G Somekh et al. „High-resolution scanning surface-plasmon microscopy“. In: *Applied optics* 39.34 (2000), pp. 6279–6287.

[46] Michael Geoffrey Somekh et al. „Optical V (z) for high-resolution 2π surface plasmon microscopy“. In: *Optics Letters* 25.11 (2000), pp. 823–825.

[47] Berit L Strand et al. „Poly-L-lysine induces fibrosis on alginate microcapsules via the induction of cytokines“. In: *Cell transplantation* 10.3 (2001), pp. 263–275.

[48] Joachim Wegener, Andreas Janshoff, and Claudia Steinem. „The quartz crystal microbalance as a novel means to study cell-substrate interactions in situ“. In: *Cell Biochemistry and Biophysics* 34 (2001), pp. 121–151.

[49] Bruce Alberts et al. *Molecular Biology of the Cell*. 5th. New York: Garland Science, 2002. ISBN: 978-0-8153-4105-5 and 978-0-8153-4106-2.

[50] Yonghong Xie and Qiang Ji. „A new efficient ellipse detection method“. In: *2002 International Conference on Pattern Recognition*. Vol. 2. IEEE. 2002, pp. 957–960.

[51] Thomas S Hug. „Biophysical methods for monitoring cell-substrate interactions in drug discovery“. In: *Assay and drug development technologies* 1.3 (2003), pp. 479–488.

[52] Hynda K Kleinman, Deborah Philp, and Matthew P Hoffman. „Role of the extracellular matrix in morphogenesis“. In: *Current opinion in biotechnology* 14.5 (2003), pp. 526–532.

[53] Kalkbrenner Lindfors et al. „Detection and spectroscopy of gold nanoparticles using supercontinuum white light confocal microscopy“. In: *Physical review letters* 93.3 (2004), p. 037401.

[54] Graham Stabler, Michael Geoffrey Somekh, and CW See. „High-resolution wide-field surface plasmon microscopy“. In: *Journal of Microscopy* 214.3 (2004), pp. 328–333.

[55] Janos Vörös. „The density and refractive index of adsorbing protein layers“. In: *Biophysical journal* 87.1 (2004), pp. 553–561.

[56] Stefan Linder and Petra Kopp. „Podosomes at a glance“. In: *Journal of cell science* 118.10 (2005), pp. 2079–2082.

[57] Philip Thomas and Trevor G Smart. „HEK293 cell line: a vehicle for the expression of recombinant proteins“. In: *Journal of pharmacological and toxicological methods* 51.3 (2005), pp. 187–200.

[58] Guoyong Yin et al. „GIT1 is a scaffold for ERK1/2 activation in focal adhesions“. In: *Journal of Biological Chemistry* 280.30 (2005), pp. 27705–27712.

[59] Mariana Ruiz Villarreal (LadyofHats). *Cross section of the different structures that phospholipids can take in an aqueous solution*. Public Domain. 2007. URL: `https://commons.wikimedia.org/wiki/File:Phospholipids_aqueous_solution_structures_diagram.svg`.

[60] Lotfi Berguiga et al. „High-resolution surface-plasmon imaging in air and in water: V (z) curve and operating conditions“. In: *Optics letters* 32.5 (2007), pp. 509–511.

[61] J. D. Hunter. „Matplotlib: A 2D graphics environment“. In: *Computing in Science & Engineering* 9.3 (2007), pp. 90–95. DOI: `10.1109/MCSE.2007.55`.

[62] Stefan A Maier et al. *Plasmonics: fundamentals and applications*. Vol. 1. Springer, 2007.

[63] Wolfgang Nolting. *Grundkurs Theoretische Physik 3: Elektrodynamik*. 8th ed. Springer, 2007. ISBN: 978-3-540-71251-0.

[64] Kouyou Watanabe, Nobuhiro Horiguchi, and Hiroshi Kano. „Optimized measurement probe of the localized surface plasmon microscope by using radially polarized illumination“. In: *Applied optics* 46.22 (2007), pp. 4985–4990.

[65] Günter Wrobel et al. „Transmission electron microscopy study of the cell–sensor interface“. In: *Journal of The Royal Society Interface* 5.19 (2008), pp. 213–222.

[66] Daniel Chappell et al. „The glycocalyx of the human umbilical vein endothelial cell: an impressive structure ex vivo but not in culture“. In: *Circulation research* 104.11 (2009), pp. 1313–1317.

[67] Rafael C Gonzalez. *Digital image processing*. Pearson education india, 2009.

[68] Cornelia Monzel et al. „Probing Biomembrane Dynamics by Dual-Wavelength Reflection Interference Contrast Microscopy“. In: *ChemPhysChem* 10.16 (2009), pp. 2828–2838.

[69] Michael G Somekh et al. „Wide-field high-resolution surface-plasmon interference microscopy“. In: *Optics letters* 34.20 (2009), pp. 3110–3112.

[70] R Vander and SG Lipson. „High-resolution surface-plasmon resonance real-time imaging“. In: *Optics letters* 34.1 (2009), pp. 37–39.

[71] Kouyou Watanabe, Goro Terakado, and Hiroshi Kano. „Localized surface plasmon microscope with an illumination system employing a radially polarized zeroth-order Bessel beam“. In: *Optics letters* 34.8 (2009), pp. 1180–1182.

[72] Michael Berndt et al. „Axial nanometer distances measured by fluorescence lifetime imaging microscopy“. In: *Nano letters* 10.4 (2010), pp. 1497–1500.

[73] Alain Carré and Valérie Lacarrière. „How substrate properties control cell adhesion. A physical–chemical approach“. In: *Journal of Adhesion Science and Technology* 24.5 (2010), pp. 815–830.

[74] Cuiying Hu, Jingang Zhong, and Jiawen Weng. „Digital holographic microscopy by use of surface plasmon resonance for imaging of cell membranes“. In: *Journal of Biomedical Optics* 15.5 (2010), pp. 056015–056015.

[75] Leon Lasdon et al. „Adaptive memory programming for constrained global optimization“. In: *Computers & Operations Research* 37.8 (2010), pp. 1500–1509.

[76] Alexander W Peterson et al. „Using surface plasmon resonance imaging to probe dynamic interactions between cells and extracellular matrix“. In: *Cytometry Part A* 77.9 (2010), pp. 895–903.

[77] Koyo Watanabe et al. „High resolution imaging of patterned model biological membranes by localized surface plasmon microscopy“. In: *Applied optics* 49.5 (2010), pp. 887–891.

[78] David Hilbert and Stephan Cohn-Vossen. *Anschauliche geometrie*. Springer-Verlag, 2011.

[79] Jongin Hong et al. „Electrical cell-substrate impedance sensing as a non-invasive tool for cancer cell study“. In: *Analyst* 136.2 (2011), pp. 237–245.

[80] Stefan Kedenburg et al. „Linear refractive index and absorption measurements of nonlinear optical liquids in the visible and near-infrared spectral region“. In: *Optical Materials Express* 2.11 (2012), pp. 1588–1611.

[81] David Nečas and Petr Klapetek. „Gwyddion: an open-source software for SPM data analysis“. In: *Open Physics* 10.1 (2012), pp. 181–188.

[82] Yi Sun et al. „Surface coating as a key parameter in engineering neuronal network structures in vitro“. In: *Biointerphases* 7.1 (2012).

[83] Koyo Watanabe et al. „Scanning and non-scanning surface plasmon microscopy to observe cell adhesion sites“. In: *Biomedical optics express* 3.2 (2012), pp. 354–359.

[84] Lihong Gao, F Lemarchand, and Michel Lequime. „Refractive index determination of SiO2 layer in the UV/Vis/NIR range: spectrophotometric reverse engineering on single and bi-layer designs“. In: *Journal of the European Optical Society-Rapid publications* 8 (2013), p. 13010.

[85] Micha E Spira and Aviad Hai. „Multi-electrode array technologies for neuroscience and cardiology“. In: *Nature nanotechnology* 8.2 (2013), pp. 83–94.

[86] Anil Thilsted. *Sketch of surface plasmon*. Accessed: 2024-09-21. 2013. URL: https://commons.wikimedia.org/wiki/File:Sketch_of_surface_plasmon.png.

[87] Alexey I Chizhik et al. „Metal-induced energy transfer for live cell nanoscopy". In: *Nature Photonics* 8.2 (2014), pp. 124–127.

[88] Suejit Pechprasarn et al. „Ultrastable embedded surface plasmon confocal interferometry". In: *Light: Science & Applications* 3.7 (2014), e187–e187.

[89] Koji Toma, Hiroshi Kano, and Andreas Offenhäusser. „Label-free measurement of cell–electrode cleft gap distance with high spatial resolution surface plasmon microscopy". In: *ACS nano* 8.12 (2014), pp. 12612–12619.

[90] Diethelm Johannsmann et al. „The quartz crystal microbalance in soft matter research". In: *Soft and Biological Matter* (2015), pp. 191–204.

[91] Lotfi Berguiga et al. „Time-lapse scanning surface plasmon microscopy of living adherent cells with a radially polarized beam". In: *Applied optics* 55.6 (2016), pp. 1216–1227.

[92] Rémi Boidin et al. „Pulsed laser deposited alumina thin films". In: *Ceramics International* 42.1 (2016), pp. 1177–1182.

[93] Takahisa Matsuzaki et al. „Quantitative evaluation of cancer cell adhesion to self-assembled monolayer-patterned substrates by reflection interference contrast microscopy". In: *The Journal of Physical Chemistry B* 120.7 (2016), pp. 1221–1227.

[94] Matthew Newville et al. „LMFIT: Non-linear least-square minimization and curve-fitting for Python". In: *Astrophysics Source Code Library* (2016), ascl–1606.

[95] Gregory Panaitov, Elmar Neumann, and Andreas Offenhäusser. „FIB characterisation of cell/device interface". In: *European Microscopy Congress 2016: Proceedings*. Wiley Online Library. 2016, pp. 105–106.

[96] Elisa Sani and Aldo Dell'Oro. „Spectral optical constants of ethanol and isopropanol from ultraviolet to far infrared". In: *Optical Materials* 60 (2016), pp. 137–141.

[97] Mirjam Schürmann et al. „Cell nuclei have lower refractive index and mass density than cytoplasm". In: *Journal of biophotonics* 9.10 (2016), pp. 1068–1076.

[98] Han-Min Tan et al. „High resolution quantitative angle-scanning widefield surface plasmon microscopy". In: *Scientific reports* 6 (2016), p. 20195.

[99] Thilo Baronsky et al. „Cell–substrate dynamics of the epithelial-to-mesenchymal transition". In: *Nano letters* 17.5 (2017), pp. 3320–3326.

[100] Keith Burridge. „Focal adhesions: a personal perspective on a half century of progress“. In: *The FEBS journal* 284.20 (2017), pp. 3355–3361.

[101] Xian-Wei Liu et al. „Plasmonic-based electrochemical impedance imaging of electrical activities in single cells“. In: *Angewandte Chemie* 129.30 (2017), pp. 8981–8985.

[102] D. Pulido and E. Hohenester. *Image from the RCSB PDB (RCSB.org) of PDB ID 5MC9 (Crystal Structure of the Heterotrimeric Integrin-Binding Region of Laminin-111)*. Initial deposition on 9 November 2016, released on 8 February 2017, latest revision on 17 January 2024, accessed on 16 June 2024, corresponding publication DOI: https://doi.org/10.1016/j.str.2017.01.002. 2017. DOI: https://doi.org/10.2210/pdb5mc9/pdb.

[103] David Pulido, Sadaf-Ahmahni Hussain, and Erhard Hohenester. „Crystal structure of the heterotrimeric integrin-binding region of laminin-111“. In: *Structure* 25.3 (2017), pp. 530–535.

[104] SCHOTT. *SCHOTT Zemax catalog 2017-01-20b*. Accessed: 2023-08-14. 2017.

[105] Xudong Zhang et al. „The influence of the electrode dimension on the detection sensitivity of electric cell–substrate impedance sensing (ECIS) and its mathematical modeling“. In: *Sensors and Actuators B: Chemical* 247 (2017), pp. 780–790.

[106] Anna M Chizhik et al. „Dual-color metal-induced and Förster resonance energy transfer for cell nanoscopy“. In: *Molecular biology of the cell* 29.7 (2018), pp. 846–851.

[107] Eva Kreysing. *Characterization of the cell-substrate interface using surface plasmon resonance microscopy*. Forschungszentrum Jülich GmbH, Zentralbibliothek, 2018.

[108] Eva Kreysing et al. „Nanometer-Resolved Mapping of Cell–Substrate Distances of Contracting Cardiomyocytes Using Surface Plasmon Resonance Microscopy“. In: *ACS nano* 12.9 (2018), pp. 8934–8942.

[109] Alexander W Peterson et al. „Mass measurements of focal adhesions in single cells using high resolution surface plasmon resonance microscopy“. In: *Plasmonics in Biology and Medicine XV*. Vol. 10509. SPIE. 2018, pp. 26–32.

[110] Taehwang Son et al. „Label-free quantification of cell-to-substrate separation by surface plasmon resonance microscopy“. In: *Optics Communications* 422 (2018). Trends in Label-Free Imaging, pp. 64–68. ISSN: 0030-4018. DOI: https://doi.org/10.1016/j.optcom.2017.10.001. URL: https://www.sciencedirect.com/science/article/pii/S0030401817308878.

[111] Yu-wen Su and Wei Wang. „Surface plasmon resonance sensing: from purified biomolecules to intact cells“. In: *Analytical and bioanalytical chemistry* 410 (2018), pp. 3943–3951.

[112] Frederic A Banville et al. „Nanoplasmonics-enhanced label-free imaging of endothelial cell monolayer integrity“. In: *Biosensors and Bioelectronics* 141 (2019), p. 111478.

[113] Arikta Biswas et al. „Cholesterol depletion by MβCD enhances cell membrane tension and its variations-reducing integrity“. In: *Biophysical journal* 116.8 (2019), pp. 1456–1468.

[114] Elton B Costa, Eloise P Rodrigues, and Helder A Pereira. „Sim-SPR: An open-source surface plasmon resonance simulator for academic and industrial purposes“. In: *Plasmonics* 14 (2019), pp. 1699–1709.

[115] Robert S Fischer et al. „Filopodia and focal adhesions: An integrated system driving branching morphogenesis in neuronal pathfinding and angiogenesis“. In: *Developmental biology* 451.1 (2019), pp. 86–95.

[116] Arindam Ghosh et al. „Graphene-based metal-induced energy transfer for sub-nanometre optical localization“. In: *Nature Photonics* 13.12 (2019), pp. 860–865.

[117] Hossein Hassani and Eva Kreysing. „Noninvasive measurement of the refractive index of cell organelles using surface plasmon resonance microscopy“. In: *Optics letters* 44.6 (2019), pp. 1359–1362.

[118] Carmel L Howe et al. „Surface plasmon resonance imaging of excitable cells“. In: *Journal of physics D: Applied physics* 52.10 (2019), p. 104001.

[119] Taehwang Son et al. „Enhanced surface plasmon microscopy based on multi-channel spatial light switching for label-free neuronal imaging“. In: *Biosensors and Bioelectronics* 146 (2019), p. 111738.

[120] Hossein Hassani et al. „Platinum substrate for surface plasmon microscopy at small angles“. In: *Optics Letters* 45.12 (2020), pp. 3292–3295.

[121] Eva Kreysing et al. „Correlating surface plasmon resonance microscopy of living and fixated cells with electron microscopy allows for investigation of potential preparation artifacts“. In: *Advanced Materials Interfaces* 7.6 (2020), p. 1901991.

[122] Jieling Zhao, Farid Manuchehrfar, and Jie Liang. „Cell–substrate mechanics guide collective cell migration through intercellular adhesion: a dynamic finite element cellular model“. In: *Biomechanics and modeling in mechanobiology* 19.5 (2020), pp. 1781–1796.

[123] Hossein Hassani. „From Surface Plasmon Microscopy to Refractive Index Microscopy: Label-Free Measurement of Cell–Substrate Distance and Intracellular Refractive Index“. Draft in preparation. PhD thesis. RWTH Aachen University, 2021.

[124] Eva Kreysing. „Discussion on the analysable fraction of data and reproducibility of measurements“. Oral communication. 2021.

[125] Ipsita Chakraborty and Hiroshi Kano. „Microscopic-characterization of photo-induced birefringence of azo-polymer thin film by focused surface plasmon“. In: *Optics & Laser Technology* 147 (2022), p. 107673.

[126] Artur Glavic and Matts Björck. „GenX 3: the latest generation of an established tool“. In: *Journal of applied crystallography* 55.4 (2022), pp. 1063–1071.

[127] Ralf Gommers et al. „scipy/scipy: SciPy 1.9. 0“. In: *Zenodo* (2022).

[128] Marcus Lindner et al. „Flow-induced glycocalyx formation and cell alignment of HUVECs compared to iPSC-derived ECs for tissue engineering applications“. In: *Frontiers in Cell and Developmental Biology* 10 (2022), p. 953062.

[129] Pegah Shokoohimehr et al. „High-aspect-ratio nanoelectrodes enable long-term recordings of neuronal signals with subthreshold resolution“. In: *Small* 18.22 (2022), p. 2200053.

[130] Jan Christoph Thiele et al. „Isotropic three-dimensional dual-color super-resolution microscopy with metal-induced energy transfer“. In: *Science Advances* 8.23 (2022), eabo2506.

[131] Shujing Wang et al. „Long-chain poly-d-lysines interact with the plasma membrane and induce protective autophagy and intense cell necrosis“. In: *Bioconjugate Chemistry* 33.5 (2022), pp. 938–947.

[132] Bogdana Cepkenovic et al. „Single-neuron mechanical perturbation evokes calcium plateaus that excite and modulate the network“. In: *Scientific reports* 13.1 (2023), p. 20669.

[133] Siqing Dai et al. „Label-free and dynamic monitoring of cell evolutions using wavelength-multiplexing surface plasmon resonance holographic microscopy“. In: *Biomedical Optics Express* 14.5 (2023), pp. 2028–2039.

[134] Lara Hauke et al. „Metal-induced energy transfer (MIET) for live-cell imaging with fluorescent proteins“. In: *ACS nano* 17.9 (2023), pp. 8242–8251.

[135] Dijo Moonnukandathil Joseph. „Software Redesign and Application of a Prototype SPR-Microscope: Comparative Analysis of Supported Lipid Bilayer Formation Protocols on Gold and Silicon Dioxide Surfaces for Novel Bioelectronic Sensor Platforms“. Master Thesis in Photonics. Master's thesis. Jena, Germany: Friedrich Schiller University, Sept. 2023.

[136] Eva Kreysing et al. „Effective cell membrane tension is independent of polyacrylamide substrate stiffness“. In: *PNAS nexus* 2.1 (2023), pgac299.

[137] Michelle Küppers et al. „Confocal interferometric scattering microscopy reveals 3D nanoscopic structure and dynamics in live cells“. In: *Nature Communications* 14.1 (2023), p. 1962.

[138] Fraunhofer Institute for Surface Engineering and Thin Films IST. *X-ray reflectometry (XRR)*. https://www.ist.fraunhofer.de/en/expertise/analytics-testing-technology/xrr.html. Accessed: 2024-10-15. 2024.

[139] Max-Planck-Gesellschaft zur Förderung der Wissenschaften e.V. *Was ist Leben?* Accessed: 2024-08-24. 2024. URL: https://www.synthetische-biologie.mpg.de/17480/was-ist-leben.

[140] National Center for Biotechnology Information. *PubChem Compound Summary for CID 57449, D-Lysine*. Accessed June 14, 2024. 2024. URL: https://pubchem.ncbi.nlm.nih.gov/compound/D-Lysine.

[141] National Center for Biotechnology Information. *PubChem Compound Summary for CID 5962, Lysine*. Accessed June 14, 2024. 2024. URL: https://pubchem.ncbi.nlm.nih.gov/compound/Lysine.

[142] Mikhail N Polyanskiy. „refractiveindex.info database of optical constants“. In: *Scientific Data* 11.1 (2024), p. 94.

[143] Ian Sands et al. „Interface-Mediated Neurogenic Signaling: The Impact of Surface Geometry and Chemistry on Neural Cell Behavior for Regenerative and Brain-Machine Interfacing Applications“. In: *Advanced Materials* (2024), p. 2401750.

[144] Justus Bednár. *SPRManalysis-2*. Version 2.3.8. Mar. 2025. DOI: 10.5281/zenodo.13140709. URL: https://doi.org/10.5281/zenodo.13140709.

[145] Justus Bednár, Eva Kreysing, and Andreas Offenhäusser. „Fully Automated SPRM Analysis Enables Large-Scale Mapping of HEK Cell Adhesion on Various Protein Coatings“. In: *To be submitted* (2025). Manuscript in preparation.

[146] Sheng Sun et al. „Auto-focus scanning surface plasmon resonance microscopy“. In: *Optics Express* 33.7 (2025), pp. 16551–16561.

[147] R. Paschotta. *Numerical Aperture*. RP Photonics Encyclopedia. DOI: 10.61835/fov. URL: https://www.rp-photonics.com/numerical_aperture.html (visited on 07/05/2024).

C Chemicals List

Chemical	Supplier
Sodium chloride (NaCl)	Sigma-Aldrich Chemie GmbH
Disodium phosphate (Na_2HPO_4)	Sigma-Aldrich Chemie GmbH
Potassium chloride (KCl)	Sigma-Aldrich Chemie GmbH
Monopotassium phosphate (KH_2PO_4)	Sigma-Aldrich Chemie GmbH
Tris	Sigma-Aldrich Chemie GmbH
DMEM (D6429)	Sigma-Aldrich Chemie GmbH
FBS (10270106)	Thermo Fisher Scientific Inc.
Penicillin-Streptomycin (15140122)	Thermo Fisher Scientific Inc.
Trypsin/EDTA	Thermo Fisher Scientific Inc.
PLL (P1399)	Sigma-Aldrich Chemie GmbH
PDL (P6407)	Sigma-Aldrich Chemie GmbH
Fibronectin bovine plasma (F1141)	Sigma-Aldrich Chemie GmbH
Laminin (L2020)	Sigma-Aldrich Chemie GmbH
ECM-Gel (E1270)	Sigma-Aldrich Chemie GmbH
Concanavalin-A (C0412)	Sigma-Aldrich Chemie GmbH
B27^{TM} (17504044)	Thermo Fisher Scientific Inc.
L-Glutamine (25030024)	Thermo Fisher Scientific Inc.
Gentamicin (G1397)	Sigma-Aldrich Chemie GmbH
Hanks' balanced salt solution (HBSS)	Thermo Fisher Scientific

Band / Volume 281
Enabling mixed microbial upcycling of plastic monomers
Y. S. Ackermann (2024), XVI, 203 pp
ISBN: 978-3-95806-749-3

Band / Volume 282
Folding and structural studies of *saccharomyces cerevisiae* Phosphoglycerate Kinase
N. Bustorff (2024), xxvi, 126 pp
ISBN: 978-3-95806-754-7

Band / Volume 283
The role of cellular development in multicellular antiphage defense of *Streptomyces*
T. Luthe (2024), vi, 173 pp
ISBN: 978-3-95806-768-4

Band / Volume 284
Probing the Transformation from Transition Metal Complexes to Extended Two-Dimensional Nanostructures
D. Baranowski (2024), XII, 103 pp
ISBN: 978-3-95806-772-1

Band / Volume 285
Neutron Scattering
Lectures of the JCNS Laboratory Course held at Forschungszentrum Jülich and at the Heinz-Maier-Leibnitz Zentrum Garching
edited by S. Förster, K. Friese, M. Kruteva, S. Nandi, M. Zobel, R. Zorn (2024), ca. 365 pp
ISBN: 978-3-95806-774-5

Band / Volume 286
***Ab initio* investigation of intrinsic antiferromagnetic solitons**
Amal Jawdat Nayef Aldarawsheh (2024), xv, 164 pp
ISBN: 978-3-95806-785-1

Band / Volume 287
Understanding the dynamics of Plant-Bacteria-Bacteriophage interactions as a means to improve plant performance
S. H. Erdrich (2024), ix, 176 pp
ISBN: 978-3-95806-791-2

Band / Volume 288
Prediction of Magnetic Materials for Energy and Information Combining Data-Analytics and First-Principles Theory
R. Hilgers (2024), xv, 215 pp
ISBN: 978-3-95806-795-0

Band / Volume 289
Biodegradation and microbial upcycling of plastics
J. de Witt (2025), XVI, 259 pp
ISBN: 978-3-95806-804-9

Band / Volume 290
Practical Methods for Efficient Analytical Control in Superconducting Qubits
B. Li (2025), 202 pp
ISBN: 978-3-95806-807-0

Band / Volume 291
Ab initio investigation of topological magnetism in two-dimensional van der Waals heterostructures
N. Abuawwad (2025), xviii, 135 pp
ISBN: 978-3-95806-808-7

Band / Volume 292
Tolerance engineering of Pseudomonas for the efficient conversion and production of aldehydes
T. Lechtenberg (2025), XVI, 185 pp
ISBN: 978-3-95806-817-9

Band / Volume 293
Exploring the process window for production of itaconic, 2-hydroxyparaconic, and itatartaric acid with engineered *Ustilago* strains
P. Ernst (2025), x, 145 pp
ISBN: 978-3-95806-825-4

Band / Volume 294
Surface Plasmon Resonance Microscopy for the Characterization of Cell-Substrate Distances
J. Bednár (2025), xxiii, 187 pp
ISBN: 978-3-95806-830-8

Weitere ***Schriften des Verlags im Forschungszentrum Jülich*** unter
http://wwwzb1.fz-juelich.de/verlagextern1/index.asp

Schlüsseltechnologien / Key Technologies
Band / Volume 294
ISBN 978-3-95806-830-8

Mitglied der Helmholtz-Gemeinschaft

JÜLICH
Forschungszentrum